The Stellar Content in Clusters of Galaxies

by

Christopher J. Bildfell
B.Sc., University of Western Ontario, 2003
M.Sc., University of Victoria, 2007

A Dissertation Submitted in Partial Fulfillment of the
Requirements for the Degree of

DOCTOR OF PHILOSOPHY

in the Department of Physics and Astronomy

The Stellar Content in Clusters of Galaxies

by

Christopher J. Bildfell
B.Sc., University of Western Ontario, 2003
M.Sc., University of Victoria, 2007

Supervisory Committee

Dr. A. Babul, Co-Supervisor
(Department of Physics and Astronomy)

Dr. H. Hoekstra, Co-Supervisor
(Department of Physics and Astronomy)

Dr. J. Willis, Departmental Member
(Department of Physics and Astronomy)

Dr. A. Brolo, Outside Member
(Department of Chemistry)

Supervisory Committee

Dr. A. Babul, Co-Supervisor
(Department of Physics and Astronomy)

Dr. H. Hoekstra, Co-Supervisor
(Department of Physics and Astronomy)

Dr. J. Willis, Departmental Member
(Department of Physics and Astronomy)

Dr. A. Brolo, Outside Member
(Department of Chemistry)

ABSTRACT

We investigate three separate topics associated with the formation and evolution of the stellar mass component in galaxy clusters. The work presented herein is based primarily on optical imaging and spectra taken with, respectively, the Canada-France-Hawaii Telescope and Gemini North/South. We confront the result from the optical data analysis with the results from the analysis of high-resolution X-ray data taken with the Chandra and XMM-Newton space observatories. Confirming earlier results, we find that 22% of brightest cluster galaxies (BCGs) show central inversions in their optical color profiles (blue-cores), indicative of recent star formation or AGN activity. Based on the extended sizes of the blue-core regions we favour recent star formation. Comparison with the host cluster central entropies (and other X-ray properties) demonstrates that the source of cold gas required to fuel the recent activity in BCG cores is direct condensation from the rapidly cooling intra-cluster medium.

We measure the giant-to-dwarf ratio (GDR) of red sequence galaxies in a sample of 97 clusters to constrain its evolution over the redshift range $0.05 < z < 0.55$.

We find that the GDR is evolving and can be parameterized by $GDR = (0.88 \pm 0.15)z + (0.44 \pm 0.03)$. We find that the intrinsic scatter in this relation is consistent with zero, after accounting for measurement error, Poisson noise and contributions from large-scale structure. After correcting for cluster mass effects we investigate the evolution of the individual dwarf and giant populations in order to probe the source of the observed GDR evolution. Beyond $z = 0.25$ the GDR evolution is driven by an increase in the number of dwarfs (consistent with interpretations from the literature), however, below $z = 0.2$ the GDR evolution is caused by a significant reduction in the number of giants. We interpret this a evidence for a significant number of major mergers in the giant population at late times. This is supported by the relatively short dynamical friction timescales for these galaxies.

We use velocity-broadened stellar template models to fit the optical spectra of 19 BCGs in order to measure their the line-of-sight component of their central velocity dispersions σ. The σ values are combined with previous measurements of effective radii r_e and effective surface brightness $\langle I \rangle_e$ to investigate the properties of the BCG fundamental plane. We measure a BCG fundamental plane parameterized by $\log r_e = \alpha \log \sigma + \beta \log \langle I \rangle_e + \gamma$ with best fit parameters $\alpha = 1.24 \pm 0.08$, $\beta = -0.80 \pm 0.1$ and $\gamma = (0.3 \pm 2.0) \times 10^{-4}$. We constrain the intrinsic scatter in this relation to be $\delta_{int} = 0.066 \pm 0.010$ in r_e, consistent with previous measures of the scatter in the fundamental plane for regular cluster ellipticals. Comparing the slope parameters (α, β) of the BCG FP to those from previous studies of the FP for regular cluster ellipticals, we find that there is no conclusive evidence for curvature in the unified FP. We use the σ measurements to estimate the BCG dynamical masses M_{dyn}. Comparing these estimates with mass proxies for the clusters (T_x, n_g) we find that BCG mass is independent of cluster mass with $M_{dyn} = (2.9 \pm 1.8) \times 10^{12} M_{\odot}$.

Contents

List of Tables

List of Figures

ACKNOWLEDGEMENTS

If it takes a village to raise a child then it must take an entire metropolis to raise a child and get said child through grad school. I am truly grateful for all the help and support that I have received throughout the years it took me to complete this degree. Although this thesis represents a tremendous personal achievement, it would have been impossible to complete without my fabulous supporting cast. And since this isn't the academy awards and the orchestra won't start playing me off stage, I have the wonderful opportunity to thank everyone here personally in full detail. So here it goes...

To begin, I would like to thank my thesis committee, Arif, Henk, Jon, Alex, for bearing with me through both rough seas and calm waters. It has been a fun ride and I'm proud of the work that we accomplished together. Several important results came out of this thesis, resolving some debates, impacting others and providing new questions for future research to address. A special thanks goes out to Ken Rines, who agreed to serve as my external examiner on short notice, bringing an outside perspective and contributing several important comments that helped to improve this work.

Though they have already been mentioned, I need to single out my co-advisors Henk Hoekstra and Arif Babul. I have learned so much from the both of you over the years. I couldn't imagine where I would be now without the valuable knowledge you have transferred into my skull. Henk, you showed me all I know about data analysis and manipulation; valuable skills in any racket. Arif you taught me how to 'connect the dots' of various findings, be it theory or observation, as well as the art of crafting a diplomatic email. I enjoyed working with you and I hope that our collaboration continues for many years to come.

As any student quickly realizes, a healthy team of administrative staff is a must if you want to survive the perils of a grad degree. These people help you navigate pitfalls, pick you up when you're down and hand you a map when you're lost in the woods. Thank you Susan, Milena, Rosemary, Chantal, Monica, Michelle and Amanda for keeping my ship on course. Likewise, I am very grateful to Stephenson Yang for fixing my computer when it was feeling sick, restoring crashed disks, keeping the network running smoothly and coming in on weekends to push the reset button. As the kids say, you're da-bomb! Well, I don't think the kids are actually saying that anymore, but you get the idea.

I would like to acknowledge all my fellow grad students through the years who, in addition to providing a sounding board for science talk, have helped to make life around the department a lot of fun. Thanks to Razzi, Andy, Niko, Sheona, Mason, the other Chris B., Azzi, J.C., Wes, Karun, Helen, Charli, Hannah, Lisa, Jillian, Melissa, Ryan, Kaushi, Frank, Sarah and Shadi. I am proud to be part of such a distinguished group and I'm looking forward to seeing where everyone ends up.

Thanks to my dutch crew, which is now liberally scattered about the globe. Your hospitality made me feel that I was truly a welcome and legitimate member of the Leiden group, even though I was only there for short periods of time. Thanks Edo, Elisabetta, Malin, Stephania, Remco, Marcel, Tim, Freeke, Craig, Rob, Ben, Hendrik, Niruj, Ernst, Olivera, Brent and Jarle for being friendly with 'that Canadian guy' and putting up with me while I weaselled my way onto your scene.

I give a verbal fist-bump to all my west-coast and Windsor friends who helped me maintain sanity during the tough times. Thanks to Andrew, Kristen S, Derek, Nam, Aaron, Rich, Torb, Kari, BJ, Kurtis, Randi, Becca, Gavin, Will, Anya, Matt, Dave, JD, Ben, Olivia, Jeff, Jean, Nick, Corinne, Erin, Kelly, Simone, Leah, Marty, Ellen, Ian, David and Kristen P (+Ellen, Eden). To the Icelanders, Brittany, Reyna, Robin, Jodi, Tom, Lois, I say takk! Lastly, I don't know what I would have done without the rich basketball community in Victoria and I thank you Mark, Vim, Ramil, Rick, Mike P, Andrew Student, Lexi, Melissa, Chansa, Andre, Matt H, Mike H and Jason, for keeping me physically fit and mentally stable.

I am ever grateful for the fantastic support of my family, who I wouldn't trade for any other in 10^6 lifetimes. Thanks Ma and Dave, Dad and Louise and Victoria, Guds and Mark, Corot and Jeri, Rob and Ros, Barbara and Charles, Ben and Paige, Quinn and Georgia, Ciara, Tessa, Nick, Kirsten, Connor. Thanks to my in-laws, Kuldip, Rajindar, Narinder and Tavleen, who made it easy to become part of their wonderful family.

I would also like to acknowledge all of my most influential teachers who showed me the rewarding path of knowledge, science, creativity and higher education. Thanks to Hneidi, Winterburn, Holmes, Spinx, Zavitz, Landstreet, Gray and VandenBerg. I most definitely would not be where I am today without your inspiration. I would also like to thank all the people associated with my own teaching experience, the people that allowed me to pass on my knowledge and passion for astronomy. Thanks Russ Robb and all my wonderful (and not so wonderful) students over the years. You helped to make the classroom both easy and fun!

Of course I need to thank all of my colleagues who's advice, input, or direct contribution was necessary for the completion of this thesis. Thank you Dave Sand, Dennis Zaritsky, Inger Jorgensen, Stephen Gwyn, Mark Voit, Michael Balogh, Ian McCarthy, Melissa Graham, Chris Pritchet, Andi Mahdavi and Sheona Urquhart.

And now I have just about reached the end of my rambling, but I can't finish without acknowledging the most important person of all. In the same way I eat my meals, I have saved the best bit for last. Thank you to my beautiful and hilarious wife Anudeep, or as you're now known, Mrs. Dr. Bildfell :P (is it acceptable to put emoticons in these things?). You are the light and love of my life, shining bright like a smiling moon, the most patient and accommodating woman, with a weird, quirky streak that I find irresistible. You are my beacon, my lighthouse, my GPS and I would be lost without you.

Thank you all so much,
Chris

DEDICATION

In memory of J. T. Bildfell

Chapter 1

Introduction

1.1 Galaxy Clusters and Their Stellar Content

Clusters of galaxies are the most massive gravitationally-bound structures in the Universe, with total masses ranging from a few $10^{14} M_{\odot}$ up to $10^{15} M_{\odot}$ or greater. Typical galaxy clusters can host hundreds of galaxies in a region of space only a few Mpc across. They are assembled hierarchically via mergers of galaxy and group-sized halos and represent the largest virialized systems in the Universe to date. As the most massive structures, clusters are also among the most recently formed, with a median formation epoch (redshift at which 1/2 of the final mass of the cluster is assembled) of $z \sim 0.6$ (Yun et al. 2008).

Clusters are composed of roughly 13% regular baryonic matter, while the remaining majority of the mass is made up of dark matter, an exotic form of matter that does not interact electromagnetically and has only been detected via its gravitational interaction. Lacking any coupling to the electro-magnetic field, dark matter can be easily simulated using gravity alone. Furthermore, as it dominates the mass budget in clusters, simulations including only dark matter can provide excellent approximations for the formation of galaxy clusters and large-scale structure in the Universe as a whole. We show an example of the formation process through the images in Figure 1.1. Each panel of the figure shows a snapshot of the dark matter density distribution at a specific redshift. The images shown here are taken from the Millennium Simulation project[1] (Springel et al. 2005). In the image in the final panel, labelled (d), a massive galaxy cluster has formed by $z = 0$. As the simulation progresses the detailed

[1] http://www.mpa-garching.mpg.de/galform/millennium/

large-scale structure of the Universe becomes more clearly defined. This structure, often referred to as the cosmic web, is constructed of filaments of high density, along with voids of low density. Massive galaxy clusters tend to form at the nodes of this web, several massive filaments meet. Examining the earliest snapshot, panel (a), one can see that despite the relatively smooth density distribution at early times, the spatial location of what will become the $z = 0$ galaxy cluster is already established at the highest initial density peak. The initial density distribution is assumed to be a result of quantum fluctuations, in an otherwise uniform density distribution, that are amplified during the period of inflation shortly ($\sim 10^{-36}$s) after the Big Bang that created the Universe. The result of this process is a cosmic density distribution similar to that seen in Figure 1.1, with the highest density peaks becoming the seeds for structure formation, eventually giving rise to galaxies, galaxy groups and galaxy clusters.

We can learn much about clusters from simulations of the evolution of the cosmic dark matter distribution, as dark matter is the dominant component of matter in the Universe. However, we cannot directly observed the dark matter component and instead we must make inferences about its distribution from the way in which it interacts gravitationally with the luminous component of baryonic matter, in its various forms. The fraction of the total mass in clusters that is in the form of baryons is measured to be $\Omega_b/\Omega_m = 0.133 \pm 0.004$ (Gonzalez et al. 2007) and is split into gaseous and stellar components, the relative contributions of which vary as a function of cluster mass. The gaseous component, referred to as the intra-cluster medium (ICM), is present in the form of a hot plasma with temperatures between 10^7K and 10^8K, which emits at X-ray wavelengths via the thermal bremsstrahlung process. The stellar component is comprised of stars that are gravitationally bound to the cluster member galaxies as well as a contribution from a group of stars that are unbound from any particular individual galaxy, orbiting freely in the potential of the cluster as a whole; the intra-cluster stars (ICS). Figure 1.2, taken from Gonzalez et al. (2007), shows the contributions of the ICM and stellar components to the total baryon fraction in clusters, as a function of cluster mass. The cluster mass is parameterized here by M_{500}, which denotes the mass contained within a cluster-centric radius of r_{500}, inside which the mean density $\langle\rho\rangle$ is 500 times the critical density ρ_c, where $\rho_c = \frac{3H^2}{8\pi G}$, with H and G represent the Hubble constant and Newton's gravitational constant, respectively.

The data in Figure 1.2 show that although the gas mass and stellar mass fractions

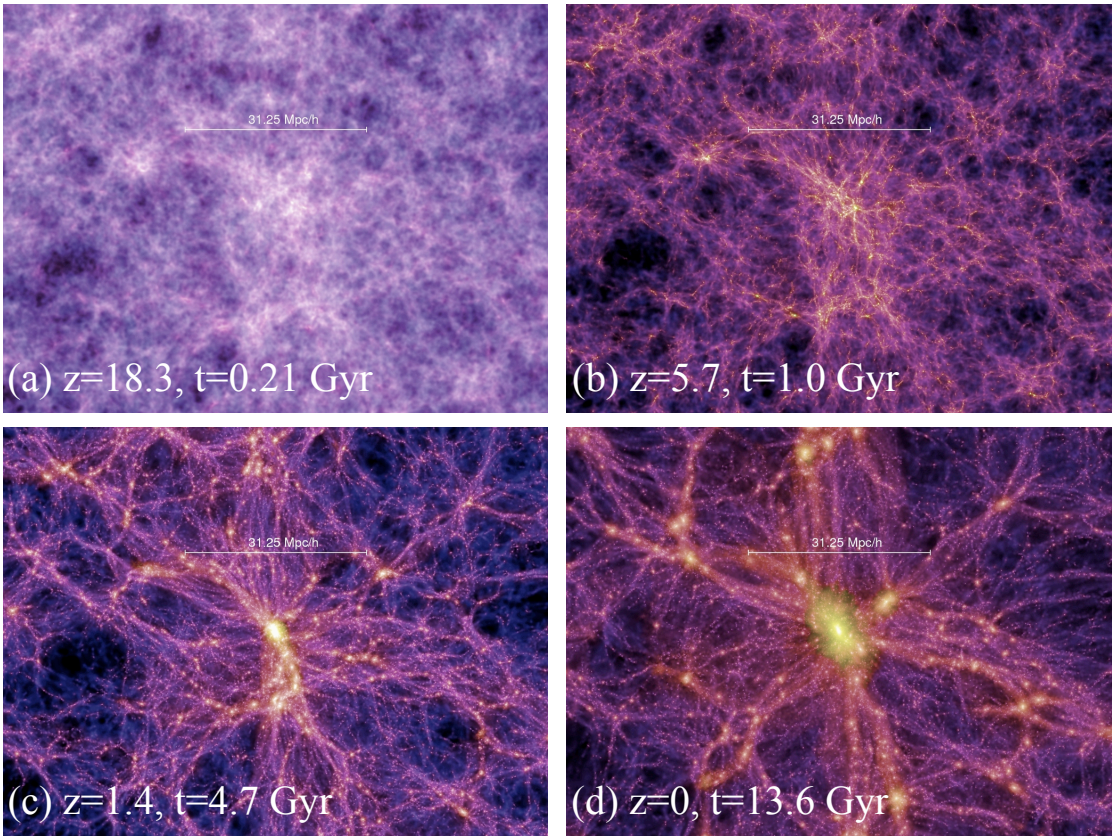

Figure 1.1: Snapshot images of the projected dark matter density distribution taken from the Millennium Simulation project (Springel et al. 2005). Each panel shows the same region of simulated space at a different redshift, or universe age. The data represent the projection of a 15 Mpc/h slice of the simulation. Black and purple areas of the figure show regions of low density while white and yellow areas of the figure show regions of high density. In the panel labelled (d) we see that a massive galaxy cluster has formed in the center of the image by $z = 0$.

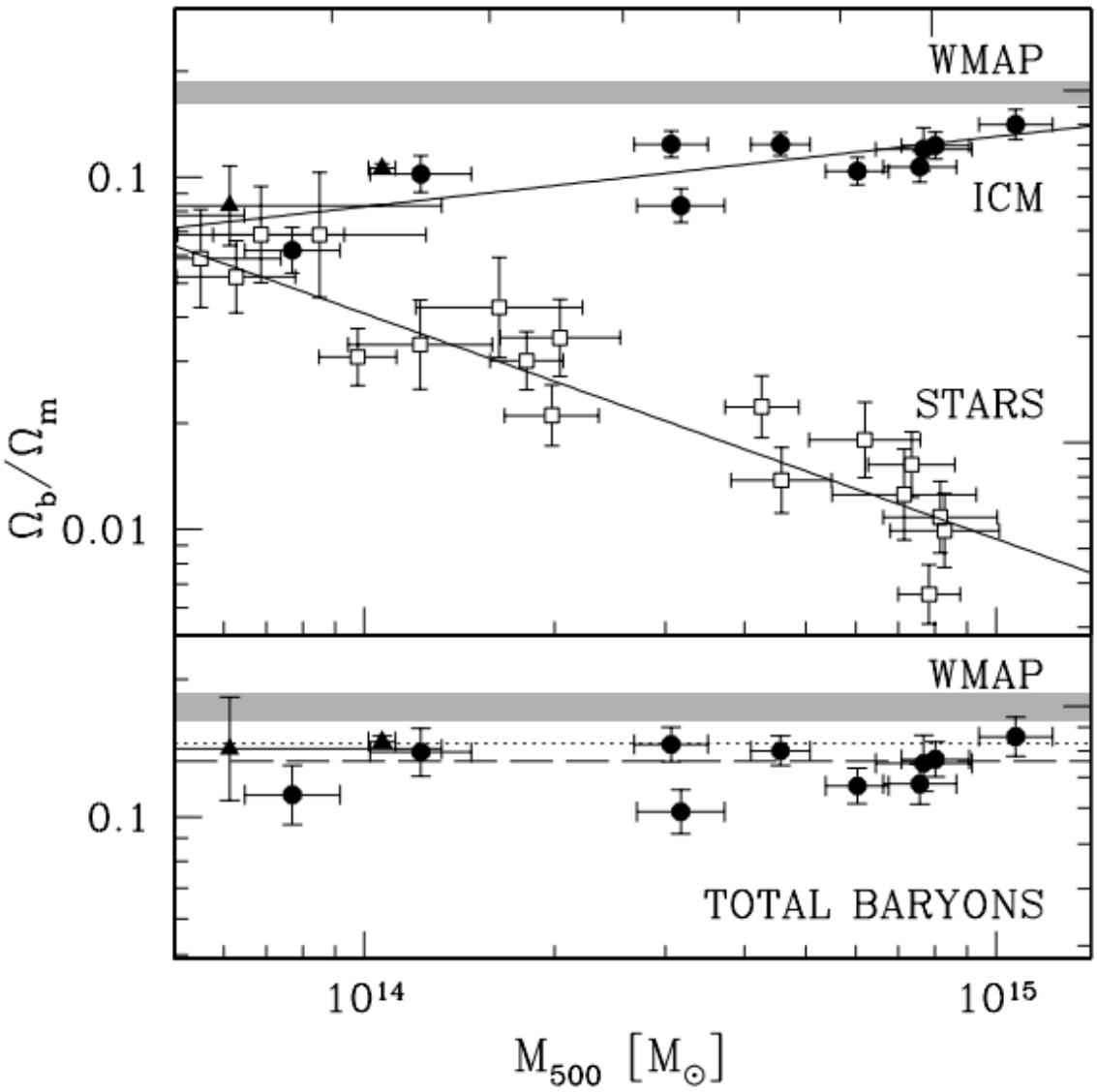

Figure 1.2: Taken from Gonzalez et al. (2007). Top: Determination of cluster and group baryon fractions within r_{500} as a function of M_{500}. Filled symbols show the X-ray gas mass fractions from Vikhlinin et al. (2006; circles) and Gastaldello et al. (2007; triangles). Open squares show the stellar mass fraction combining BCG + ICS + galaxies. The shaded region shows the $WMAP$ 1σ confidence region for the universal baryon fraction (Spergel et al. 2006). Bottom: The total baryon fraction derived for Vikhlinin et al. (2006) and Gastaldello et al. (2007) clusters after correcting for the best fit stellar baryon fraction versus M_{500} relation. The weighted mean for the sample (dashed line) is $\Omega_b/\Omega_m = 0.133 \pm 0.004$ (statistical errors only). The un-weighted mean for the combined Zhang et al. (2007) and Rasmussen et al. (2004) samples (dotted line) is included to provide a sense of systematic uncertainties.

in clusters do indeed vary with the mass of the main halo, they compensate for one another to preserve a constant total baryon fraction. The grey shaded region in the figure indicates the 1σ confidence interval for the universal baryon fraction as determined by the Wilkinson Microwave Anisotropy Probe data (WMAP; Spergel et al. 2006), showing that clusters are quite efficient at retaining their baryons. After considering the large systematic errors involved with measuring the value of Ω_b/Ω_m in clusters, Gonzalez et al. (2007) conclude that there is no compelling evidence for undetected baryons in clusters. This independent confirmation of the WMAP universal baryon fraction highlights the power of cluster observations as cosmological probes; a topic that is discussed in more detail below. It is important to note that this type of baryon accounting relies on analysis of multi-wavelength observations (X-ray, optical) to measure the ICM gas mass and stellar mass of the galaxies, BCG and ICS. The ICS is particularly challenging to measure, owing to its diffuse nature and consequently low surface brightness. With the current generation of instruments this is only possible for the lowest redshift clusters, as cosmological dimming and systematic errors associated with the point spread function (PSF) and flat-fielding prohibit constraining the ICS fraction beyond $z \sim 0.15$.

There are three main mechanisms discussed in the literature that are believed to contribute to the intra-cluster stellar population. These are galaxy harassment, galaxy interactions, in-situ star formation. Galaxy harassment (Moore et al. 1996) describes the influence of a massive galaxy or cluster core in tidally stripping the outer regions of less massive satellite galaxies over the course of many peri-centric passages. Harassment operates preferentially in clusters of galaxies where the orbital velocities of galaxies about the cluster (galaxian velocity dispersion) is large compared to the orbital velocities of stars about the galaxies (stellar velocity dispersion). Galaxy interactions describe a more complete tidal disruption of galaxies over only a few orbits. Galaxy interactions are thus more important on group scales where the stellar velocity dispersions about individual galaxies are comparable to the galaxian velocity dispersion about the main cluster/group halo. In contrast with these two mechanisms, which are driven solely by gravitational processes, in-situ star formation can occur when gas-rich cluster galaxies are ram-pressure stripped on infall. The stripped gas is then free to cool and form stars directly in the ICM, a mechanism which has recently observed (eg. Boissier et al. 2012, Vollmer et al. 2012). These various mechanisms make different predictions for the ICS fraction owing to their dependence on the mass of the main halo. Recent work by Puchwein et al. (2010) based on high-

resolution hydrodynamical simulations of clusters including AGN feedback predicts that the ICS population is put in place as early as $z > 1$, with intra-cluster stellar fractions representing $\sim$45% of the total stellar mass, almost independently of cluster mass. While these values are higher than those obtained from observations of the ICS population, these simulations can provide insight into the dominant process governing ICS production. Further progress however, requires better observational constraints on the ICS population, both as a function of cluster mass and look-back time. The coming generation of $\sim$ 30 m telescopes should help shed light on this problem.

Figure 1.2 also shows another way in which the observation of the stellar content of clusters is important to astronomy. The declining stellar mass fraction with increasing M_{500} hints at a growing inefficiency of star formation in more massive systems. This relates to the unresolved question of how the various processes associated with galaxy evolution (star formation, gas mass, central black hole growth) depend on the environment in which the galaxy resides, a topic of vigorous debate for decades. Since the discovery of the morphology-density relation (Dressler 1980), it is well established that environment is an important consideration for galaxy evolution, with some of the earliest evidence for the influence of environment coming from Hubble and Humason (1931).

Figure 1.3 shows the fractions of elliptical (E), lenticular (S0) and spiral+irregular (S+Irr) galaxies as a function of the projected local density. The fraction of spiral galaxies falls off steadily with increasing local density, while the lenticulars and elliptical show the opposite behavior. More recent studies (eg. Bamford et al. 2009, van der Wel et al. 2010), carefully accounting for the natural correlation between galaxy mass and morphology, have confirmed the morphology density relation holds at fixed galaxy mass, at least in the low redshift Universe. Further evidence arises from the examination of galaxy colors. The fraction of red or passive galaxies at a fixed stellar mass is higher in groups and clusters than it is in the field (Weinmann et al. 2006, Baldry et al. 2006, Kimm et al. 2009).

There are several factors related to environment that may be playing a role in the way that galaxies form and evolve. For instance, galaxies residing in more dense environments are more likely to be subject to interactions with other nearby galaxies, though this effect competes with the effect of the main halo's velocity dispersion, which reduces galaxy interactions in progressively more massive groups and clusters. The local density of the surrounding intra-cluster or intra-group gas may also be important as this can affect the efficiency of ram-pressure stripping, removing gas

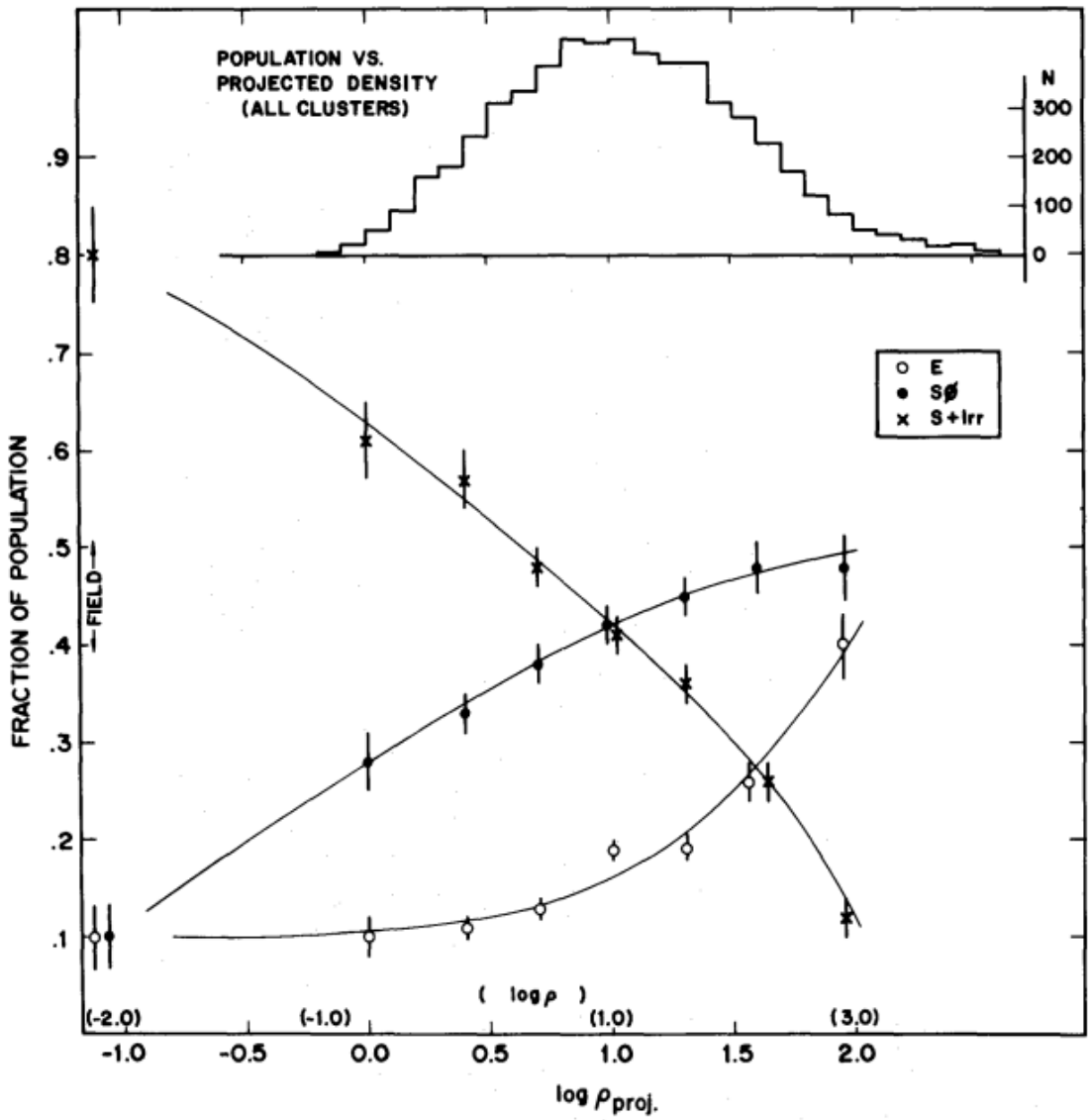

Figure 1.3: Taken from Dressler (1980). The fractions of elliptical (E), lenticular (S0) and spiral+irregular (S+Irr) galaxies as a function of the projected local density in galaxies Mpc^{-2}. The histogram at the top of the figure shows the number density of galaxies in each bin that are used to measure the relative fractions of each morphological type.

from galaxies, shutting down star formation and transforming morphologies. Furthermore, ram pressure stripping is proportional to the square of the infall velocity ($P_{ram} \propto \rho v^2$). The environments with the highest density (ρ) are associated with the most massive group/cluster halos. Such massive halos, with their deep gravitational potentials, also generate the highest infall velocities (v), further boosting the effect of ram pressure. We should also consider timing arguments associated with the initial density distribution of the universe. The highest density peaks in this distribution will collapse first, forming galaxies locally at the earliest times. By this mechanism the galaxies in the densest environments are also expected to be the oldest ones, which could also lead to a difference in the observed morphology of galaxies in high versus low - density environments. Yet another possibility is that star-formation efficiency, the efficiency with which gas is converted to stars within galaxies, is itself dependent on the local density.

There are clearly many competing effects related to the density of the local environment which may influence the evolution of galaxies, transforming their luminosities, colors and morphologies. A detailed picture of how these ingredients come together to shape the observable features of galaxies has yet to emerge. However, it is evident that future advancements will depend critically on placing tight constraints on the properties of the stellar content in galaxies in order to compare with increasingly complex numerical models. Observations of the stellar content of galaxies in groups and clusters will continue to be important probes as we seek to understand the effect of environment on the evolution of galaxies.

Another area of research to which clusters are important is in the study of cosmology. Over the last decade there have been significant advancements in the field of cosmology. Precision measurements of the anisotropy in the cosmic microwave background (CMB; Spergel et al. 2003, Komatsu et al. 2011), a relic of the big bang, combined with results based on the observations of type Ia supernovae (SNIa; Riess et al. 2009), have lead to a widely accepted set of cosmological parameters. This current cosmological paradigm consists of the visible matter (baryons) a component of cold dark matter (unspecified particle) and a component of energy density Λ acting against gravity thought to be associated with the vacuum. This model is often referred to as the ΛCDM cosmology and consist of a set of ten or more parameters including, the age of the universe $t_0 = 13.75 \pm 0.11$Gyr, the Hubble constant $H_0 = 70.4 \pm 1.3$km s^{-1}Mpc^{-1}, various energy densities in different forms ($\Omega_b = 0.0456 \pm 0.0016$, $\Omega_c = 0.227 \pm 0.014$, $\Omega_\Lambda = 0.728 \pm 0.015$; baryons, dark matter,

Λ, respectively), and others (Jarosik et al. 2011).

It is also possible to study cosmology using galaxy clusters, which would allow us to confirm the CMB+SNIa results, as well as break some of the degeneracy on parameter constraints. Clusters act like cosmographic beacons in the web of large-scale structure. Measurements of the space density of clusters as a function of cluster mass and redshift are sensitive to a variety of cosmological parameters. One of the simplest ways to infer cosmological parameters from cluster observations is to count the number of clusters above a given mass and compare these results with cosmological simulations of structure formation. The use of clusters in this context of cosmological probes requires the following three conditions: (1) a large sample of clusters with a well understood selection function, (2) a low-cost observable 'x' that can be used as a high-precision mass proxy, and (3) a robustly calibrated scaling relation between the mass proxy 'x' and the 'true' mass of the cluster, where the 'true' mass refers to the relevant mass for comparison with simulations. The current status of cluster cosmology seems to be limited primarily by items (2) and (3). The crux of the problem is that masses of clusters are difficult to measure, with each observable mass proxy 'x' subject to unique biases that must be well understood before progress can be made. Mass proxies exist across a wide range of wavelengths from microwave to X-ray. One of the earliest cluster mass proxies, the line of sight velocity dispersion of cluster galaxies, lead to some of the first evidence for the existence of dark matter (Zwicky 1933). However, this measure of the cluster mass requires obtaining spectroscopic redshifts for a large number of cluster members, an observationally expensive endeavour.

More recent studies tend to favor mass proxies derived from observations of the weak gravitational lensing signal, inverse compton scattering of CMB photons (Sunyaev-Zel'dovich effect; SZ effect) and the X-ray emission from the hot ICM because they are less expensive to obtain and therefore better suited for large surveys. Relevant to this thesis, a detailed knowledge of the stellar component in clusters is critical to fully understanding the biases associated with these mass proxies. The weak lensing signal, typically measured at optical wavelengths, is obtained from the analysis of the shapes of background galaxies. This process is dependent on minimizing contamination by cluster members, often rejected on the basis of the color of their stellar populations. Weak lensing also depends on selecting an appropriate cluster center, which has been shown to be affected by incorrect assumptions regarding galaxy colors (Mandelbaum et al. 2010). A full understanding of the X-ray observations of cluster involves detailed modelling of the interplay between non-gravitational bary-

onic processes such as radiative cooling, AGN heating, turbulence, heating, shocks and star formation. Star formation and black hole accretion represent the ultimate sink for the cooling gas. Multi-wavelength studies of the stellar content of the central galaxies in cluster can provide a measure of the amount of gas that condenses out of the ICM as a byproduct of competition between heating and cooling. As for the SZ signal, it is not directly dependent on the stellar content in clusters but it is indirectly dependent through necessary calibration of SZ mass proxies, which requires comparison with either X-ray, lensing. For a more complete review of clusters as cosmological probes see Allen et al. (2011).

As mentioned briefly above, a full understanding of the state of the intra-cluster gas requires that models incorporate a wide range of non-gravitational processes such as radiative cooling, star formation, feedback from AGN, conduction, turbulence, metal enrichment, stellar winds and more. The early cooling flow models of galaxy clusters (Fabian 1994), based on radiative cooling alone, implied that clusters ought to be in a quasi-equilibrium state where the loss of thermal energy causes mass to flow inward and drop out of the X-ray emitting phase at the rate of hundreds to thousands of solar masses per year. X-ray spectra observations by Peterson et al. (2003), however, show that the level of cold gas in the cores of cluster is much less than that expected for a cooling flow model, implying that a significant amount of heating must be taking place in order to offset the radiative losses. The quantification of star formation indicators at radio, optical and infrared wavelengths by Bildfell et al. (2008), Cavagnolo et al. (2008) and Rafferty et al. (2008) find that a significant fraction of BCG are hosts to low levels of recent star formation. Furthermore these studies also find that the source of cold gas that fuels this activity is consistent with expectations for the cooling ICM, albeit at much lower rates than the predictions of cooling flow models. Taken together, these results suggest a complex model for the evolution of cluster gas, in which the heating is insufficient to stop the gas from cooling completely and instead is only able to temper star formation rates. Realistic models must incorporate the vast array of physical processes mentioned above in order to provide a complete and satisfactory description of clusters. Such models are much too complex to write down analytically and instead must be handled numerically. The existing computing technology is not powerful enough to model all relevant non-gravitational processes directly, as this would require simultaneous resolution of a single system on scales as large the cluster itself ($\sim$Mpc) and as small as the accretion disk of the central AGN ($\sim$pc). Because of these challenges, much of the baryonic

physics in numerical cluster models must be approximated, which requires calibration using observational constraints. Further study of the stellar content of BCGs is also required, as star formation is a critical ingredient in tracing the energy and mass flow throughout the life of these systems. Specifically, progress requires high spatial and spectral resolution observations of BCGs across a broad range in wavelengths in order to place more stringent constraints on their star formation histories, which can then be used to calibrate numerical models.

It is evident that the observation of stellar content of clusters of galaxies is an important part of a complete understanding of several fields in astronomy. From the cosmology to galaxy formation to the makeup and evolution of the clusters themselves, the stars in clusters are sensitive probes of many important baryonic process in these systems. Furthermore through their gravitational interaction with dark matter, they provide a method by which to trace this otherwise invisible component of mass. In the remainder of this thesis I will detail several projects relating to the topics discussed above, which are all in some way linked by the common theme of the stellar content in galaxy cluster.

1.2 Description of Primary Data Samples

The work described in this thesis is based primarily on the combination of two separate surveys of galaxy clusters, the Canadian Cluster Comparison Project (CCCP) and the Multi-Epoch Nearby Cluster Survey (MENeaCS). While most of the data used comes from these two surveys, to be described in more detail below, the results presented here have been supplemented with further data from various archives where needed. These supplementary data are discussed in each chapter where they are relevant. To provide some context with which to compare our results to similar work in the literature, we outline here some of the more important characteristics of the CCCP and MENeaCS primary data sets.

The purpose of the CCCP is to compare baryonic tracers of clusters mass, such as richness and weak lensing signal, to the mass derived from analysis of the hot, diffuse intra-cluster medium (ICM) as derived from the modelling of high-high resolution X-ray observations. Further goals of the CCCP include the detailed calibration of cluster X-ray and optical scaling relations including quantification of their observational and intrinsic scatter. This survey has already lead to several publications (eg. Bildfell et al. 2008, Hoekstra et al. 2012, Mahdavi et al. 2013) and further investigations using

these data are ongoing. The CCCP cluster sample contains 52 clusters and is drawn from two separate cluster sample sources. Of these 52 clusters, 20 are selected based on the existence of deep archival B and R band imaging taken with the CFH12k instrument on the Canada-France-Hawaii Telescope (CFHT). To expand this sample of 20 clusters we add 30 more clusters selected from the cluster catalog of Horner (2001), which itself is created from the X-ray imaging and spectroscopy data taken with the Advanced Satellite for Cosmology and Astrophysics (ASCA). The ASCA clusters are selected with the requirement that their ASCA temperature be above $T_x > 5$ keV and that they be in the redshift range $0.15 < z < 0.55$; criteria that the CFH12k archival clusters also satisfy. In order to provide sensitivity to cluster morphology and thermal state (ie. cool-core/non-cool-core), the ASCA clusters are also selected such that the final data set spans the full observed range of scatter seen in the ASCA $L_x - T_x$ relation. These additional 30 clusters are observed for at least 1600 s in the g' band and 2400 s in the r' band with the MegaCam instrument at CFHT. To mitigate problems associated with a decreasing lensing signal, for the clusters at $z > 0.3$ the exposure times in g' and r' are 800 and 1200 s longer respectively. We add to this two additional clusters found in the MegaCam fields bringing the total number of CCCP clusters to 52, although these last two clusters do not strictly satisfy the redshift and temperature selection criteria mentioned above.

The primary science goals of the MENeaCS are threefold. First, to monitor clusters and identify supernovae (SN) within them in order to measure the SN type Ia (SNIa) rate in clusters for the purpose of constraining the SNIa progenitor mechanism(s). Second, to employ galaxy-galaxy weak lensing as a means to measure the truncation scales of dark matter halos as a function of cluster-centric distance. Lastly to directly and indirectly measure the fraction of stars in clusters which are unbound from any given host galaxy; the intra-cluster stars (ICS). The sample consists of 58 clusters selected from the BAX X-rays Galaxy Clusters database[2], which is based on published data from a large variety of X-ray observatories. The lensing goals require a large number of background sources to accurately measurement of the shapes of individual cluster galaxies, which imposes a redshift constraint $0.05 < z < 0.15$ on the sample selection. To restrict the sample to massive clusters only we impose an X-ray luminosity selection limit of $L_x > 3 \times 10^{44}$ erg s^{-1}. We note that due to a lack of deep X-ray coverage, for many of the clusters in this redshift range L_x is the best available mass proxy. There are 55 clusters in the BAX database that satisfy these

[2]bax.ast.obs-mip.fr

criteria, to which we add 3 clusters with the slightly relaxed criteria, $L_x > 1.5 \times 10^{44}$ erg s^{-1} and $0.044 < z < 0.15$ for a total of 58 clusters. The principal MENeaCS data set consists of several individual 120 s g' and r' MegaCam images per queue run, over a period of 3 years. This particular cadence is used in order to facilitate the detection of photometric transient in real time. Detected transients then trigger the spectroscopic followup observations (see Sand et al. 2012 for details) with followup priority dependent upon the properties of the nominal host galaxy. The exposures for each cluster are also combined to produce a deep stack image, which provide the basis for the analysis of MENeaCS clusters in the following chapters of this thesis. In generation of these deep stack images, to minimize contamination of galaxy colors we reject exposures in which there was a detected SN. To ensure good spatial resolution we also reject any exposures with a PSF Full Width at Half Maximum (FWHM) $FWHM_{PSF} > 1.0$ arcseconds. The resulting MENeaCS deep stacks have effective exposure times of 1.08×10^3 to 3.60×10^3 s in both g' and r'.

The data sets described above form the basis for the samples and optical data analysis used in this thesis. Further relevant details of the MENeaCS and CCCP optical samples are discussed further in later chapters where required. Throughout this thesis these samples are supplemented with further optical, infra-red, ultra-violet, X-ray and radio observations. These data supplements are discussed in detail in within the individual chapters that make use of them.

1.2.1 BCG Identification

Much of the work in this thesis is focused on the properties of the Brightest Cluster Galaxies (BCGs). The term BCG is used extensively in the literature, but there is no standard definition. Naively one would assume that each cluster has a single, easily identifiable BCG. However, it is important to recognize that BCG identification can be influenced by several factors including the wavelength range used for observations, the assumed parametric shape of the surface-brightness profile (affects magnitude measurements) as well as the proximity to the cluster center (in cases where cluster-centric distance cut is applied). In the majority of cases the BCG is unambiguous regardless of the exact selection criteria, but for the significant minority of systems where this is not the case it is necessary to outline the exact selection procedure. This becomes increasingly important with increasing redshift where dynamic relaxation of the most massive galaxies may not yet be fully achieved (Lidman et al. 2012). For

our purposes, probing the link between the BCG and the ICM, we are interested in the properties of the BCG candidate that is associated with the cluster core (ie. the focal point of radiative cooling). Therefore, in cases of BCG ambiguity, with several BCG candidates within a few tenths of a magnitude from one another, we chose the galaxy that is closest in projection to the peak in the X-ray distribution. This is only made possible by the high-resolution X-ray data (from Chandra and/or XMM-Newton) available for the entire CCCP sample and a significant portion of the MENeaCS sample. In practice however, the lack of availability of high-resolution X-ray data for many of the MENeaCS sample is not an issue because in each of these clusters there is only a single BCG candidate, likely owing to the dynamic relaxation argument discussed above. For further details on the BCG selections for individual CCCP clusters see Bildfell et al. (2008).

1.3 Concurrent Work not Detailed in this Thesis

Throughout the course of this thesis I have participated in several collaborations that lead to papers on which I was not the lead author. The work done as part of these projects has taken up a significant portion of the time that I have spent working towards obtaining my PhD degree. Because of this I include here a brief description of the most interesting results that were obtained owing in part to my contributions.

1.3.1 Recent Star Formation in BCGs: UV-Optical data

In Bildfell et al. (2008) we find that many BCGs have anomalously blue colors (a feature that is discussed in detail in Chapter 2), which are believed to be indicators of recent star formation. To follow this up we examine the properties of blue and red core BCGs at ultra-violet (UV) wavelengths which are highly sensitive to any recent star formation over the past 2 Gyr. In Pipino et al. (2009) we compare the UV-optical colors of BCGs within the CCCP sample. Specifically we measure the r' or R band magnitudes of the BCGs from the CFHT imaging and cross-reference their positions with the GALEX UV source catalog. We combine the NUV magnitude with the optical data measurement to obtain a $(NUV - r')$ color for the subset of BCGs with matching UV sources in the catalog. These colors are then compared to those predicted for a single stellar population (SSP) model that assumes solar metallicity, no dust and an instantaneous burst of star formation at $z = 3$ with a Salpeter (1955)

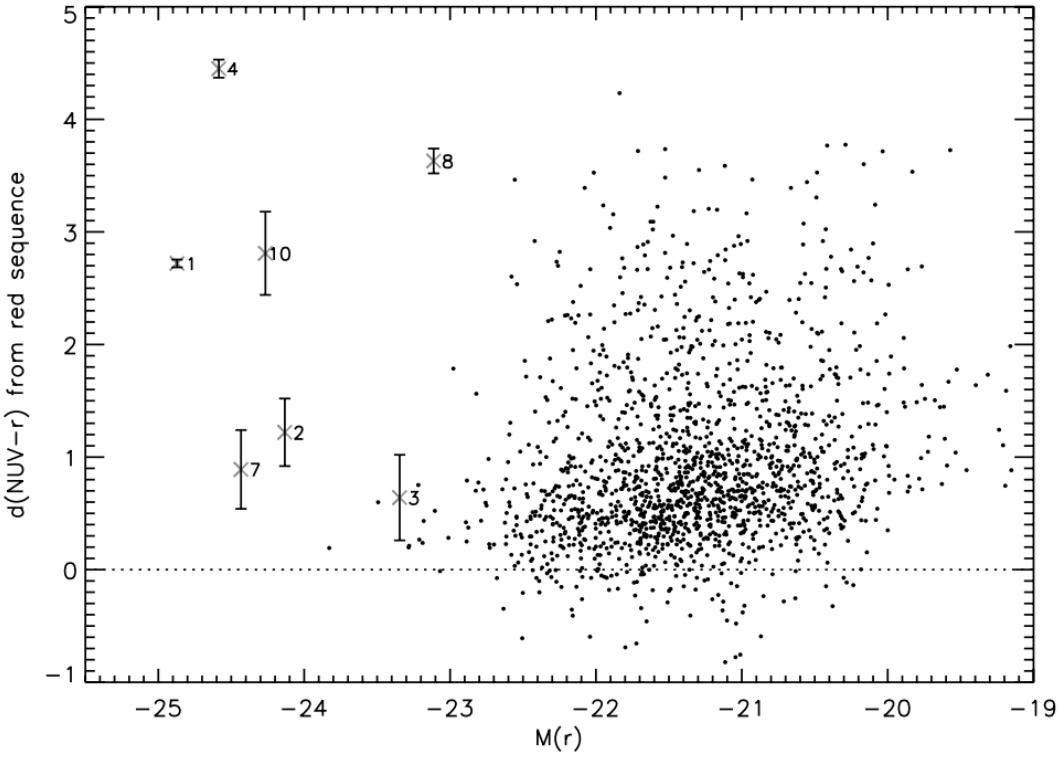

Figure 1.4: Taken from Pipino et al. (2009). The figure shows the color excess $d(NUV - r)$ from the passive galaxy red sequence position for each BCG at its given redshift. The color of the reference model (passive red sequence galaxy) is calculated using a solar-metallicity SSP which forms at $z = 3$. The CCCP BCGs are shown as crosses while the observations of local early-type galaxies from Kaviraj et al. (2007) are shown as small black dots. The numbers identify the galaxies according to Table 1 of Pipino et al. (2009).

Initial Mass Function (IMF).

We compute the $(NUV - r)$ color difference $d(NUV - r)$ between observations and model for each BCG in the subsample, at its given redshift, and plot the results in Figure 1.4. The BCGs in this figure are shown by crosses while the black dots indicate the color difference for regular ellipticals from Kaviraj et al. (2007). It is important to note that the model generally fails at reproducing the observed color of ellipticals (black dots) with a typical $d(NUV - r)$ between 0 and 1. This is likely due to the failure of the SSP models in reproducing the behaviour of the UV-excess thought to be associated with the uncertain later stages of stellar evolution. We find that the BCGs with optically blue cores from Bildfell et al. (2008) (labeled 1, 4, 8, 10 in Figure 1.4) all have anomalously blue $(NUV - r)$ color, several magnitudes bluer than that of a typical regular elliptical. In contrast, the BCGs with optically red cores from Bildfell et al. (2008) (labeled 2, 3, 7 in Figure 1.4) have $(NUV - r)$ colors that agree very well with the typical $(NUV - r)$ of regular ellipticals. This one-to-one correspondence between optically-blue BCGs and UV-blue BCGs provides strong, independent evidence that these systems have indeed undergone some level of recent star formation over the past 2 Gyr.

Having established that there is recent star formation in the blue core systems Pipino et al. (2009) then models the UV and optical colors of both red-core and blue-core BCGs using a two-burst composite stellar population model. The parameters of the model are the same as those described above with the exception that the age of the younger component (t_{yc}) is allowed to vary along with the mass fraction of the younger component (f_{yc}). The age of the older component is held fixed at the elapsed time between the z_c and $z = 3$, where z_c is the redshift of the cluster. The results show that for red-core BCGs the best fit younger stellar components all have ages $t_{yc} > 1$ Gyr. In contrast to this the best fit ages for the young stellar component in blue-core BCGs is $t_{yc} < 0.2$ Gyr. Although we must be careful not to overinterpret results based on small samples (in this case 7 BCGs), the best fit t_{yc} values found in this study imply that once a BCG begins to form new stars this star formation cannot be quenched by feedback from an AGN. For if AGN feedback were able to halt a resurgence of star formation in these systems then we would expect to see a broad range of t_{yc} values in red-core BCGs, specifically some values of $t_{yc} < 1$ Gyr.

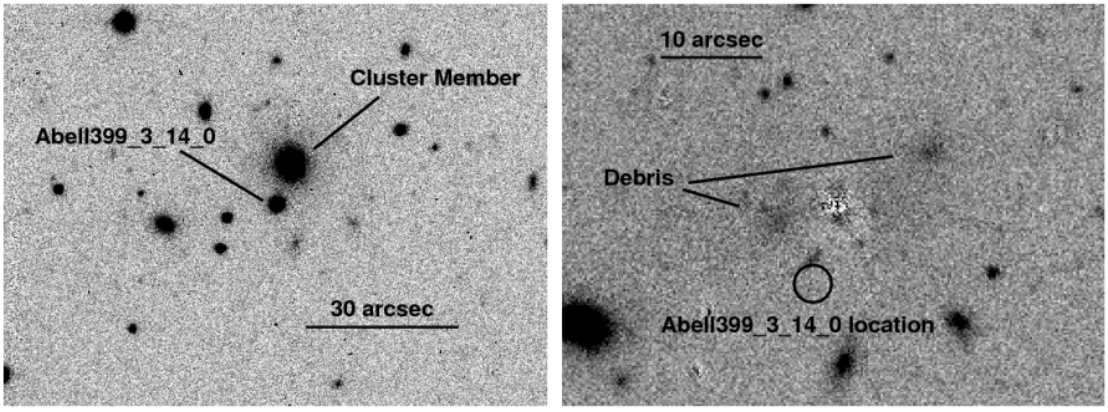

Figure 1.5: Taken from Sand et al. (2011). The panel on the left shows the discovery r' image of an IC SN in Abell 399 (Abell399_3_14_0), located $\sim$ 620 kpc southwest of the BCG. We note the nearby bright red sequence galaxy identified as 'cluster member' in the figure and dubbed Galaxy 1. The panel on the right shows a close-up view of the SN location in our deep stack, SN-free image, where the best GALFIT model (Peng et al. 2002) of Galaxy 1 has been subtracted. Note the residual debris remaining after the GALFIT model subtraction.

1.3.2 Intra-Cluster Supernovae and the Intra-Cluster Stellar Mass Fraction

As mentioned above, one of the primary goals of the MENeaCS is to investigate the properties of SN and their host galaxies within the context of massive clusters. To this end, throughout the duration of the survey I was charged with the task of generating galaxy catalogs and evaluating the status of red sequence membership for individual cluster galaxies. This step is critical for prioritizing the spectroscopic followup of transient SN candidates, with the apparently hostless candidates given top priority as they represented possible intra-cluster SN. The next priority down was given to the candidates that appear to be hosted by red sequence galaxies as these have a high probability of being true cluster members as opposed to foreground/background interlopers. Furthermore, the color of the host galaxy relative to the red sequence is an important metric that reveals whether or not the host galaxy has undergone recent star formation, a question related to the poorly constrained models for SNIa progenitor scenarios. Lastly, I was also directly involved in the photometric calibration of MENeaCS data, which we show is accurate to the $\delta m < 0.04$ magnitude level. In the paragraphs that follow we describe some of the more interesting MENeaCS

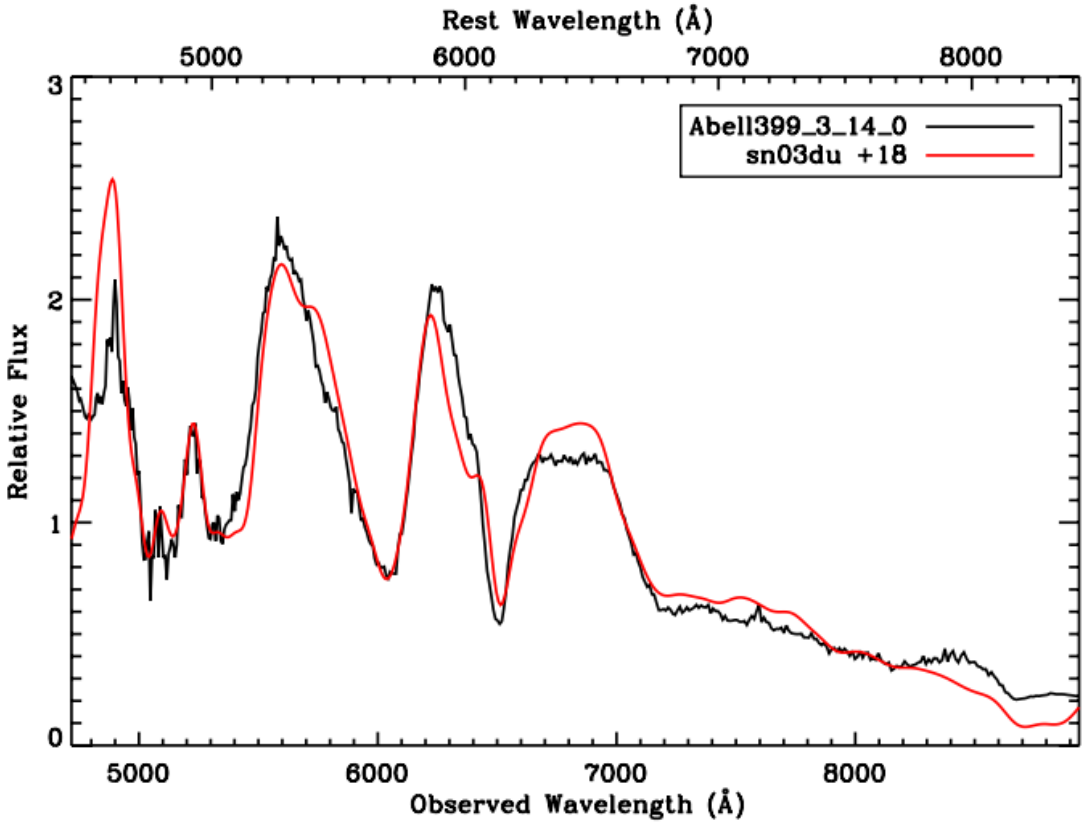

Figure 1.6: Taken from Sand et al. (2011). The figure shows the Gemini/GMOS spectrum of Abell399_3_14_0, along with the best-fitting SN template, a normal type-Ia, whci is overplotted in red.

results that rely on these contributions.

In Sand et al. (2011) we discuss the discovery of 4 apparently hostless SNIa's. We argue that these are bonafied Intra-Cluster SNe (IC SNe) and we show that assuming a standard cluster luminosity function allows only a 0.1% chance that any of these events are associated with a faint host below our detection limit. One of the IC SNe (Abell399_3_14_0) is associated with a nearby red sequence galaxy (Galaxy 1), however at a radius of ~ 10 time this galaxy's effective radius and a velocity offset of 1000 km/s this SN is unbound and therefore truly a member of the population of Intra-Cluster Stars (ICS). Figures 1.5 and 1.6 show a summary of the imaging and spectral analysis associated with this particular IC SN.

We use the 4 IC SNe found in Sand et al. (2011) to place limits on the typical fraction of stellar mass in clusters that is present in the ICS component. We consider two possible scenarios. In the first case we assume that the IC stellar population is similar to that of the cluster galaxies. We then estimate the IC stellar fraction as the ratio of the number of detected IC SNIa to the total number of hosted (both red sequence and non-red sequence hosts) plus hostless SNIa detected in clusters. We note that several correction factors are applied to account for hosted to hostless SN detection efficiency, spectroscopic availability bias and hostless follow-up bias (see Sand et al. (2011) for a more detailed description of these corrections). We find that the representative ICS fraction for the MENeaCS clusters is $0.16^{+0.13}_{-0.09}$. The second scenario considered is one in which the IC stellar population is exclusively old. In this scenario, we estimate the IC stellar fraction as the ratio of the number of IC SNIa to the number of hostless plus red sequence-hosted SNIa (ie. excluding SNIa in non-red sequence hosts). After applying the same correction factors used in the previous scenario we find an upper limit on the ICS fraction of < 0.47 for the case of an exclusively old IC stellar population. Figure 1.7 shows our constraints on the ICS fraction in comparison with other measurements of the IC and intra-group stellar mass fractions available from the literature. Our measurement of the ICS mass fraction is consistent with the bulk of the results in the literature, which generally find $\sim 10\% - 30\%$ at the mass scale associated with galaxy clusters (Gal-Yam et al. 2003, Gonzalez et al. 2005, Zibetti et al. 2005, Krick et al. 2007). We also show in Figure 1.7 the ICS fractions from direct surface brightness measurements for a set of 23 groups and clusters from Gonzalez et al. (2007) after correcting for effects caused by differences in field of view and the presence of a BCG, which represents $\sim 20\%$ of the BCG+ICS system. The Gonzalez et al. (2007) results based on direct measurement

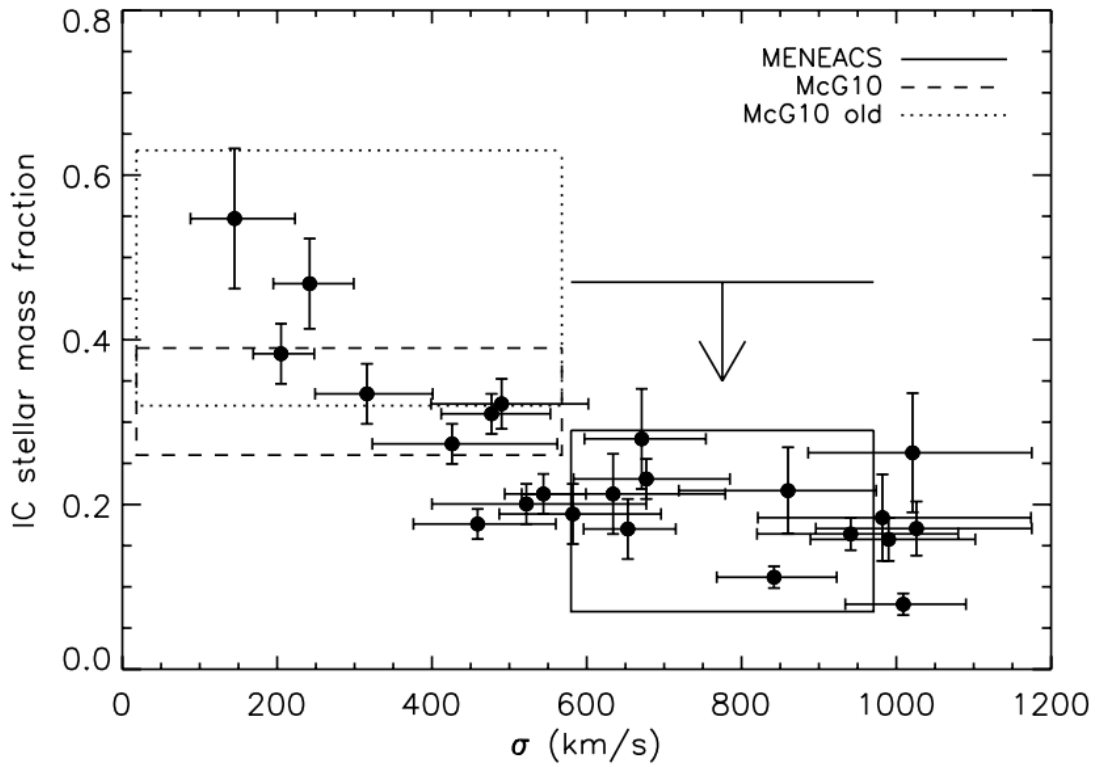

Figure 1.7: Taken from Sand et al. (2011). Comparison of our results with those in the literature. The figure shows the constraints on the IC stellar mass fraction measured in Sand et al. (2011) as a solid box. The upper limit of this box assumes that the IC stars are universally old. Results from Gonzalez et al. (2007) are plotted as points with error bars and represent the IC stellar mass fractions from 23 low-redshift clusters obtained from direct surface brightness measurements. The intragroup SN results of McGee and Balogh (2010) are shown as a dashed box. Applying the assumption that the IC stellar population is composed of only old stars transforms the McGee and Balogh results to the dotted box. The combination of the SN results confirm the declining IC stellar mass fraction as a function of cluster mass seen by Gonzalez et al. (2007)

of the ICS are in excellent agreement with our own constraints on the IC stellar mass fraction from IC SNe observations. Lastly, we also plot in Figure 1.7 the results of McGee and Balogh (2010) (dashed box) and these same results after assuming that the ICS is exclusively old (dotted box), analogous to our second scenario. Regardless of whether the ICS is exclusively old or not, their SN results, when taken with our own, confirm the declining IC stellar fraction with increasing velocity dispersion seen by Gonzalez et al. (2007).

The results presented in Sand et al. (2011) demonstrate a novel technique for measuring the IC stellar fraction that provides an independent measurement in good agreement with techniques that rely on direct detection. The use of IC SN to measure the ICS fraction represents a complementary technique that can be used at higher redshifts ($z > 0.1$) where SN are still detectable but direct measurement of the ICS is not possible owing to the increasing significance of cosmological surface brightness dimming. A followup project (MENeaCS2) seeking to improve on the statistics presented here, with the possibility of constraining the evolution in the ICS fraction is under way; currently at the data acquisition phase.

1.3.3 Type Ia Supernovae in Clusters: Rates and Host Properties

Another important aspect of the MENeaCS project is the use of our cluster SNIa observations to measure the SNIa rate in clusters and constrain the delay time distribution, the times between the original burst of star formation and the onset of SNIa explosion. The delay time distribution implicitly contains information regarding the progenitor mechanism(s) for type Ia SNe, a missing ingredient in the current theory of how these distant explosions are created. As a complementary probe of the type Ia progenitor mechanism we also examine the optical properties of the host galaxies. In particular, we would like to know whether or not the host galaxies show signs of recent star formation, which if present would indicate a preference for the single degenerate progenitor scenario (requiring a white dwarf plus main sequence binary) versus the double degenerate scenario (requiring a binary system with two white dwarfs). A third mechanism called the double detonation scenario, a variant of the single degenerate scenario, is also widely considered in the literature. It is critical that we understand the details of the progenitor mechanism(s) since SNIa's are important both for understanding the chemical enrichment of the universe and

for their use as standard candles for cosmography.

With the aim to constrain the progenitor mechanism(s) of type Ia supernovae, Sand et al. (2012) uses the the 23 SNIa's detected in the MENeaCS observations to measure SNIa rates in clusters, constrain the late-time delay time distribution (> 2 Gyr) and probe the optical properties of the SN host galaxies. We measure an overall SNIa rate of $0.049^{+0.021}_{-0.018}$ SNuM for clusters at $z \sim 0.1$, where SNuM is a unit of SN rate per unit stellar mass with 1 SNuM being equivalent to 1.0 SN per 100 yr per $10^{10} M_{\odot}$. We also measure a separate SNIa rate for red sequence galaxies, finding a rate of $0.041^{+0.024}_{-0.019}$ SNuM. Assuming that red sequence galaxies are synonymous with early-types, in contrast to several other studies (Sharon et al. 2007, Mannucci et al. 2008, Dilday et al. 2010) this work finds no evidence for a cluster rate enhancement with respect to the SNIa rate in field ellipticals. However, the large uncertainty of the MENeaCS red sequence SNIa rate measurement along with the current SNIa rate measurements for field ellipticals limit the power of this comparison; our result differs from the field by $\lesssim 1\sigma$.

Assuming that stellar populations of red sequence galaxies formed in an instantaneous burst at $z = 3$, we convert our red sequence SNIa rate into a measurement of the delay time distribution at $z = 0.1$ or $t \sim 9.5$ Gyr. Combining our results with several others from the literature (Mannucci et al. 2008, Dilday et al. 2010, Graham et al. 2008, Barbary et al. 2012) we plot the delay time distribution Ψ in Figure 1.8. In this figure our measurement is represented by the star shaped symbol, while the literature values are marked with circles. Overplotted against the data we show the best fit delay time distribution (solid line) $\Psi \propto t^{-1.62 \pm 0.54}$. Also shown are the delay time distributions expected for the double degenerate ($\Psi \propto t^{-1}$) and double detonation ($\Psi \propto t^{-2}$) progenitor scenarios as the dashed and dotted lines, respectively. Our analysis slightly favours the double detonation scenario but is also consistent with the double degenerate scenario. Models of the single degenerate scenario generally predict steeper late time delay time distributions than $\Psi \propto t^{-2}$ but cannot be fully ruled out by our data. We note that an improved measurement of the SNIa rate in early type galaxies at $z = 0.5$ would provide a significant improvement in efforts to constrain the late time delay time distribution, allowing discrimination between progenitor models at greater than the 1σ level currently achieved.

A complementary method of shedding light on the type Ia progenitor mechanism is to examine the properties of the galaxies that host them. In Sand et al. (2012) we measure the $(g - r)$ color offset of SNIa host galaxies from the red sequences of their

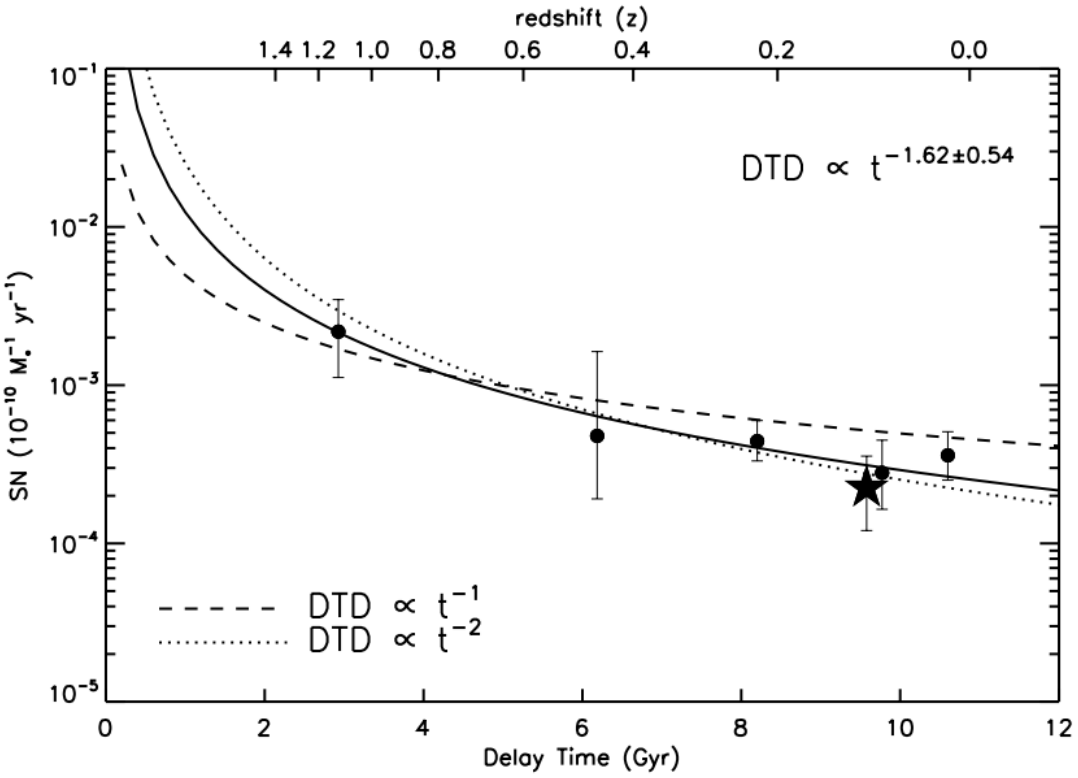

Figure 1.8: Taken from Sand et al. (2012). The figure shows the delay time distribution (DTD) based on early-type/red-sequence SN Ia rates in clusters, assuming that the stellar population is formed in a single burst of star formation at $z = 3$. The star-shaped point represents the data from the MENeaCS, while the other data points represent various studies in the literature (see table 6 of Sand et al. (2012) for exact values and sources). The solid DTD curve shows the best-fit power law, with $\Psi \propto t^s$, and an s value of -1.62. We also show the best-fit t^{-1} and t^{-2} power laws for illustrative purposes, corresponding to the double degenerate and double detonation progenitor scenarios, respectively.

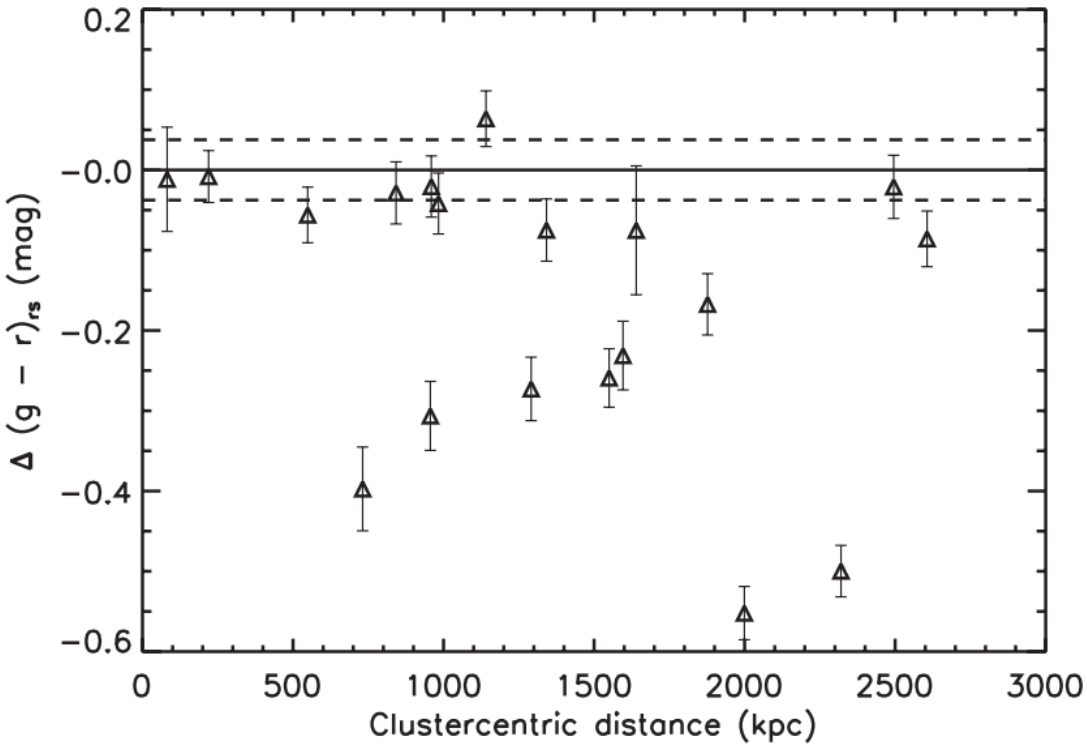

Figure 1.9: Taken from Sand et al. (2012). Optical color offset from the red sequence $(g-r)_{rs}$ for SNIa hosts in the MENeaCS versus projected distance from the cluster center (BCG postiion). Negative values of $(g-r)_{rs}$ indicate galaxies that are bluer than the red sequence. The dashed lines mark the median scatter of the red sequence over the entire MENeaCS data set. Note that even the SNIa host galaxies which are consistent with being red sequence members are located preferentially on the blueward side of the scatter.

respective clusters. We plot this quantity as $\Delta(g-r)_{rs}$ against the host's projected distance from the BCG in Figure 1.9. We also show using dashed lines in this figure the median scatter of the red sequence for the MENeaCS sample as a whole. We find that for 10 out of the 19 SNIa events observed were consistent with being hosted by red sequence galaxies. That leaves 9 out of 10 SNIa events that were hosted by non-red sequence galaxies. This result is expected as several studies (eg. Scannapieco et al. 2005, Mannucci et al. 2006) argue for the existence of two channels for SNIa production; one associated with the old population (delayed) and another associated with recent star formation (prompt). Upon closer examination of Figure 1.9 we note that those SNIa hosts that are consistent with the red sequence are dominated by negative values of the color offset ($\Delta(g-r)_{rs}$) indicating a preference for the blueward side of the scatter in the red sequence. The offsets are small, by definition they must be within the scatter of the red sequence in order to be classified as red sequence hosts. However, the preferentially blue color of these hosts is intriguing as it may indicate signs of recent star formation in these galaxies. If confirmed, this result would suggest that all SNIa events are hosted by galaxies that host recent star formation, indicating that the delayed component in SNIa rate modelling is simply measuring the prompt component that is associated with a small resurgence of star formation in these systems. Further investigation of the spectro-photometric properties of SNIa hosts using observations at wavelengths sensitive to recent star formation (UV, IR, emission line spectra) are required to investigate this further.

1.3.4 Type II Supernovae in Clusters: Rates and Host Properties

Unlike type Ia supernovae, which are though to arise from a white dwarf exceeding or approaching the Chandrasekhar mass limit, type II supernovae (SNII) are known to be the result of catastrophic core collapse of iron cores in massive stars ($8 < M \lesssim 20 M_{\odot}$) at the end of their fusion-supported lifetimes. Because massive stars evolve much faster than their low mass counterparts SNII delay times are relatively short compared to SNIa's, following $\lesssim 30 Myr$ after a burst of star formation (Henyey et al. 1959). With such short delay times the SNII rate can be used as a direct measure of the star formation rate in galaxies. Although they occur infrequently SNII are bright. In principle this may make SNIIs superior probes of the star formation rate for galaxy populations with the lowest star formations rates, where indicators such as UV and

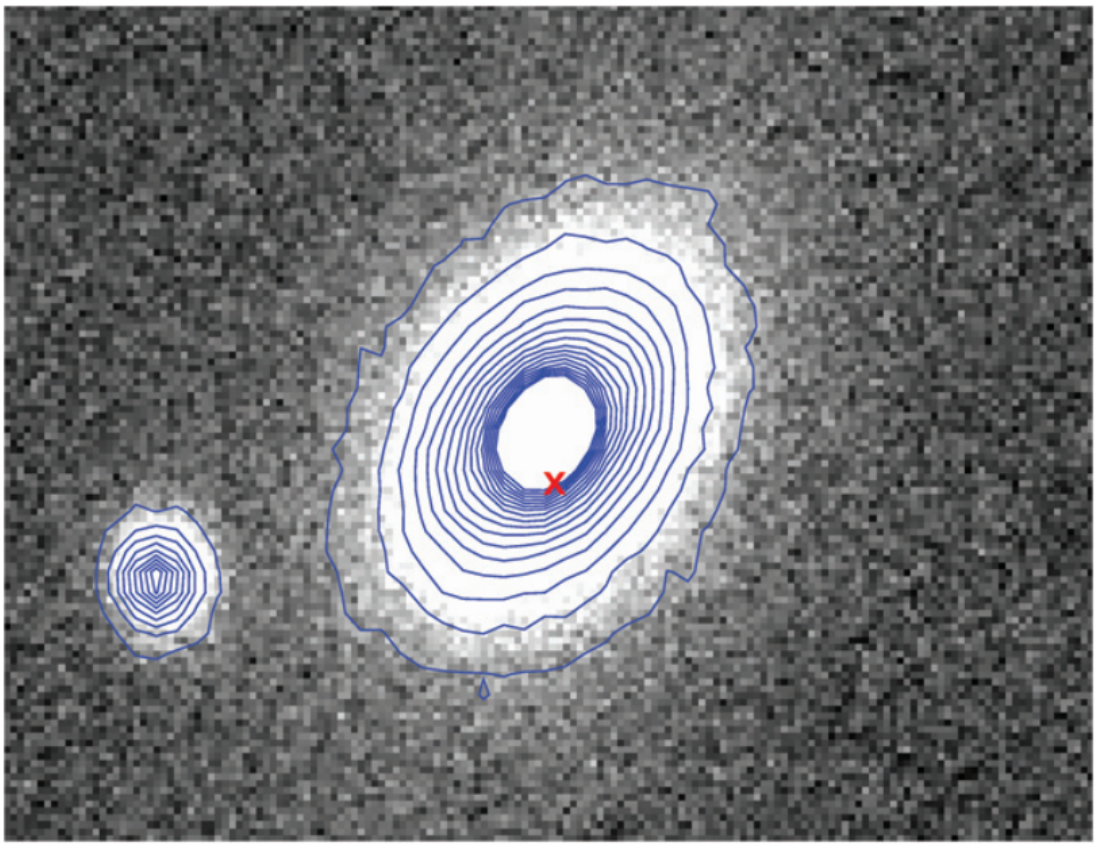

Figure 1.10: Taken from Graham et al. (2012). Image of the red sequence galaxy that hosts a type II supernova. The red "x" marks the spot where the SNII is detected. Note that this image is produced from the deepstack containing no exposures in which the SN was present. The surface brightness contours (thin blue lines) clearly illustrate this galaxy's elliptical morphology.

emission line luminosities are very faint and prohibit detection. Furthermore, the SNII rate is an unambiguous indicator of star formation, unlike the UV luminosity, which is affected by the uncertain late stages of stellar evolution, or emission lines, which are affected by the presence of an AGN.

In Graham et al. (2012) we investigate the 7 SNII events detected in galaxy clusters at $0.05 < z < 0.15$ discovered within the MENeaCS data set. We convert this number into a type II supernova rate within R_{200} of $0.026^{+0.085}_{-0.018}(\mathrm{stat})^{+0.003}_{-0.001}(\mathrm{sys})$ SNuM. This result is in agreement with the only other known measurement of the SNII rate in clusters of $0.072^{+0.028}_{-0.021}$ by Mannucci et al. (2008). However, perhaps the more interesting result in Graham et al. (2012) is the discovery of a SNII event in

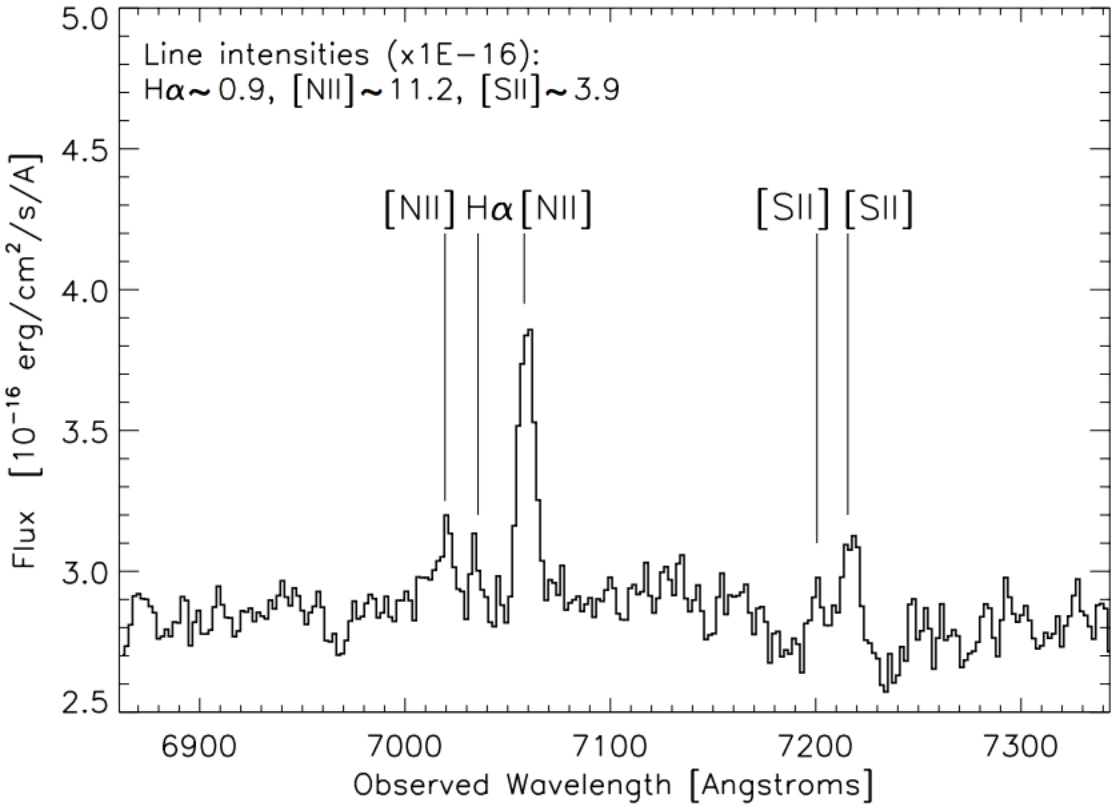

Figure 1.11: Taken from Graham et al. (2012). Optical spectra of the red sequence SNII host galaxy taken with the Blue Channel Spectrograph at the MMT Observatory. Known NII, H_α and SII lines are identified.

an early-type, red sequence galaxy. Figure 1.10 shows an image of this host galaxy from our SN-free deepstacks. The surface brightness contours overlaid in this image clearly indicate an elliptical morphology, while the $\Delta(g-r)_{rs} = -0.02 \pm 0.04$ making it consistent with the red sequence population. We search for a coincident UV source in the GALEX catalog and find that none is present at the location of this galaxy. A closer inspection of the GALEX images themselves likewise shows no hint of a UV source at this position. Based on the work of Schawinski (2009) and Kaviraj (2010) the GALEX detection limit implies a mass fraction of stars formed via a recent burst $\lesssim$ 100Myr to be $< 1\%$. Combining our photometry with the K band magnitude of the coincident source in the Two Micron All Sky Survey (2MASS), using the models of Li et al. (2007), we calculate a mass fraction of $\lesssim 0.5\%$ of the stellar mass is younger than 0.5 Gyr.

We also took optical spectra of our SNII red sequence host galaxy using the Blue Channel Spectrograph at the MMT Observatory in order to look for signs of recent star formation in the form of emission lines. Figure 1.11 shows the resulting optical spectrum with the known NII, H_α and SII lines identified. A simple analysis of this galaxy's line ratios, using the results from Kewley et al. (2006), shows that the line emission is more consistent with being produced by a low-ionization nuclear emission line region (LINER, a type of AGN) than being the result of recent star formation.

After looking at data in several wavelength regimes known to be sensitive to star formation, we find no evidence for any recent star formation activity apart from the detection of the SNII in this galaxy. The detection of a SNII in a red sequence, elliptical galaxy provides independent confirmation of the low level star formation seen in some early types via analysis of the UV-optical color (Kaviraj 2010). Furthermore, this result demonstrates that for extremely low levels of star formation or when AGN contamination is an issue, the use of SNII to measure the star formation rate may be the best technique available.

1.3.5 Combining Xray, Lensing and SZ observations of Galaxy Clusters

One way to use galaxy clusters as cosmological probes is to measure the space density of clusters as a function of mass (mass function) and compare the results directly to cosmological numerical simulations capable of resolving and predicting the evolution of large-scale structure in the Universe. On the observational side of the comparison,

this requires unbiased, precision measurements of cluster masses. Cluster masses are typically measured via the gravitational lensing of background galaxies, modelling the X-ray properties of the hot ICM or via inverse Compton Scattering of CMB photons, known as the Sunyaev-Zel'dovich (SZ) effect. More direct measurements of cluster masses are possible by combining the signal from strong gravitational lensing with dynamical data of cluster galaxies (eg. Sand et al. 2008). However, this technique is not applicable to clusters that do not display strong gravitational arcs and can be prohibitively expensive for large samples of clusters due to the need for medium resolution spectroscopy for a significant number of member galaxies in each. For these reasons, there is a need for cheap, well-understood cluster mass proxies that are easy to measure and applicable to large samples. To this end, we carry out a detailed study of the X-ray, weak lensing and SZ scaling relations in Hoekstra et al. (2012) and Mahdavi et al. (2013).

Hoekstra et al. (2012) present the weak lensing analysis for the CCCP clusters, comparing weak lensing masses to the amplitude of the SZ effect as quantified by the integrated compton y-parameter (Y) values in the literature. We a best fit power law slope $\alpha = 0.6$, which is consistent with models based on the assumption of self-similarity. Furthermore, for the relation between M_{2500} and Y, where M_{2500} is the projected lensing mass integrated over the region where the mean density is 2500 times the critical density, we find an intrinsic scatter of only $12\pm5\%$ at fixed Y. When comparing M_{500} (projected lensing mass where the mean density is 500 times the critical density) with Y we find an intrinsic scatter of $19^{+6}_{-7}\%$ at fixed Y. This is lower but consistent with the $\sim 20\%$ intrinsic scatter found by Marrone et al. (2012). These results derive an important calibration for the use of the SZ Y parameter as a cluster mass proxy. Moreover we quantify the accuracy of such a technique ($\sim 20\%$), verifying observationally that Y can indeed be used as a relatively cheap and accurate proxy.

Using the lensing masses of Hoekstra et al. (2012), Mahdavi et al. (2013) study combined X-ray, optical, weak-lensing scaling relations. In particular, we examine various correlations between pairs of parameters such as X-ray luminosity L_x, X-ray temperature T_x, central entropy K_0, X-ray centroid shift w_x, X-ray power ratio $P3/P0$, X-ray pseudo-pressure Y_x, projected offset between the BCG and X-ray peak D_{BCG}, hydrostatic mass M_{hydro}, gas mass M_{gas}, weak lensing mass M_{WL} and BCG ellipticity e_{BCG}. For a detailed description of how each of these quantities are defined and measured we refer the reader to Mahdavi et al. (2013). After comparing several

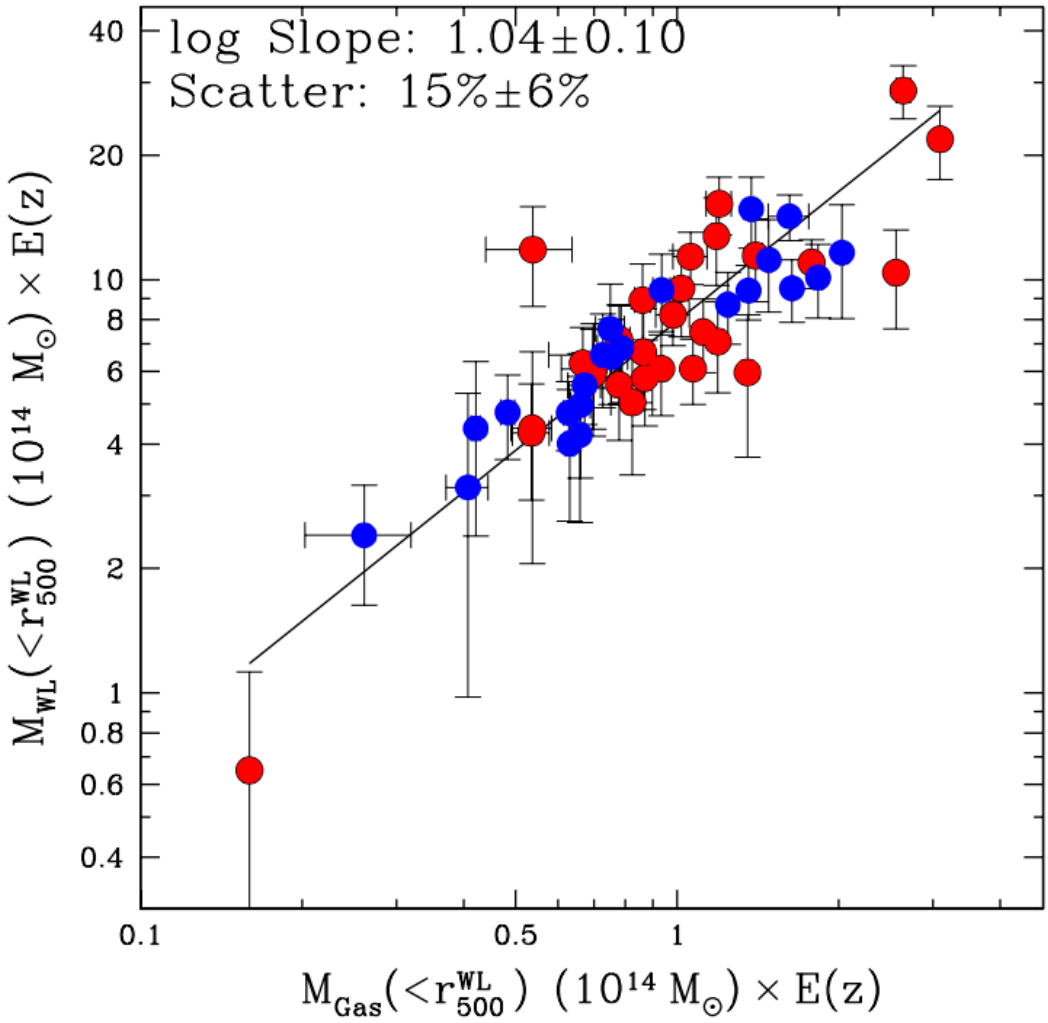

Figure 1.12: Taken from Mahdavi et al. (2013). The scaling relation between weak lensing mass $M_{WL}(r < R_{500})$ and gas mass determined from X-ray observations $M_{gas}(r < R_{500})$. Blue symbols indicate systems with small BCG to X-ray peak offsets ($D_{BCG} < 0.01$ Mpc), while red symbols indicate systems with large offsets ($D_{BCG} > 0.01$ Mpc). The solid black line shows the best fit scaling relation, including errors in two dimensions and accounting for intrinsic scatter. Of all X-ray parameters investigated, the gas mass is the best proxy for the weak lensing mass with an intrinsic scatter of only $15 \pm 6\%$. Restricting the analysis to the blue points with small D_{BCG} yields a relation with even smaller intrinsic scatter ($< 6\%$).

weak lensing versus X-ray scaling relations we find M_{gas} to be the most robust predictor of the weak lensing mass, with an intrinsic scatter of only 15±6% if measured inside R_{500} (see Figure 1.12). Separating the sample into disturbed ($D_{BCG} > 0.01$ Mpc) and relaxed subsamples ($D_{BCG} < 0.01$ Mpc) we find that the relaxed subsample has an intrinsic scatter of $< 6\%$ at fixed $M_{gas}(r < R_{500})$, consistent with zero intrinsic scatter. Similarly, dividing the sample on entropy at $K_0 = 70$ keV cm^2 yields a subsample of clusters in which the intrinsic scatter between $M_{gas}(r < R_{500})$ and $M_{WL}(r < R_{500})$ is $< 10\%$ at fixed $M_{gas}(r < R_{500})$. We also find that using a fixed aperture to define the gas mass ($M_{gas}(r < 1$ Mpc)) and the weak lensing mass ($M_{WL}(r < R_{500})$) yields a nearly identical intrinsic scatter of 16±10% at fixed ($M_{gas}(r < 1$ Mpc)), which is useful for comparisons where prior knowledge of r_{500} is not available. Aside from M_{gas}, we also comfirm that Y_x, the X-ray pseudo pressure, can be used as a relatively robust mass proxy with an intrinsic scatter in the $M_{WL}(r < R_{500})$ versus $Y_x(r < R_{500})$ scaling relation of $23 \pm 6\%$ at fixed $Y_x(r < R_{500})$.

Weak gravitational lensing provides a measure of the projected mass along the line of sight. Because of this, weak lensing derived cluster masses may be biased high when the long axis of clusters are aligned with the observer's viewing angle. To investigate this empirically, assuming that BCG ellipticity traces the ellipticity of the cluster as a whole, we consider the question of whether BCG ellipticity is correlated with any observed discrepancies between the weak lensing and X-ray determined mass estimates. A similar investigation is carried out by Marrone et al. (2012) in which they compared the residuals in the scaling relation between weak lensing mass and SZ compton-y parameter (scaled to weak lensing mass) to the ellipticity of the BCG. In Figure 1.13 we show the ratio of X-ray mass to weak lensing mass for the inner regions of clusters (within R_{2500}) versus BCG ellipticity taken from Mahdavi et al. (2013). In Figure 1.13 we distinguish between relaxed ($D_{BCG} < 0.01$Mpc) and disturbed ($D_{BCG} > 0.01$Mpc) using blue and red symbols, respectively. We find that there is an overall trend between $M_x/M_{WL}(r < R_{2500})$ with BCG ellipticity but that the trend appears to be driven by the disturbed systems. The weak correlation found when considering all systems, with a linear slope of 0.24 ± 0.15, strengthens to 0.54 ± 0.11 when considering the disturbed systems alone. A simple fit to the data for relaxed systems, parameterized by a constant yields $\chi^2/\nu = 1.29$, demonstrating that they are consistent with an X-ray to weak lensing mass ratio of unity, regardless of BCG ellipticity. In contrast, the same model fit to disturbed systems yields $\chi^2/\nu = 2.41$, ruling out a constant mass ratio. It is difficult to compare our results directly to those

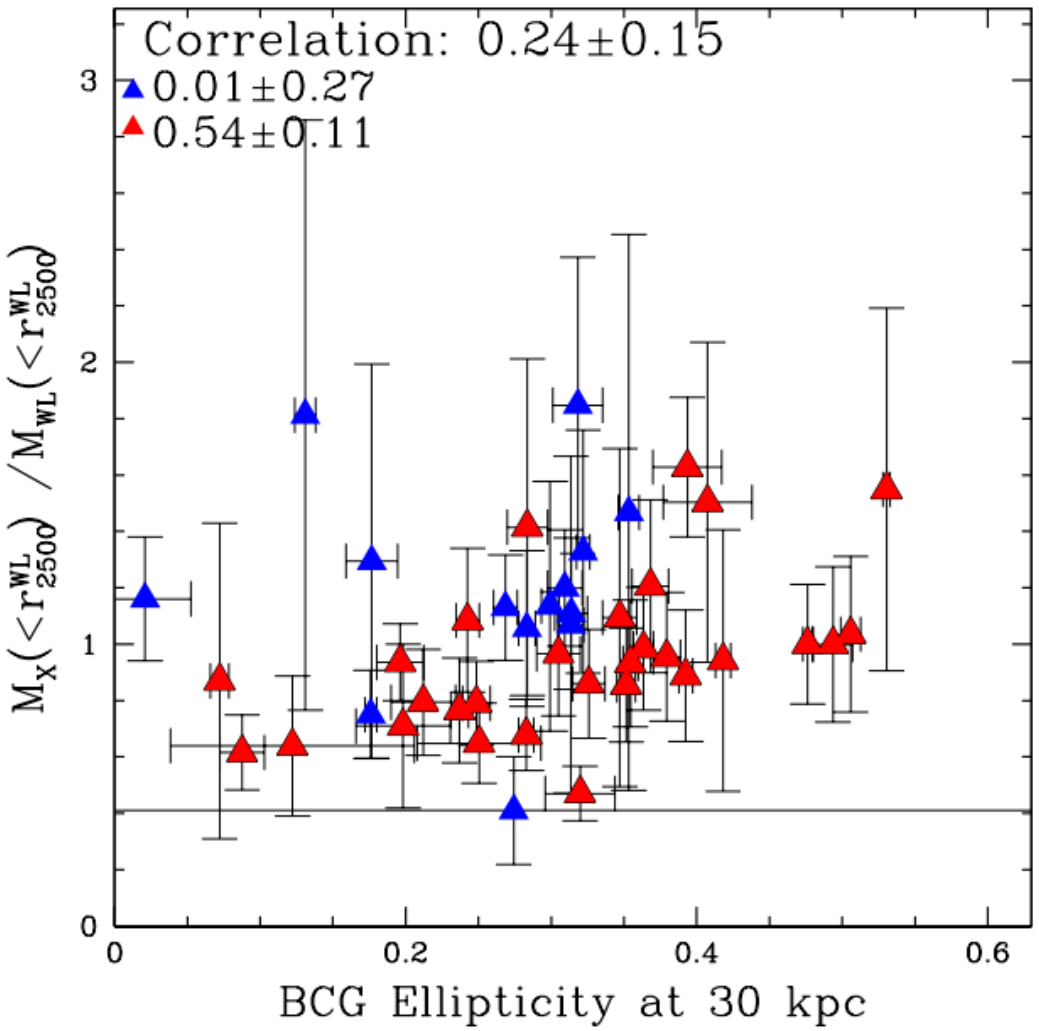

Figure 1.13: Taken from Mahdavi et al. (2013). The X-ray to weak lensing mass ratio as a function of BCG ellipticity for 43 BCGs with measureable ellipticities at 30 kpc. Blue symbols indicate relaxed systems ($D_{BCG} < 0.01$ Mpc) while red symbols indicate disturbed systems ($D_{BCG} < 0.01$ Mpc). The observed correlation is significant among the disturbed systems, but the relaxed systems are consistent are consistent with a constant mass ratio of unity.

of Marrone et al. (2012) since they probe weak lensing to SZ mass discrepancy while we probe weak lensing to X-ray mass discrepancy. However, despite this difference it is worth noting that Mahdavi et al. (2013) find a correlation between lensing mass discrepancy and e_{BGG} in disturbed systems only but Marrone et al. (2012) find a correlation between lensing mass discrepancy and e_{BCG} in the relaxed systems only. These results are not easily interpreted because it is difficult to disentangle the effects of elongation along the line of sight (which would chiefly bias the weak lensing mass high) from the effects of non-hydrostatic gas (which would chiefly bias the X-ray masses low). A study examining M_x/M_{WL} versus Y_{SZ}/M_{WL}, including a consideration of BCG ellipticity would help to make progress in this area.

1.3.6 CL09104+4109

Current models of galaxy and cluster formation commonly invoke feedback from an AGN in order to both suppress the efficiency at which gas cools to form stars in giant galaxies, and to establish the wide range of X-ray properties seen in clusters (eg. entropy, luminosity). Numerical models that implement this mechanism are indeed able to reproduce the observed colors of galaxies (Bower et al. 2006, Croton et al. 2006) as well as the X-ray temperature, density and entropy distribution of groups and low-mass clusters (McCarthy et al. 2011). In these models it is assumed that most of the feedback occurs at early epochs ($z > 1$) and is done mainly while the AGN is in 'quasar-mode', driving winds which heat the IGM/ICM by removing cold gas (Hopkins et al. 2005) and driving shocks. Despite the success of quasar feedback in numerical models, which is not directly resolved and must therefore be approximated by semi-analytics, the direct impact of a quasar on its surrounding environment is largely untested by observations. Quasars are rare below $z \lesssim 1$ where the current generation of observational instruments have sufficient spatial and velocity resolution to study how they impact their immediate surroundings. A few local examples have been studied to date using Chandra and XMM-Newton, showing no evidence of strong quasar mode heating. However, a clear interpretation of these results is complicated by a lack of knowledge regarding the accretion state of the systems, as well as the difficulty of identifying disturbed cold structures. With these observational challenges in mind, we identify an ideal cluster from the CCCP sample that can be exploited to shed light on the role of quasar mode heating on its immediate environs. In O'sullivan et al. (2012) we carry out a detailed multi-wavelength study of area around

the galaxy IRAS 0910+4109 (IRAS09), the central dominant galaxy (ie. the BCG) in the massive cool-core cluster ($M_{vir} = 7.9^{+4.0}_{-3.0} \times 10^{14} M_{\odot}$ Hoekstra et al. 2012) at $z = 0.442$ named CL 09104+4109 (CL09). IRAS09 is a hyperluminous infrared galaxy (HLIRG; Sanders & Mirabel 1996) and is known to hosts a type 2 quasar and an FR I radio source. From measurements of the [OII] equivalent width, Bildfell et al. (2008) estimate a star formation rate for this galaxy of 41±12 $M_{\odot}$ yr^{-1}. The analysis of Pipino et al. (2009) suggests that this recent surge of star formation is less than 200 Myr old, implying that IRAS09 has experienced a significant amount of cold gas accretion over this short time. These properties, along with the presence of several resolved, cold gas filaments around the central galaxy, make the IRAS09 - CL09 system an ideal candidate for studying the impact of quasar mode heating on its immediate environment and the conditions that lead to the creation of such energetic nuclear sources.

Figure 1.14 shows a composite color image of the area around IRAS09 generated from two HST WFPC2 images taken using the $F622W$ and $F814W$ wide band filters (similar to R and I bands, respectively). A number of features are clearly identified in the image including the central disk of the galaxy (yellow color), several extended filaments that are bright in emission, the 'whiskers' associated with the optical/UV scattering cones of the AGN (Hines et al. 1999), and the faintly visible extended stellar halo of the galaxy. The origin of the filamentary gas is not entirely clear, with two preferred scenarios proposed in O'Sullivan et al. (2012); that it represents cold gas stripped from interacting cluster galaxies, or that the filaments are formed from gas cooling directly out of the ICM. A third possibility is that the filaments are simply material that is illuminated by the AGN through openings in the dust distribution enshrouding the central source. The large distance between source and filament, along with the filament's thin, radial morphology however, make this particular scenario unlikely.

We analyze radio observations of the area around IRAS09 obtained with the Giant Metrewave Radio Telescope (GMRT) and Very Large Array (VLA). We confirm the presence of a bright central radio source with large-scale ($\sim$ 50kpc) symmetrical straight jets ending in small lobes. Their radio spectrum is well fit with an unbroken power law, with steep spectral index $\alpha = 1.25 \pm 0.01$, indicating that the jets are not currently active and the source is passively ageing. The radiative age estimated for a source with this spectral index is $t_{rad} \sim 130$ Myr. The straightness of these jets implies that the BCG has not moved much since this time. Analysis of archival

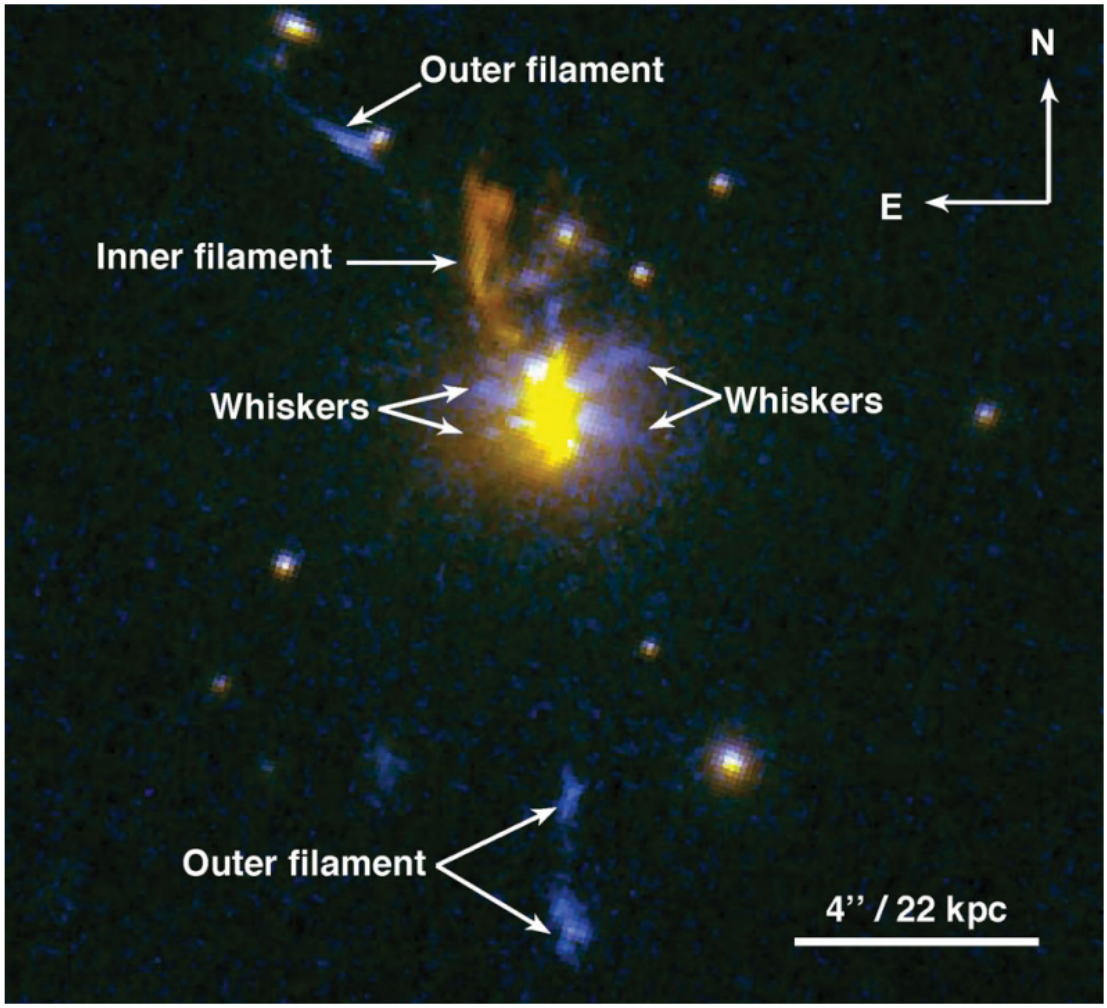

Figure 1.14: Taken from O'Sullivan et al. (2012). This figure shows a false colour HST image of IRAS 0910+4109 and its immediate surroundings. The color image is generated by combining two separate images taken in $F622W$ (R) band and $F814W$ (I) band. Several compact filamentary structures are easily seen and labels are placed for ease of reference throughout the paper. The filaments trace gaseous structures which are seen in line emission. The red color of the inner filament is due to the strong [OIII] 5007 emission associated with this region (Armus et al. 1999).

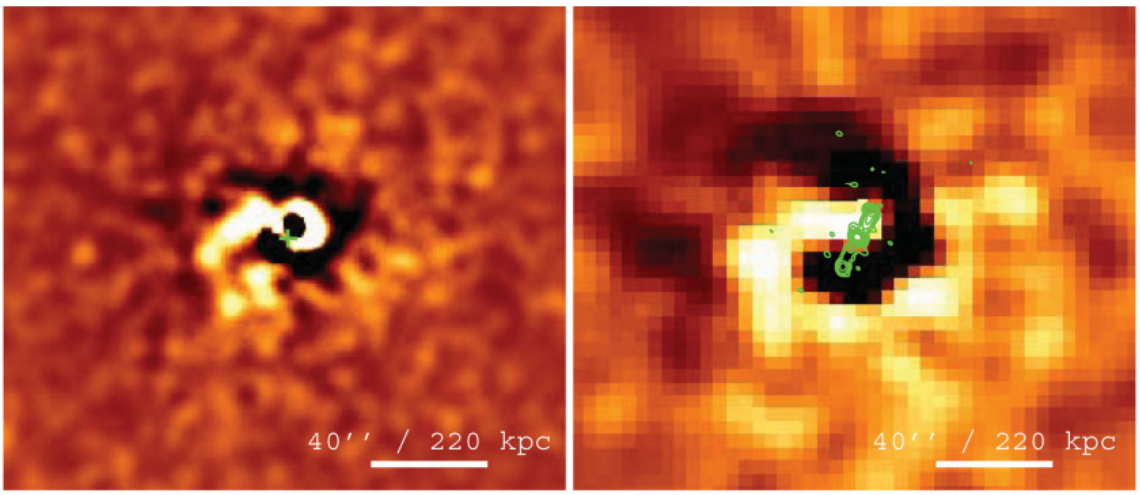

Figure 1.15: Taken from O'Sullivan et al. (2012). Both images shown here represent the residual X-ray images after subtracting the best fitting β model and heavily smoothing. The image on the left is generated from a Chandra 0.3-3 keV band exposure and is smoothed using a ~ 6 arcsec gaussian kernel. The image on the right is generated from an XMM-Newton 0.5-3 keV band exposure and is smoothed using a ~ 13.2 arcsec gaussian kernel. The green cross in the left hand image shows the position of the BCG. The right hand image also shows the 1.28 GHz GMRT radio contours. A spiral pattern formed by regions of positive and negative residual, and extending to $r \sim 200$ kpc, is clearly visible in both images.

data from the Very Long Baseline Array reveals that the central radio source seen in GMRT and VLA data is itself a small-scale double-lobed source ~ 200 pc in width, with an estimated dynamical timescale of $t_{dyn} \sim 10^5$ yr. We interpret this as evidence of a second more recent episode of radio activity that is separate from the episode of activity that lead to the creation of the large-scale jets. The main axis of the inner double-lobed source differs from that of the large-scale jets by an angle of $\sim 17^\circ$ when projected into the plane of the sky, suggesting that the axis of the AGN has changed.

O'Sullivan et al. (2012) also perform an analysis of archival X-ray data from Chandra (77 ks exposure) and XMM-Newton (14 ks exposure) for CL09. We find that the central cooling time within ~ 27 kpc is $9.9 \pm 0.9 \times 10^8$yr with an isobaric cooling rate of $\lesssim 235 M_\odot$ yr^{-1} within this radius, confirming that this system is a strong cool-core cluster. The coldest gas observed in the X-ray imaging has a temperature $kT \lesssim 5$ keV and is distributed along an axis that is correlated with the optically bright filaments seen in the HST imaging and is anti-correlated with the axis of the large-scale radio jets. Subtracting the best-fitting elliptical β model from the Chandra image reveals the presence of two X-ray cavities with radius ~ 25 kpc that are aligned with the axis of the large-scale radio jets. An estimate of the refill time for these cavities yields $t_{refill} \sim 120 - 160$ Myr. Lastly, Figure 1.15 shows the β-subtracted X-ray residual after heavily smoothing with a gaussian kernel (smoothing scales of 6 and 13 arcsecs for Chandra and XMM, respectively). We find a $r \sim$200 kpc spiral structure emanating from the cluster center and traced by both positive and negative residual. This spiral feature is similar to those seen in simulations of merging clusters (Poole et al. 2006), suggesting a possible group or cluster merger beginning 4-6 Gyr ago, with a core merger occurring 0.5-1 Gyr ago.

The large-scale jets associated with IRAS09 are no longer powered by the AGN, but are relics of activity which ceased ~ 130 Myr ago as estimated by their radiative age. This agrees well with the refill times-scales estimated for the X-ray cavities that are spatially associated with these jets ($t_{refill} \sim 120 - 160$ Myr). Furthermore, the optical/NUV estimated age of the most recent burst of star formation in this system is also in good agreement with $t_{SF} \sim$ 70-200 Myr (Pipino et al. 2009). These results strongly suggest that IRAS09 has recently ($\sim$ 200 Myr ago) experienced a major influx of cold gas, leading to a burst of star formation, re-alignment of the AGN axis, and a significant change in accretion rate of the central engine that transformed the previously radio-mode AGN into a radiatively efficient quasar-mode AGN. Taken together with the spiral structure seen in the X-ray residual images, the most likely

scenario is that this dramatic increase in cold gas accretion was brought on by the final stages of a merger with a gas-rich substructure, however the lack of a visible secondary and the straightness of the large-scale radio jets may pose a problem for this interpretation. An alternate possibility is that the recent influx of cold gas originated in the ICM, cooling and falling onto IRAS09 from a direction misaligned with the accretion disk of the AGN. Indeed the thin optical filaments associated with the coldest X-ray gas are aligned with the gas disk of the galaxy, perpendicular to the axis defined by the UV-optical scattering cones of the AGN.

Regarding the effect of the AGN on its surroundings, the estimated mechanical power of the radio jets from cavity enthalpy is sufficient to balance the radiative losses, providing that this mechanical power is efficiently coupled to the ICM. While no direct evidence for heating of the X-ray gas is observed, the weak shocks typically associated with jet sources would be difficult to detect considering the age of the jets and the relatively shallow Chandra exposure. We analyze archival spectroscopy taken with the GMOS integral field unit (IFU) on Gemini North, finding some evidence for AGN outflows on small scales. However, we find no evidence of large-scale radiatively driven winds of the sort predicted by simulations of quasar feedback in dense environments. Furthermore, the lack of a central cavity in the X-ray, rise in temperature or outflowing gas suggests that either the quasar is not luminous enough, or has had insufficient time to effectively heat the ICM, let alone disrupt the cool core. It is also noted that the quasar is still enshrouded by $\sim 3 \times 10^9 M_\odot$ of cool gas, which the quasar has failed to destroy or sweep out of the BCG. IFU observations of the central galaxy and the nearby optical filaments in the infrared, with high spatial and spectral resolution ($\lesssim 2$ kpc and $\lesssim 50$ km s^{-1}, respectively) would allow detailed velocity and ionization mapping of the region around the quasar, enabling a much clearer picture of its effect on the nearby gas.

1.4 Outline

This concludes the description of the additional work pursued concurrently to the the major projects that make up this thesis. In the following chapters we outline the details of these major thesis projects, which are commonly linked by the theme of stellar content in galaxy clusters. In Chapter 2 we describe the analysis of BCG optical color profiles. These results are then combined with results from the analysis of high-resolution X-ray data and their implications are discussed. Chapter 3 describes

the measurement of the Giant-to-Dwarf ratio among red sequence galaxies in clusters. We quantify the evolution in this ratio and, relating again to the X-ray properties of the host clusters, we seek to understand the source of the observed evolution. Chapter 4 presents the measurement of deep, longslit optical spectra for a subsample of BCGs from the CCCP. We use these spectra to measure the BCG central velocity dispersions, investigate the fundamental plane of BCGs and measure their dynamical masses. Lastly, Chapter 5 contains some brief concluding remarks about the impact of this thesis as a whole on our knowledge of the stellar content in galaxy clusters.

For convenience, we include a table of commonly used terms and their definitions in the Appendix B (see Table B.1).

1.5 References

Baldry, I., Balogh, M., Bower, R., Glazebrook, K., Nichol, R., Bamford, S., Budavari, T., 2006, MNRAS, 373, 469

Bamford, S., Nichol, R., Baldry, I., Land, K., Lintott, C., Shawinski, K., Slosar, A., Szalay, A., Thomas, D., Torki, M., Andreescu, D., Edmondson, E., Miller, C., Murray, P., Raddick, M., Vandenberg, J., 2009, MNRAS, 393, 1324

Barbary, K., Aldering, G., Amanullah, R., et al. 2012, ApJ, 745, 32

Bildfell, C., Hoekstra, H., Babul, A., Mahdavi, A., 2008, MNRAS, 389, 1637

Boissier, S., Boselli, A., Duc, P., Cortese, L., van Driel, W., Heinis, S., Voyer, E., Cucciati, O., Ferrarese, L., Cote, P., Cuillandre, J., Gwyn, S., Mei, S., 2012, A&A, 545, 142

Bower, R., Benson, A., Malbon, R., Helly, J., Frenk, C., Baugh, C., Cole, S., Lacey, C., 2006, MNRAS, 370, 645

Cavagnolo, K., Donahue, M., Voit, G., Sun, M., 2008, ApJ, 682, 821

Croton, D., Springel, V., White, S., DeLucia, G., Frenk, C., Gao, L., Jenkins, A., Kauffmann, G., Navarro, J., Yoshida, N., 2006, MNRAS, 365, 11

Dilday, B., Bassett, B., Becker, A., et al., 2010, ApJ, 715, 1021

Dressler, A., 1980, ApJ, 236, 351

Fabian, A., 1994, ARAA, 32, 277

Gal-Yam, A., Maoz, D., Guhathakurta, P., Filippenko, A., 2003, AJ, 125, 1087

Gastaldello, F., Buote, D., Humphrey, P., Zappacosta, L., Bullock, J., Brighenti, F., Mathews, W., 2007, ApJ, 669, 158

Gonzalez, A., Zabluddof, A., Zaritsky, D., 2005, ApJ, 618, 195

Gonzalez, A., Zaritsky, D., Zabludoff, A., 2007, ApJ, 666, 147
Graham, M., Sand, D., Bildfell, C., Pritchet, C., Zaritsky, D., Hoekstra, H., Just, D., Herbert-Fort, S., Sivanandam, S., Foley, R., 2012, ApJ, 753, 68
Graham, M., Pritchet, C., Sullivan, M., et al. 2008, AJ, 135, 1343
Henyey, L., Lelevier, R., Levee, R., 1959, ApJ, 129, 2
Hines, D., Schmidt, G., Wills, B., Smith, P., Sowinski, L., 1999, ApJ, 512, 145
Hoekstra, H., Mahdavi, A., Babul, A., Bildfell, C., 2012arXiv1208.0606, (submitted to MNRAS)
Horner, D., 2001, PhD Thesis
Hopkins, P., Hernquist, L., Cox, T., Di Matteo, T., Martini, P., Robertson, B., Springel, V., 2005, ApJ, 630, 705
Hubble, E., Humason, M., ApJ, 74, 43
Jarosik, N., Bennett, C., Dunkley, J., Gold, B., Greason, M., Halpern, M., Hill, R., Hinshaw, G., Kogut, A., Komatsu, E., Larson, D., Limon, M., Meyer, S., Nolta, M., Odegard, N., Page, L., Smith, K., Spergel, D., Tucker, G., Weiland, J., Wollack, E., Wright, E., 2011, ApJS, 192, 14
Kaviraj, S., GALEX Collaboration, 2007, ApJS, 173, 619
Kaviraj, S., 2010, MNRAS, 408, 170
Kimm, T., Somerville, R., Yi, S., van den Bosch, F., Salim, S., Fontanot, F., Monaco, P., Mo, H., Pasquali, A., Rich, R., Yang, X., 2009, MNRAS, 394, 1131
Komatsu, E., Smith, K., Dunkley, J., Bennett, C., Gold, B., Hinshaw, G., Jarosik, N., Larson, D., Nolta, M., Page, L., Spergel, D., Halpern, M., Hill, R., Kogut, A., Limon, M., Meyer, S., Odegard, N., Tucker, G., Weiland, J., Wollack, E., Wright, E., 2011, ApJS, 192, 18
Krick, J., Bernstein, R., 2007, AJ, 134, 466
Li, Z., Han, Z., Zhang, F., 2007, A&A, 464, 853
Lidman, C., Suherli, J., Muzzin, A., Wilson, G., Demarco, R., Brough, S., Rettura, A., Cox, J., DeGroot, A., Yee, H., Gilbank, D., Hoekstra, H., Balogh, M., Ellingson, E., Hicks, A., Nantais, J., Noble, A., Lacy, M., Surace, J., Webb, T., 2012, MNRAS, 427, 1298
Mahdavi, A., Hoekstra, H., Babul, A., Bildfell, C., Jeltema, T., Henry, P., 2013, ApJ, 767, 116
McCarthy, I., Schaye, J., Bower, R., Ponman, T., Booth, C., Dalla Vecchia, C., Springel, V., 2011, MNRAS, 412, 1965
Sand, D., Treu, T., Ellis, R., Smith, G., Kneib, J., 2008, ApJ, 674, 711

Sand, D., Graham, M., Bildfell, C., Pritchet, C., Hoekstra, H., Just, D., Herbert-Fort, S., Sivanandam, S., Foley, R., Mahdavi, A., 2012, ApJ, 746, 163
Mannucci, F., Della Valle, M., Panagia, N., 2006, MNRAS, 370, 773
Mannucci, F., Maoz, D., Sharon, K., et al. 2008, MNRAS, 383, 1121
Marrone, D., et al., 2012, ApJ, 754, 119
McGee, S., Balogh, M., 2010, MNRAS, 403, L79
Moore, B., Katz, N., Lake, G., Dressler, A., Oemler, A., 1996, Natur, 379, 613
O'Sullivan, E., Giacintucci, S., Babul, A., Raychaudhury, S., Venturi, T., Bildfell, C., Mahdavi, A., Oonk, J., Murray, N., Hoekstra, H., Donahue, M., 2012, MNRAS, 424, 2971
Peng, C., Ho, L., Impey, C., Rix, H., 2002, AJ, 124, 266
Pipino, A., Kaviraj, S., Bildfell, C., Babul, A., Hoekstra, H., Silk, J., 2009, MNRAS, 395, 462
Poole, G., Fardal, M., Babul, A., McCarthy, I., Quinn, T., Wadsley, J, 2006, MNRAS, 373, 881
Rafferty, D., McNamara, B., Nulsen, P., 2008, ApJ, 687, 899
Rasmussen, J., Ponman, T., 2004, MNRAS, 349, 722
Riess, A., Macri, L., Casertano, S., Sosey, M., Lampeitl, H., Ferguson, H., Filippenko, A., Jha, S., Li, W., Chornock, R., Sarkar, D., 2009, ApJ, 699, 539
Salpeter, E., 1955, ApJ, 121, 161
Sand, D., Graham, M., Bildfell, C., Foley, R., Pritchet, C., Zaritsky, D., Hoekstra, H., Just, D., Herber-Fort, S., Sivanandam, S., ApJ, 729, 142
Sand, D., Graham, M., Bildfell, C., Zaritsky, D., Pritchet, C., Hoekstra, H., Just, D., Herbert-Fort, S., Sivanandam, S., Foley, R., Mahdavi, A., 2012, ApJ, 746, 163
Mandelbaum, R., Seljak, U., Baldauf, T., Smith, R., 2010, MNRAS, 405, 2078
Sanders, D., Mirabel, I., 1996, ARA&A, 34, 749
Scannapieco, E., Bildsten, L., 2005, ApJ, 629, L85
Schawinski, K., 2009, MNRAS, 397, 717
Sharon, K., Gal-Yam, A., Maoz, D., Filippenko, A., Guhathakurta, P., 2007, ApJ, 660, 1165
Spergel, D., Verde, L., Peiris, H., Komatsu, E., Nolta, M., Bennett, C., Halpern, M., Hinshaw, G., Jarosik, N., Kogut, A., Limon, M., Meyer, S., Page, L., Tucker, G., Weiland, J., Wollack, E., Wright, E., 2003, ApJS, 148, 175
Springel, V., White, S., Jenkins, A., Frenk, C., Yoshida, N., Gao, L., Navarro, J., Thacker, R., Croton, D., Helly, J., Peacock, J., Cole, S., Thomas, P., Couchman, H.,

Evrard, A., Colberg, J., Pearce, F., 2005, Natur, 435, 629
van der Wel, A., Bell, E., Holden, B., Skibba, R., Rix, H., 2010, ApJ, 714, 1779
Vikhlinin, A., Kravtsov, A., Forman, W., Jones, C., Markevitch, M., Murray, S., Van Speybroeck, L., 2006, ApJ, 640, 691
Vollmer, B., Soida, M., Braine, J., Abramson, A., Beck, R., Chung, A., Crowl, H., Kenney, J., van Gorkom, J., 2012, A&A, 537, 143
Weinmann, S., van den Bosch, F., Yang, X., Mo, H., 2006, MNRAS, 366, 2
Yun, L., Mo, H., Gao, L., 2008, MNRAS, 389, 1419
Zhang, Y., Finoguenov, A., Bohringer, H., Kneib, J., Smith, G., Czoske, O., Soucail, G., 2007, A&A, 67, 437
Zibetti, S., White, S., Schneider, D., Brinkmann, J., 2005, MNRAS, 258, 949
Zwicky, F., 1933, Helv. Phys. Acta, 6, 110

Chapter 2

BCG color profiles

2.1 Introduction

Galaxy clusters are the largest virialized structures in the universe, forming at the nodes in the cosmic web, where many galaxies are gravitationally attracted into huge systems as massive as $\sim 10^{15}$ M_{sol}. Within these structures, the brightest cluster galaxies (BCGs) represent a special class of systems that have formed at the highest density peaks, and at late times (by $z \sim 0$) they are the most massive galaxies in the Universe. Because of this privileged position they provide a unique opportunity for insight into both galaxy and cluster formation models. According to the galaxy 'downsizing' paradigm, which is based on observations showing that the epoch of peak star formation is oldest for the most massive galaxies and moves towards more recent epochs as galaxy mass decreases (Guzman et al. 1997, Brinchmann & Ellis 2000, Kodama et al. 2004, Juneau et al. 2005, Bell et al. 2005, Bundy et al. 2005), the stellar content of these galaxies should be comprised of the oldest stars still in existence. The consequence of this is that the color of BCGs should be exclusively red. In most clusters this is indeed true; however, there are now several studies that have observed BCGs with anomalously blue colors in their central regions (McNamara et al. 2006, Bildfell et al. 2008, Rafferty et al. 2008). Many of these same anomalously blue systems have also been observed to have line emission that is associated with either recent star formation and/or AGN activity (Salome et al. 2008, Edwards et al. 2009, Cavagnolo et al. 2008, McDonald et al. 2012).

Some work has been done to test whether or not the blue color and/or line emission is connected to the cooling of the X-ray bright intra-cluster medium (ICM) using large

samples of galaxy clusters. Bildfell et al. (2008) find that BCGs with blue central regions are ubiquitous in clusters with large X-ray luminosity excess compared to L_x-T_x scaling relation, an indicator of the cooling strength of the cluster. Cavagnolo et al. (2008) find that H_α emission is associated with clusters that have very low values of central entropy. Rafferty et al. (2008) find that BCGs with anomalously blue $U-I$ and $U-R$ of BCGs are present only in clusters with low central entropy and short central cooling times. Their sample is heavily biased towards cool core clusters however, with only 2 cluster having central entropy greater than 100 keV cm^2, and to definitively link the anomalous colors with cooling in ICM also requires a good understanding of the appearance of BCGs in extreme non-cool core clusters.

These same processes (star formation, AGN) that are expected to explain the anomalous spectro-photometric observations of BCGs are also important in current models seeking to explain the formation and evolution of galaxies in general. In particular, heating from AGN feedback is required in order to regulate star formation in order to reproduce the observed number densities of massive galaxies. Consequently, a detailed understanding of these interaction of these baryonic processes and how they depend on the local reservoir of cold gas is critical to constructing fully consistent simulated galaxies.

To further explore the link between possible recent star formation and AGN in BCGs with the degree of radiative cooling taking place in their environments we perform here a detailed comparison between the BCG optical color profiles and the entropy, cooling time and metallicity of the ICM for a large sample of order 100 clusters. Furthermore, we confront the conclusions of this comparison with the available measurements of the radio output of these systems in order to test the robustness of our interpretation.

The layout of this chapter is as follows. In §2.2 we give details regarding the optical and X-ray data used in this study. In §2.3 we discuss our procedure for measuring the surface brightness profiles of BCGs. In §2.4 we describe how the surface brightness profiles are combined to obtain color profiles and we discuss some of their characteristics. In §2.5 we compare the inner parts of the BCG color profiles with the X-ray properties of the host clusters as obtained from high resolution X-ray observations taken with the Chandra and XMM-Newton satellites. In §2.6 we compare the results of the X-ray and optical analyses to the radio data available for a subset of our sample. Lastly, in §2.7 we present our conclusions. Throughout this chapter we assume a cosmology parameterized by $\Omega_m = 0.3$, $\Lambda = 0.7$ and $H_0 =$

70km/s/Mpc.

2.2 Data Sample

The BCG sample studied here is comprised of two separate sub-samples; the Canadian Cluster Comparison Project (CCCP) and the Multi-Epoch Nearby Cluster Survey (MENeaCS), both of which are essentially X-ray selected cluster samples. Briefly, for the purposes of comparison with other work, we describe the main characteristics of these two surveys.

The CCCP consists of 50 clusters in the redshift range $0.15 < z < 0.55$, selected from the cluster catalog of Horner (2001), which is based on observations taken with the Advanced Satellite for Cosmology and Astrophysics (ASCA). The CCCP clusters all have X-ray temperatures $T_x > 3$ keV and are selected such they fully sample the observed scatter in the L_x vs T_x plane. The MENeaCS clusters are selected from the BAX X-ray galaxy cluster database[1] and represent all clusters in the database that are observable from CFHT, with redshift $0.05 < z < 0.15$ and X-ray luminosity $L_x > 2 \times 10^{44}$ erg s^{-1}. There are 55 clusters satisfying these criteria, to which we add 3 clusters with the slightly relaxed criteria, $L_x > 1.5 \times 10^{44}$ erg s^{-1} and $0.044 < z < 0.15$ for a total of 58.

The combined sample used in this study contains 108 BCGs over the redshift range $0.05 < z < 0.55$ and is summarized in table 2.1. Column 1 gives the names of our BCGs, which is most often simply the cluster name (in the case where the BCG identification is trivial); however we have also included more than one BCG in certain clusters where the identification of the BCG is ambiguous (see Bildfell et al. 2008 for details). The full table of BCGs is sorted by cluster redshift, which is listed in column 2. Columns 3, 4 and 5 list, respectively, the right ascension and declination (α, δ) and optical filter set studied for each of our selected BCG targets. Column 6 gives $\gamma_{(g'-r')} \approx d(g'-r')/d\log(r)$ for the inner 20 kpc region of the BCG (see §2.4 for details). Lastly, column 7 list the core-color for each BCG, determined by examining the color profiles by eye (CB). This is included in order to compare differences in results obtained through visual versus automated core-color classification methods.

[1] http://bax.ast.obs-mip.fr/

Table 2.1: Summary table of BCGs in our sample. The coordinates of the BCG are given, along with the optical filter set used for measuring their color profiles. The quantity $\gamma_{(g'-r')}$ denotes the slope of a linear fit to the inner part of the logarithmic colour gradient $d(g'-r')/d\log(r)$; data converted from $(B-R)$ using the transformations of Lupton (2005) - see text. The final column, "Visual Class" refers to the BCG core-color as classified by eye from the color profile.

Name	z	α hh:mm:ss	δ dd:mm:ss	Optical Filters	$\gamma_{(g'-r')}$	$\gamma_{(g'-r')}$ error	Visual Class
Abell119	0.044	00:56:16.10	-01:15:19.0	g', r'	-0.048	0.001	red
MKW3S	0.045	15:21:51.84	+07:42:31.9	g', r'	-0.082	0.001	red
Abell780	0.054	09:18:05.65	-12:05:43.5	g', r'	0.146	0.011	blue
Abell754	0.054	09:08:32.37	-09:37:47.2	g', r'	-0.066	0.003	red
Abell85	0.055	00:41:50.45	-09:18:11.1	g', r'	-0.015	0.003	red
Abell2319	0.056	19:21:10.00	+43:56:44.5	g', r'	-0.060	0.002	red
Abell133	0.057	01:02:41.71	-21:52:55.1	g', r'	-0.070	0.003	red
Abell1991	0.059	14:54:31.48	+18:38:33.4	g', r'	-0.067	0.002	red
Abell1795	0.062	13:48:52.49	+26:35:34.8	g', r'	0.045	0.004	blue
Abell553	0.066	06:12:41.09	+48:35:44.6	g', r'	-0.091	0.003	red
Abell644	0.070	08:17:25.61	-07:30:45.0	g', r'	-0.069	0.003	red
Abell399	0.072	02:57:53.09	+13:01:51.3	g', r'	-0.040	0.003	red
Abell2065	0.073	15:22:29.17	+27:42:27.8	g', r'	-0.083	0.003	red
Abell401	0.074	02:58:57.78	+13:34:58.3	g', r'	-0.038	0.002	red
ZwCl1215	0.075	12:17:41.13	+03:39:21.2	g', r'	-0.071	0.002	red
Abell2670	0.076	23:54:13.67	-10:25:08.2	g', r'	-0.077	0.003	red
Abell2029	0.077	15:10:56.09	+05:44:41.5	g', r'	-0.058	0.002	red
Abell2495	0.078	22:50:19.71	+10:54:12.7	g', r'	-0.034	0.005	blue
RXSJ2344m04	0.079	23:44:18.20	-04:22:48.8	g', r'	-0.064	0.004	blue
ZwCl0628	0.081	06:31:22.69	+25:01:06.8	g', r'	0.002	0.005	blue
Abell2033	0.082	15:11:26.51	+06:20:56.9	g', r'	-0.076	0.003	red
Abell1650	0.084	12:58:41.49	-01:45:41.0	g', r'	-0.046	0.002	red

Continued on next page...

Table 2.1 continued...

Name	z	α hh:mm:ss	δ dd:mm:ss	Optical Filters	$\gamma_{(g'-r')}$	$\gamma_{(g'-r')}$ error	Visual Class
Abell1651	0.085	12:59:22.49	-04:11:45.7	g', r'	-0.072	0.003	red
Abell2420	0.085	22:10:18.76	-12:10:13.9	g', r'	-0.070	0.002	red
Abell2597	0.085	23:25:19.72	-12:07:26.7	g', r'	0.122	0.008	blue
Abell478	0.088	04:13:25.27	+10:27:55.1	g', r'	-0.035	0.007	blue
Abell2440	0.091	22:23:56.92	-01:34:59.5	g', r'	-0.074	0.003	red
Abell2142	0.091	15:58:19.99	+27:14:00.4	g', r'	-0.086	0.003	red
Abell1927	0.095	14:31:06.79	+25:38:01.6	g', r'	-0.108	0.002	red
Abell21	0.095	00:20:36.98	+28:39:32.9	g', r'	-0.038	0.002	red
Abell2426	0.098	22:14:31.58	-10:22:26.1	g', r'	-0.054	0.002	red
Abell2055	0.102	15:18:45.72	+06:13:56.4	g', r'	0.001	0.017	blue
Abell1285	0.106	11:30:23.82	-14:34:52.3	g', r'	-0.036	0.004	red
Abell7	0.106	00:11:45.25	+32:24:56.6	g', r'	-0.136	0.004	red
Abell2443	0.108	22:26:07.92	+17:21:23.7	g', r'	-0.100	0.004	red
RXCJ0352p19	0.109	03:52:58.99	+19:40:59.8	g', r'	-0.036	0.009	red
Abell2703	0.114	00:05:23.95	+16:13:09.3	g', r'	-0.061	0.003	red
Abell2069	0.116	15:24:08.42	+29:52:55.6	g', r'	-0.074	0.004	red
Abell1361	0.117	11:43:39.60	+46:21:20.7	g', r'	-0.023	0.004	red
Abell2050	0.118	15:16:17.92	+00:05:20.9	g', r'	-0.069	0.003	red
RXCJ0736p39	0.118	07:36:38.08	+39:24:52.8	g', r'	-0.052	0.005	red
Abell1348	0.119	11:41:24.19	-12:16:38.5	g', r'	0.053	0.014	blue
Abell961	0.124	10:16:22.86	+33:38:17.7	g', r'	-0.087	0.006	red
Abell1033	0.126	10:31:44.32	+35:02:29.2	g', r'	-0.105	0.005	red
Abell2627	0.126	23:36:42.08	+23:55:29.5	g', r'	0.062	0.022	blue
Abell655	0.127	08:25:29.05	+47:08:00.9	g', r'	-0.056	0.005	red
Abell646	0.129	08:22:09.53	+47:05:53.3	g', r'	-0.034	0.011	blue
Abell1132	0.136	10:58:23.65	+56:47:42.0	g', r'	-0.045	0.006	red
Abell795	0.136	09:24:05.29	+14:10:21.8	g', r'	0.002	0.004	red
Abell1068	0.138	10:40:44.48	+39:57:11.5	g', r'	0.178	0.027	blue
Abell1413	0.143	11:55:18.00	+23:24:18.1	g', r'	-0.088	0.005	red
ZwCl1023	0.143	10:25:57.98	+12:41:08.7	g', r'	-0.053	0.005	red
Abell990	0.144	10:23:39.91	+49:08:38.8	g', r'	-0.028	0.005	red

Continued on next page...

Table 2.1 continued...

Name	z	α hh:mm:ss	δ dd:mm:ss	Optical Filters	$\gamma_{(g'-r')}$	$\gamma_{(g'-r')}$ error	Visual Class
Abell2409	0.148	22:00:53.49	+20:58:42.1	g', r'	-0.115	0.007	red
A2204	0.150	16:32:46.95	+05:34:33.1	g', r'	0.079	0.034	blue
A2104	0.160	15:40:07.91	-03:18:16.1	g', r'	-0.126	0.008	red
A2259	0.160	17:20:09.63	+27:40:08.5	g', r'	-0.096	0.006	red
A1234	0.166	11:22:29.92	+21:24:22.0	g', r'	-0.099	0.006	red
A1914	0.170	14:26:03.87	+37:49:53.6	g', r'	-0.077	0.005	red
A586	0.170	07:32:20.27	+31:38:01.0	g', r'	-0.329	0.016	red
MS0906	0.170	09:09:12.75	+10:58:29.3	B, R	-0.104	0.008	red
A2218	0.176	16:35:49.22	+66:12:44.8	B, R	-0.066	0.007	red
A1689	0.183	13:11:29.50	-01:20:27.7	B, R	-0.192	0.006	red
A383	0.187	02:48:03.37	-03:31:44.7	B, R	0.266	0.009	blue
A1246	0.190	11:23:58.79	+21:28:50.0	g', r'	-0.089	0.011	red
MS0440	0.190	04:43:09.90	+02:10:19.3	g', r'	-0.182	0.008	red
A115	0.200	00:56:00.24	+26:20:32.7	g', r'	-0.089	0.010	red
A115N	0.200	00:55:50.59	+26:24:37.7	g', r'	0.029	0.010	blue
A2163	0.200	16:15:48.96	-06:08:41.4	g', r'	-0.481	0.031	red
A2261	0.200	17:22:27.19	+32:07:57.9	g', r'	-0.146	0.007	red
A520	0.200	04:54:14.02	+02:57:10.3	g', r'	-0.404	0.036	red
A209	0.206	01:31:52.52	-13:36:39.8	B, R	-0.099	0.011	red
A963	0.206	10:17:03.62	+39:02:49.9	B, R	-0.187	0.006	red
A223a	0.210	01:38:02.27	-12:45:19.7	g', r'	-0.194	0.011	red
A223b	0.210	01:37:55.97	-12:49:10.0	g', r'	-0.159	0.009	red
A1942	0.220	14:38:21.87	+03:40:13.5	g', r'	-0.155	0.010	red
A1763	0.223	13:35:20.10	+41:00:04.5	B, R	-0.165	0.007	red
A2219	0.226	16:40:19.83	+46:42:41.5	B, R	-0.132	0.006	red
A2390	0.228	21:53:36.82	+17:41:44.3	B, R	0.506	0.031	blue
A2111	0.230	15:39:40.48	+34:25:27.6	g', r'	-0.092	0.015	red
A267	0.230	01:52:41.94	+01:00:26.1	B, R	-0.164	0.015	red
MS1231a	0.235	12:33:54.70	+15:26:20.2	B, R	-0.062	0.049	red
MS1231b	0.235	12:33:55.34	+15:25:59.3	B, R	-0.218	0.026	red
A1835	0.250	14:01:02.07	+02:52:42.6	g', r'	0.838	0.021	blue

Continued on next page...

Table 2.1 continued...

Name	z	α hh:mm:ss	δ dd:mm:ss	Optical Filters	$\gamma_{(g'-r')}$	$\gamma_{(g'-r')}$ error	Visual Class
A521	0.250	04:54:06.86	-10:13:24.5	g', r'	-0.135	0.025	red
A68	0.255	00:37:06.84	+09:09:24.7	B, R	0.113	0.025	blue
MS1455	0.257	14:57:15.11	+22:20:34.7	B, R	0.095	0.031	blue
CL1938	0.260	19:38:18.10	+54:09:40.3	g', r'	-0.231	0.025	red
A1758b	0.280	13:32:38.39	+50:33:36.0	g', r'	-0.215	0.014	red
A697	0.280	08:42:57.54	+36:21:59.9	g', r'	-0.157	0.040	red
A611	0.290	08:00:56.80	+36:03:23.7	g', r'	-0.139	0.012	red
A959	0.290	10:17:35.93	+59:34:01.9	g', r'	-0.097	0.031	red
A2537	0.300	23:08:22.21	-02:11:31.5	g', r'	-0.157	0.015	red
MS1008	0.300	10:10:32.29	-12:39:52.7	g', r'	-0.082	0.024	red
MS1224	0.326	12:27:13.46	+19:50:56.3	B, R	0.015	0.025	red
MS1358	0.329	13:59:50.59	+62:31:05.3	B, R	-0.184	0.022	red
MS1512	0.373	15:14:22.49	+36:36:21.5	B, R	0.105	0.056	blue
A370a	0.375	02:39:52.69	-01:34:18.3	B, R	-0.056	0.029	red
A370b	0.375	02:39:53.09	-01:34:55.5	B, R	-0.127	0.037	red
CL0024	0.390	00:26:35.66	+17:09:43.7	B, R	-0.164	0.057	red
A851	0.410	09:42:57.43	+46:58:49.9	g', r'	-0.098	0.050	blue
MS1621a	0.428	16:23:35.16	+26:34:28.6	B, R	-0.260	0.135	red
MS1621b	0.428	16:23:35.43	+26:34:14.7	B, R	-0.388	0.068	red
CL0910	0.440	09:13:45.50	+40:56:28.6	g', r'	1.821	0.046	blue
RXJ1347	0.450	13:47:30.61	-11:45:09.5	g', r'	0.155	0.064	blue
3C295	0.460	14:11:20.51	+52:12:10.3	g', r'	0.448	0.082	blue
RXJ1524	0.516	15:24:38.34	+09:57:43.5	g', r'	-0.649	0.105	red
MS0451	0.540	04:54:10.82	-03:00:51.4	g', r'	0.047	0.232	red
MS0016	0.547	00:18:33.55	+16:26:16.5	B, R	-0.585	0.365	red

2.2.1 Optical data

All of the optical data used in this study are obtained with the Canada-France-Hawaii Telescope (CFHT)[2]. Each cluster is observed in two different optical filters, either the g', r' combination or the B, R combination, depending on the instrument used to perform the observations. There are 20 clusters in the CCCP that have deep, multi-filter optical data in the CFHT archive. These systems were observed using the CFH12K detector and the B and R filters. The remaining CCCP clusters and all of the MENeaCS clusters were observed at a later date using the MegaCam detector and the g' and r' filters. The exposure times for the clusters observed with CFH12K range from 3000 to 1.5×10^4 s for the B band and 3000 to 1.4×10^4 s for the R band. The exposure times for the clusters observed with MegaCam are 1800 s in g', with2400 s in r' for the CCCP and 4800 to 2600 s in both g' and r' for the MENeaCS. The unique combination of long integration times and sub-arcsecond resolution allows us to simultaneously resolve the cores of BCGs and reliably trace their color profiles out to large radii ($r > 40$ kpc), which makes this data set ideal for the purpose of our study.

For further details on the properties of the optical data we refer the reader to Hoekstra (2007), Hoekstra et al. (2012) for CCCP and Sand et al. (2012) for MENeaCS. For the purpose of comparing the optical color gradients with the X-ray data (see §2.5) we convert the $(B-R)$ data to $(g'-r')$ using the transformations of Lupton (2005)[3].

2.2.2 X-ray data

To probe the link between the optical properties of the BCGs and the properties of the ICM of their host clusters, we rely on high resolution X-ray data obtained from the Chandra and XMM-Newton data archives. These data are processed using the Joint-Analysis for Cluster Observations (JACO) software package (see Mahdavi et al. 2007 for further information on the code). Briefly, JACO combines the various sources of high-resolution X-ray data from the Chandra and XMM-Newton telescopes to perform a fully consistent analysis of the hot, X-ray emitting intra-cluster medium.

[2]Based on observations obtained with MegaPrime/MegaCam, a joint project of CFHT and CEA/DAPNIA, at the Canada-France-Hawaii Telescope (CFHT) which is operated by the National Research Council (NRC) of Canada, the Institut National des Science de l'Univers of the Centre National de la Recherche Scientifique (CNRS) of France, and the University of Hawaii.

[3]http://www.sdss.org/dr5/algorithms/sdssUBVRITransform.html#Lupton2005

The JACO analysis constrains the cluster temperature (T_x) and entropy (S) profiles, central cooling time (t_c) and the mean metallicity of the ICM ($\langle Z/Z_\odot \rangle$). We compare these results with the optical core-color of the BCGs later in §2.5. For a more complete discussion of the details regarding the X-ray analysis (for CCCP only) see Mahdavi et al. (2013). The X-ray results for the MENeaCS clusters were obtained using a similar JACO analysis.

2.3 Surface Brightness Profiles

In this section we present surface brightness profiles for the two-filter optical data of each cluster, along with the analysis procedure used to create them. The BCGs reside in the dense, crowded cores of their host clusters. In these environments there is often a significant amount of confusion between neighboring sources. As a result it can be difficult to determine whether or not a given image pixel should be assigned to the BCG or some other neighboring galaxy or foreground star. The first step in the measurement of the BCG surface profile is therefore to create a carefully determined pixel mask, which isolates those pixels where we are confident that the pixel flux is dominated by the BCG.

The pixel mask is constructed from 3 separate mask layers. The first layer is automatically generated using the astronomical image analysis software package SExtractor (Bertin & Arnouts 1996). Using the segmentation image that is output by SExtractor for the r' or R image, we mask all pixels that are associated with a detected source (star or galaxy) that is not the BCG. This becomes the first layer of the mask. The second layer is generated by carefully examining each image by eye and masking, by hand, regions of the image that contain cosmetic defects. These defects, common in MegaCam and CFH12K data, are caused by a variety of effects such as hot pixels, interpolation across chip-gaps, bleeding from a saturated source or secondary internal reflections of very bright sources. The second layer also contains extensions to the first layer of the mask around the brightest extended galaxies and groups of galaxies where SExtractor does not sufficiently trace all the source flux out to large radii. The third and final layer of the pixel mask is also generated manually, but it only applies to the crowded central region of the cluster where the SExtractor segmentation map tends to leave a significant portion of pixels, which are clearly above the background level, unidentified with any particular source. From the other two layers of the mask we remove a circle centered on the BCG with a diameter of 1'.

We then carefully examine this region by eye and manually mask all visible sources and substructures, except for the BCG itself, such that no pixels are obviously above the background level within this aperture (unless they are associated with the BCG). We adjust the contrast level and repeat this step for a wide range of image contrast until we are confident that either the BCG or the background is the dominant source of flux for each remaining unmasked pixel. We then take all three layers (SExtractor segmentation layer, obvious image defects layer, central region layer) and combine them to create a single image mask. Specifically, the final mask is created by first taking the union of layers 1 and 2 and then using layer 3 to replace the central 1.0' aperture around the BCG. This procedure for creating an appropriate BCG mask is similar to that used in Bildfell et al. (2008). Figure 2.1 shows an example of a typical mask resulting from this procedure. The example shown is the mask for Abell 2259 and it has been overlaid on top of the r'-band image to illustrate which parts of the image are allowed to contribute to the background measurement and/or BCG surface brightness profile. Abell 2259, at $z = 0.16$, is near the median redshift of our sample and as such Figure **??** is a representative example.

By comparing the left and right sides of the example shown in figure 2.1 it is clear that the most obviously visible sources are effectively masked. Nonetheless, there remains some low level of unmasked flux present around the edges of some of the masked galaxies. This unmasked flux is primarily an issue for the determination of the background level and the measurement of the BCG surface brightness on $\sim$100 kpc scales. However, as this work focuses on the surface brightness and color profiles of the inner 20 kpc of BCGs our results are not affected by this level of mask incompleteness.

The surface-brightness profiles are measured using a software package developed for this study in the Interactive Data Language (IDL) programming environment. This software takes advantage of the 'histogram' routine in IDL to assign each unmasked image pixel to a particular radial bin. The total flux in each radial bin is calculated by integrating the pixel values using the histogram 'reverse indices' and then dividing by total number of unmasked pixels to obtain the mean surface-brightness (μ). We subtract from this a constant background level measured in an annulus at large radius from the BCG centroid. For the lowest redshift clusters in our sample at $z = 0.05$ we use a minimum radius for the background annulus of ~ 425", corresponding to ~ 415 kpc and for the highest redshift clusters at $z = 0.55$ we use a minimum radius for the background annulus of ~ 150", corresponding to ~ 1000 kpc. We note that the use of different-sized background annuli for low and high z clusters is not a

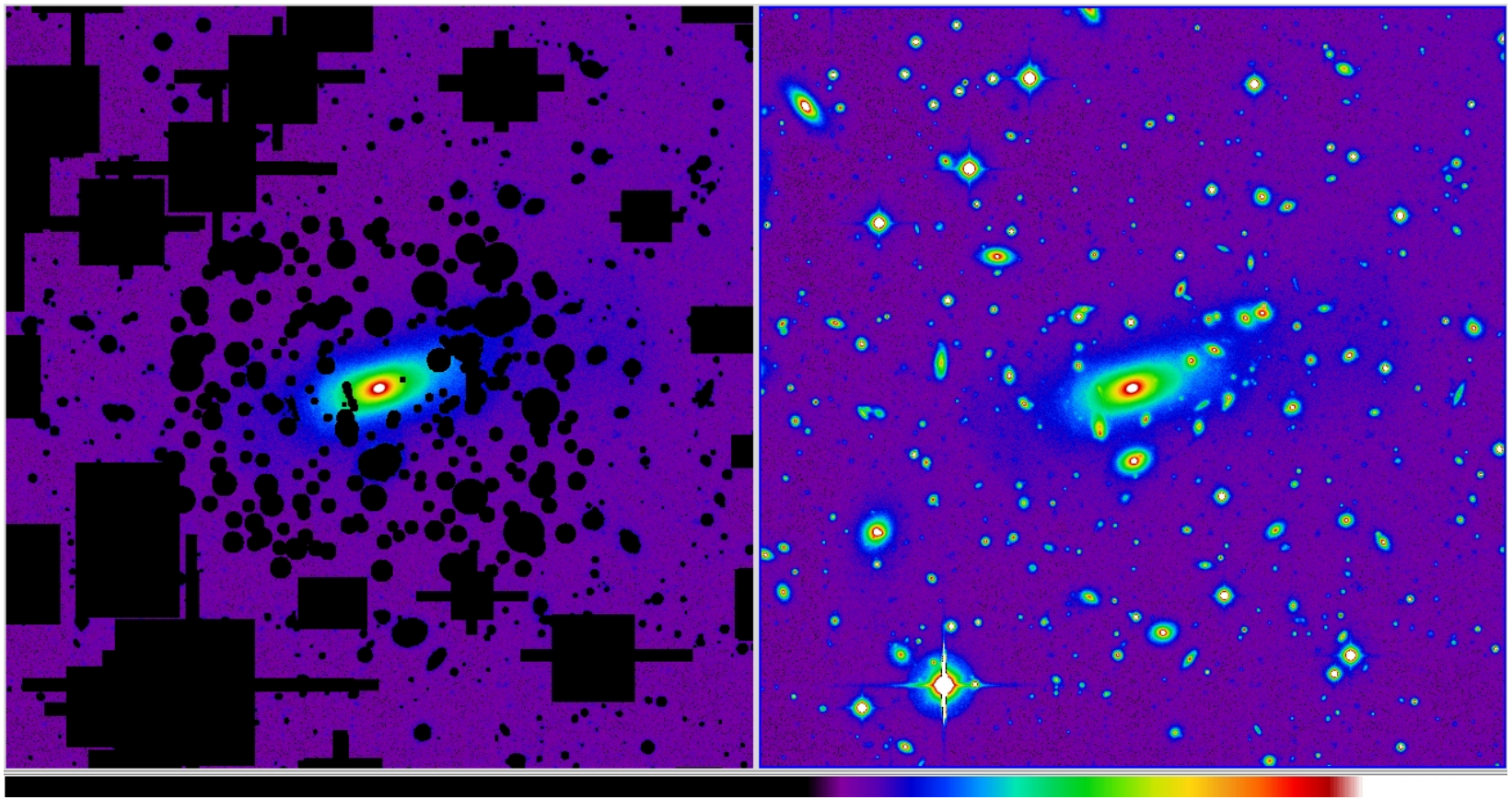

Figure 2.1: Example of a typical mask used for BCG surface brightness measurement. The cluster shown in this example is Abell 2259 and is displayed using a logarithmic scale. On the left side of the figure we have replaced the value of the masked pixels with an extreme negative value. This allows us to easily see which pixels are masked as well as the surface-brightness distribution of the unmasked pixels. The right side of the figure shows the same field, with same display settings, except that the mask has been removed. Comparing the two frames (right versus left) we can conveniently identify which sources were masked and how aggressively they were masked, a property which is important when discussing the more subjective, manually mask layers.

problem here since we are only interested in the central 20 kpc regions of the BCGs, where the surface-brightness is many times brighter than that of the background, regardless of whether the background is measured at 400 or 1000 kpc. The errors on the the mean surface brightness in each bin are estimated by calculating the standard deviation of the pixel values and dividing by the square root of the number unmasked pixels in that bin. To this we also add in quadrature the error on the background level. This error estimate accounts for random error associated with photon noise but does not include any contributions from potential systematics.

Figures 2.2 through 2.9 show the resulting surface-brightness profiles in two-filter optical data for each cluster in our sample. The red points in these figures show the behavior of the longer-wavelength optical data (R or r') while the blue points show the shorter-wavelength optical data (B or g'). For reference, each panel in the surface-brightness plots has been labeled with a dashed line that indicates the physical distance in kpc corresponding to an angular distance of 1.0" from the BCG centroid. This 1.0" limit represents the characteristic maximum scale of the Point Spread Function (PSF) for these data, though most of the data have a sub-arcsecond PSF.

The surface-brightness profiles for the BCGs in our sample exhibit a relatively shallow decrease with increasing radius that is expected for large elliptical galaxies. Owing to this shallow falloff in surface-brightness we are able to trace the the profile out to ~ 100 kpc or further in many cases without making any assumptions about the profile shape. There are some exceptions, however, where the profile is significantly steeper (ie. CL0910, A1835). These clusters are at the high-z end of our sample and it may be that the BCGs in these cluster have not yet been fully assembled. Furthermore, these clusters are cool-core systems and it is possible that the profiles appear steeper because these central regions of these BCGs are concentrated sites of recent star formation associated with the cooling X-ray gas. The maximum radius to which the BCG measurement can be traced is determined by examining the color profiles (§2.4). Specifically, we truncate the measurement of both surface-brightness and color profiles at the location where the color profile exhibits a strong discontinuity in slope. These abrupt changes in slope are indicative of where the BCG flux becomes faint compared to the background flux. In a few cases where there is a very bright star near to the BCG (in projection) the stellar light heavily contaminates the BCG surface brightness profile, severely limiting our ability to constrain the shape of the extended profile (eg. Abell2204). However, this does not affect our results,

as we are only interested in the central 20 kpc of the surface-brightness profile. The predominantly smooth shape and monotonic nature of the profiles suggests that the masking technique is effective at preventing contamination from neighboring sources, which would otherwise appear as bumps and kinks in the profiles.

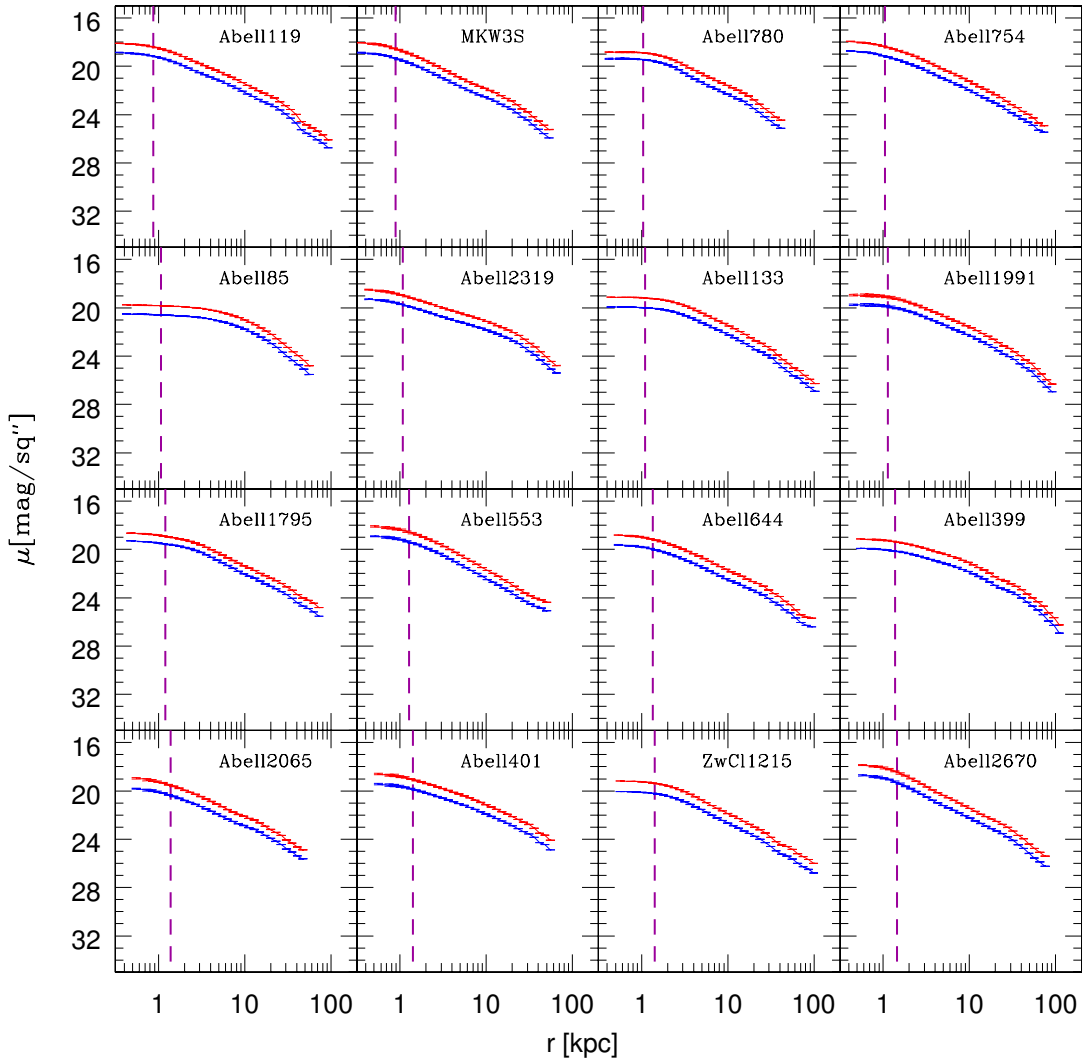

Figure 2.2: Surface brightness profiles for BCGs. Upper (red) curves show the data for the r'-band, while lower (blue) curves show the data for the g'-band. Vertical dashed lines indicate the characteristic maximum PSF scale of these data, placed at the projected physical distance corresponding to 1.0".

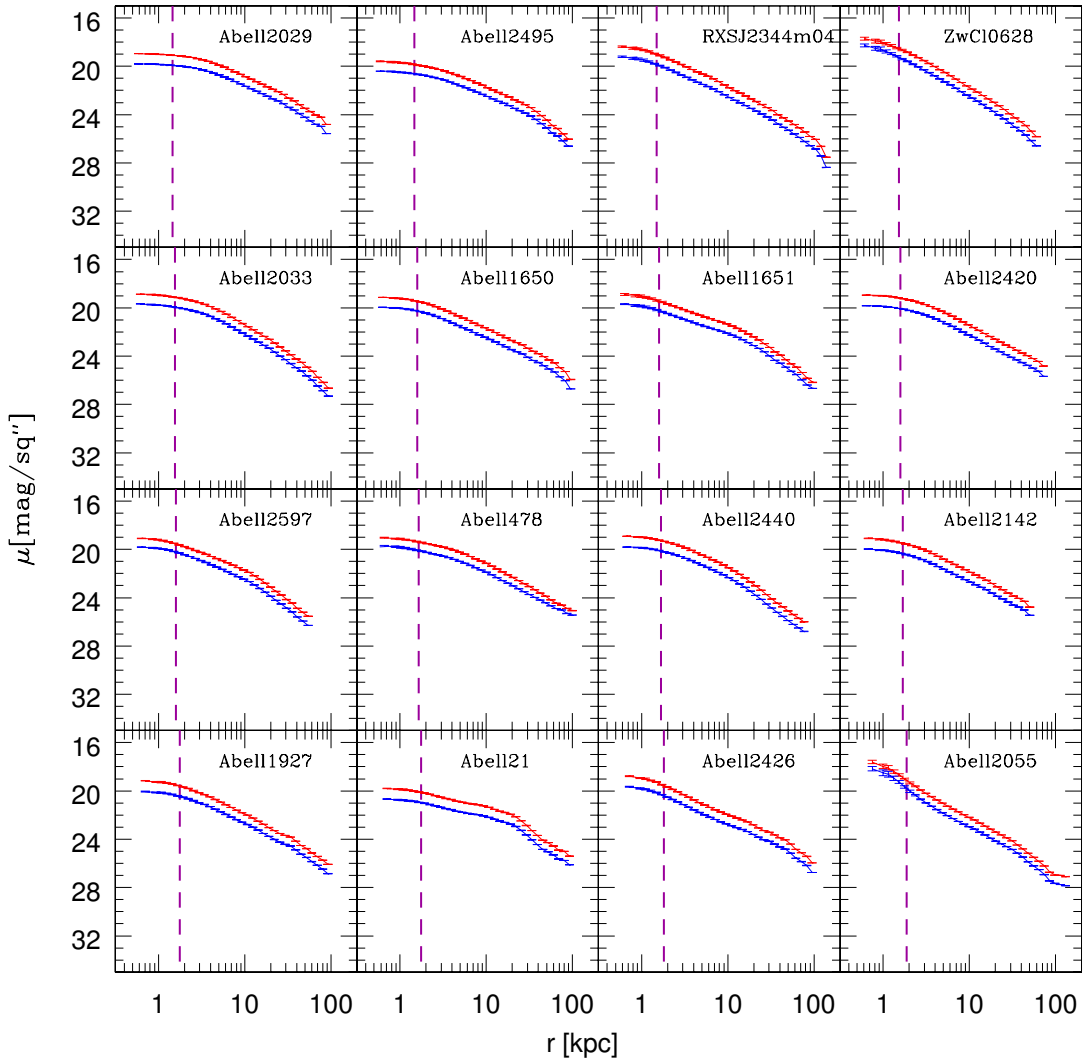

Figure 2.3: Surface brightness profiles for BCGs. Upper (red) curves show the data for the r'-band, while lower (blue) curves show the data for the g'-band. Vertical dashed lines indicate the characteristic maximum PSF scale of these data, placed at the projected physical distance corresponding to 1.0".

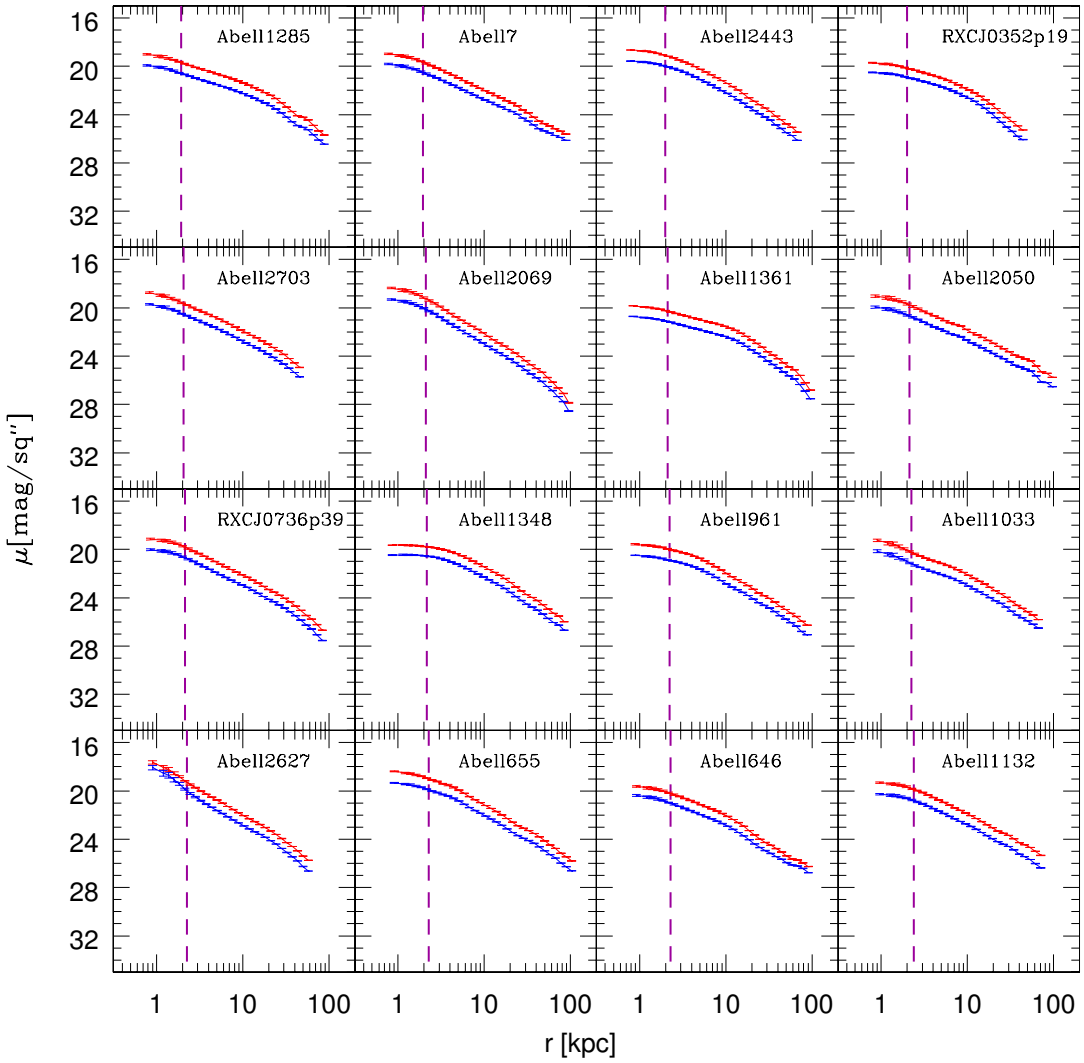

Figure 2.4: Surface brightness profiles for BCGs. Upper (red) curves show the data for the r'-band, while lower (blue) curves show the data for the g'-band. Vertical dashed lines indicate the characteristic maximum PSF scale of these data, placed at the projected physical distance corresponding to 1.0".

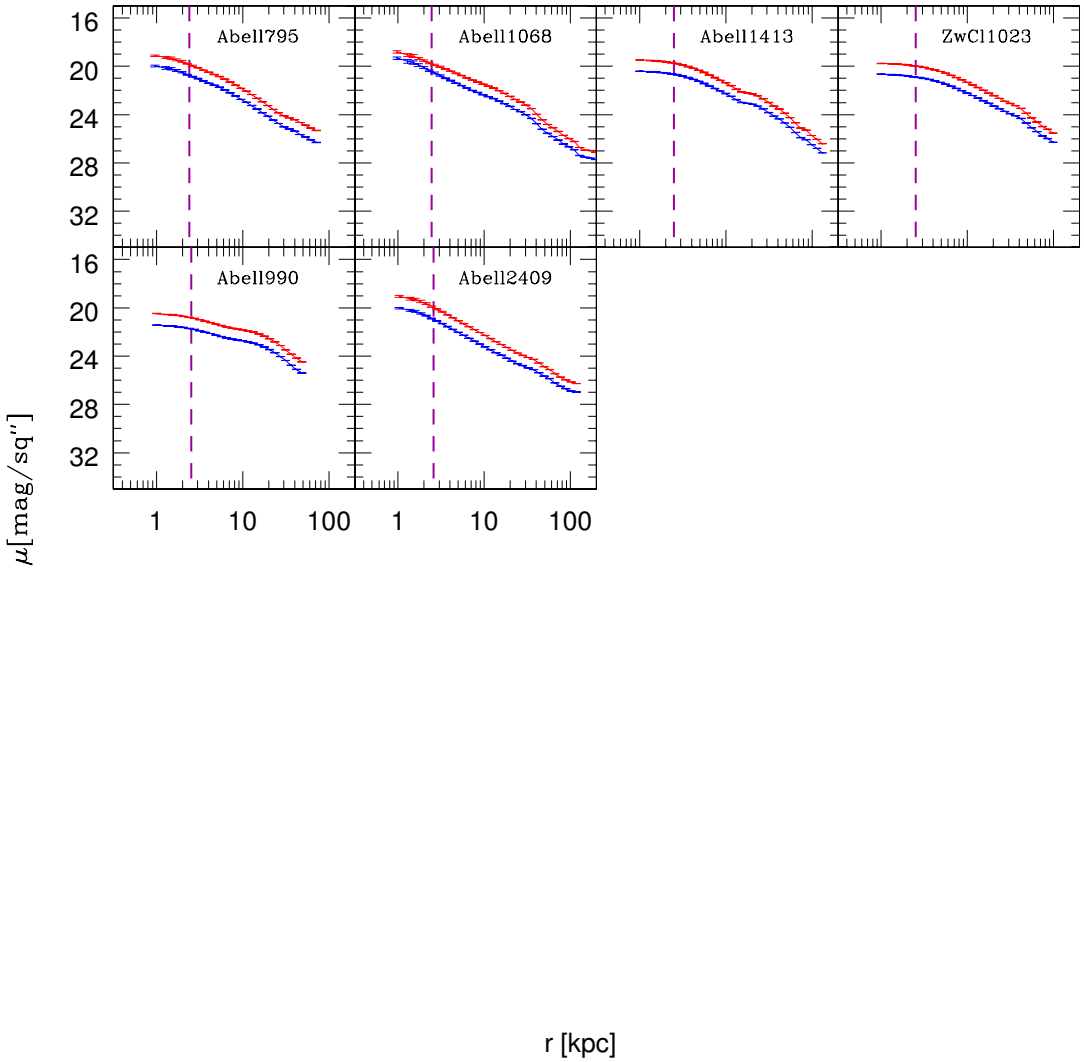

Figure 2.5: Surface brightness profiles for BCGs. Upper (red) curves show the data for the r'-band, while lower (blue) curves show the data for the g'-band. Vertical dashed lines indicate the characteristic maximum PSF scale of these data, placed at the projected physical distance corresponding to 1.0".

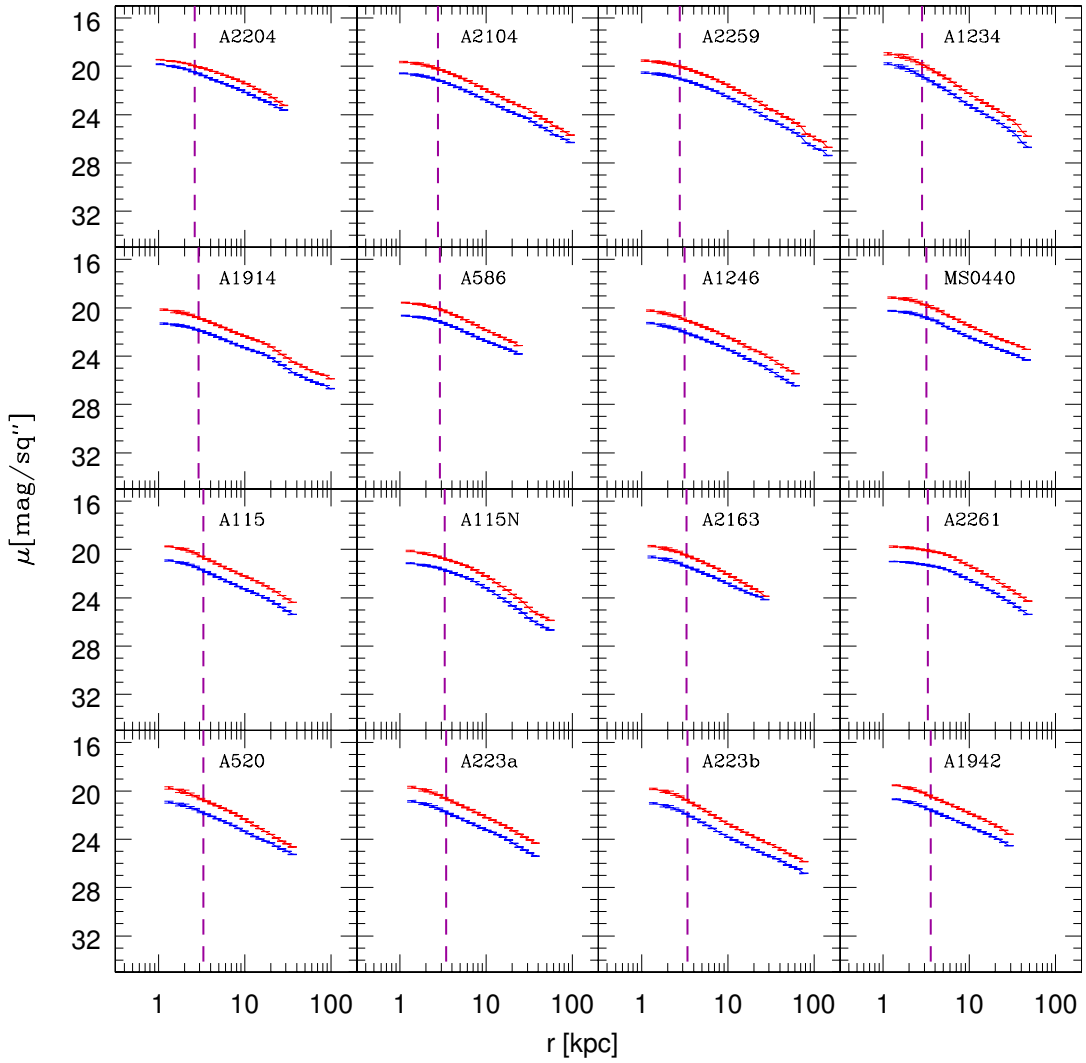

Figure 2.6: Surface brightness profiles for BCGs. Upper (red) curves show the data for the r'-band, while lower (blue) curves show the data for the g'-band. Vertical dashed lines indicate the characteristic maximum PSF scale of these data, placed at the projected physical distance corresponding to 1.0".

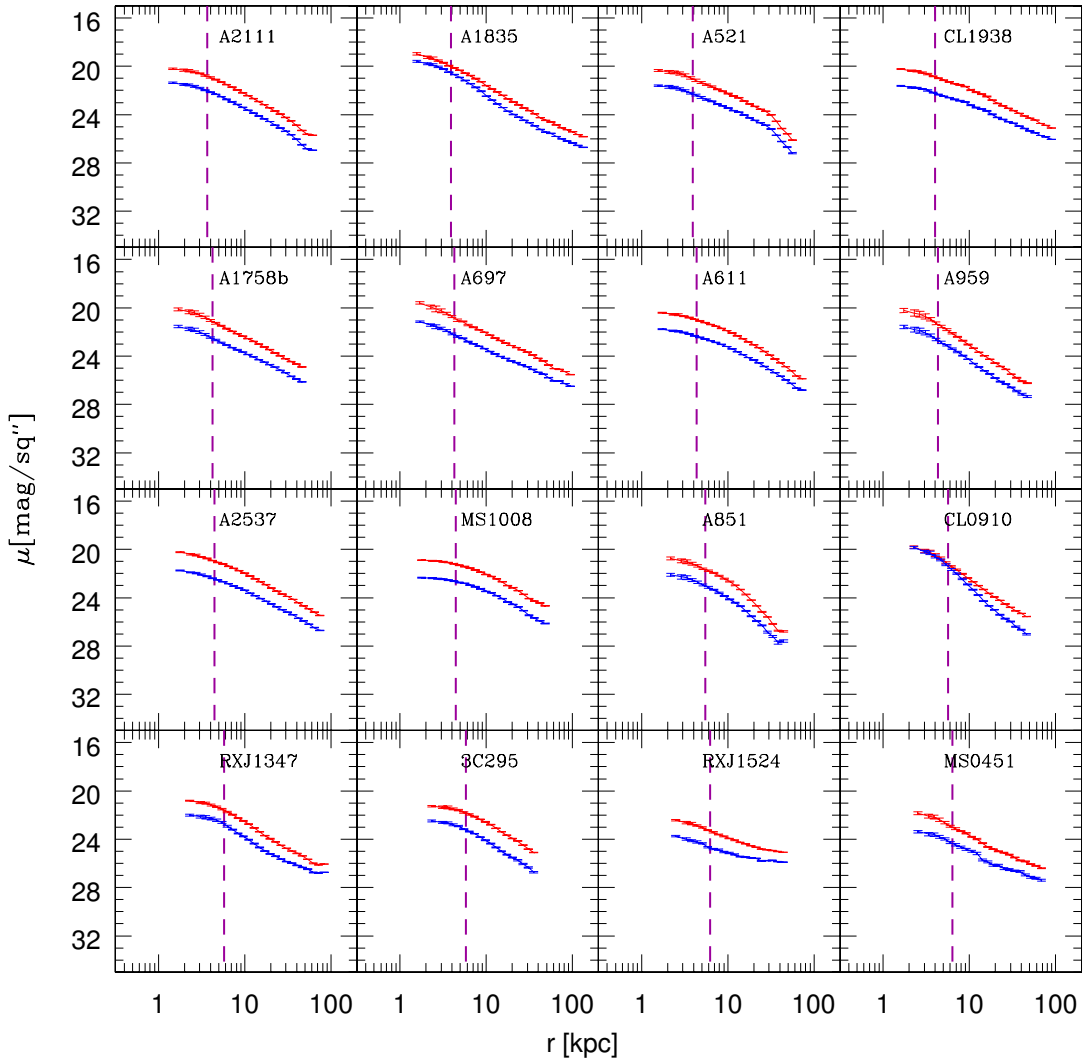

Figure 2.7: Surface brightness profiles for BCGs. Upper (red) curves show the data for the r'-band, while lower (blue) curves show the data for the g'-band. Vertical dashed lines indicate the characteristic maximum PSF scale of these data, placed at the projected physical distance corresponding to 1.0".

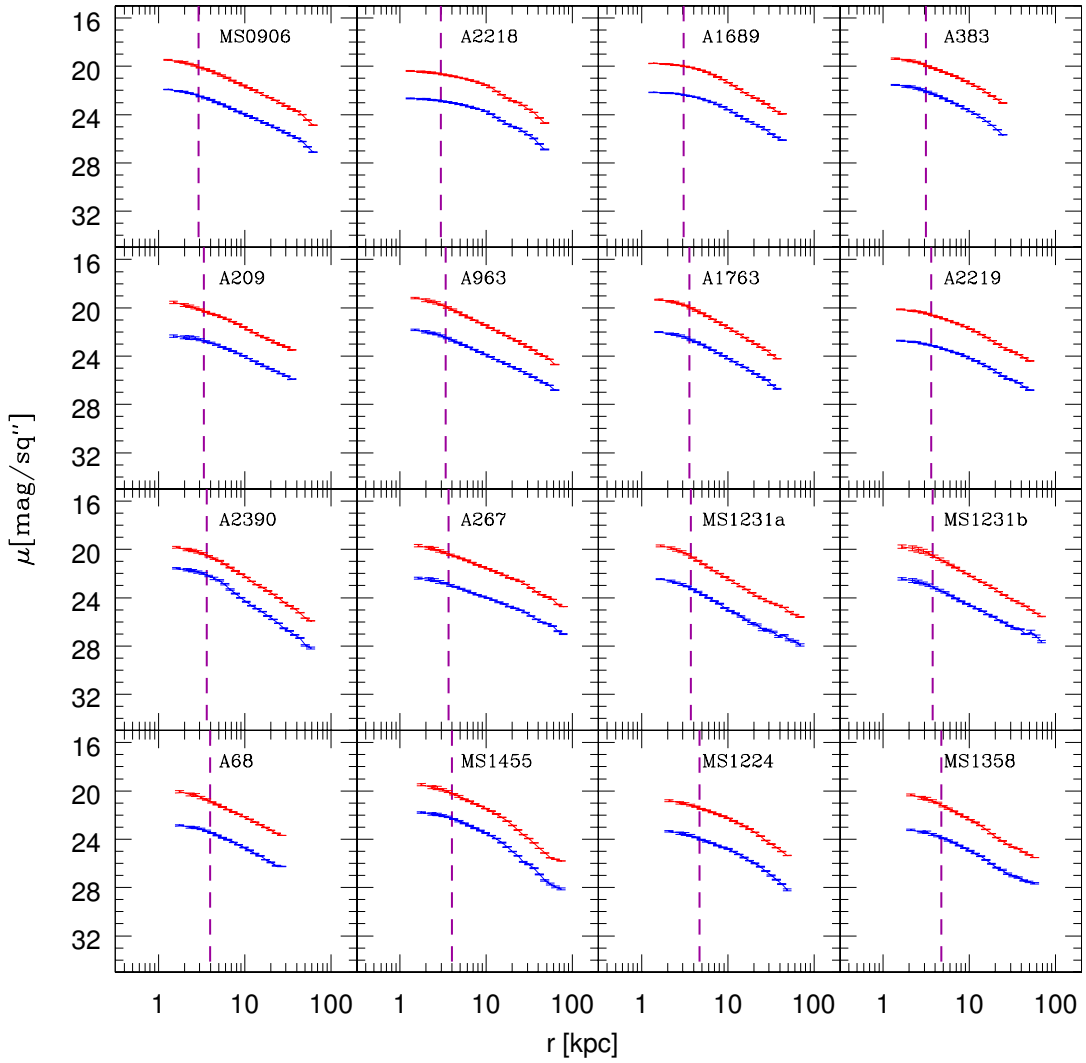

Figure 2.8: Surface brightness profiles for BCGs. Upper (red) curves show the data for the R-band, while lower (blue) curves show the data for the B-band. Vertical dashed lines indicate the characteristic maximum PSF scale of these data, placed at the projected physical distance corresponding to 1.0".

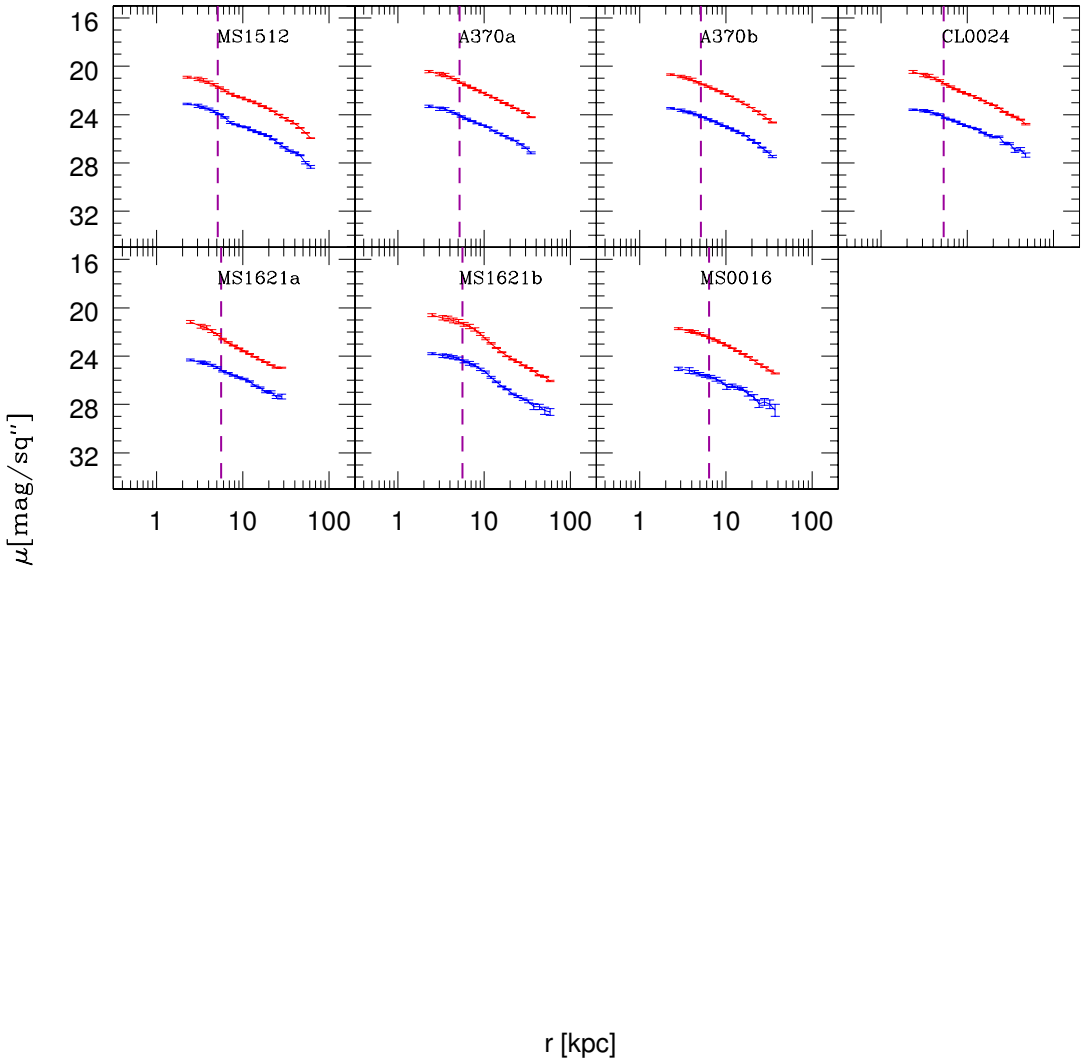

Figure 2.9: Surface brightness profiles for BCGs. Upper (red) curves show the data for the R-band, while lower (blue) curves show the data for the B-band. Vertical dashed lines indicate the characteristic maximum PSF scale of these data, placed at the projected physical distance corresponding to 1.0".

2.4 Color Profiles

The optical colors of galaxies are affected by a variety of physical characteristics of their stellar populations such as age, metallicity, the presence of dust, the shape of the initial mass function, as well as the poorly constrained processes governing the behavior of stars in the late stages of stellar evolution (Bruzual & Charlot 2003, Maraston et al. 2009, Conroy et al. 2009, 2010a, 2010b). Because of this sensitivity, the color profiles of BCGs are interesting as they carry information regarding the stellar population gradients within them.

In this section we discuss the construction of the optical color profiles as well as the procedure used to quantify the change in color over the central 20 kpc. The $(g' - r')$ and $(B - R)$ color profiles are constructed simply by taking the difference between the surface-brightness profiles, subtracting the data observed in the filter using the longer effective wavelength (r' or R) from that observed using the filter with the shorter effective wavelength (g' or B). The errors on the colors are calculated by adding in quadrature the errors on individual surface-brightness profiles. As mentioned briefly in §2.3, we inspect the individual color profiles by eye to determine the maximum radius to which the data are a reliable measure of the BCG colors. We truncate the color profiles at large radius where the slope of the profile becomes discontinuous, indicating that the BCG is no longer the dominant contribution to the color profile. The most likely explanation for this transition is contamination from the PSF wings of nearby bright stars, large-scale variability in the background or flat-fielding errors. Alternatively, If the color of the intra-cluster star population deviates significantly from the outermost color of BCG this could also trigger profile truncation. In addition to truncating the color profiles, we also apply this same truncation radius to the surface-brightness profiles presented in §2.3. We note however, that the precise location of the truncation radius does not affect the results presented hereafter.

We show in Figures 2.10 through 2.17 the $(g' - r')$ or $(B - R)$ color profiles for the BCGs in our sample. With the parameterization used here, larger, more positive values of the $(g' - r')$ or $(B - R)$ color indicate redder galaxies, while galaxies with smaller, or more negative values of these colors are bluer. As in the surface-brightness profiles, the radius corresponding to the maximum PSF size of 1.0" is shown by a horizontal, dashed line. The majority of the BCGs have relatively featureless, shallow color profiles with weakly negative color gradients that become bluer with increasing radius. These color gradients can be explained by the presence of metallicity gradients

within the BCGs, which have been directly observed at lower redshift (Loubser et al. 2012). Simulations show that negative radial metallicity gradients can arise naturally in systems that grow partly through minor, dry mergers (Kawata et al. 2006). There are, however, a significant number of BCGs where the color in the central core is blue and the color gradient is positive but then turns over and flattens at larger radii; except in CL0910 where we do not detect a turnover. We refer to these systems as blue-core BCGs. This phenomenon has been identified previously in work on BCG optical color profiles (Bildfell et al. 2008, Rafferty et al. 2008) and it has been argued in these studies that this is likely due to the presence of recent star formation in the central regions of these galaxies. It may also be possible to create blue cores in BCGs without requiring recent star formation by invoking AGN activity or metallicity gradient inversions. However, AGNs should be ruled out as the sole source of blue cores based on the large radial extent of the blue regions, which are typically several times larger than the PSF scale. Metallicity gradient inversion should also be ruled out as it would require an outside-in formation scenario, which is inconsistent with the current view of structure formation. Furthermore, because only a fraction of BCGs have blue cores, this would require two separate mechanisms for BCG formation; one leading to monotonic metallicity gradients and another which is capable of producing inverted gradients. Lastly, the high UV fluxes associated with blue-core BCGs cannot be explained by metallicity gradients alone and most likely require the presence of a young stellar component in these systems (Pipino et al. 2009). The recent star formation mechanism is thus the most favorable one for creating blue cores in BCGs. However, further confirmation through medium-resolution observations of the spectra of these galaxies, particularly in the blue and UV is required in order to be certain.

We classify each BCG in our sample as red or blue core based on visual inspection of the color profiles shown in Figures 2.10 through 2.17. These classifications for individual systems are listed in Table 2.1 under the heading visual class. We find that 24 of the total sample of 108 BCGs in our sample have a blue visual classification. Although the sample likely suffers from some effects of selection-bias, if we assume that the clusters are randomly selected, we find that $22.2 \pm 4.5\%$ of BCGs possess blue cores, where the errors are determined by shot noise. This is compatible with the results of Bildfell et al. (2008) who find 25% of their sample contains blue-core BCGs, though there is significant overlap between our sample and theirs, especially at the high-z end. If we consider only the subset of lower-z cluster that is not present in Bildfell et al. (2008) (ie. MENeaCS clusters) then we find 22.2 ± 6.4 of their

BCGs have blue-cores, which is in excellent agreement with the higher-z subsample (ie. CCCP clusters). We caution however that this result is dependent upon the details of our sample selection and thus should not be used to quantify the absolute evolution of the blue-core frequency.

While there are merits to visual classification schemes they are dependent upon the particular individual who performs said classification. It is therefore difficult to reproduce results that depend on visual class or compare with similar studies that each use their own visual classification. To mitigate these concerns we also perform an automated classification based on a simple fit to the data. In addition to being repeatable, this has the added benefit that we obtain a numerical estimate of the blue-ness of the core, which is an improvement over the binary classification (blue or red) of the visual scheme. We approximate value of the color gradient in the inner most region [$\gamma_{(g'-r')} \approx d(g'-r')/d\log(r)$ or $\gamma_{(B-R)} \approx d(B-R)/d\log(r)$] as the slope of a linear fit to the color profile over the range in projected radial distance from $r_{PSF} < r < 20$ kpc. Here the value of r_{PSF} signifies the innermost radius resolvable in our data, which we conservatively set to the radius corresponding to 1.0". Although the bluing trend may continue inward beyond the PSF cutoff, we are mainly interested in identifying systems which have resolved blue-cores and are thus more likely associated with star-formation than AGN. We choose to use physical units measured in kpc rather than units scaled to the BCG's effective radius because the effective radius of an individual BCG is model-dependent and ambiguous (Bildfell et al. 2008). Moreover, we do not expect that the size of the star-forming core, the appearance of which is driven by gas processes in the central regions, to be dependant on the size of the galaxy itself. The choice of 20 kpc as the upper bound on the fitting range is based on the observed sizes of blue-core regions in Bildfell et al. (2008). We indicate the fitting region in Figures 2.10 through 2.17 as that between the solid, blue lines and the best fit is indicated as a thick pink band (note that we are only concerned with the slope here). We compute the error on $\gamma_{(g'-r')}$ and $\gamma_{(B-R)}$ using a bootstrapping technique that is run for 1000 realizations. To compare the data taken in different optical filter combinations fairly, we convert the values of $\gamma_{(B-R)}$ to $\gamma_{(g'-r')}$ (see §2.5 for details). Our final values of $\gamma_{(g'-r')}$ are listed in table 2.1. Using $\gamma_{(g'-r')}$ as our discriminating metric for automated classification we find that $20.4 \pm 4.3\%$ of the BCGs in our sample have positive values of $\gamma_{(g'-r')}$ (blue core). This is in excellent statistical agreement with the fraction of BCGs that are visually classified as blue-core. Although we do not observe a direct one-to-one correspondence between

blue-core systems as classified visually versus classified automatically, we find that statistically, the fraction of our sample that is classified as blue-core is identical, regardless of the classification method used. Specifically we find that 17.59% of our sample is classified as blue-core in both classification schemes, 75.93% of our sample is red in both classification schemes, while 6.48% of our sample is more ambiguous with a classification of blue-core in one scheme and red-core in the other. The source of this ambiguity can likely be attributed to the low amplitude of the small-scale blue anomaly relative to the underlying negative gradient of the more extended color profile in some BCGs (eg. Abell2495).

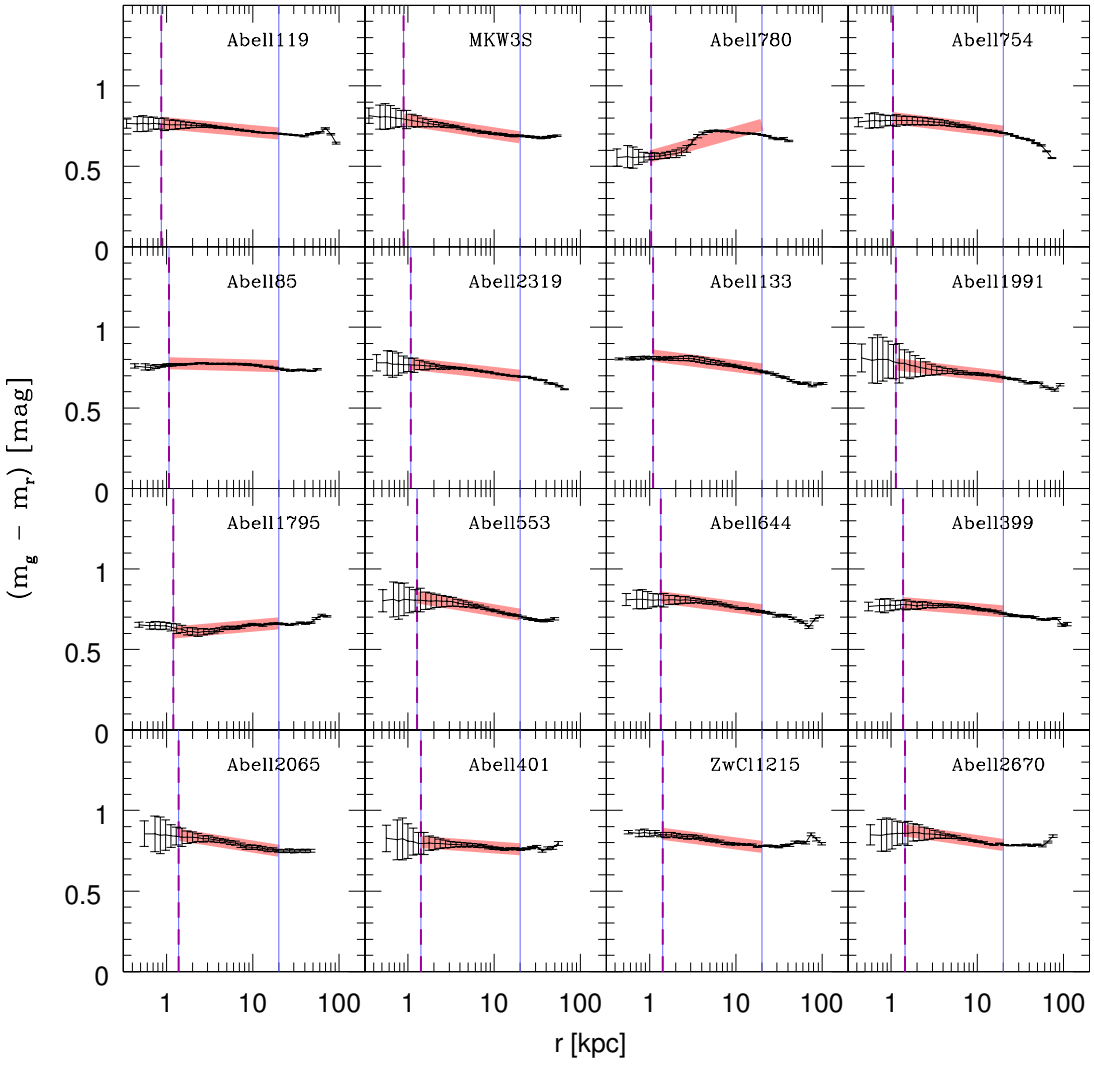

Figure 2.10: Colour profiles for BCGs as observed in the $(g' - r')$ filter combination. Dashed vertical lines denote the radius corresponding to 1.0", the characteristic maximum PSF scale (r_{PSF}). The thick pink band shows the results of a linear fit to the data over the radial range $r_{PSF} < r < 20$ kpc (denoted by thin vertical lines). We use the slope of this line ($\gamma_{(g'-r')}$) classify the BCG core color: $\gamma_{(g'-r')} > 0$ blue-core, $\gamma_{(g'-r')} < 0$ red-core.

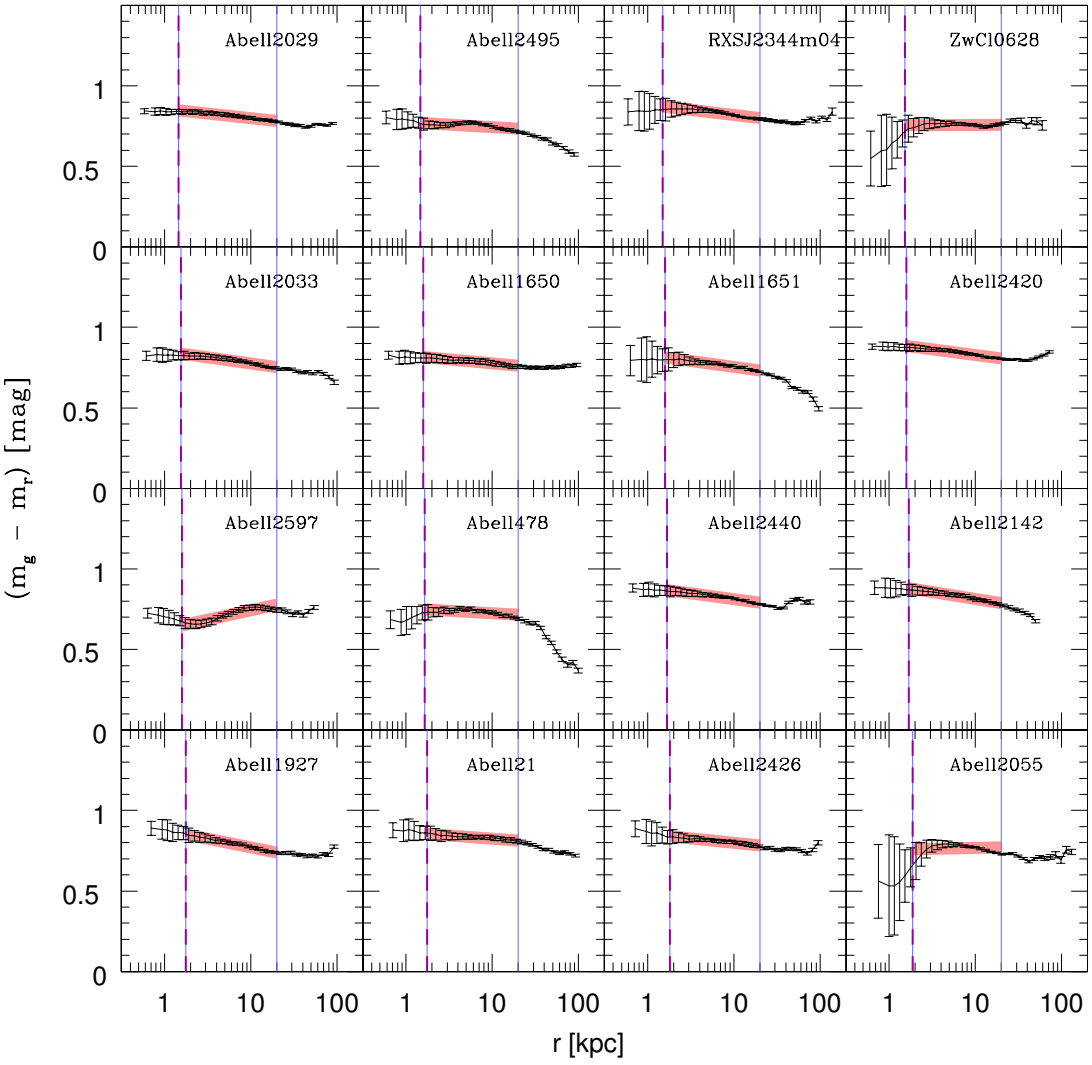

Figure 2.11: Colour profiles for BCGs as observed in the $(g' - r')$ filter combination. Dashed vertical lines denote the radius corresponding to 1.0", the characteristic maximum PSF scale (r_{PSF}). The thick pink band shows the results of a linear fit to the data over the radial range $r_{PSF} < r < 20$ kpc (denoted by thin vertical lines). We use the slope of this line ($\gamma_{(g'-r')}$) classify the BCG core color: $\gamma_{(g'-r')} > 0$ blue-core, $\gamma_{(g'-r')} < 0$ red-core.

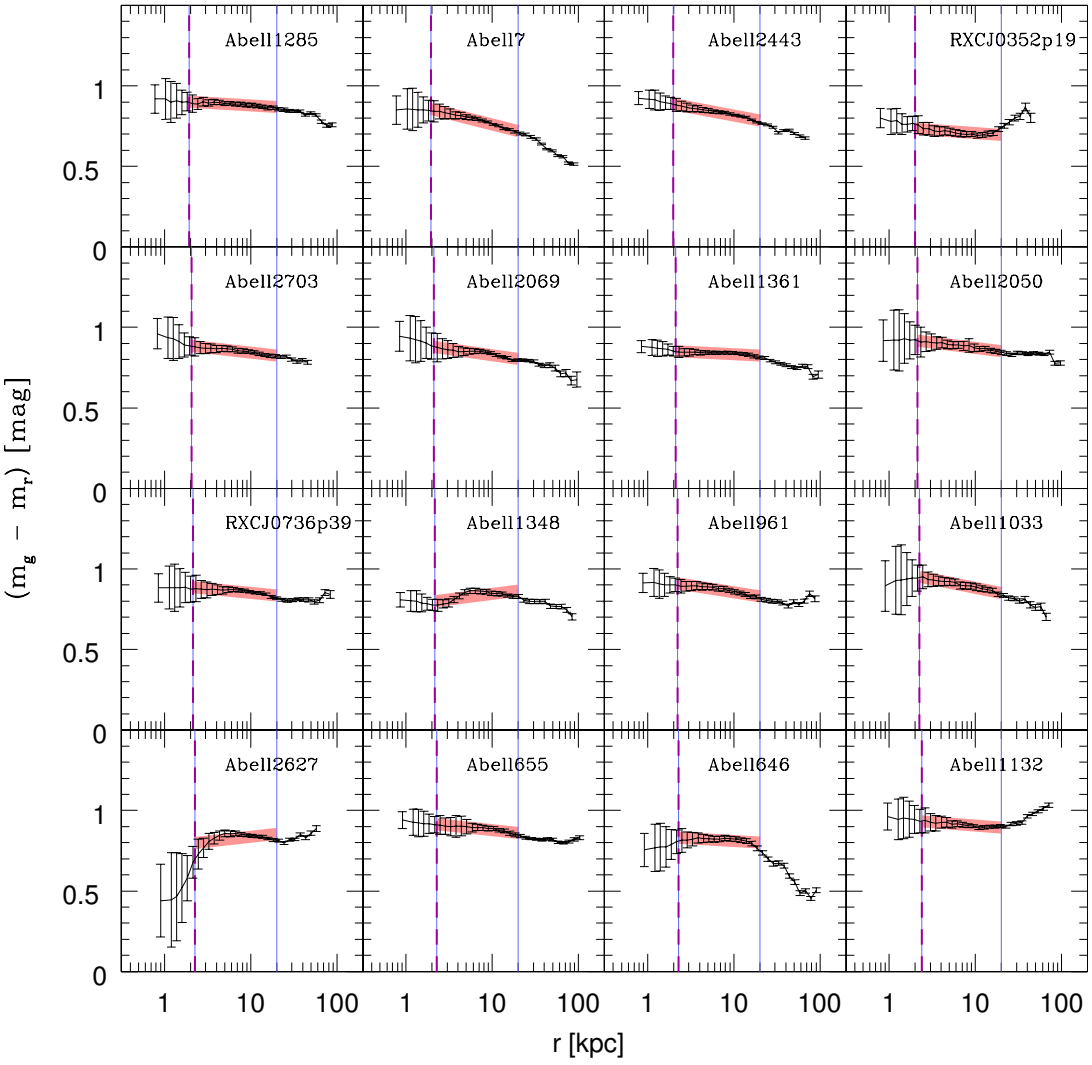

Figure 2.12: Colour profiles for BCGs as observed in the $(g' - r')$ filter combination. Dashed vertical lines denote the radius corresponding to 1.0", the characteristic maximum PSF scale (r_{PSF}). The thick pink band shows the results of a linear fit to the data over the radial range $r_{PSF} < r < 20$ kpc (denoted by thin vertical lines). We use the slope of this line ($\gamma_{(g'-r')}$) classify the BCG core color: $\gamma_{(g'-r')} > 0$ blue-core, $\gamma_{(g'-r')} < 0$ red-core.

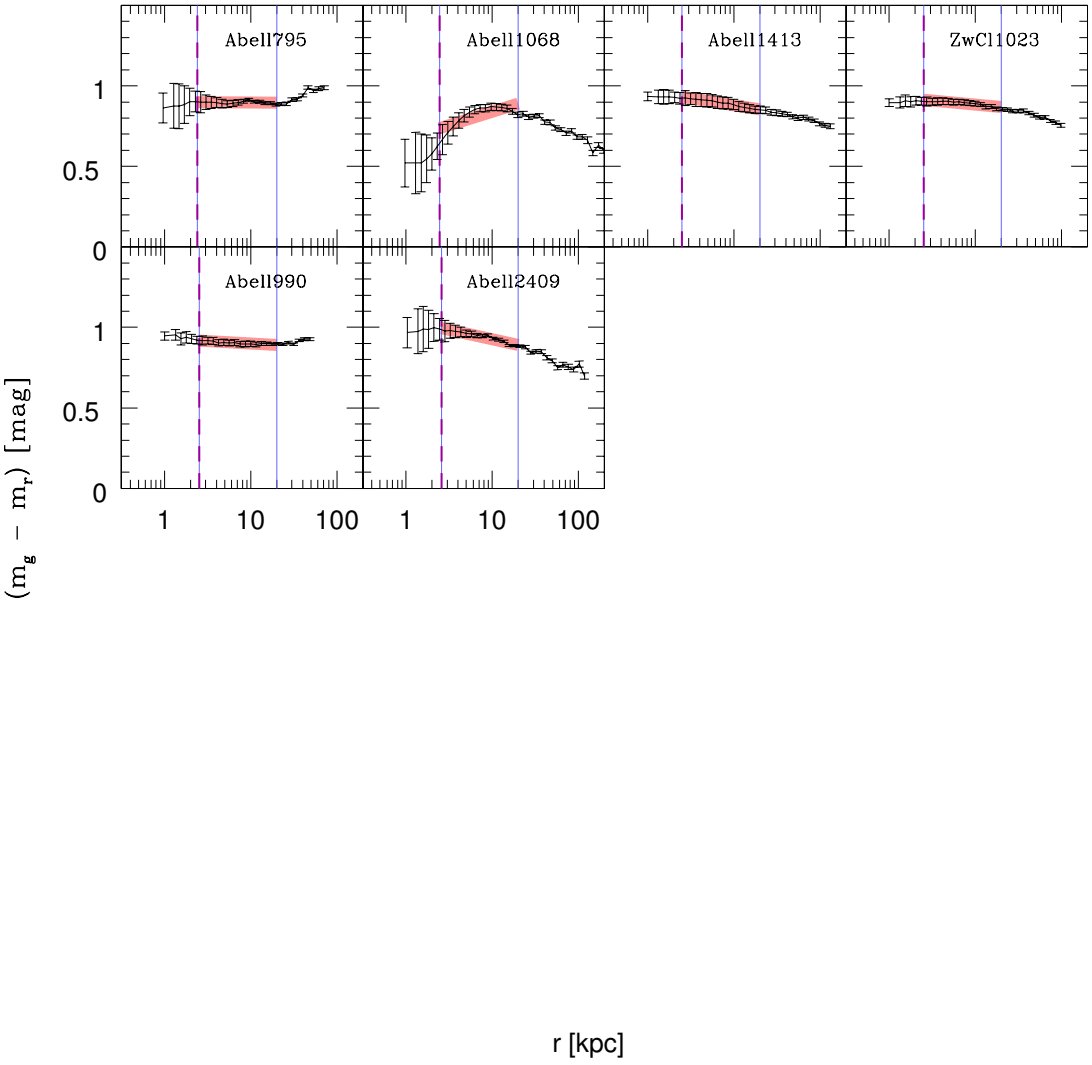

Figure 2.13: Colour profiles for BCGs as observed in the $(g' - r')$ filter combination. Dashed vertical lines denote the radius corresponding to 1.0", the characteristic maximum PSF scale (r_{PSF}). The thick pink band shows the results of a linear fit to the data over the radial range $r_{PSF} < r < 20$ kpc (denoted by thin vertical lines). We use the slope of this line ($\gamma_{(g'-r')}$) classify the BCG core color: $\gamma_{(g'-r')} > 0$ blue-core, $\gamma_{(g'-r')} < 0$ red-core.

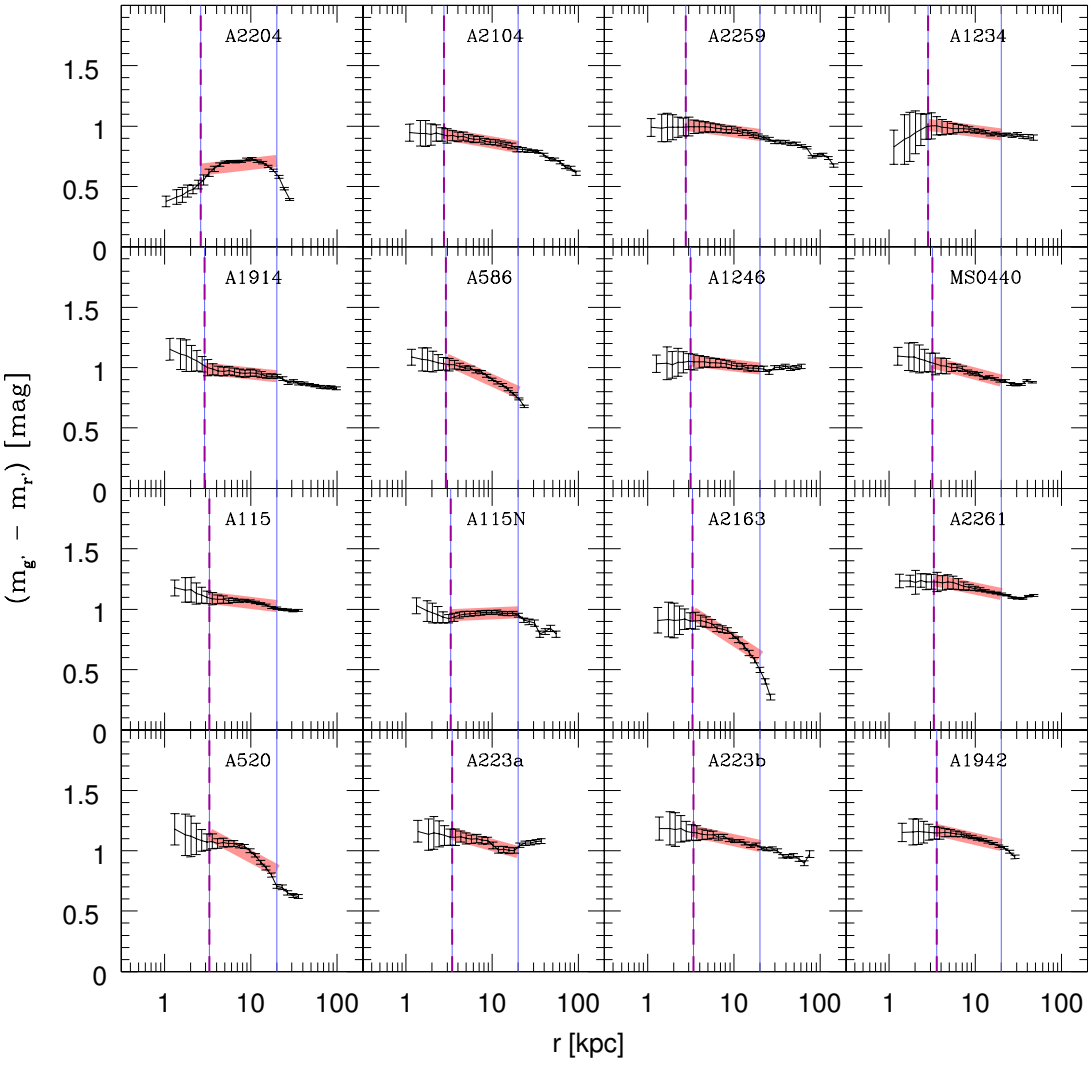

Figure 2.14: Colour profiles for BCGs as observed in the $(g' - r')$ filter combination. Dashed vertical lines denote the radius corresponding to 1.0", the characteristic maximum PSF scale (r_{PSF}). The thick pink band shows the results of a linear fit to the data over the radial range $r_{PSF} < r < 20$ kpc (denoted by thin vertical lines). We use the slope of this line ($\gamma_{(g'-r')}$) classify the BCG core color: $\gamma_{(g'-r')} > 0$ blue-core, $\gamma_{(g'-r')} < 0$ red-core.

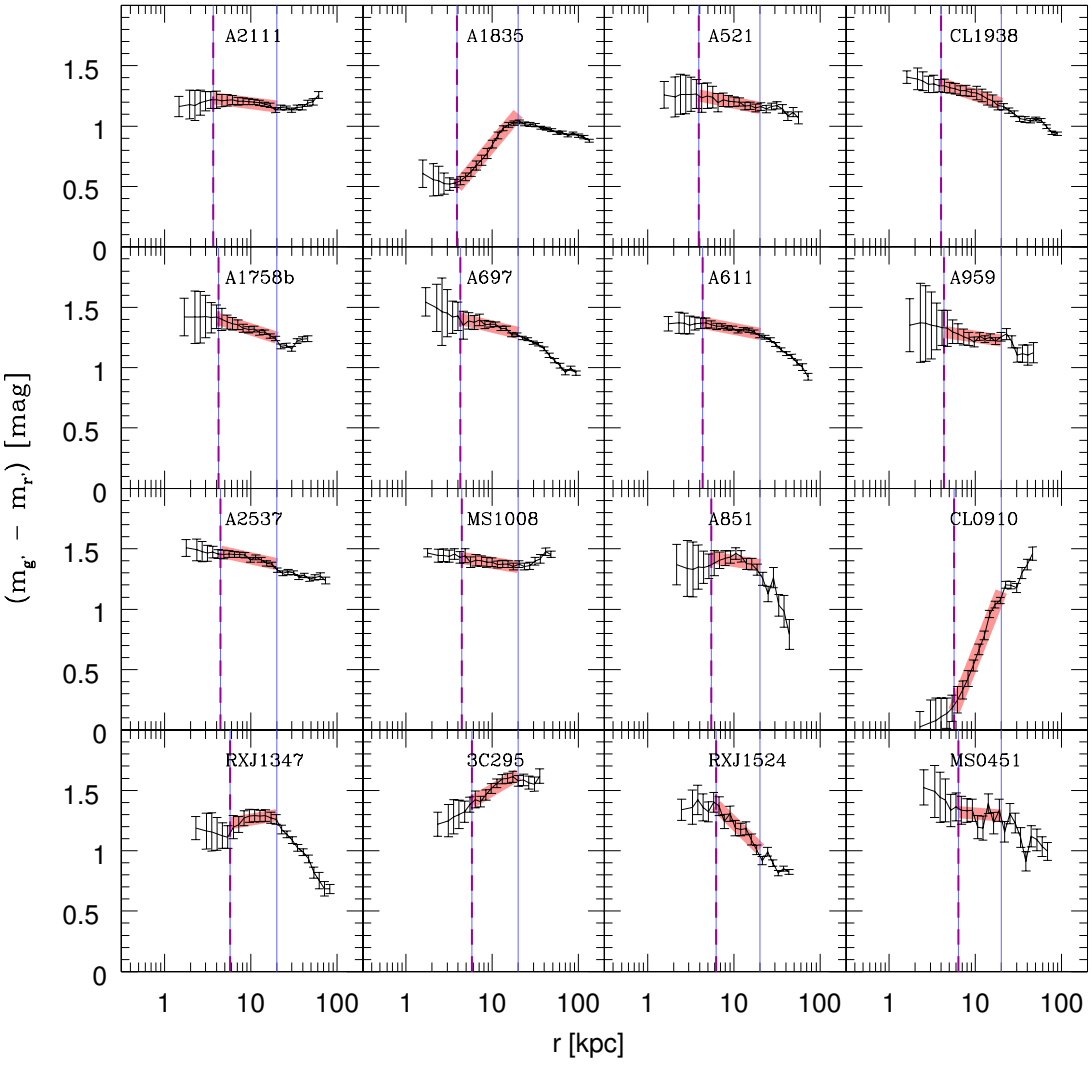

Figure 2.15: Colour profiles for BCGs as observed in the $(g' - r')$ filter combination. Dashed vertical lines denote the radius corresponding to 1.0", the characteristic maximum PSF scale (r_{PSF}). The thick pink band shows the results of a linear fit to the data over the radial range $r_{PSF} < r < 20$ kpc (denoted by thin vertical lines). We use the slope of this line ($\gamma_{(g'-r')}$) classify the BCG core color: $\gamma_{(g'-r')} > 0$ blue-core, $\gamma_{(g'-r')} < 0$ red-core.

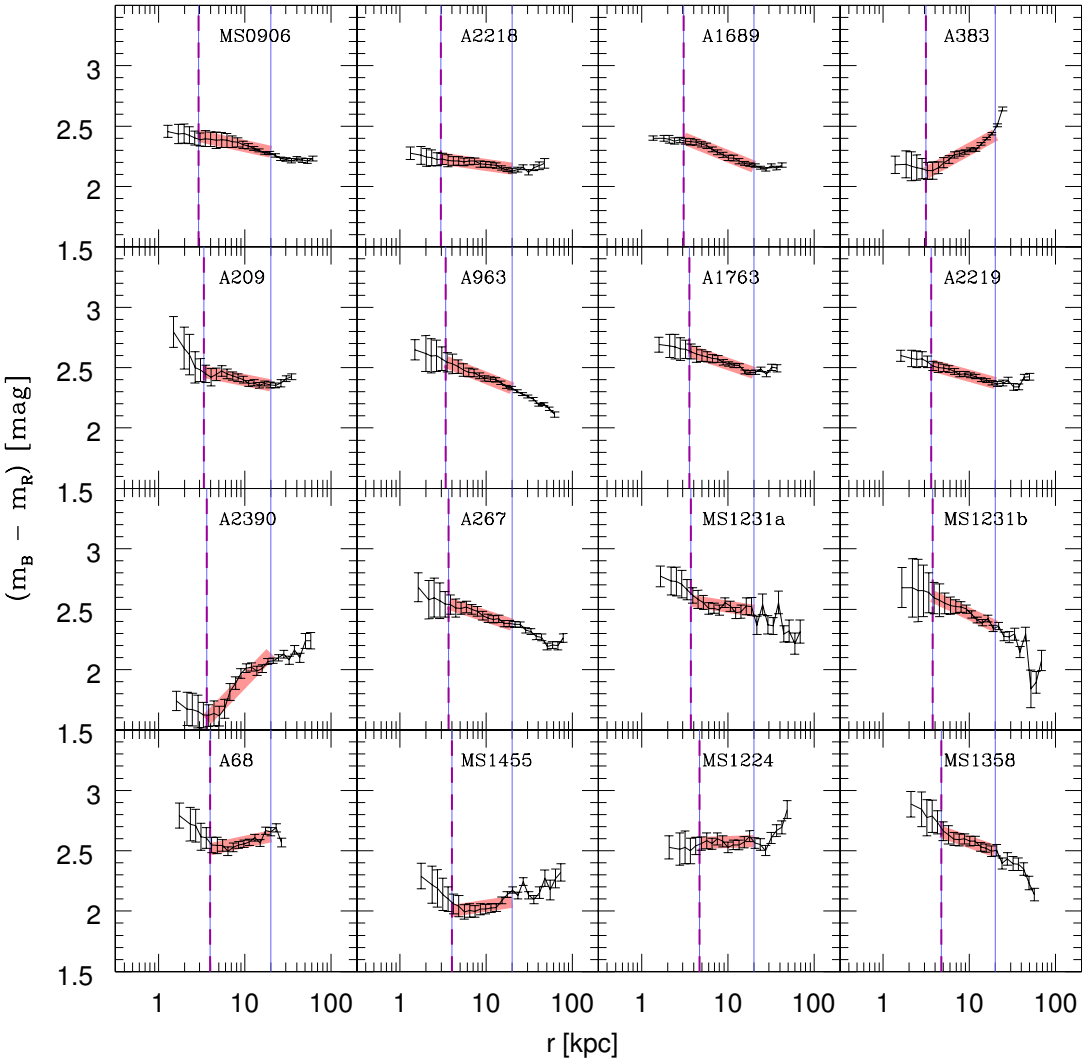

Figure 2.16: Colour profiles for BCGs as observed in the $(B-R)$ filter combination. Dashed vertical lines denote the radius corresponding to 1.0", the characteristic maximum PSF scale (r_{PSF}). The thick pink band shows the results of a linear fit to the data over the radial range $r_{PSF} < r < 20$ kpc (denoted by thin vertical lines). We use the slope of this line ($\gamma_{(B-R)}$) classify the BCG core color: $\gamma_{(B-R)} > 0$ blue-core, $\gamma_{(B-R)} < 0$ red-core.

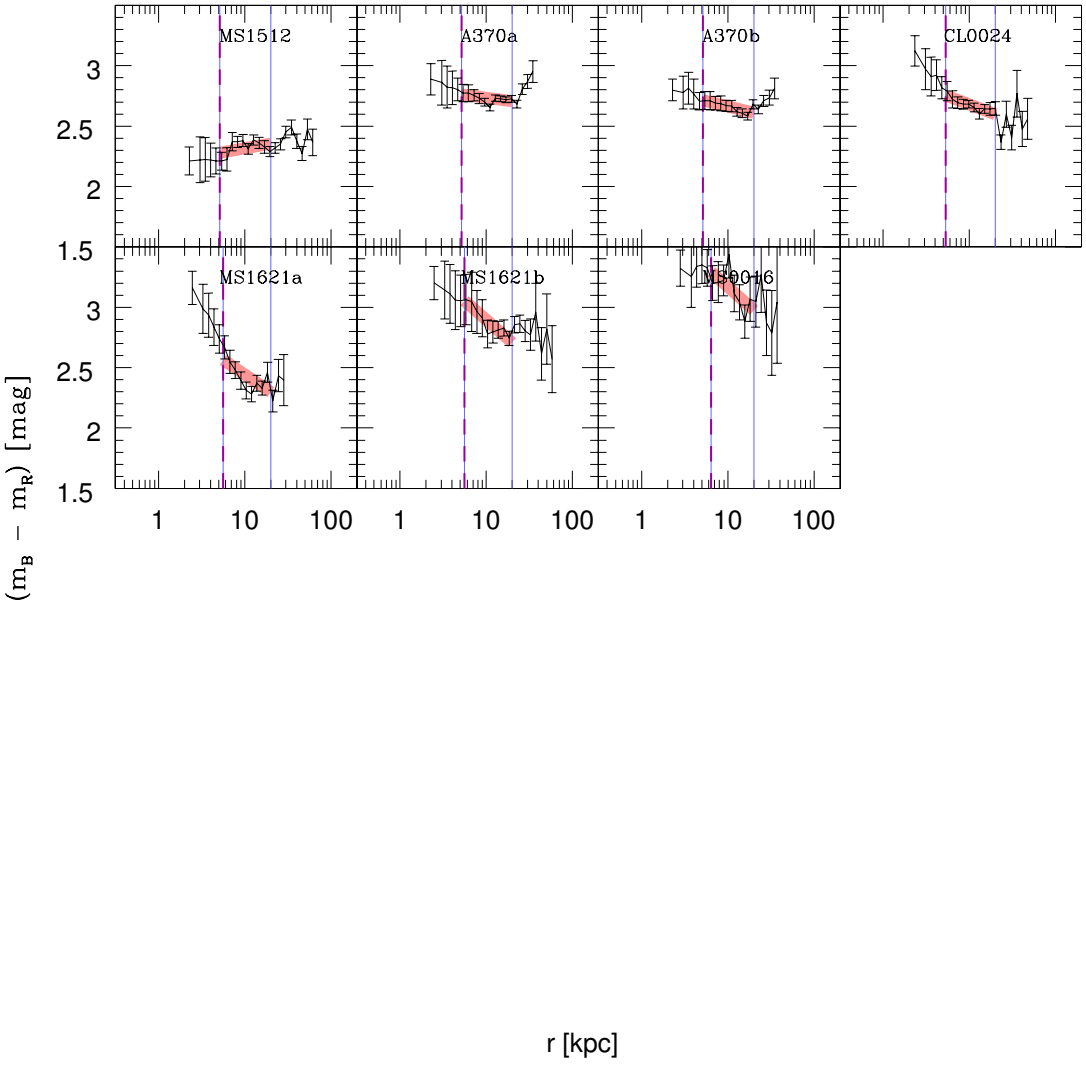

Figure 2.17: Colour profiles for BCGs as observed in the $(B-R)$ filter combination. Dashed vertical lines denote the radius corresponding to 1.0", the characteristic maximum PSF scale (r_{PSF}). The thick pink band shows the results of a linear fit to the data over the radial range $r_{PSF} < r < 20$ kpc (denoted by thin vertical lines). We use the slope of this line ($\gamma_{(B-R)}$) classify the BCG core color: $\gamma_{(B-R)} > 0$ blue-core, $\gamma_{(B-R)} < 0$ red-core.

2.5 Comparison to X-ray Properties

In this section we compare the optical colors of BCGs to various X-ray properties of their host clusters (central entropy, central cooling time, projected distance between BCG and X-ray peak emission, metallicity of the ICM) for all systems where high-resolution X-ray data are present in the Chandra and XMM-Newton archives. This yields a sample of 50 clusters for the CCCP component and 30 clusters for the MENeaCS component. All of the X-ray analysis presented below is conducted using the JACO software package. For the CCCP clusters the X-ray analysis has been conducted primarily by Andisheh Mahdavi and is published in Mahdavi et al. (2013). For the MENeaCS clusters the X-ray analysis is done by Weihan Chang (entropy, metallicity) and Chris Bildfell (projected BCG to X-ray peak offset) and will be presented in a future paper.

The X-ray properties investigated here are modelled as a function of radius within the cluster, assuming that the clusters are in spherical symmetry and hydrostatic equilibrium. Because we are interested in the X-ray properties in the innermost regions, and to compare the X-ray data fairly across all clusters in the sample, we interpolate or extrapolate these properties to a specific radius (20 kpc). For completeness, we include Figure 2.18, which shows the minimum radii of the sample of cluster models investigated here. The solid line in this plot shows the cumulative fraction of the sample measured as a function of the minimum radii of the models. The dashed and dotted lines show respectively, the cumulative fractions for the MENeaCS and CCCP subsamples. The vertical red, orange, yellow and blue lines indicate the limiting minimum radii that contain 95%, 90%, 80% and 65% of the sample respectively. Figure 2.18 shows that choosing a fixed radius of 20 kpc implies that roughly one half of the sample is interpolated and the other half must be extrapolated. The choice of 20 kpc is balanced between the need to sample the inner parts of the X-ray profiles, where cool-core clusters differ from non-cool-core clusters and the desire to minimize the number of clusters requiring extrapolations. We note however, that errors introduced via extrapolation are only expected to increase the scatter of any observed trend between optical properties of BCGs and the X-ray properties of the hosts. Accordingly, any trends discovered in the extrapolated data would simply indicate an even tighter trend with the underlying true X-ray properties.

As mentioned in §2.4, to limit unwanted biases that may be introduced by an inhomogeneous set of optical filters when comparing BCG color gradients to cluster

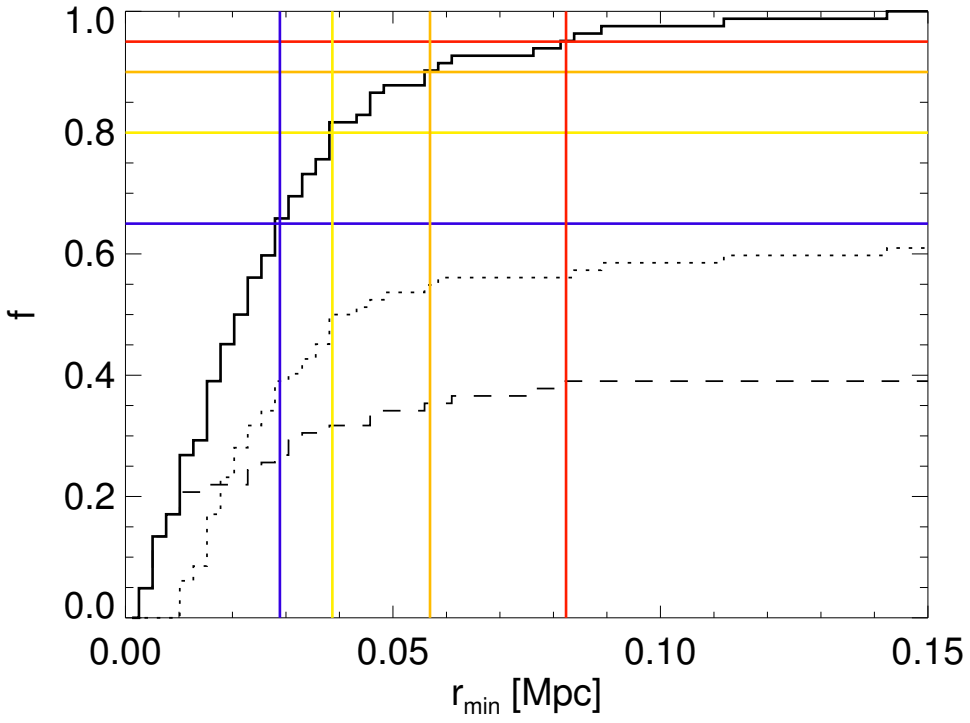

Figure 2.18: The cumulative fraction of clusters as a function of the minimum radius to which their X-ray properties are resolved. The solid line indicates the full sample, while the dashed in dotted lines indicate the MENeaCS and CCCP subsamples respectively. The vertical red, orange, yellow and blue lines indicate the limiting minimum radii that contain 95%, 90%, 80% and 65% of the sample respectively.

X-ray properties, the values of $\gamma_{(B-R)}$ can be converted to $\gamma_{(g'-r')}$ using the transformations of Lupton (2005)[4]. These transformations can be combined to obtain the following relation:

$$\gamma_{(g'-r')} \approx \frac{d(g'-r')}{d\log(r)} = 0.6681\frac{d(B-R)}{d\log(r)} \tag{2.1}$$

Throughout the rest of this section we use only the values of $\gamma_{(g'-r')}$.

[4]http://www.sdss.org/dr5/algorithms/sdssUBVRITransform.html#Lupton2005

Table 2.2: Summary table of the X-ray data for the BCG host clusters in our sample. Along with the cluster names we list the projected X-ray-to-optical peak offset D_{XO}, central entropy S_0, the central cooling time $t_{c,0}$ and the central metallicity of the ICM Z.

Name	D_{XO} kpc	S_0 keV cm^2	$t_{c,0}$ Gyr	$Z/Z_\odot$
Abell119	40.6 ± 40.6	301.6 ± 52.7	13.65 ± 1.92	0.31 ± 0.09
MKW3S	0.8 ± 1.5	42.2 ± 0.5	0.98 ± 0.01	0.93 ± 0.05
Abell780	0.5 ± 3.9	25.9 ± 0.2	0.59 ± 0.00	0.42 ± 0.01
Abell754	787.4 ± 179.4	201.3 ± 8.4	6.84 ± 0.25	0.40 ± 0.08
Abell85	0.9 ± 3.0	38.1 ± 0.6	0.72 ± 0.01	1.12 ± 0.05
Abell2319	26.5 ± 41.6	206.6 ± 6.3	5.55 ± 0.15	0.42 ± 0.09
Abell133	1.7 ± 4.4	30.2 ± 0.5	0.68 ± 0.01	1.05 ± 0.05
Abell1991	9.7 ± 2.4	23.6 ± 0.3	0.64 ± 0.01	0.75 ± 0.03
Abell1795	8.8 ± 6.8	35.1 ± 0.5	0.69 ± 0.01	0.66 ± 0.03
Abell644	20.7 ± 38.2	126.3 ± 7.5	2.89 ± 0.18	0.66 ± 0.17
Abell399	-	456.9 ± 42.3	15.79 ± 1.48	0.50 ± 0.14
Abell2065	2.7 ± 7.4	75.5 ± 5.7	1.98 ± 0.12	0.80 ± 0.11
Abell401	21.8 ± 43.8	258.3 ± 23.6	7.16 ± 0.67	0.44 ± 0.12
ZwCl1215	14.3 ± 16.7	187.9 ± 11.7	7.16 ± 0.37	0.36 ± 0.06
Abell2670	0.8 ± 1.4	105.4 ± 9.8	4.17 ± 0.45	0.57 ± 0.14
Abell2029	0.4 ± 1.2	45.8 ± 0.8	0.71 ± 0.01	0.83 ± 0.03
Abell1650	6.1 ± 12.0	71.8 ± 2.3	1.58 ± 0.04	0.60 ± 0.05
Abell1651	17.0 ± 13.6	94.3 ± 4.9	2.17 ± 0.14	0.63 ± 0.14
Abell2420	-	388.2 ± 147.5	10.37 ± 3.89	-
Abell2597	2.1 ± 4.2	22.8 ± 0.4	0.48 ± 0.01	0.49 ± 0.02
Abell478	3.6 ± 4.5	-	-	-
Abell2440	3.8 ± 4.5	59.5 ± 5.0	1.73 ± 0.11	0.94 ± 0.11
Abell2142	24.2 ± 18.8	62.4 ± 2.5	1.32 ± 0.05	0.36 ± 0.03
Abell2055	3.9 ± 5.4	1966.7 ± 719.4	79.71 ± 38.00	-
Abell2443	0.4 ± 24.7	541.7 ± 96.1	11.94 ± 2.68	-
RXCJ0352p19	0.5 ± 3.7	14.6 ± 0.7	0.45 ± 0.01	0.27 ± 0.03

Continued on next page...

Table 2.2 continued...

Name	D_{XO} kpc	S_0 keV cm^2	$t_{c,0}$ Gyr	$Z/Z_\odot$
Abell2069	-	276.2 ± 37.7	13.60 ± 1.24	0.37 ± 0.12
Abell1361	4.9 ± 7.8	-	-	-
Abell2050	-	117.5 ± 8.0	3.76 ± 0.19	0.32 ± 0.03
Abell2627	0.7 ± 1.4	-	-	-
Abell795	0.8 ± 5.2	46.9 ± 5.7	1.10 ± 0.07	0.62 ± 0.11
Abell1068	1.1 ± 3.1	-	-	-
Abell1413	3.0 ± 14.7	86.3 ± 5.7	1.75 ± 0.12	0.57 ± 0.11
Abell2409	91.1 ± 88.4	142.2 ± 39.7	3.76 ± 0.85	-
A2204	0.8 ± 2.0	17.3 ± 0.3	0.25 ± 0.00	0.65 ± 0.02
A2104	6.4 ± 2.1	201.7 ± 37.6	5.43 ± 1.00	0.24 ± 0.06
A2259	72.5 ± 8.8	134.7 ± 33.6	3.87 ± 0.77	-
A1914	57.4 ± 4.9	128.7 ± 9.6	2.51 ± 0.20	0.33 ± 0.06
A586	10.6 ± 2.1	140.1 ± 23.2	2.84 ± 0.45	-
MS0906	2.8 ± 2.0	148.9 ± 22.5	2.81 ± 0.54	0.60 ± 0.14
A2218	56.4 ± 4.3	317.9 ± 47.1	8.45 ± 1.38	0.32 ± 0.06
A1689	3.7 ± 2.0	72.5 ± 3.4	1.18 ± 0.05	0.31 ± 0.02
A383	0.6 ± 2.0	21.3 ± 1.0	0.41 ± 0.02	0.76 ± 0.08
MS0440	0.9 ± 2.0	30.1 ± 6.8	0.64 ± 0.11	-
A115	143.2 ± 5.2	192.8 ± 49.8	7.48 ± 1.88	0.42 ± 0.11
A115N	9.4 ± 2.0	30.0 ± 1.7	0.69 ± 0.02	0.72 ± 0.10
A2163	101.5 ± 9.3	336.0 ± 17.9	8.67 ± 0.45	0.21 ± 0.03
A2261	0.3 ± 2.0	60.0 ± 8.7	1.13 ± 0.14	0.38 ± 0.08
A520	244.5 ± 10.8	590.1 ± 39.7	19.95 ± 1.35	0.34 ± 0.05
A209	14.4 ± 2.5	152.7 ± 34.1	4.21 ± 0.89	0.46 ± 0.07
A963	5.5 ± 2.0	63.1 ± 4.7	1.31 ± 0.07	0.52 ± 0.13
A223b	9.3 ± 2.5	133.5 ± 28.7	4.19 ± 0.80	0.55 ± 0.13
A1942	5.0 ± 2.0	230.6 ± 79.3	6.50 ± 2.34	0.31 ± 0.14
A1763	7.8 ± 2.0	419.5 ± 54.0	10.51 ± 1.38	0.53 ± 0.08
A2219	6.8 ± 2.1	243.2 ± 30.6	5.84 ± 0.77	0.23 ± 0.05
A2390	2.4 ± 2.0	31.6 ± 1.0	0.58 ± 0.01	0.48 ± 0.05
A2111	83.5 ± 50.4	203.8 ± 91.8	7.02 ± 2.26	-

Continued on next page...

Table 2.2 continued...

Name	D_{XO} kpc	S_0 keV cm^2	$t_{c,0}$ Gyr	$Z/Z_\odot$
A267	65.2 ± 5.0	160.8 ± 19.8	4.14 ± 0.51	0.37 ± 0.08
MS1231a	71.8 ± 2.6	131.5 ± 20.6	5.75 ± 0.76	0.32 ± 0.08
A1835	4.5 ± 2.0	19.7 ± 0.4	0.29 ± 0.00	0.46 ± 0.03
A521	31.3 ± 5.0	75.6 ± 17.7	2.43 ± 0.37	0.49 ± 0.14
A68	14.0 ± 2.4	214.2 ± 35.3	4.31 ± 0.73	0.15 ± 0.05
MS1455	3.6 ± 2.0	23.6 ± 0.6	0.39 ± 0.01	0.46 ± 0.03
A1758b	15.7 ± 3.7	194.5 ± 20.6	6.16 ± 0.64	-
A697	13.9 ± 2.6	240.0 ± 48.8	5.88 ± 1.12	0.43 ± 0.14
A611	3.4 ± 2.0	57.0 ± 10.0	1.32 ± 0.21	-
A959	34.1 ± 3.2	203.8 ± 48.4	8.93 ± 1.45	-
A2537	15.1 ± 2.3	91.8 ± 20.0	2.02 ± 0.39	0.38 ± 0.13
MS1008	7.1 ± 5.3	97.9 ± 46.4	2.79 ± 1.26	-
MS1358	3.4 ± 2.0	39.3 ± 3.7	0.73 ± 0.06	0.20 ± 0.14
MS1512	7.4 ± 2.2	26.4 ± 17.2	0.28 ± 0.34	-
A370a	19.2 ± 8.2	500.1 ± 163.2	13.41 ± 4.61	0.37 ± 0.12
CL0024	31.3 ± 13.4	61.2 ± 29.9	1.36 ± 0.43	-
A851	261.4 ± 55.3	479.7 ± 79.9	16.87 ± 2.38	-
MS1621a	41.2 ± 3.4	182.1 ± 71.9	7.29 ± 2.14	-
CL0910	3.7 ± 2.0	17.0 ± 1.1	0.24 ± 0.01	0.61 ± 0.09
RXJ1347	1.1 ± 2.0	29.7 ± 2.1	0.30 ± 0.02	0.38 ± 0.05
3C295	13.2 ± 2.4	12.8 ± 2.7	0.13 ± 0.05	0.46 ± 0.08
RXJ1524	29.3 ± 3.2	123.9 ± 64.7	4.78 ± 2.07	-
MS0451	22.2 ± 3.2	235.3 ± 45.5	3.96 ± 0.78	0.37 ± 0.07
MS0016	33.1 ± 3.3	171.0 ± 30.0	3.87 ± 0.60	0.39 ± 0.11

2.5.1 Central Entropy

In order to work with more convenient units, in X-ray cluster astronomy entropy (S) is defined somewhat differently from the standard definition in thermodynamics. Specifically, we define the entropy of a cluster S as:

$$S = \frac{k_B T_x}{n_e^{2/3}} \tag{2.2}$$

where k_B is the Boltzmann constant, T_x is the X-ray temperature and n_e is the electron density. Entropy S is typically measured in units of keV cm^2 and is related to the more general definition of entropy (s) via:

$$s = k_B \ln (S^{3/2} (\mu m_p)^{5/2}) + s_0 \tag{2.3}$$

where μ represents the mean molecular weight, m_p is the rest-mass of the proton and s_0 is a constant (Balogh et al. 1999, Voit 2005). Radiative cooling acts to decrease S while processes like shock heating and dissipation of turbulent motions will lead to an increase in S. This makes S a good discriminator of the current balance between heating and cooling in the ICM and the central value of S in the cluster S_0 is often used to distinguish between cool-core (CC) and non-cool-core (NCC) clusters. For our purposes, throughout the remainder of this work we define the central entropy S_0 to be the entropy of the cluster evaluated at a projected radius of 20 kpc (see §2.5).

In an analysis of archival Chandra data, H_α luminosities and radio power, Cavagnolo et al. (2008) model cluster entropy profiles as:

$$K(r) = K_0 + K_{100} \left(\frac{r}{100\text{kpc}} \right)^\alpha \tag{2.4}$$

where K_{100} entropy at $r = 100$ kpc, K_0 is the excess central entropy and α is the power law index. Their results imply that that only clusters with central entropy excess $K_0 < 30$ keV cm^2 are able to cool enough gas from the ICM onto the BCG to fuel detectable levels of recent star formation, as indicated by H_α and radio power. Our measure of central entropy S_0 is related to their measure K_0, at least for cool-core clusters where entropy profiles obey a nearly perfect power-law, simply by $S_0 \approx K_0$. Using the inner optical color gradient as a probe of recent star formation, we show in Figure 2.19 relationship between $\gamma_{(g'-r')}$ and the central entropy of the host cluster's ICM. Recall that positive values of $\gamma_{(g'-r')}$ are classified as blue-cores while negative values indicate red-cores. The BCGs that are visually classified as blue-core are labelled with an open blue square. We also label with a solid vertical line the threshold value for recent star formation of $S_0 = 30$ keV cm^2 corresponding to the findings of Cavagnolo et al. (2008); assuming $S_0 \approx K_0$.

From Figure 2.19 we find that 13 out of 15 of the BCGs with positive values of

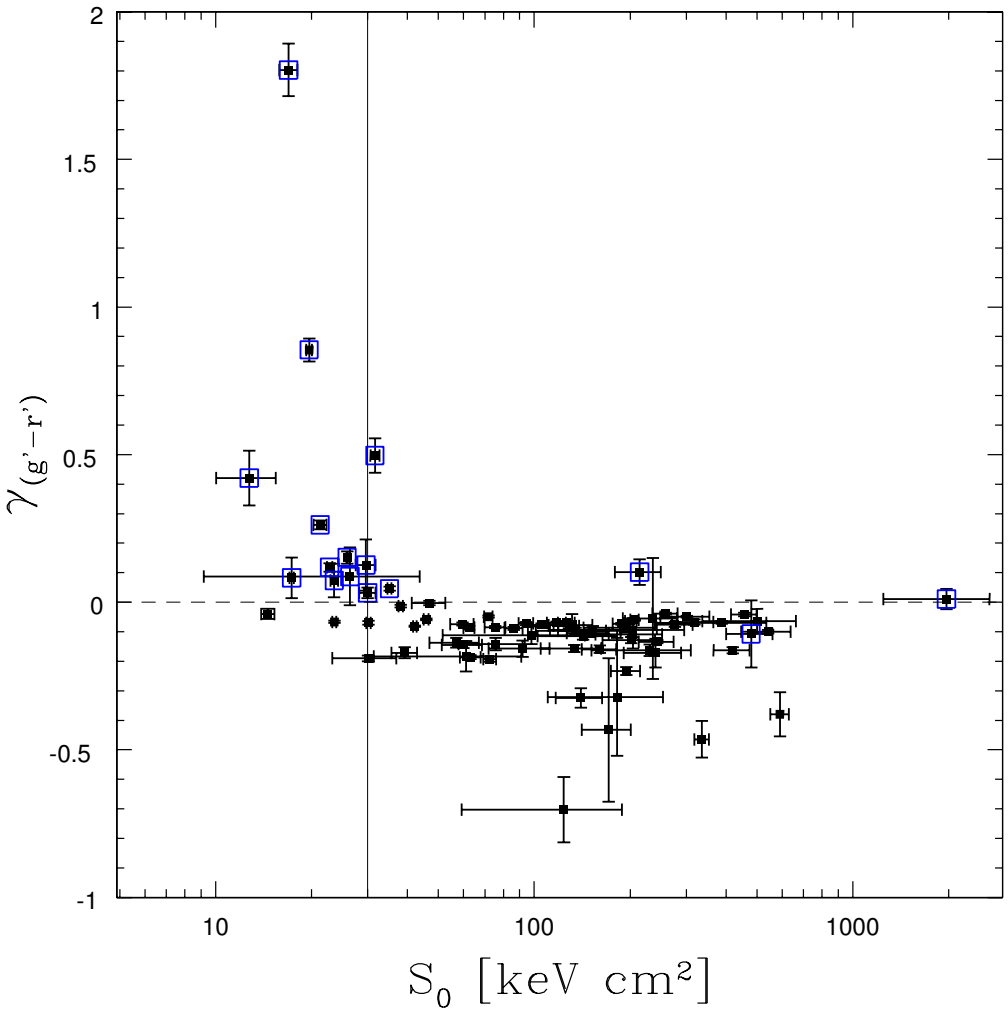

Figure 2.19: Logarithmic central colour gradient $\gamma_{(g'-r')}$ versus central entropy S_0. Open blue squares indicate systems that are visually classified as blue-core BCGs. The vertical line at 30 keV cm^2 indicates the S_0 value corresponding to the entropy threshold for BCG star formation found by Cavagnolo et al. (2008).

$\gamma_{(g'-r')}$ are in clusters with low central entropy (ie. $S_0 < 40$ keV cm^2). Similarly, 13 out 16 of the BCGs that are visually classified as blue-core are in clusters with $S_0 < 40$ keV cm^2. Looking at both classifications together, 13 out of 15 BCGs with both $\gamma_{(g'-r')} > 0$ and a blue visual class are below this entropy threshold, with Abell 68 and Abell 2055 being the exceptions. The observed threshold in S_0 required for the presence of blue-cores in BCGs is analogous to the entropy threshold for H_α and radio detection seen in Cavagnolo et al. (2008), however, they find a threshold K_0 that is slightly lower at 30 keV cm^2. This difference in the exact entropy threshold should not be taken as absolute since our samples are not identical and the assumption that $S_0 \approx K_0$ is not perfect, likely introducing systematic error into the comparison. Furthermore, observables used as indicators of recent star formation differ between these two studies and may not be expected to trace star formation identically. The existence of an entropy threshold for the presence of spatially-resolved blue-cores in BCGs should be seen as an independent confirmation of the results seen in Cavagnolo et al. (2008). When taken together, these findings strongly suggest that the dominant mechanism that gives rise to blue-cores is recent star formation and that this recent star formation is fuelled by a mechanism associated with physics that gives rise to low entropy clusters, likely radiative cooling. The presence of a small few outlying blue-core systems with $S_0 > 100$ keV cm^2 could be explained by recent merger activity, which is known to temporarily increase entropy on cluster scales (Poole et al. 2007) and fuel star-formation and AGN on galactic scales (Patton et al. 2011, Ellison et al. 2011).

2.5.2 central cooling time

Another measure of a cluster's cooling strength from literature on modelling the X-ray emission of the ICM is the cooling time t_c, which estimates the time it would take for a parcel of cluster gas to radiate all of its energy at its current X-ray luminosity L_x. Throughout most galaxy clusters, t_c is longer than the Hubble time t_H (age of the universe) but many clusters have been observed to have central cooling times $t_{c,0}$ that are shorter than t_H and thus the gas at the cluster center has the potential to radiate all of its energy away at X-ray wavelengths, establishing a cooling flow. It is known from recent observations however, that cooling flows do not form with the mass deposition rates expected from this simple picture (Peterson 2003), indicating the need for some kind of heating mechanism (AGN, thermal conduction, cosmic rays,

etc.) to offset the radiative cooling. Despite this complication, the central cooling time provides a useful relative measure of the cooling strength from one cluster to another. Throughout the remainder of this work we define the central cooling time $t_{c,0}$ to be the cooling time of the cluster evaluated at a projected radius of 20 kpc (see §2.5).

As another probe of the connection between optical blue-cores in BCGs and their host cluster's cooling strength, we plot in Figure 2.20 the central color gradient $\gamma_{(g'-r')}$ versus central cooling time $t_{c,0}$. The open blue squares show the BCGs that are visually classified as blue-core. We also show the cooling time threshold for the presence of $(U-I)$ blue cores in BCGs (vertical line) found by Rafferty et al. (2008), though they derived this threshold for $t_c(12\text{ kpc})$ rather than $t_{c,0}$. We find an analogous result here, with a threshold value for the presence of optical blue-cores in BCGs at $t_{c,0} \sim 1$ Gyr. Specifically, 13 of 16 visually classified blue-core BCGs are in clusters with $t_{c,0} < 1$Gyr, while 13 of 15 BCGs with $\gamma_{(g'-r')} > 0$ are in clusters with $t_{c,0} < 1$Gyr. If we examine the intersection of the two classification schemes, 13 of the 15 BCGs that are both visually and automatically classified as blue cores lie in clusters with $t_{c,0} < 1$Gyr. These results are similar to those found for the comparison between $\gamma_{(g'-r')}$ and S_0, which is not surprising since S_0 and $t_{c,0}$ are highly correlated. This analysis nonetheless provides an optical wavelength confirmation of the effect found by Rafferty et al. (2008). One key difference however, is that our sample contains many more clusters with long cooling times of order ~ 10 Gyr or more. This is an important difference since the association of the blue-core phenomenon with radiative cooling of the ICM requires not only to observe blue-core BCGs in clusters with short cooling times but also requires that clusters with long cooling times ($t_c \approx t_H$) host almost exclusively red-core BCGs.

Comparing Figures 2.20 and 2.19 it is easy to see that $\gamma_{(g'-r')}$ exhibits similar behaviour when comparing with both S_0 and $t_{c,0}$. Both data relationships show a primarily quiescent distribution of red BCGs at high S_0 and $t_{c,0}$ with thresholds below which the blue-core systems are found. These results have been presented independently for the purpose of explicit comparison with the existing literature, however we note that this similar behaviour might be expected as the values of S and t_c are calculated using similar basic quantities. Namely the cooling time t_c depends on a similar combination of temperature and electron densisty:

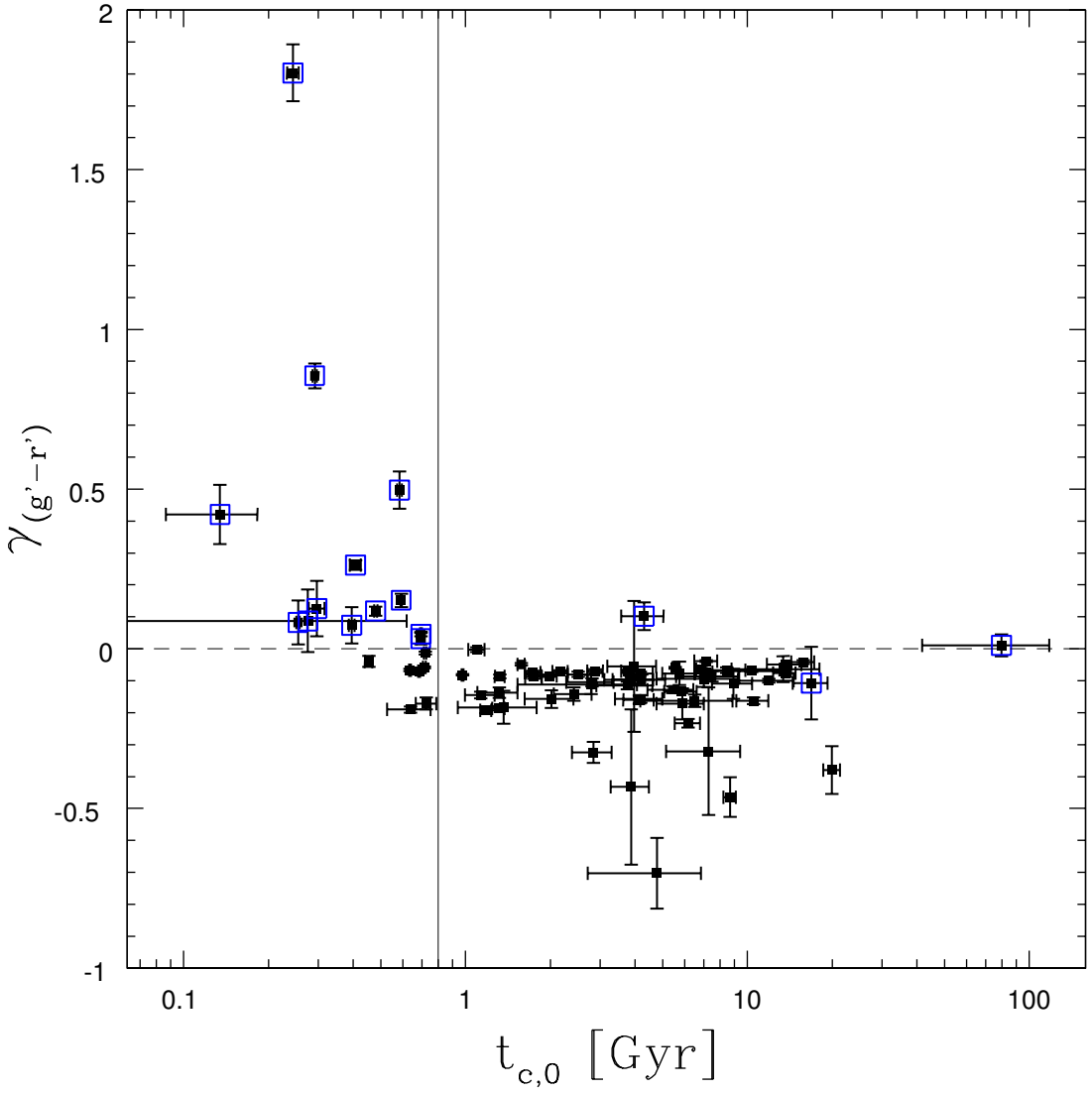

Figure 2.20: Logarithmic central colour gradient $\gamma_{(g'-r')}$ versus central cooling time $t_{c,0}$. Open blue squares indicate systems that are visually classified as blue-core BCGs. The vertical line at $t_{c,0} = 800$ Myr shows the value corresponding to the cooling time threshold for $(U - I)$ blue-core BCGs found by Rafferty et al. (2008).

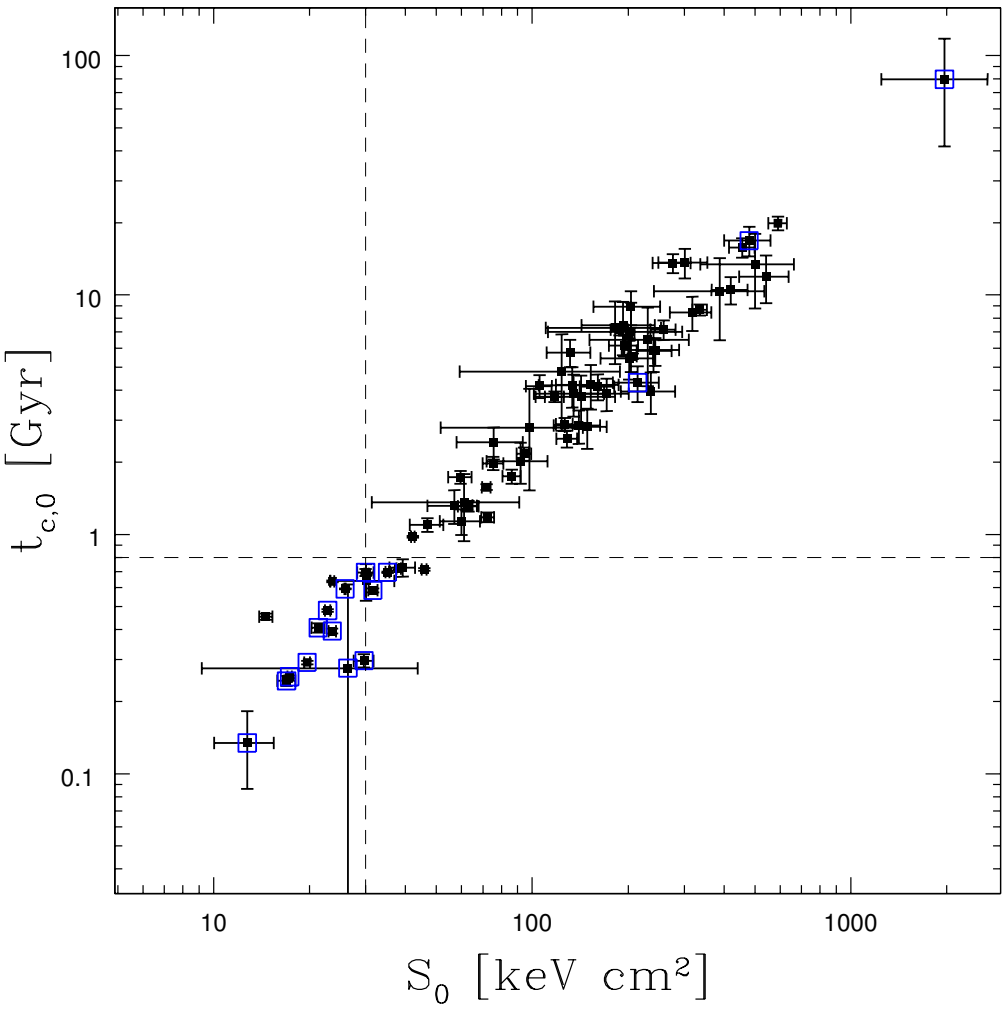

Figure 2.21: Central cooling time $t_{c,0}$ versus central entropy S_0. BCGs with visually classified blue cores are shown as open blue squares. Dashed lines indicate the thresholds for signs of recent star-formation taken from Cavagnolo et al. (2008) and Rafferty et al. (2008) - see text.

$$t_c \propto \frac{T_x^{1/2}}{n_e} \tag{2.5}$$

differing from S primarily by a factor of $T_x^{1/2} n_e^{1/3}$. This means that clusters with low central entropy most often also have low central cooling times. As a verification of this we show in Figure 2.21 the central cooling time $t_{c,0}$ plotted with the central entropy S_0. As expected, there is a tight relationship between these two variables. The clusters with short $tc, 0$ are indeed those with small values of S_0. The dashed lines in this figure indicate the thresholds from Cavagnolo et al. (2008) and Rafferty et al. (2008) described above.

2.5.3 BCG to X-ray Peak Offset

We define the projected distance between a BCG (the optical peak) and its host cluster's peak in X-ray emission as the quantity D_{XO}. It is interesting to examine whether or not the presence of blue cores in BCGs correlates with D_{XO}. If the optically blue regions are a result of radiative cooling in the ICM then we would expect to see blue-core BCGs in systems with small D_{XO} only. In Figure 2.22 we plot the relationship between $\gamma_{(g'-r')}$ and D_{XO}. As in figures 2.20 and 2.19 we show the systems that are visually classified as blue-core BCGs with an open blue square. The distribution of D_{XO} range from $0 < D_{XO} < 1000$ kpc but is dominated by systems with smaller ($< 50 kpc$) offsets. The D_{XO} distribution of blue-core BCGs, however, is quite different than that of the red-core BCGs. In particular, 17 of the 18 systems that are visually classified as blue-core BCGs are at $D_{XO} < 15$ kpc. Of the BCGs that are classified as blue-core by the condition $\gamma_{(g'-r')} > 0$, all 15 are within $D_{XO} < 15$ kpc. In contrast, the BCGs that classified as red-core ($\gamma_{(g'-r')} < 0$) have D_{XO} values that span the entire observed range. It is important to note that the presence of red-core BCGs with small D_{XO} does not contradict the hypothesis that blue-cores in BCGs are a result of radiative cooling in the ICM. The centrally-located red core red-core systems may simply be in clusters with long cooling times; a possibility that is investigated further below. There is also a small chance that a BCG may have a small D_{XO} due to projection effects, though this should be rare and is unable to explain the D_{XO}-distribution of red-core BCGs. Lastly, the vertical line in Figure 2.22 at $D_{XO} = 15$ kpc corresponds to the maximum D_{XO} for clusters with $L_x - T_x$ residuals (ΔL_x) above the threshold required for the presence of blue-cores from Bildfell et al.

(2008).

To probe the connection between the position of the BCG and the origin of blue-cores we show in Figure 2.23 the central entropy S_0 as it depends on D_{XO}. As in previous plots the visually-classified blue-core BCGs are denoted with open blue square symbols. This figure verifies that the main difference between the blue-core versus red-core BCGs at low BCG-to-Xray peak offset ($D_{XO} < 15$ kpc) is that the ones with blue cores are all in clusters with low central entropy, whereas the ones with red cores are predominantly in clusters with $S_0 > 30$ keV cm^2. The simultaneous correlation of blue-core BCGs with both the proximity to the assumed focus of radiative cooling (Xray peak) and the degree to which radiative cooling is dominant over heating effects (central entropy) is consistent with the hypothesis that the origin of blue cores in BCGs is associated with the degree of cooling in the ICM. There are exceptions however, as BCGs in four clusters with $S_0 < 30$ keV cm^2 and BCGs at $D_{XO} < 15$ kpc have red cores. It is possible that these four systems are transition objects, only now beginning the transformation to blue cores. Alternatively, it is also possible that these systems are active (AGN or star formation) only at a low level that is undetectable by our analysis but may yet be detectable through other tracers of such activity (eg. spectral emission lines or radio power). These outliers may also point to a third parameter, possibly the cluster mass, as an important consideration for the presence/absence of blue cores in BCGs.

While the vast majority of blue-core systems are consistent with AGN or star formation activity fuelled by cooling intra-cluster gas, it is also important to consider secondary mechanisms that may lead to blue-core BCGs. For instance, there are three blue-core BCGs in figure 2.23 that have $S_0 > 100$ keV cm^2, one of which is at $D_{XO} > 200$ kpc. Mergers and galaxy-galaxy harassment are both expected to operate in clusters at low to intermediate redshifts. These processes can lead to an influx of gas into the BCG cores, inducing star formation, AGN or both, and may explain the presence of a small number of systems that do not fit with the cooling ICM-fuelled scenario.

2.5.4 ICM Metallicity

The leading physical processes believed to explain the presence of optically blue colors in BCGs (recent star formation, AGN) are also expected to contribute to the metallicity enrichment of the ICM through stellar winds, entrainment of material

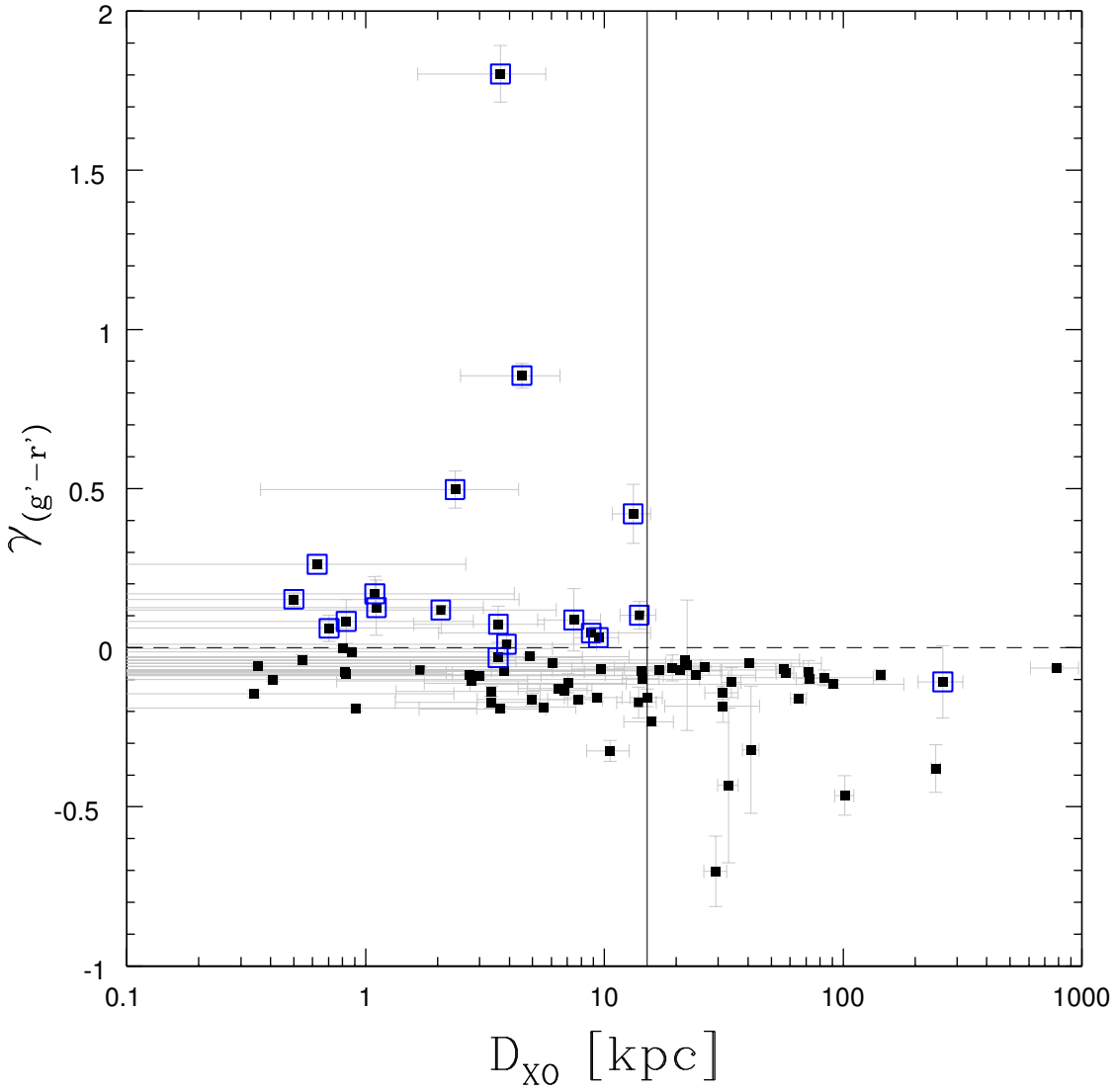

Figure 2.22: Logarithmic central colour gradient $\gamma_{(g'-r')}$ versus X-ray - to - optical peak offset D_{XO}. The vertical line at 15 kpc indicates the maximum D_{XO} for high ΔL_x clusters found in Bildfell et al. (2008).

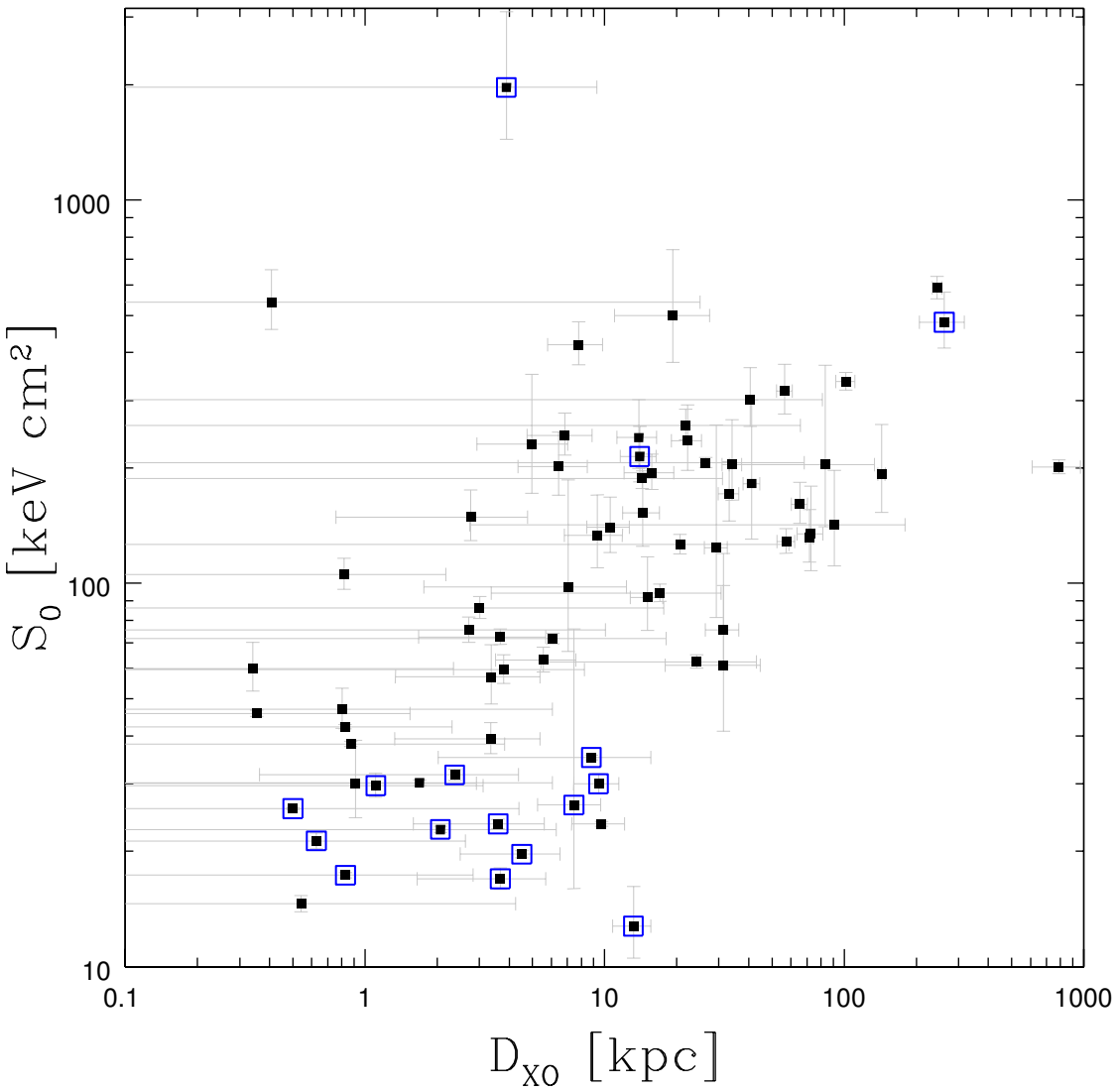

Figure 2.23: BCG-to-Xray peak offset D_{XO} versus central entropy S_0. BCGs with visually classified blue cores are shown as open blue squares.

in buoyant bubbles and high-velocity outflows. Another factor to consider is that highly efficient metal-line cooling could increase the amount of cold gas available to fuel the AGN or recent star formation thus increasing the blue-core effect. There are of course many other channels for ICM metal enrichment (intra-cluster supernovae, stripping of pre-processed galactic gas upon cluster infall) which might dilute the signal of the BCG-associated enrichment effects. However, it is nonetheless interesting to examine whether or not the metallicity of the ICM as inferred from X-rays and the presence/absence of blue-cores in BCGs are correlated.

We show in Figure 2.24 the central color gradient $\gamma_{(g'-r')}$ as a function of the observed ICM metallicity Z measured at a projected radius $r = 20$ kpc. As in previous figures, the visually classified blue-core BCGs are labeled with open blue squares. There is no strong correlation observed between Z and $\gamma_{(g'-r')}$. However, it appears that the Z distribution of blue-core BCGs has a higher mean Z than that of the red-core BCGs. To check this, we measure the mean metallicity ($\langle Z \rangle$) of BCGs with $\gamma_{(g'-r')} > 0$ and $\gamma_{(g'-r')} < 0$ separately. We find that BCGs with $\gamma_{(g'-r')} > 0$ have a $\langle Z/Z_{\odot} \rangle = 0.517 \pm 0.016$ while BCGs with $\gamma_{(g'-r')} < 0$ have a $\langle Z/Z_{\odot} \rangle = 0.487 \pm 0.014$, which we show in Figure 2.24 with solid blue and dashed red vertical lines respectively. A Kolmogrov-Smirnov test of the two separate distributions reveals that the probability that they are drawn from the same parent distribution is approximately 10%. These results indicate that, while the signal is likely diluted by the many different channels for chemical enrichment of the ICM, the presence of blue-cores in BCGs is tentatively associated with clusters of elevated metallicity. This result, when taken with the link between blue-core BCGs and low S_0, is consistent with the finding that cool-core clusters with low central entropy are observed to have increased ICM metallicity in their central regions when compared to non-cool-core clusters (Leccardi et al. 2010). Though not shown in Figure 2.24, we also compare the mean metallicity of clusters with $D_{XO} < 15$ kpc to that of the clusters with $D_{XO} > 15$ kpc. We find that the clusters with BCGs within 15 kpc from their peak X-ray emission have $\langle Z/Z_{\odot} \rangle = 0.509 \pm 0.012$, while clusters with BCGs that are further away have $\langle Z/Z_{\odot} \rangle = 0.423 \pm 0.038$. This observed difference in mean metallicity hints at the possibility that outflows from the BCG, induced by star formation and/or AGN, may play an important role in the chemical enrichment of the central regions of the ICM. Alternatively, clusters with the most enriched ICM may have shorter cooling times owing to the efficiency of metal-line cooling. Short cooling times would then lead to low central entropy and condensation of cold gas onto the BCG with

which to fuel star formation and/or AGN activity. More stringent constraints on the metallicity distributions within clusters are required in order to confirm this tentative association and shed light on its possible origin.

It is also interesting to note that the clusters with the highest values of Z interpolated at $r = 20$ kpc (ie. $Z/Z_{\odot} > 0.8$) do not host blue-core systems. This is qualitatively consistent with the findings of Sanderson et al. (2009) who plot ICM metallicity as a function of entropy (their Figure 11) and find that there is a peak in the metallicity distribution at ~ 30 keV cm^2, which then decreases at lower entropies. This may explain why the clusters hosting blue-core BCGs, which exhibit the lowest central entropies (< 30 keV cm^2), do not belong to the subset of clusters with the highest central metallicities ($Z/Z_{\odot} > 0.8$).

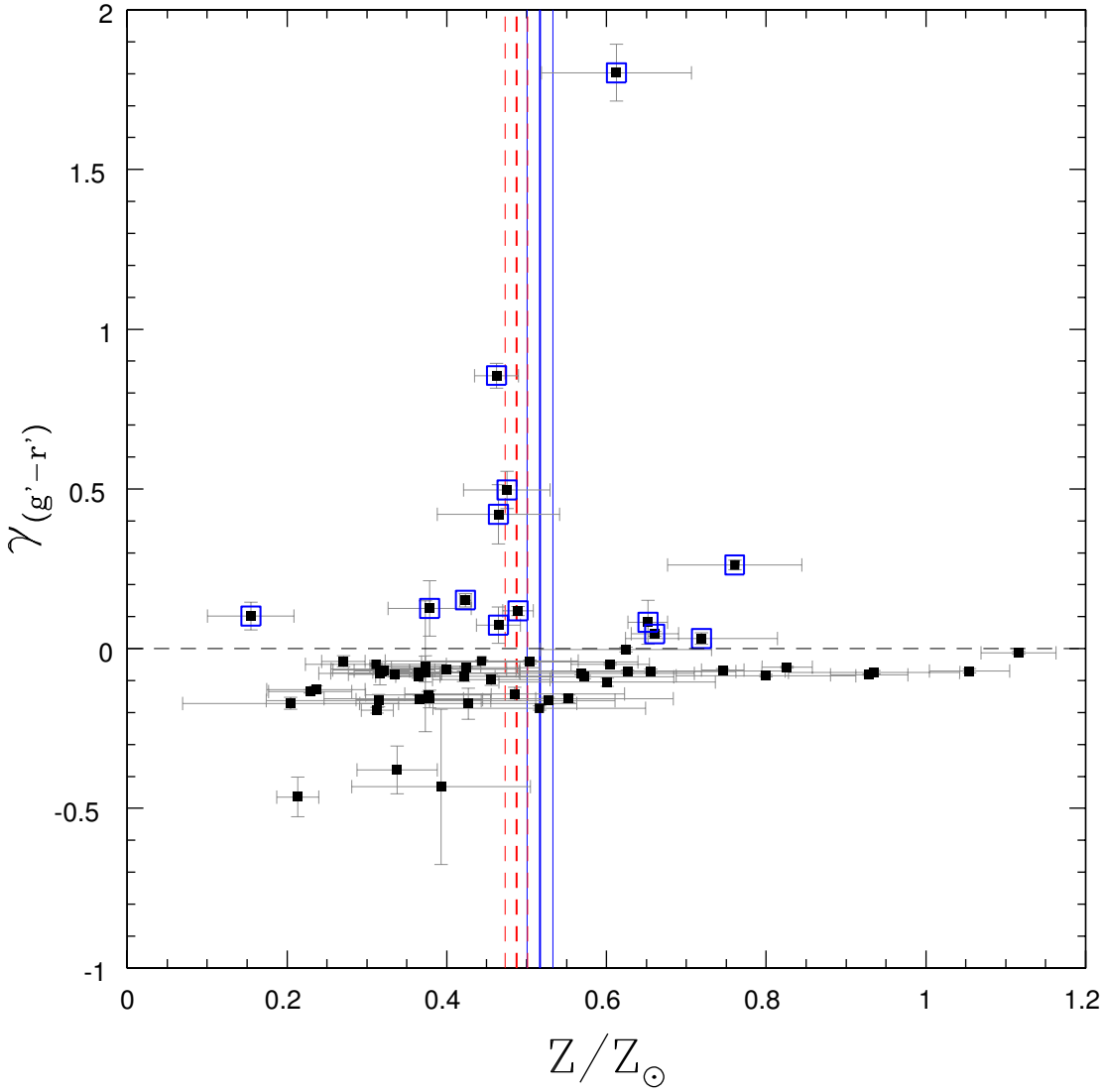

Figure 2.24: Logarithmic central colour gradient $\gamma_{(g'-r)}$ versus metallicity of the ICM $Z/Z_\odot$ as measure at 20 kpc. Blue (solid) and red (dashed) vertical lines indicate the mean metallicities, and their errors, of the subsamples of BCGs with $\gamma_{(g'-r')} > 0$ and $\gamma_{(g'-r')} < 0$ respectively.

2.6 Radio Power

The proposed mechanisms for generating blue cores in BCGs (AGN, star formation) are expected to leave a traceable signature at radio wavelengths. It is therefore interesting to examine whether or not our conclusion based on the Xray-optical analysis presented here are also consistent with the available radio data for these systems. To this end, we cross-correlate the BCGs in our sample with the 1.4 GHz source catalog of the Very Large Array's (VLA) Faint Images of the Radio Sky at Twenty Centimetres (FIRST)survey (Becker et al. 1995). We match BCGs to FIRST survey catalog sources using a maximum angular distance of 10.0 arcseconds and consider the closest source to the BCG coordinates, within this limit, to be a positive match. Using the integrated fluxes of the matching 1.4 GHz sources, assuming the radio source is at the same redshift of the cluster, we compute the radio power-density $P_{1.4\mathrm{GHz}}$. We also apply a k-correction to the $P_{1.4\mathrm{GHz}}$, using a power-law spectrum with a power-law index $\alpha = -0.75$. For the BCGs that are within the FIRST survey area but do not appear as detected sources in the catalog we compute upper limits on $P_{1.4\mathrm{GHz}}$. We compare the resulting radio power-densities with central entropies in Figure 2.25.

The black points in Figure 2.25 show the $P_{1.4\mathrm{GHz}}$ and S_0 values for the 27 systems detected in the FIRST survey catalogs for which we also have Xray data. The grey arrow symbols in this figure represent the upper limits on $P_{1.4\mathrm{GHz}}$ for the BCGs which are in the FIRST survey footprint but were not detected as radio sources. The large blue squares indicate the BCGs that are visually-classified as blue-cores. As in Figure 2.19 the dashed vertical line illustrates the entropy threshold for H_α and radio detection found in Cavagnolo et al. (2008). Similar to the their study, we find that all 13 systems with $S_0 < 50$ keV cm^2 are associated with 1.4 GHz radio sources. Furthermore, all 9 visually-classified blue-core BCGs which are in the FIRST survey footprint and for which we have high resolution X-ray data are associated with bright 1.4 GHz radio source having $P_{1.4\mathrm{GHz}} > 4.0 \times 10^{25}$ W Hz^{-1}. Looking at the $P_{1.4\mathrm{GHz}}$ distribution for BCGs in clusters with $S_0 > 50$ keV cm^2, we see that while there are many radio-bright systems, the majority (21/35) of BCGs are not-detected and have corresponding upper limits on radio power-density $P_{1.4\mathrm{GHz}} < 4.0 \times 10^{25}$ W Hz^{-1}. The observed clear association between visually-classified blue-cores and bright 1.4 GHz radio sources, combined with the lack of a similar clear association for red-core BCGs rules out the possibility that the origin of the blue color is due to metallicity gradient inversions (see §2.4). It is also interesting that the red-core systems with $S_0 < 50$ keV

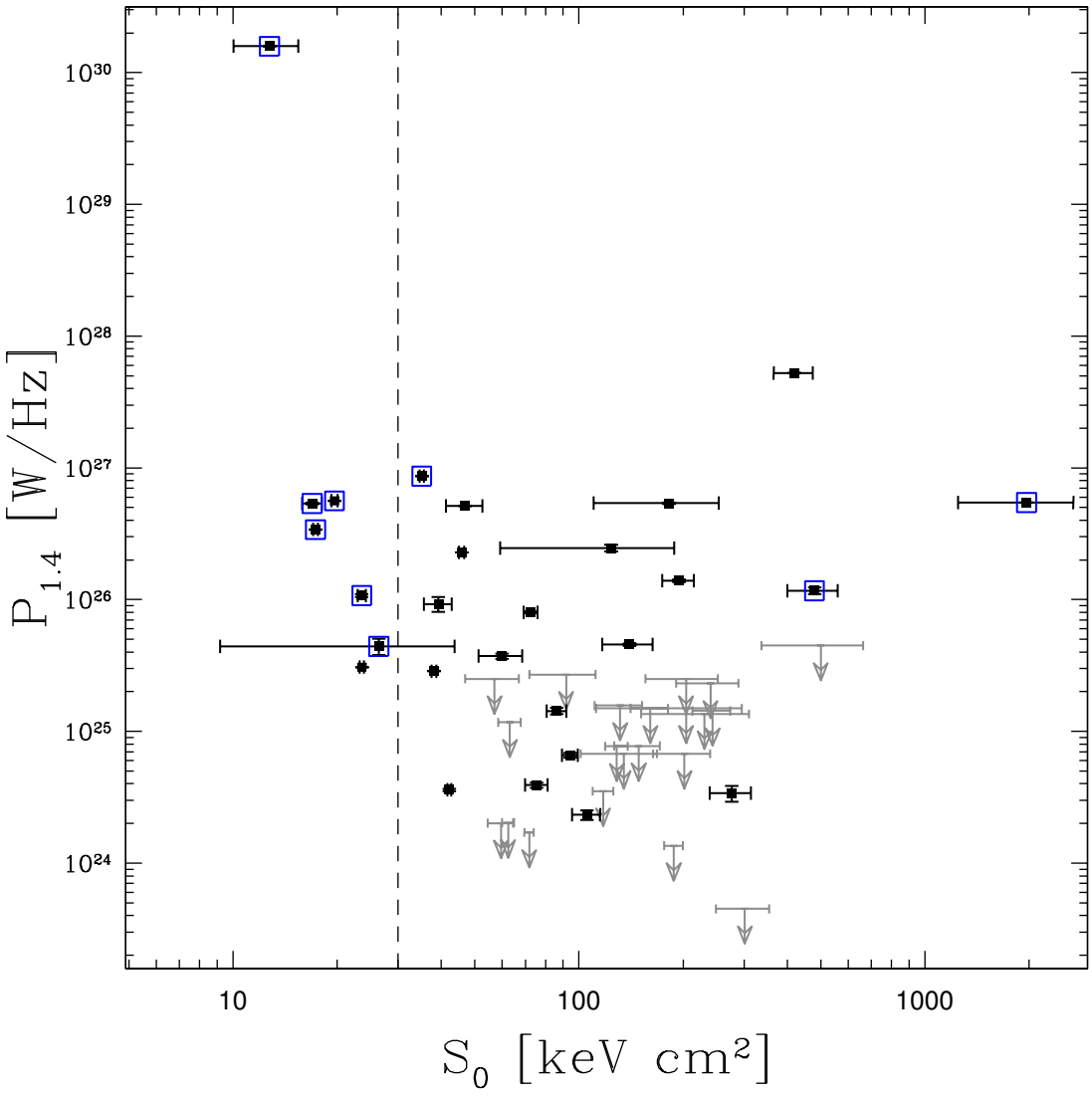

Figure 2.25: Radio power-density $P_{1.4\mathrm{GHz}}$ from the VLA FIRST survey versus central entropy S_0. Grey symbols represent uppper limits where no radio source was detected at the position of the BCG. Large blue squares denote the systems with visually-classified blue cores. The dashed vertical line shows the entropy threshold for star-formation indicators found in Cavagnolo et al. (2008).

cm^2, all of which are within $D_{XO} < 10$ kpc, are all associated with 1.4 GHz radio sources. This supports the hypothesis that the BCGs in these systems are indeed active (with either AGN or star formation) but, while this activity is detectable at radio wavelengths, it is not vigorous enough to transform the optical core color.

There are several BCGs associated with bright 1.4 GHz radio sources ($P_{1.4} > 10^{26}$ W Hz^{-1}) in clusters with $S_0 > 100$ keV cm^2 that do not show optically blue cores. It is tempting to consider these systems as evidence for a cyclical heating and cooling process in clusters that proceeds as follows: (1) radiative cooling in the ICM creates an instability that generates a cool core with low central entropy, (2) gas cools and condenses onto the BCG to fuel star formation and AGN feedback, (3) the resulting AGN feedback heats the cluster core, increasing its entropy and shutting off the cold gas supply, (4) AGN and star formation cease, (5) in the absence of heating, cooling begins to dominate again, returning to (1). If such a cyclical process is indeed taking place we should expect to see a wide range of stellar ages in blue core BCGs ($t_{yc} \sim 10^8$yr up to $t_{yc} \sim$ few 10^9 yr; where t_{yc} is the elapsed time since the most recent star formation activity). However, Pipino et al. (2009) use GALEX UV data to show that $t_{yc} < 2 \times 10^8$ yr for all blue-core BCGs in their sample, while the most recent star formation in their red-core systems is constrained to $t_{yc} > 2 \times 10^9$ yr. Despite the low number statistics, with only 7 clusters in their sample (4 blue-core, 3 red-core), the Pipino et al. (2009) results do not favour the cyclical heating model. Instead, they point to a model in which BCG star formation is 'always on' in cool core clusters and AGNs act only to temper the flow of cold gas onto the BCG rather than shut it down completely.

Table 2.3: Summary table of the radio data (from the FIRST survey) for the BCGs in our sample. We list here the cluster names and their rest-frame 1.4 GHz radio power. For the case where no detected source exists in the in the overlapping FIRST survey data we give the limit on the 1.4 GHz radio power.

Name	$\log P_{1.4}$ W/Hz
Abell119	< 23.65
MKW3S	24.56 ± 22.85
Abell85	25.46 ± 23.14
Abell1991	25.49 ± 23.09
Abell1795	26.94 ± 23.14
Abell2065	24.59 ± 23.24
ZwCl1215	< 24.13
Abell2670	24.37 ± 23.29
Abell2029	26.36 ± 23.33
Abell2033	< 24.21
Abell1650	< 24.23
Abell1651	24.82 ± 23.43
Abell2440	< 24.30
Abell2142	< 24.31
Abell1927	25.26 ± 23.53
Abell2055	26.74 ± 23.63
Abell2069	24.53 ± 23.66
Abell1361	27.16 ± 23.68
Abell2050	< 24.55
RXCJ0736p39	< 24.55
Abell961	< 24.59
Abell1033	< 24.61
Abell655	< 24.61
Abell646	26.35 ± 23.78
Abell1132	26.09 ± 23.87

Continued on next page...

Table 2.3 continued...

Name	$\log P_{1.4}$ W/Hz
Abell795	26.71 ± 23.86
Abell1068	25.63 ± 23.84
Abell1413	25.15 ± 23.89
ZwCl1023	26.68 ± 23.90
Abell990	< 24.73
A2204	26.53 ± 23.91
A2104	< 24.83
A2259	< 24.83
A1234	26.90 ± 24.00
A1914	< 24.89
A586	25.66 ± 24.04
MS0906	< 24.89
A1689	25.90 ± 24.13
A1246	< 24.99
A2261	25.57 ± 24.21
A963	< 25.07
A1942	< 25.13
A1763	27.72 ± 24.20
A2219	< 25.16
A2111	< 25.17
A267	< 25.17
MS1231a	< 25.20
MS1231b	< 25.20
A1835	26.75 ± 24.41
MS1455	26.03 ± 24.41
A1758b	26.14 ± 24.56
A697	< 25.36
A611	< 25.40
A959	< 25.40
A2537	< 25.43
MS1224	< 25.51

Continued on next page...

Table 2.3 continued...

Name	$\log P_{1.4}$ W/Hz
MS1358	25.97 ± 25.08
MS1512	25.65 ± 24.79
A370a	< 25.65
A370b	25.83 ± 24.83
A851	26.07 ± 24.86
MS1621a	26.73 ± 24.92
MS1621b	< 25.78
CL0910	26.73 ± 24.93
3C295	30.20 ± 26.14
RXJ1524	26.39 ± 25.14

2.7 Conclusions

We present $(g' - r')$ and $(B - R)$ color profiles for 108 BCGs in clusters in the redshift range $0.05 < z < 0.55$. We find that the majority of the BCGs in our sample have shallow, negative color gradients similar to those observed in more regular elliptical galaxies, consistent with metallicity profiles that decrease from the central region outward. However, we also find that 22% of the BCGs in our sample have spatially resolved inversions in their color profiles such that they get bluer with decreasing radius (blue cores). We perform several tests to examine how the presence/absence of blue cores depends upon the X-ray properties of the ICM. The aim of this comparison is to see whether or not the blue-core phenomenon is consistent with being due to recent star formation or AGN activity fuelled by cold gas as it condenses from the ICM and flows inward onto the BCG.

We compare the value of the BCG inner color gradients $\gamma_{(g'-r')}$ with the entropies S_0 and central cooling times $t_{c,0}$ of the ICM in their host clusters. We find that there are thresholds in both S_0 and $t_{c,0}$ above which blue core BCGs are rare, but below which they are almost ubiquitous. Specifically, where X-ray comparison is possible, nearly all blue-core BCGs (13/15) are found to be in clusters with $S_0 < 40$ keV cm^2 and $t_{c,0} < 1$ Gyr. These thresholds are consistent with previous work comparing

other potential indicators of star formation in BCGs (eg, $(U - I)$ color, H_α, radio power) to the entropies and cooling times of host clusters (Cavagnolo et al. 2008, Rafferty et al. 2008). Furthermore, we find that all blue-core BCGs are centrally located in the cluster, with $D_{XO} < 15$ kpc. These results confirm that the blue-core BCG phenomenon is directly linked to the radiative cooling of the ICM. The large angular sizes of the blue regions (greater than the PSF scale) favor the explanation that the recent star formation is responsible for the anomalously blue color and not AGN.

While no strong trend exists between the $\gamma_{(g'-r')}$ of the BCG and metallicity Z of the ICM, we do find that the mean metallicity of blue-core BCGs ($\langle Z/Z_\odot \rangle = 0.517 \pm 0.016$) is higher than that of the red-core BCGs ($\langle Z/Z_\odot \rangle = 0.487 \pm 0.014$) albeit with marginal significance. This result, when considered with those discussed above, is qualitatively consistent with previous work (Leccardi et al. 2010) finding metallicity enhancement in cool-core clusters (low S_0) compared to non cool-cores (high S_0).

Lastly, we use data from the FIRST survey to examine the relationship between $P_{1.4\mathrm{GHz}}$, S_0 and the BCG core color. All of the 9 visually-identified blue-core BCGs are associated with 1.4 GHz radio sources, however, the majority of BCGs (21/35) in the FIRST survey footprint are not detected. We confirm the presence of an entropy threshold (Cavagnolo et al. 2008) at $S_0 < 40$ keV cm^2, below which all BCGs are radio-bright ($P_{1.4\mathrm{GHz}} > 4.0 \times 10^{25}$ W Hz^{-1}). Below this threshold in S_0 the range in radio power is significantly more broad.

We have demonstrated that for the MENeaCS + CCCP sample the core color of BCGs is correlated with the X-ray properties of the ICM in their host clusters. The leading explanations for the anomalously blue core color are the recent onset of star formation or AGN (or both). The X-ray to optical correlations investigated herein are consistent with this recent activity being linked to the radiative cooling properties of the ICM such that the activity is present in the most strongly cooling systems but absent from the systems which are not strongly cooling. Of the two mechanisms for blue-core production, AGN versus star formation, we have argued that the data favor the star formation scenario. However, if the AGN are able to ionize and heat emission line nebulae at large distances from the central engine in the BCG nucleus then it could be possible to produce similarly extended blue cores. To distinguish between these two scenarios requires a large survey with spatially resolved spectra (eg. using an integral-field unit, long-slit or multi-object spectrograph) that is capable of detecting

blue continuum emission from a young stellar population. While some such studies of emission nebulae in BCGs have been done (eg. Edwards et al. 2009, McDonald et al. 2010), they are based on only a few BCGs and lack the sensitivity to the continuum, relying on heating and ionization models to distinguish between these scenarios. The results of these heating and ionization models are not conclusive, though we note that differences exist between their samples and methodology. Edwards et al. (2009) find a mix of ionization mechanisms (star formation, AGN) while McDonald et al. (2012) argue for a single low-ionization source like star formation. More sensitive observations, with larger samples would likely resolve this apparent discrepancy.

2.8 References

Balogh, M., Babul, A., Patton, D., 1999, MNRAS, 307, 463
Becker, R., White, R., Helfand, D., 1995, ApJ, 450, 559
Bell, E., Baugh, C., Cole, S., Frenk, C., Lacey, C., 2003, MNRAS, 343, 367
Bertin, E., Arnouts, S., 1996, A&A Supplement, 317, 393
Bildfell, C., Hoekstra, H., Babul, A., Mahdavi, A., 2008, MNRAS, 389, 1637
Brinchmann, J., Ellis, R., 2000, ApJ, 536, L77
Bruzual, G., Charlot, S., 2003, MNRAS, 344, 1000
Bundy, K., et al., 2006, ApJ, 651, 120
Cavagnolo, K., Donahue, M., Voit, G., Sun, M., 2008, ApJ, 683, 107
Conroy, C., Gunn, J., White, M., 2009, ApJ, 699, 486
Conroy, C., White, M., Gunn, J., 2010a, ApJ, 708, 58
Conroy, C., Gunn, J., 2010b, ApJ, 712, 833
Edwards, L., Robert, C., Molla, M., McGee, S., 2009, MNRAS, 369, 1953
Ellison, S., Patton, D., Mendel, J., Scudder, J., 2011, MNRAS, 418, 2043
Guzman R., Gallego, J., Koo, D., Phillips, A., Lowenthal, J., Faber, S., Illingworth, G., Vogt, N., 1997, ApJ, 489, 559
Hoekstra, H., 2007, MNRAS, 379, 317
Hoekstra, H., Mahdavi, A., Babul, A., Bildfell, C., 2012, MNRAS, 427, 1298
Juneau, S., et al., 2005, ApJ, 619, L135
Kawata, D., Mulchaey, J., Gibson, B., Sanchez-Blazquez, P., 2006, ApJ, 648, 969
Kodama, T., et al., 2004, MNRAS, 350, 1005
Leccardi, A., Rossetti, M., Molendi, S., 2010, A&A, 510, 82
Loubser, S., Sanchez-Blazquez, P., 2012, MNRAS, 425, 841

Lupton, R., 2005, (http://www.sdss.org/dr5/algorithms/sdssUBVRITransform.html)
Mahdavi, A., Hoekstra, H., Babul, A., Sievers, J., Myers, S., Henry, J., 2007, ApJ, 664, 162
Mahdavi, A., Hoekstra, H., Babul, A., Bildfell, C., Jeltema, T., Henry, P., 2013, ApJ, 767, 116
Maraston, C., Stromback, G., Thomas, D., Wake, D., Nichol, R., 2009, MNRAS, 394, 107
McDonald, M., Veilleux, S., Rupke, D., 2012, ApJ, 746, 153
McNamara, B., Rafferty, D., Birzan, L., Steiner, J., Wise, M., Nulsen, P., Carilli, C., Ryan, R., Sharma, M., 2006, ApJ, 648, 164
Patton, D., Ellison, S., Simard, L., McConnachie, A., Mendel, J., 2001, MNRAS, 412, 591
Peterson, J., Kahn, S., Paerels, F., Kaastra, J., Tamura, T., Bleeker, J., Ferrigno, C., Jernigan, J., 2003, ApJ, 590, 207
Pipino, A., Kaviraj, S., Bildfell, C., Babul, A., Hoekstra, H., Silk, J., 2009, MNRAS, 395, 462
Poole, G., Babul, A., McCarthy, I., Fardal, M., Bildfell, C., Quinn, T., Mahdavi, A., 2007, MNRAS, 380, 437
Rafferty, D., McNamara, B., Nulsen, P., 2008, ApJ, 687, 899
Salome, P., Combes, F., Revaz, Y., Edge, A., Hatch, N., Fabian, A., Johnstone, R., 2008, A&A, 484, 317
Sand, D., Graham, M., Bildfell, C., Zaritsky, D., Pritchet, C., Hoekstra, H., Just, D., Herber-Fort, S., Sivanandam, S., Foley, R., Mahdavi, A., 2012, ApJ, 746, 163
Sanderson, A., O'Sullivan, E., Ponman, T., 2009, MNRAS, 395, 764
Voit, G., 2005, RevModPhys, 77, 207

Chapter 3

The Giant-to-Dwarf Ratio

3.1 Introduction

Non-starforming galaxies in clusters exhibit a tight sequence in color-magnitude space known as the red sequence (eg. Visvanathan 1978; Bower et al. 1992), which is in place as early as $z \sim 1$ (eg. Bell et al. 2004, Mei et al. 2006). Less understood is how the number of red sequence galaxies and their distribution with stellar mass/absolute magnitude evolves with cosmic time. Understanding the assembly history of the red sequence is critical as these galaxies represent the bulk of the stellar mass in clusters at the present epoch. A useful metric for probing this assembly history is the ratio of the number of luminous red sequence galaxies (giants) to the number of faint red sequence galaxies (dwarfs). This is essentially a non-parametric representation of the luminosity function using only 2 bins and is commonly referred to as the Giant-to-Dwarf ratio (GDR).

There is an ongoing debate regarding the presence or absence of evolution in the GDR and/or its reciprocal the Dwarf-to-Giant ratio (DGR). De Lucia et al. (2007) for instance, finds significant evolution in the GDR, amounting to a change from GDR$\sim$ 0.45 to GDR$\sim$ 0.95 over the redshift range $0.4 < z < 0.8$. The analysis of low redshift ($0.08 < z < 0.19$) cluster data by Capozzi et al. (2010) supports the extrapolation of this trend to lower redshift. Stott et al. (2007) and Gilbank et al. (2008) also find strong evolution in the DGR using somewhat brighter absolute magnitude limits for the definition of dwarfs. In contrast, Crawford et al. (2009) look at 59 clusters at redshift $0 < z < 0.5$ and, though they do not measure the GDR directly, conclude that there is little evolution in the faint-end slope of the

luminosity function. Andreon (2008), in an analysis of 28 clusters in the redshift range $0 < z < 1.3$, asserts that the DGR is consistent with no evolution. More specifically, he states that the strong trend observed by de Lucia et al. (2007) can be ruled out. Andreon (2008) discusses some of the differences between his analysis and those of de Lucia et al. (2007) and Gilbank et al. (2008), arguing that their selection of filters that do not bracket the 4000 angstrom break over the entire range of redshifts introduces systematic errors that mimic evolution. Furthermore, he argues that in the work of Stott et al. (2007) and de Lucia et al. (2007) the use of control fields taken in separate filter sets than the cluster fields causes significant systematics related to the interloper-removal process.

The selection of target clusters may also be important. The Andreon (2008) clusters are all spectroscopically confirmed and identified in X-rays, while those used in de Lucia et al. (2007) are not and may contain line-of-sight superpositions at the low-mass end.

Perhaps the most significant difference between Andreon (2008) and others is the use of a Bayesian approach to fit the luminosity function of red sequence galaxies, which is then converted to a DGR to facilitate comparison with the literature. It is stated that this is a superior method because it uses all of the available data, particularly at the faint-end of the luminosity function, beyond the limits of the de Lucia et al. (2007) definition of a dwarf galaxy (the most common definition). We suspect however, that there are distinct disadvantages to the Andreon (2008) type approach because in forcing the parametric form of the luminosity function one is introducing an undesirable model dependence and it may therefore be incorrect to compare with non-parametric results. Moreover, a procedure that takes all available data and allows the fitted domain to vary from cluster to cluster potentially creates a systematic bias. This is because the clusters that are sampled to the faintest absolute magnitudes will have more stringent constraints on their faint end slope than those that are truncated at a brighter limit.

With so many subtle differences between the various ways that the GDR has been measured in the literature it may be no surprise that there appears to be some disagreement. Our analysis, however, is carried out on observations taken in a single filter pair, from a single telescope/instrument (including control fields), and with a sample of exclusively X-ray-confirmed clusters. These attributes allow us to avoid many of the criticisms mentioned above. Moreover, we calculate the effect of many potential sources of systematics (K-correction, projected distance from the brightest

cluster galaxy (BCG), color selection method, color error bias and the presence of large scale structure) to estimate their role in the apparent disagreements in the literature. When coupled with the sheer number of clusters in our sample, this survey provides the most accurate and robust measure of the GDR over this redshift range to date.

If indeed there is an evolving GDR in galaxy clusters, it becomes interesting to investigate the mechanism(s) responsible for driving that evolution. For instance, gas-poor (dry) merging of galaxies at the bright end of the red sequence could lead to a depletion of the giant population. In competition with this process, star-forming galaxies move onto the red sequence through the quenching of ongoing star formation and the resulting color transformation. However, the observed downsizing behavior of stellar mass assembly (Bell et al. 2004, Juneau et al. 2005, Bundy et al. 2005, Faber et al. 2007, Scarlata et al. 2007) suggests that this effect may become less important with decreasing redshift as the specific star formation rate at a fixed galaxy mass declines. While these mechanisms are complementary in that they act to reduce the number of giants with respect to dwarfs, their relative importance as a function of look-back time is poorly constrained. The detailed behaviour of these mechanisms is likely an important benchmark for galaxy formation models. For example, Gilbank & Balogh (2008) show that the Galform model of Bower et al. (2006) is unable to reproduce both the observed DGR evolution and the DGR difference between cluster and field populations. This is somewhat surprising given the success of Galform in predicting the observed K-band luminosity function of galaxies (Bower et a. 2006). Using a toy model, Gilbank & Balogh (2008) are able to show that reducing the efficiently of hot gas removal from infalling satellite galaxies results in better DGR agreement between the model and the observations.

As mentioned above, all of our clusters are confirmed in X-rays and the majority of them have X-ray temperature measurements, which can be used as independent mass proxies. This information is necessary for disentangling any cluster mass dependence and allows us, for the first time, to properly probe the mechanism(s) that drive GDR evolution at these redshifts.

The layout of the chapter is as follows. In §3.2 we discuss the data, along with some tests for completeness and data quality to ensure that our measurements are not significantly biased by systematics. In §3.3 we describe the data reduction and analysis procedure used to measure the red sequence and extract from it the GDR. Following this, §3.4 discusses the results of our GDR analysis along with tests of how varying the selection method can affect the GDR measurement and a detailed

comparison with previous results from the literature. In §3.5 we discuss the potential dependence of the GDR on cluster mass as implied by the X-ray temperature. An investigation of the mechanisms responsible for GDR evolution is in §3.6. Finally, §3.7 contains our conclusions. Throughout this work we assume a cosmology parameterized by $\Omega_m = 0.3$, $\Lambda = 0.7$ and $H_0 = 70$km/s/Mpc.

The work presented in this Chapter is published in the peer-reviewed journal "Monthly Notices of the Royal Astronomical Society" (Bildfell et al., 2012).

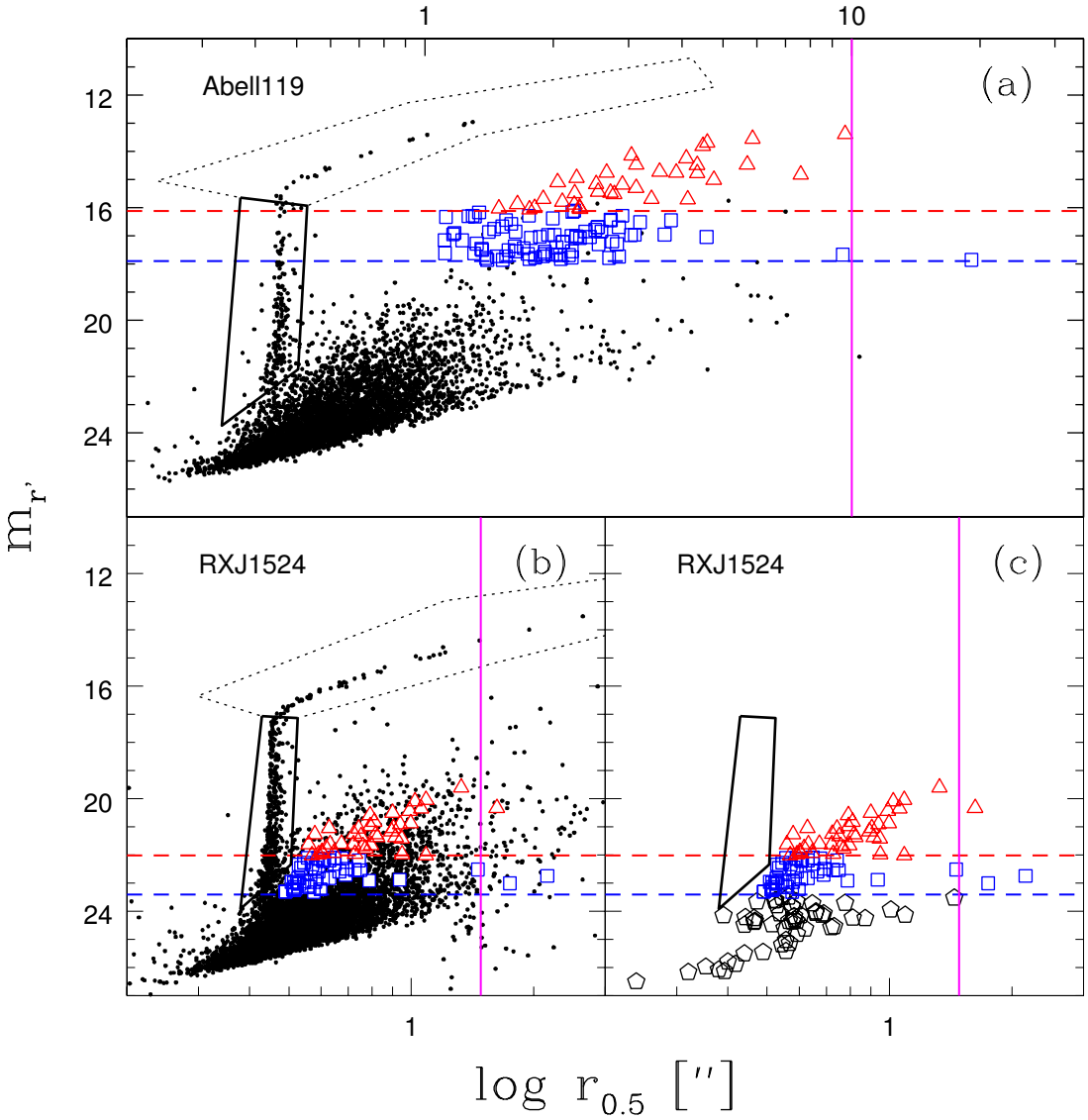

Figure 3.1: Half-light radius vs apparent magnitude in the r' band for the clusters Abell119 at $z = 0.05$(a) and RXJ1524 at $z = 0.516$ (b & c). The black polygons illustrate our star removal procedure. The red triangles and blue squares represent all of the giant and dwarf galaxies respectively (see §3.4 for details of the selection procedure). For clarity we show only 5% of regular objects but 100% of the selected giants and dwarfs. The $m_{r'}$ giant and dwarf selection limits are shown by the red and blue dashed lines. The solid vertical magenta line shows the equivalent size of a $z = 0.05$ galaxy measuring 10" after taking into account the PSF and the change in angular diameter distance. The (c) panel shows only the giants, dwarfs and fainter galaxies (black pentagons) that also matched the red sequence color selection (see §3.4). The large size of these fainter galaxies with respect to the stellar distribution indicates a clear separation of stars and red sequence galaxies based on our selection criteria.

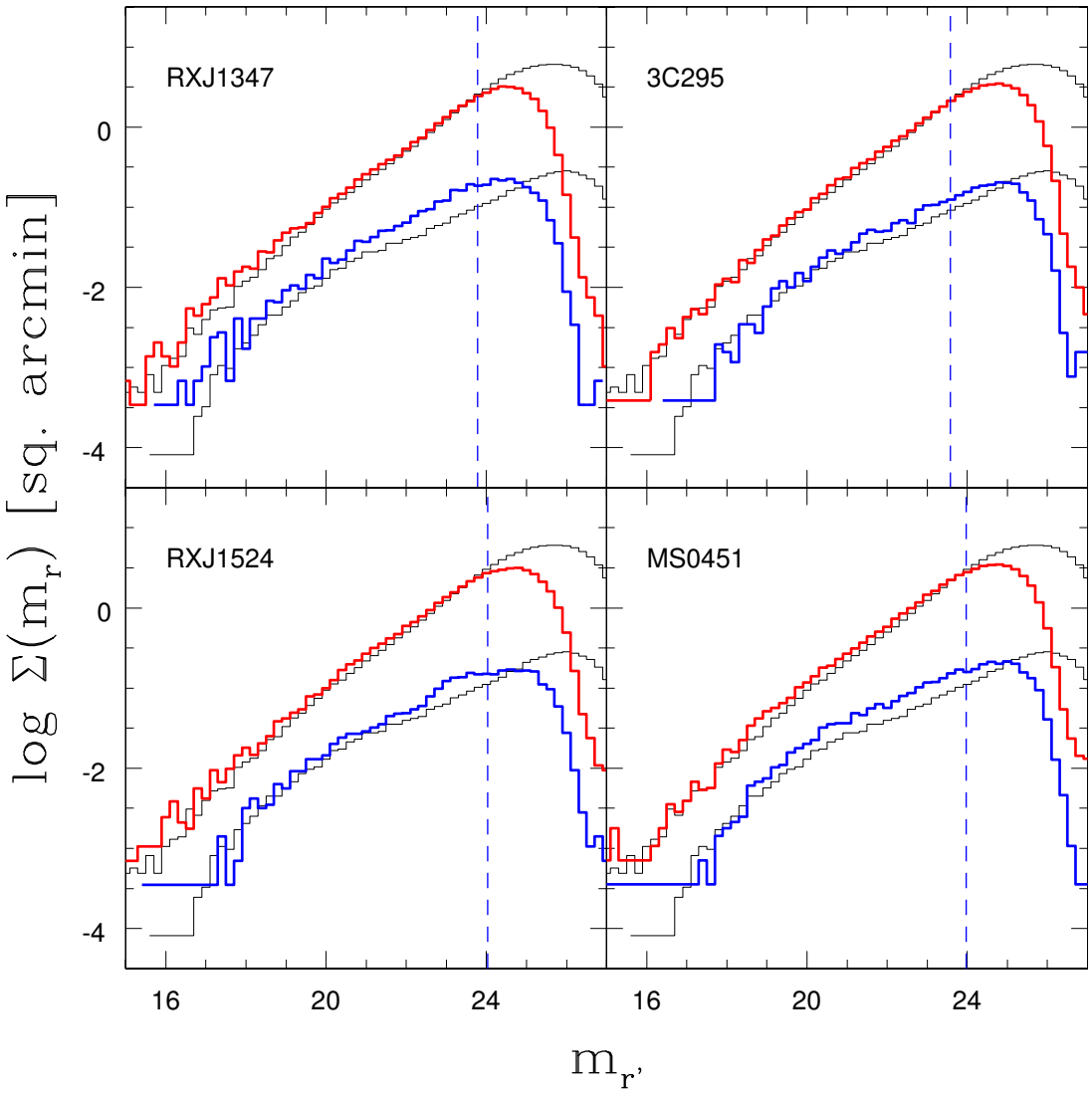

Figure 3.2: Histograms showing the surface-density of galaxies per sq. arcmin for 4 of the highest redshift clusters in our sample. The thick lines in each panel show the galaxies detected within a wide (red) and narrow (blue) color slice (see text). The corresponding thin black lines show the surface-density of galaxies detected in the CFHTLS Deep images using the same selection criteria. The blue vertical dashed line shows the location of the faint-end magnitude limit used to select dwarf galaxies (see §3.4 for details). The data are complete up to this limit for the full redshift range investigated.

3.2 Data

The data for this study are obtained using the MegaCam[1] wide-field imager (0.187"/pix) on the Canada-France-Hawaii Telescope (CFHT) with the g' and r' optical filter set. The cluster sample is comprised of 101 clusters with redshift $0.05 < z < 0.55$ and is assembled from 3 subsamples: 58 clusters from the Multi-Epoch Nearby Cluster Survey (MENeaCS), 32 clusters from the Canadian Cluster Comparison Project (CCCP) and 11 additional clusters from the CFHT archive. The MegaCam field is nearly square, subtending approximately 3450 arcseconds on a side. With the clusters centered in the field of view these data cover projected distances out to 1.49 Mpc from the cluster center at the lowest redshift and 11.05 Mpc at the highest redshift.

To clarify the characteristics of our sample, for the purpose of comparison with other studies, we discuss here some of the selection strategies employed in the subsamples. The MENeaCS clusters are selected from the BAX X-ray galaxy cluster database[2] and represent all clusters in the database that are observable from CFHT, with redshift $0.05 < z < 0.15$ and X-ray luminosity $L_x > 2 \times 10^{44}$ erg s^{-1}. There are 55 clusters satisfying these criteria, to which we add 3 clusters with the slightly relaxed criteria, $L_x > 1.5 \times 10^{44}$ erg s^{-1} and $0.044 < z < 0.15$ for a total of 58. The CCCP consists of 50 clusters in the redshift range $0.15 < z < 0.55$, selected from the cluster catalog of Horner (2001). The CCCP clusters all have X-ray temperatures $T_x > 3$ keV and are selected such that they fully sample the observed scatter in the L_x vs T_x plane. For the purpose of maintaining a uniform observational configuration, we restrict the current analysis to the 32 CCCP clusters observed with MegaCam g' and r'. Lastly, as mentioned above, we add 11 clusters from the CFHT archive that are also observed with this instrumental configuration.

All of our data are initially calibrated with CFHT's Elixir software pipeline. The Elixir analysis includes a photometric zeropoint that is determined for each individual run. To account for non-photometric conditions, the magnitudes of objects in common between exposures are compared. For the CCCP photometric conditions were requested and the comparison of exposures indicates that the uncertainty in the zeropoints are < 0.05 magnitudes, which implies an impact on the color that

[1]Based on observations obtained with MegaPrime/MegaCam, a joint project of CFHT and CEA/DAPNIA, at the Canada-France-Hawaii Telescope (CFHT) which is operated by the National Research Council (NRC) of Canada, the Institut National des Science de l'Univers of the Centre National de la Recherche Scientifique (CNRS) of France, and the University of Hawaii.

[2]http://bax.ast.obs-mip.fr/

is smaller. The MENeaCS data are obtained over many queue runs, most of which were during photometric conditions. The results for clusters that overlap with SDSS show agreement within < 0.04 magnitudes. The archival data were reprocessed using the same technique of comparing magnitudes of objects common to multiple exposures and similarly, we find that the uncertainty on individual zeropoints is < 0.05 magnitudes.

From the combined sample of 101 clusters, we remove 4 from the analysis because of their low richness (see §3.4.1) leaving a total of 97. Basic information for our targets is listed in Table 3.1. Further details on the CCCP survey will be presented in a future paper (Hoekstra et al. 2012, Mahdavi et al. 2013), while a more detailed description of the MENeaCS survey can be found in Sand et al. (2012). The largest seeing disc of our images has a FWHM of 1.0" with the majority being significantly smaller. For background determination, we make use of the CFHT Legacy Survey (CFHTLS) Deep images. These data are processed and hosted by S. Gwyn[3] (see Gwyn 2008 for details) and consist of four fields that are not targeted at, nor dominated by, individual galaxy clusters. The CFHTLS Deep fields are observed using the same instrument and filters as our targeted observations but to greater depth. As such, they provide excellent control fields for statistical background subtraction (discussed further in §3.4).

[3]http://www1.cadc-ccda.hia-iha.nrc-cnrc.gc.ca/community/CFHTLS-SG/docs/cfhtlsDeep.html

Table 3.1: Table of clusters used in our sample. RA (α) and DEC (δ) give the coordinates of the BCG. Cluster identifiers marked with a * are excluded from the final analysis due to low richness (see §3.4.1).

Name	z	α hh:mm:ss	δ dd:mm:ss
Abell119	0.044	00:56:16.10	-01:15:19.0
MKW3S	0.045	15:21:51.84	07:42:31.9
Abell780	0.054	09:18:05.65	-12:05:43.5
Abell754	0.054	09:08:32.37	-09:37:47.2
Abell85	0.055	00:41:50.45	-09:18:11.1
Abell2319	0.056	19:21:10.00	43:56:44.5
Abell133	0.057	01:02:41.71	-21:52:55.2
Abell1991	0.059	14:54:31.48	18:38:33.4
Abell1781*	0.062	13:44:52.54	29:46:15.6
Abell1795	0.062	13:48:52.49	26:35:34.8
Abell553	0.066	06:12:41.09	48:35:44.6
Abell644	0.070	08:17:25.61	-07:30:45.0
Abell399	0.072	02:57:53.09	13:01:51.3
Abell2065	0.073	15:22:29.17	27:42:27.8
Abell401	0.074	02:58:57.78	13:34:58.3
ZwCl1215	0.075	12:17:41.13	03:39:21.2
Abell2670	0.076	23:54:13.67	-10:25:08.2
Abell2029	0.077	15:10:56.09	05:44:41.4
Abell2495	0.078	22:50:19.71	10:54:12.8
RXSJ2344-04	0.079	23:44:18.20	-04:22:48.8
ZwCl0628	0.081	06:31:22.69	25:01:06.8
Abell2033	0.082	15:11:26.51	06:20:56.8
Abell1650	0.084	12:58:41.49	-01:45:41.0
Abell1651	0.085	12:59:22.49	-04:11:45.7
Abell2420	0.085	22:10:18.76	-12:10:13.9
Abell2597	0.085	23:25:19.72	-12:07:26.7

Continued on next page...

Table 3.1 continued...

Name	z	α hh:mm:ss	δ dd:mm:ss
Abell763*	0.085	09:12:35.18	16:00:01.0
Abell478	0.088	04:13:25.27	10:27:55.1
Abell2440	0.091	22:23:56.92	-01:34:59.5
Abell2142	0.091	15:58:19.99	27:14:00.5
Abell1927	0.095	14:31:06.79	25:38:01.6
Abell21	0.095	00:20:36.98	28:39:33.0
Abell2426	0.098	22:14:31.58	-10:22:26.1
Abell2055	0.102	15:18:45.72	06:13:56.4
Abell1285	0.106	11:30:23.82	-14:34:52.3
Abell7	0.106	00:11:45.25	32:24:56.6
Abell2064*	0.108	15:20:52.24	48:39:38.7
Abell2443	0.108	22:26:07.92	17:21:23.8
RXCJ0352+19	0.109	03:52:58.99	19:40:59.8
Abell2703	0.114	00:05:23.95	16:13:09.3
Abell2069	0.116	15:24:08.42	29:52:55.6
Abell1361	0.117	11:43:39.60	46:21:20.7
Abell2050	0.118	15:16:17.92	00:05:20.9
RXCJ0736+39	0.118	07:36:38.08	39:24:52.8
Abell1348	0.119	11:41:24.19	-12:16:38.5
Abell961	0.124	10:16:22.86	33:38:17.7
Abell1033	0.126	10:31:44.32	35:02:29.2
Abell2627	0.126	23:36:42.08	23:55:29.5
Abell655	0.127	08:25:29.05	47:08:00.9
Abell646	0.129	08:22:09.53	47:05:53.3
Abell1132	0.136	10:58:23.65	56:47:42.0
Abell795	0.136	09:24:05.29	14:10:21.8
Abell1068	0.138	10:40:44.48	39:57:11.5
Abell1413	0.143	11:55:18.00	23:24:18.1
ZwCl1023	0.143	10:25:57.98	12:41:08.7
Abell990	0.144	10:23:39.91	49:08:38.8
Abell2409	0.148	22:00:53.49	20:58:42.1

Continued on next page...

Table 3.1 continued...

Name	z	α hh:mm:ss	δ dd:mm:ss
RXCJ0132-08*	0.149	01:32:41.11	-08:04:04.6
Abell2204	0.150	16:32:46.96	05:34:33.0
Abell545	0.154	05:32:25.18	-11:32:39.3
Abell2104	0.160	15:40:07.92	-03:18:16.1
Abell2259	0.160	17:20:09.65	27:40:08.5
Abell1234	0.166	11:22:29.94	21:24:22.2
Abell1914	0.170	14:26:03.88	37:49:53.8
Abell586	0.170	07:32:20.30	31:38:01.3
Abell1246	0.190	11:23:58.82	21:28:50.0
MS0440	0.190	04:43:09.90	02:10:19.5
Abell115S	0.200	00:56:00.25	26:20:32.8
Abell115N	0.200	00:55:50.61	26:24:37.7
Abell2163	0.200	16:15:48.98	-06:08:41.0
Abell2261	0.200	17:22:27.22	32:07:57.9
Abell520	0.200	04:54:14.05	02:57:10.8
Abell223N	0.210	01:38:02.28	-12:45:19.7
Abell223S	0.210	01:37:55.98	-12:49:09.9
Abell1942	0.220	14:38:21.87	03:40:13.5
Abell2111	0.230	15:39:40.50	34:25:27.7
Abell2125	0.246	15:41:14.75	66:16:03.8
Abell1835	0.250	14:01:02.09	02:52:42.9
Abell521	0.250	04:54:06.87	-10:13:24.4
CL1938	0.260	19:38:18.10	54:09:40.4
Abell1758W	0.280	13:32:38.41	50:33:36.2
Abell697	0.280	08:42:57.56	36:21:59.6
Abell611	0.290	08:00:56.82	36:03:24.0
Abell959	0.290	10:17:36.00	59:34:02.0
Abell2537	0.300	23:08:22.21	-02:11:31.5
MS1008	0.300	10:10:32.32	-12:39:52.6
Abell851	0.410	09:42:57.45	46:58:50.1
RXJ0856	0.411	08:56:12.69	37:56:15.9

Continued on next page...

Table 3.1 continued...

Name	z	α hh:mm:ss	δ dd:mm:ss
RXJ2228	0.412	22:28:33.70	20:37:16.6
RXJ1003	0.416	10:03:04.62	32:53:41.4
MS1621	0.426	16:23:35.14	26:34:28.3
MACS1206	0.440	12:06:12.14	-08:48:03.1
CL0910	0.440	09:13:45.50	40:56:28.7
RXJ1347	0.450	13:47:30.64	-11:45:08.9
RXJ1701	0.453	17:01:23.51	64:14:12.0
3C295	0.460	14:11:20.55	52:12:10.1
RXJ1524	0.516	15:24:38.37	09:57:43.6
MS0451	0.540	04:54:10.83	-03:00:51.2

3.2.1 Source Extraction

The data are bias-subtracted and flat fielded using the Elixir software package. We combine the images and perform background subtraction using SWarp (Bertin et al. 2002). After data reduction and image stacking we mask obvious image defects and regions around bright stars that could severely bias the photometry. We then run SExtractor (Bertin & Arnouts 1996) in dual image mode on each set of g' and r' images using the masks merged with exposure maps as weight images. To maximize the detection of faint dwarf galaxies, even when they are embedded in the halos of much larger giant galaxies, we adjust some of the SExtractor parameters from their default values. We briefly discuss here some of these parameters that can affect the number of sources detected in crowded regions and the values we use for our extractions. The DETECT_THRESH and ANALYSIS_THRESH values are set to 1.5 relative to the background variance and the DETECT_MINAREA is set to 3 pixels. To enable the detection of faint galaxies near to bright ones in these crowded fields we set the DEBLEND_MINCONT to 10^{-7} and the DEBLEND_NTHRESH to 64. There are also several parameters that control the way the background is measured and subtracted from the detected sources and, therefore, these can affect the apparent magnitudes of galaxies especially at the faint end. For these we use a BACK_SIZE of

128 pixels and a BACK_FILTERSIZE of 3 pixels. Lastly, SExtractor has the option to "CLEAN" the source catalog of artifacts and false detections. We find that setting CLEAN =Y with a CLEAN_PARAM= 2.0 not only removes many of the artifacts and false detections but also increases the number of real objects detected compared to the case of CLEAN=N. Tests comparing these results to those obtained using more relaxed parameters (ie. DEBLEND_MINCONT= 10^{-4}, DEBLEND_NTHRESH=16 and CLEAN=N) show that our modified parameter choices can yield of order 2 additional dwarfs and giants per cluster.

Throughout this chapter we use SExtractor MAG_AUTO for galaxy magnitudes and MAG_APER for galaxy colors. The aperture magnitudes are extracted using a 3" diameter aperture, which is several times larger than the worst case seeing disc of the sample (see §3.2). All catalogs are corrected for foreground galactic extinction using E(B-V) values from Schlegel et al. (1998) and the extinction curve of Cardelli et al. (1989).

3.2.2 Stars & Extended Galaxies

The object catalogs discussed in §3.2.1 include stars. To obtain a galaxy catalog we remove the objects that lie along the locus defined by point sources in the half-light radius ($r_{0.5}$) vs apparent r' magnitude ($m_{r'}$) plane. Figure 3.1 illustrates this process for two clusters in our sample; one at the lowest redshift and one at the highest. The thick, solid, black box outlines the objects that are identifiable as unsaturated stars while the thin dotted polygon similarly identifies the saturated ones. At magnitudes fainter than the limit of the solid box it becomes impossible to confidently distinguish point sources from extended ones by this method. For this reason, we retain all sources fainter than this limit in our galaxy catalogs so as not to remove the faintest galaxies. We verify, however, that any remaining stellar contamination does not bias our results by examining whether the GDR (as measured in §3.4) changes when excluding clusters at galactic latitude $b < 35$ degrees, which it does not.

The blue squares and red triangles in Figure 3.1 show the red sequence dwarf and giant galaxies respectively, with the blue and red dashed lines showing the corresponding magnitude limits for their selection. These limits are adopted from the de Lucia et al. (2007) definitions (dwarfs: $-20.0 < M_V < -18.2$ & giants: $M_V < -20.0$) which are converted to the corresponding $m_{r'}$ values at the appropriate redshift (see §3.4 for details of this conversion). We note the presence of a small number of de-

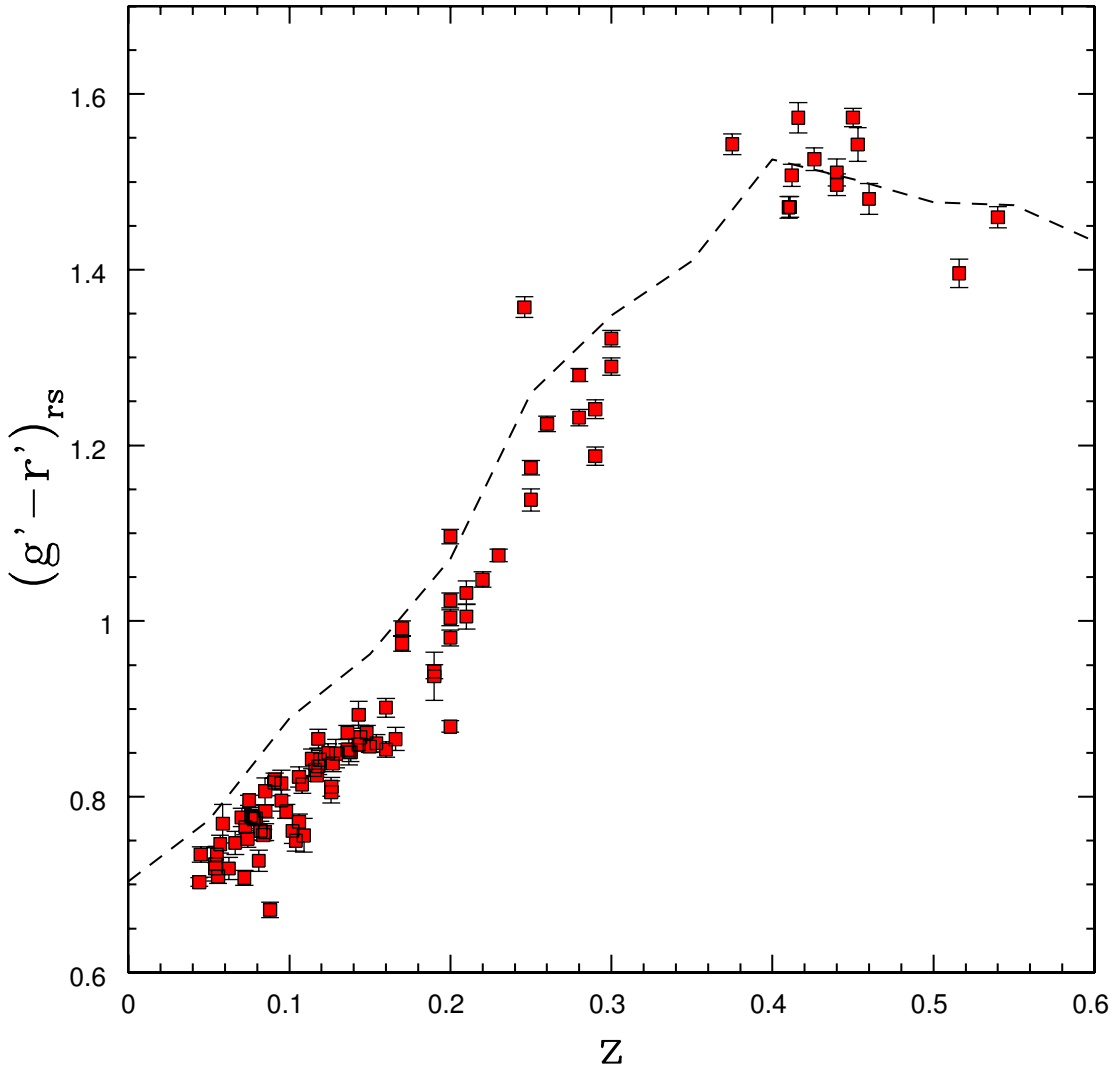

Figure 3.3: The average observed $(g'-r')$ color of red sequence galaxies with $-20.82 < M_{r'} < -19.82$ determined using a bootstrap method. This absolute magnitude bin corresponds to half a mag on either side of the division between dwarfs and giants. The data are plotted as a function of redshift. The strong correlation observed is the effect of the g' filter moving across the 4000 $\mathring{A}$ break with increasing redshift. The dashed line represents a simple model of the red sequence (see Appendix A for details)

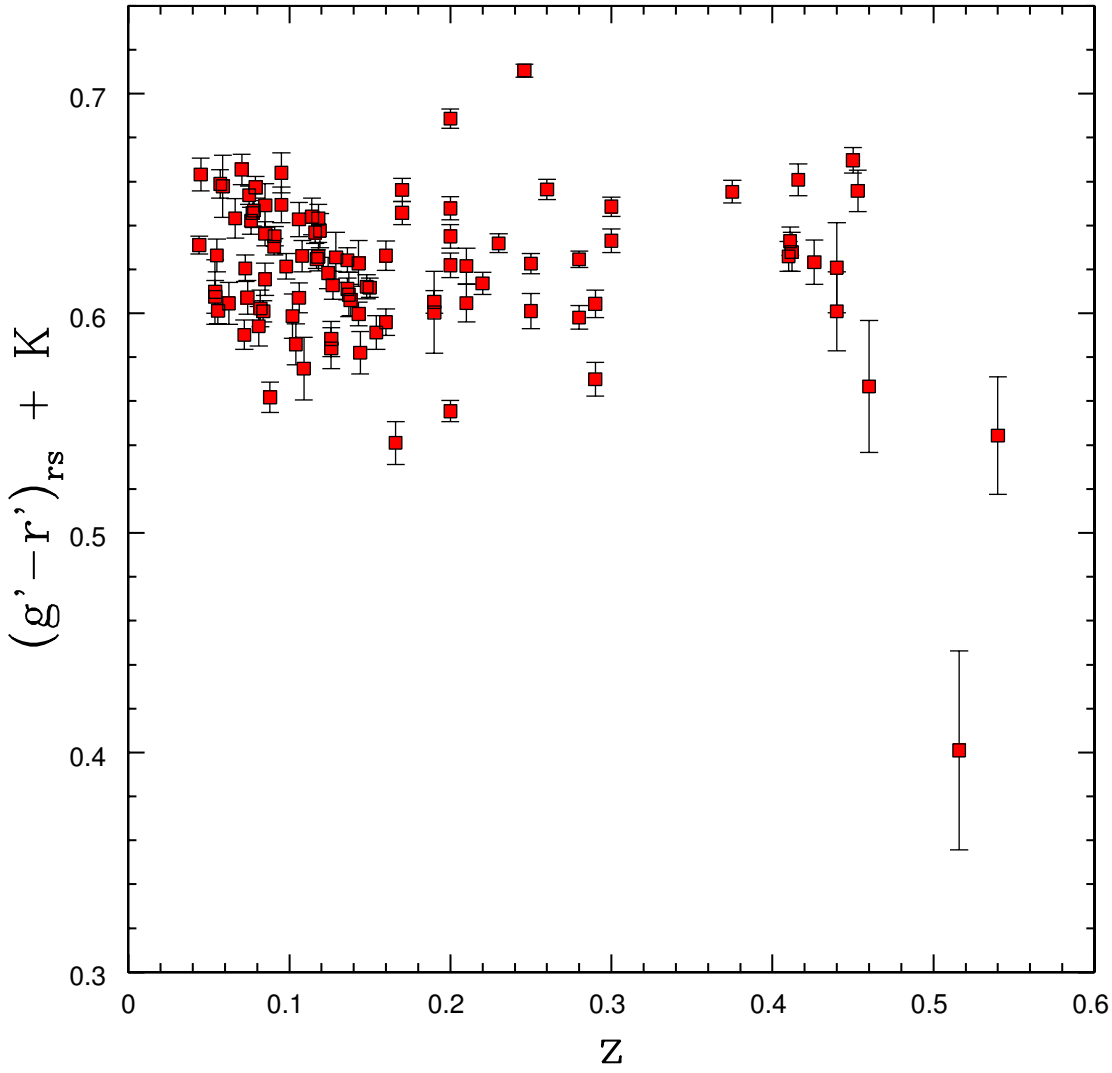

Figure 3.4: The average K-corrected $(g' - r')$ color of red sequence galaxies with $-20.82 < M_{r'} < -19.82$ determined using a bootstrap method. The data are plotted as a function of redshift. It is clear that after K-correction the mean $(g' - r')$ color at the division between dwarf and giant galaxies is roughly constant.

tections with $r_{0.5} > 1.0$" and $m_{r'} > 24.0$ for some images (eg. RXJ1524). We have investigated these by eye and conclude that they are all false detections and, because they do not enter the dwarf and giant selection limits, they do not affect the GDR.

To verify that the number of dwarfs or giants is not affected by the detection efficiency of galaxies with relatively low central surface brightness, we examine the most extended galaxies near the detection limit in each cluster. From visual inspection of $r_{0.5}$ vs $m_{r'}$ (eg. Figure 3.1), we find that at $z \sim 0.05$ there are very few galaxies detected that are larger than 10". At $z \sim 0.05$, after subtracting in quadrature the size of the PSF, we estimate the physical size of the limiting half-light radius to be $r_{0.5} \sim 8.5$ kpc. This limit is then converted back to an angular size at the appropriate redshift, corrected for PSF effects and then overplotted as the solid magenta line in Figure 3.1. The analogs of these extended galaxies are well above our detection limit in the high z end of our sample. We conclude that the evolution of the number of dwarf and giant galaxies is not affected by the detectability of dwarfs with extended surface brightness profiles. Furthermore the fraction of such galaxies is small in both the dwarf and giant populations.

3.2.3 Completeness

To investigate the completeness of our galaxy catalogs we compare them with the catalogs obtained from the CFHTLS Deep data (see §3.2). We generate Galactic extinction-corrected, star-cleaned catalogs in both g' and r' for each of the 4 Deep fields using the same procedure as described in sections 3.2.1 and 3.2.2. We compare the number of galaxies as a function of magnitude $m_{r'}$ in our sample with those in the CFHTLS Deep (control) using both a wide color window $[-1.0 < (g' - r') < 4.0]$ and a narrow one $[1.0 < (g' - r') < 1.2]$. Figure 3.2 shows the surface density of galaxies selected with these criteria for 4 clusters at the upper redshift limit of our sample. The thick red and blue histograms show the distributions of sources outside a projected radius of 750 kpc in each of our cluster fields for the wide color window (red) and the narrow window (blue) while the underlying thin black histograms show the corresponding distributions of sources in the CFHTLS Deep survey area. The vertical blue dashed lines show the location of the faint end limit for dwarf galaxies (see §3.4). The slopes of the counts distributions are in agreement between our cluster data and the CFHTLS Deep fields. Some cluster fields show a small excess of objects with respect to the control sample, but this is expected due to enhancement

from cluster galaxies that lie further than 750 kpc from the BCG. Some fields also exhibit a small jump at $m_{r'} \sim 22$ (eg. RXJ1524, MS0451) which corresponds to the apparent magnitude where we can no longer reliably distinguish stars from galaxies. The clusters that exhibit the largest jumps are those in the galactic plane $b < 35°$. As mentioned in §3.2.2 we verified that these clusters do not bias our results by repeating our analysis with $b < 35°$ removed and obtaining consistent measurements of the GDR evolution. The CFHTLS Deep data is several magnitudes deeper in the r' band than our cluster sample, thus the surface-density begins to fall off in the clusters fields at brighter $m_{r'}$ than in the control fields. In all cases however, the sharp drop in counts observed in our sample occurs at magnitudes fainter than the faint dwarf limit (vertical dashed line). We conclude that the GDR measurements presented in §3.4 are not affected by incompleteness in the dwarf population.

3.3 Analysis

In this section we describe the various criteria we use to select galaxies belonging to the dwarf and giant populations within clusters and present some simple tests to show that these selection criteria are robust.

3.3.1 Red Sequences

With the unambiguous stars removed from our catalogs, we plot the color-magnitude diagrams (CMD) of the remaining objects and fit their red sequences. We present an overview of the red sequence fitting results here but for a more detailed description of the fitting procedure we refer the reader to Appendix A. Briefly, we use the biweight estimator of Beers et al. (1990) to fit the color-magnitude relation (CMR), employing a statistical background subtraction method similar to that of Pimbblet et al. (2002).

To check the quality of our photometry and red sequence fitting procedure, we plot in Figure 3.3 the color of the red sequence ($(g' - r')_{rs}$) at a fixed $M_{r'}$ versus redshift. The $(g' - r')_{rs}$ color shown is calculated using a bootstrap method, finding the average $(g' - r')$ of the red sequence member galaxies lying within $\Delta m_{r'} = \pm 0.5$ mag on either side of the $m_{r'}$ value that separates dwarfs from giants (see §3.4 for detail of dwarf and giant selection). The strong dependence of $(g' - r')_{rs}$ color on redshift seen in Figure 3.3 is a result of the 4000 angstrom break spectral feature, that is prominent in early type galaxies, shifting across the g' band with increasing

redshift. The errors shown, which are typically smaller than the symbol size, account only for statistical variance and do not include any systematics. We also show, as a dashed line, the expected $(g' - r')_{rs}$ for our model red sequences (see appendix A). The slope of the $(g' - r')_{rs}$ evolution is similar between the observations and the model, with a flattening at $z \sim 0.4$. There is however a significant systematic offset between the two from $0.05 < z < 0.3$, as discussed in appendix A and is likely a consequence of the overly simplistic star formation history assumed in the model.

3.3.2 Magnitude Limits

We measure the ratio of luminous (giant) to faint (dwarf) red sequence galaxies (defined as $|\Delta(g' - r')| < 0.2$ from the best fit red sequence) using the absolute magnitude cuts defined by de Lucia et al. (2007) $M_V = [-20.0, -18.2]$ which we transform to Megacam $M_{r'}$ using the single stellar population red sequence model described in appendix A. Thus, we define giant galaxies as those with $M_{r'} < -20.32$ and dwarf galaxies as those with $-20.32 < M_{r'} < -18.52$. Note that these converted limits are identical to those used in Capozzi et al. (2010), who looked at the GDR using similar filters in the Sloan digital sky survey (SDSS). The excellent agreement with the Capozzi et al. (2010) limits at all redshifts indicates that the difference introduced by comparing across photometric systems is negligible.

At this stage, a choice in methodology must be made before these cuts can be applied to the data. One can either transform the data to absolute magnitudes or transform the absolute magnitude cuts to apparent magnitudes. We choose to do the latter because the former method requires a K-correction to all of the data, and since a K-correction based on only the g' and r' filters becomes degenerate beyond $z \sim 0.6$ this would allow additional high-redshift background objects to enter the dwarf and giant samples. Therefore our dwarf/giant sample selection is performed in observed space by transforming the above-mentioned absolute magnitude cuts following the relation:

$$m_{r'} = M_{r'} + 5\log(D_l) + 25 - (K + E) \tag{3.1}$$

where D_l represents the luminosity distance of the cluster in Mpc and the K-and E terms represent the K-correction and the evolution correction respectively. These corrections are described in detail in §3.3.3.

3.3.3 $K + E$ Correction

We assume that the luminosity evolution correction (E) takes the form of $2.5 \times \log(1+z)$, which is appropriate for passively evolving elliptical galaxies on the red sequence. The K-correction is calculated from the Charlot & Bruzual (CB07) synthetic spectra, assuming a solar metallicity $Z_{\odot} = 0.02$ with a 3% contribution by stellar mass from ultra-metal poor stars (see appendix A). The age of the spectral template is assigned by matching its redshifted $(g' - r')$ color to the $(g' - r')$ color of a galaxy on the best fitting red sequence at a given $m_{r'}$. The appropriate K-correction is then calculated and this procedure is repeated for a sample of $m_{r'}$ values along the red sequence. Inverting equation 3.1 we generate the function that describes the K-correction as it depends on absolute magnitude. This is then interpolated for the dwarf and giant absolute magnitude limits described above to obtain the K-corrections that are specific to the color-magnitude coordinates of said limits along the best fit red sequence.

To verify that our K-correction is working properly we use a bootstrap method to compute the color of the red sequence member galaxies in an $m_{r'}$ bin that extends ± 0.5 around the cut in $m_{r'}$ that divides the dwarfs from the giants. Figure 3.4 shows the redshift dependence of this color after K-correction. Once the K-correction has been accounted for the $(g' - r')$ color around the dwarf/giant division remains relatively flat. There is one cluster (RXJ1524) that is a significant outlier, at $z \sim 0.5$ with a K-corrected $(g' - r')_{rs} \sim 0.4$. Inspection of the color-magnitude diagram for this cluster reveals a second red sequence located at slightly bluer color than that of RXJ1524, which is consistent with being the source of the observed color bias. This contamination likely also biases the GDR measurement for this cluster but it does not affect our conclusions regarding the GDR of the ensemble. The constant color seen in Figure 3.4 is expected for massive early type galaxies in this redshift range and lends confidence to the K-correction procedure. The direct impact of the K-correction on GDR is investigated in §3.4.3.

3.3.4 Giant-to-Dwarf Color Difference

As a further check, we compute the $(g' - r')$ color of both dwarf and giant galaxies and examine the evolution of the giant-to-dwarf color difference (GDCD) as defined by:

$$GDCD_{(g'-r')} = \langle (g' - r')_g \rangle - \langle (g' - r')_d \rangle \tag{3.2}$$

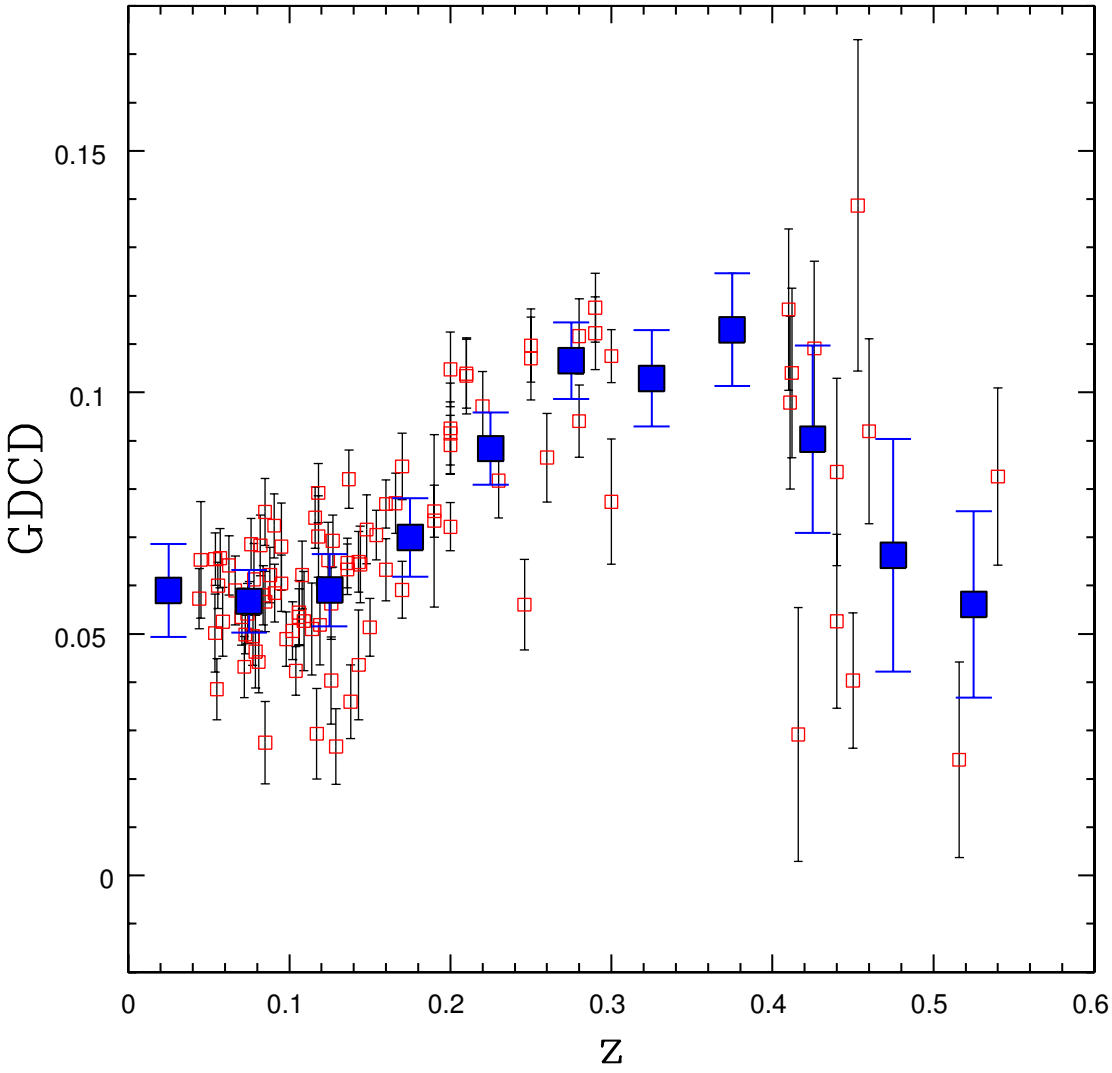

Figure 3.5: The giant-to-dwarf color difference (GDCD) as it depends on redshift. Large symbols represent the error-weighted mean GDCD in each redshift bin. As a differential measurement, GDCD is unaffected by photometric zeropoint errors, making it a good benchmark for models of the red sequence.

where $\langle (g' - r')_g \rangle$ and $\langle (g' - r')_d \rangle$ are the mean colors of giant and dwarf galaxies respectively as calculated for individual clusters. Because the GDCD is a relative measurement, it is not affected by systematics that induce a shift in the photometric zero point over the entire image. Thus, it may provide a useful test of the galaxy properties in cluster formation simulations. Figure 3.5 shows the GDCD plotted against redshift. This quantity is effectively a measure of the red sequence slope as sampled by the individual member galaxies. From the model red sequences we expect the slope to increase with redshift out to $z \sim 0.4$ and then turn over as the $(g' - r')$ filter combination becomes less sensitive to the 4000 angstrom break. Moreover, this loss of sensitivity to the 4000 angstrom break results in a reduced color separation between red sequence and blue cloud members, increasing the level of red sequence contamination. Such behavior is reflected in the GDCD, though with a significant scatter. This highlights the concern that the level of contamination by the blue cloud is a function of redshift and could falsely contribute to the evolution signal in the GDR. We attempt to correct for this effect in §3.4.1, but we note here that if it were artificially creating a redshift trend in the GDR, then we would expect to see similar GDR values at both $z = 0.1$ and $z = 0.5$. This is not the case.

3.4 Giant-to-Dwarf Ratio

In this section we discuss issues that deal directly with the GDR measurements. First, in section §3.4.1 we describe the statistical background subtraction method and corrections for biasing effects introduced by uncertainty in $(g' - r')$ color. This is followed in §3.4.2 by the results of GDR measurements for individual clusters. As mentioned in §3.3.2, we use magnitude limits defined by de Lucia et al. (2007) and convert to $m_{r'}(z)$. Our criterion for color selection of dwarf and giant galaxies on the red sequence is based on the offset in $(g' - r')$ from the best fit red sequence ($|\Delta(g' - r')| < 0.2$). We further require as a spatial criterion that the projected distance from the BCG is $R < 750$ kpc. Unless stated otherwise, the union of these three criteria define our dwarf and giant selection and are referred to as the default selection method. Within the literature however, there is no clear consensus on a set of criteria that defines the dwarf and giant populations, owing in part to varying data quality, instrumentation and redshift range of observation. To facilitate a more direct literature comparison, in §3.4.3 we examine the sensitivity of the GDR to variations in the selection criteria described above. Lastly, in §3.4.4, we compare our GDR values

to previous results.

3.4.1 Background Subtraction and Color-Error Correction

We apply the selection limits discussed above to our CMDs to find the number of dwarfs and giants in each cluster. The resulting numbers, however, are contaminated by interlopers. To correct for this contamination we apply a statistical subtraction method that uses the catalogs generated from the CFHTLS Deep field images (see §3.2.3). For each cluster, we take the $m_{r'}$ and $(g' - r')$ limits for dwarfs and giants and apply these same limits to the CMD of the merged Deep field catalogs. We then correct the cluster counts in the following way:

$$n_c = n_o - n_b \frac{A}{A_b} \tag{3.3}$$

where n_c is the background-corrected number of cluster galaxies, n_o is the observed number of galaxies, n_b is the number of galaxies in the background catalog and A and A_b are the area of the target and background samples respectively.

An additional correction is made to account for the bias introduced by the uncertainty in the observed $(g' - r')$ color. For instance, an intrinsically narrow red sequence will be broadened colorwise, which can result in galaxies being scattered outside of the color selection limits, especially at the highest redshifts. It is also possible for cluster members in the blue cloud to be observationally scattered into the red sequence, increasing the resulting number of red sequence galaxies and acting in opposition to the previously described effect. Both are statistically significant effects and failure to account for this observational bias can mimic an evolution in the GDR.

To correct for the color-error bias, we estimate the number of galaxies observed to be red sequence members as a fraction of the number that are intrinsically on the red sequence (ie. the selection fraction). We simulate this process by taking the distribution of $m_{r'}$ and $(g' - r')$ and perturbing each value by a normally distributed random number that is scaled to the 1σ measurement uncertainty on each of these quantities. We compute the background-subtracted number of dwarfs and giants both before and after this perturbation and repeat the procedure for 1000 realizations. No perturbation is applied to the background galaxies as their color-magnitude errors are much smaller than those of the target sample. We assume that the selection fraction (f_s) can be approximated by $f_s \approx n_{rs}/n'_{rs}$ where n_{rs} and n'_{rs} are the number of red sequence galaxies before and after the perturbation respectively. This approximation

is valid as long as the difference $(n_{rs} - n'_{rs})$ is small compared to n_{rs}. For the giants and dwarfs below $z < 0.3$ the effect is of order 5%, beyond $z > 0.3$ it grows to a maximum of 20%. The appropriate selection fraction is calculated for both the dwarf and giant populations and is compensated for by applying f_s to n_c from equation 3.3 to compute the total number of galaxies $n_t = n_c/f_s$ respectively.

To assess the importance of background subtraction and the color-error correction we show in Figure 3.6 the fraction of galaxies (f_c) that must be subtracted to correct for these effects as a function of redshift. We define this parameter as follows:

$$f_c = (n_o - n_t)/n_t \tag{3.4}$$

The blue triangles and red squares in Figure 3.6 indicate dwarfs and giants respectively. The correction fractions are typically larger for the dwarfs than they are for the giants. The giants correction is typically constrained between 0-20% while the dwarfs exhibit a larger range in correction fraction. Note that f_c can become negative at high z for some of the dwarf populations, which is expected due to increasingly fewer background galaxies in the selection box and increasingly larger color-error; ultimately allowing the color-error correction to dominate over the background subtraction. We show only the clusters with background and area-corrected number dwarfs plus giants larger than 50 ($n_d + n_g > 50$). Four clusters that are poorer than this limit can have f_c values in excess of 50% and we have excluded them from the rest of the analysis that follows. The excluded clusters are marked with an asterisk in Table 3.1.

3.4.2 GDR results

Figure 3.7 shows the GDR as a function of redshift for all of the clusters in our sample (filled red symbols). The data indicate that the GDR increases with redshift. The uncertainties include contributions from the shot noise in both the cluster field and background populations and a term that accounts for the error introduced by the presence of large-scale structure in the background. For each cluster we estimate the large-scale structure term by randomly placing 100 apertures onto the CFHTLS Deep fields with radii of 750 kpc and then calculating the 68% inclusion limits for the number of background dwarfs and giants assuming a Poisson distribution. The solid blue line in Figure 3.7 shows the results of a best fit linear relationship between GDR and z parameterized by $GDR = \alpha z + \beta$. We use the MPFITEXY routine of

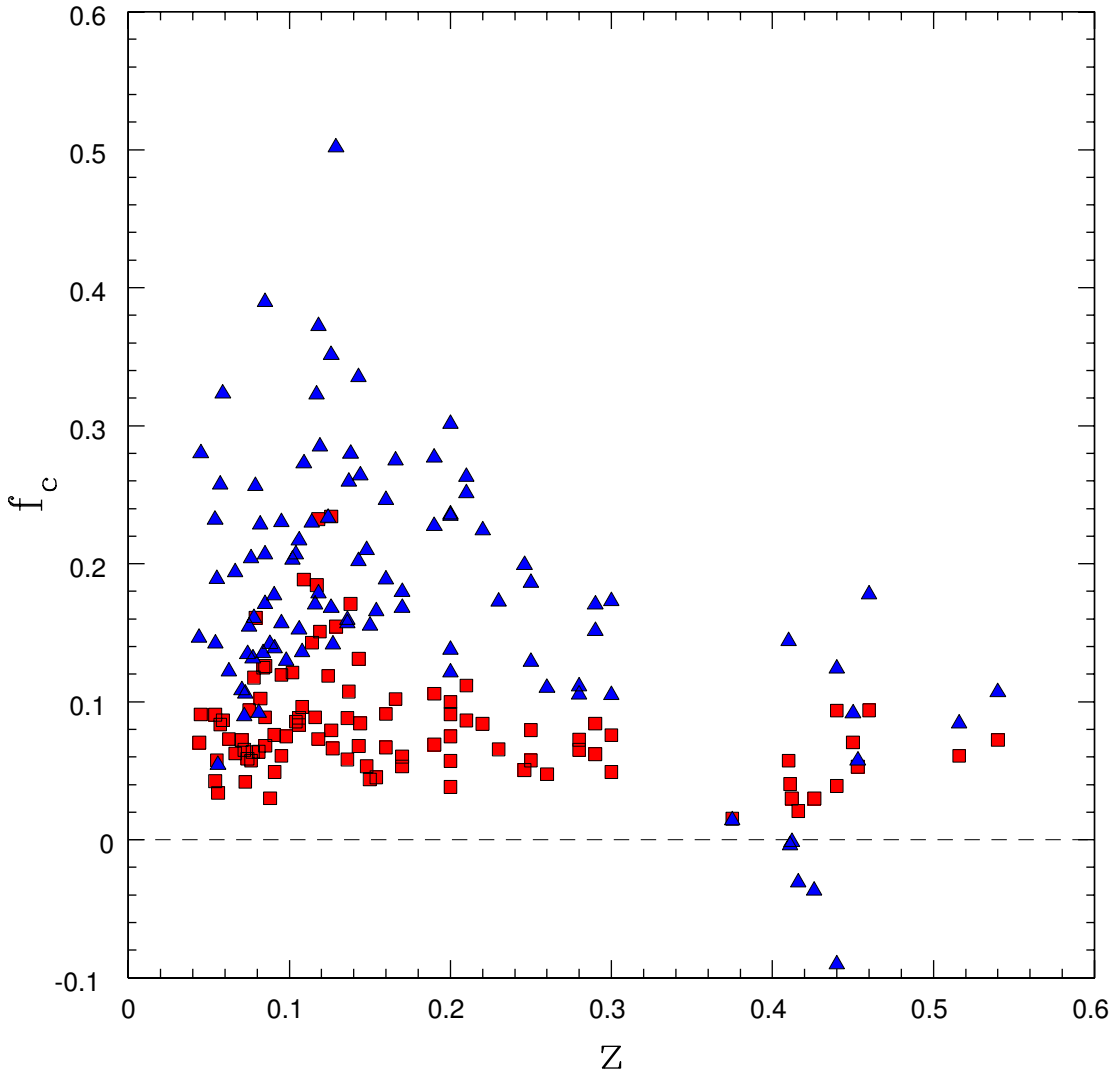

Figure 3.6: The effect of background subtraction and color-error correction expressed as a fraction of the total corrected counts for dwarfs (blue triangles) and giants (red squares) plotted against cluster redshift. The correction fraction becomes slightly negative for the high redshift dwarfs when the color-error correction begins to dominate over the background subtraction.

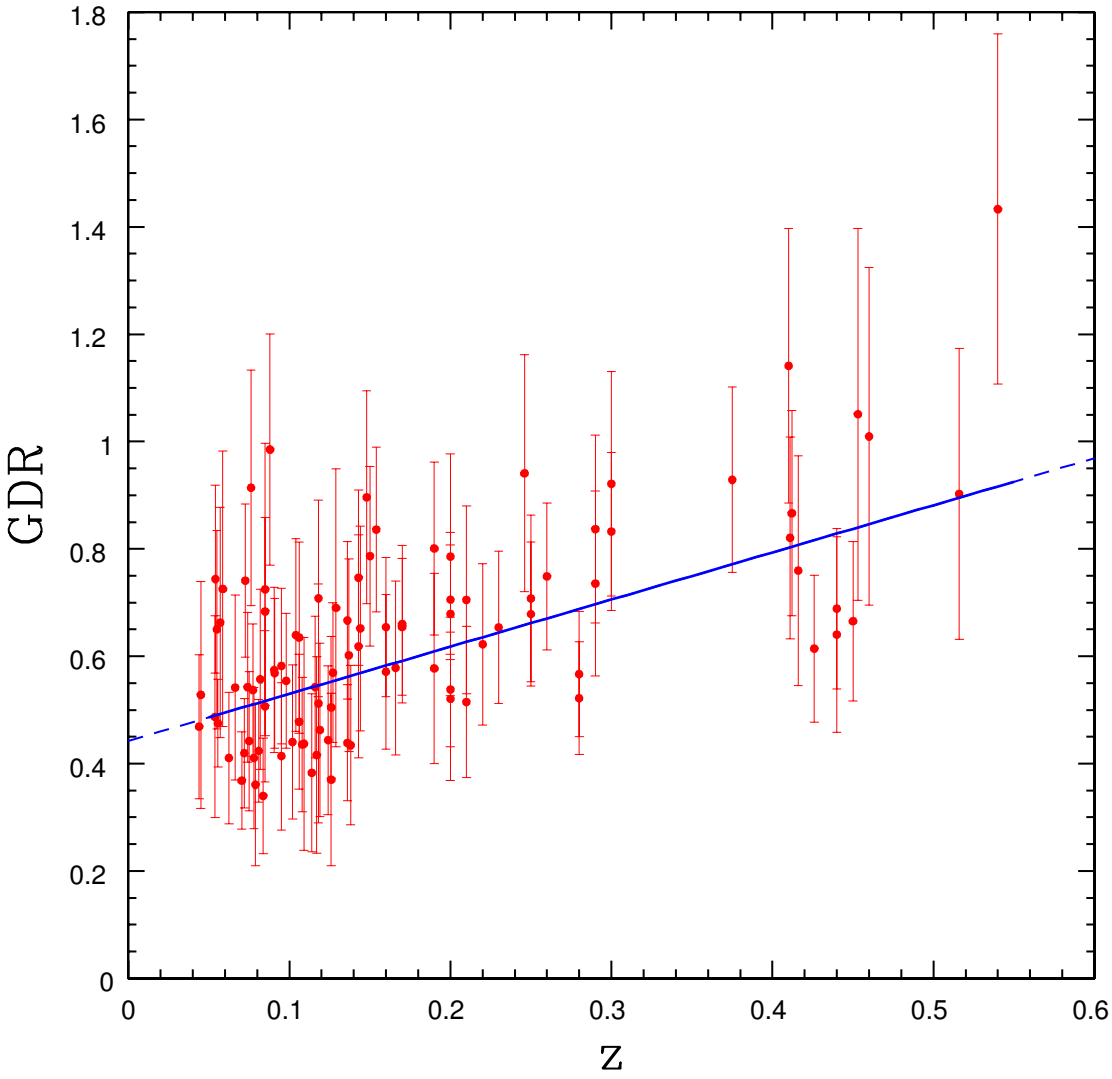

Figure 3.7: The Giant-to-Dwarf ratio (GDR) plotted against redshift. Individual clusters are marked by the filled red symbols. The blue line show the best fit linear redshift dependence.

Williams et al. (2010) to derive best fit values of α and β, which uses the MPFIT package by Markwardt (2009). We also allow for some intrinsic scatter in the GDR (σ_{int}), which is allowed to vary in the fit. The data are bootstrap sampled for 1000 realizations to obtain an empirical estimate of the uncertainties on the parameters. We find $\alpha = 0.88 \pm 0.15$, $\beta = 0.44 \pm 0.03$. The reduced χ^2 of the fit is approximately equal to unity for all realizations, indicating that σ_{int} is consistent with zero. If the large-scale structure error is neglected, however, the best fit parameters are similar $\alpha = 0.91 \pm 0.14$, $\beta = 0.47 \pm 0.03$ but the required $\sigma_{int} = 0.088 \pm 0.017$. This suggests that large-scale structure is the dominant source of this scatter. A Spearman's rank test (non-parametric) of the GDR vs z correlation returns $\rho = 0.54$ with a significance of greater than 5σ over the null hypothesis. The data and their best fit parameter values clearly favour an evolving GDR, but we reserve further discussion of this and a detailed comparison with results from the literature for §3.4.4. A list of the GDR measurements for each cluster, along with the number of dwarfs and giants both before and after the background+color-error correction (see §3.4.1) is given in Table 3.2.

Table 3.2: The GDR measurements. The columns give the name, the redshift (z), the fully-corrected GDR (GDR), the statistical uncertainty on the GDR (σ_{GDR}), the number of giants and dwarfs after data corrections (n_g & n_d respectively) along with the number of giants and dwarfs prior to data corrections (n_g^{raw} & n_d^{raw} respectively). The numbers of galaxies have been adjusted to account for the image area that was masked in the detection procedure.

Name	z	GDR	σ_{GDR}	n_g	n_g^{raw}	n_d	n_d^{raw}
Abell119	0.04	0.47	0.13	33.2	35.6	70.9	81.3
MKW3S	0.05	0.53	0.21	22.2	24.2	42.0	53.8
Abell780	0.05	0.49	0.19	22.3	24.3	45.7	56.3
Abell754	0.05	0.74	0.17	56.9	59.3	76.4	87.3
Abell85	0.05	0.65	0.18	39.1	41.3	60.1	71.5
Abell2319	0.06	0.48	0.08	83.5	86.3	175.7	185.2
Abell133	0.06	0.66	0.21	30.0	32.5	45.3	56.9
Abell1991	0.06	0.73	0.26	27.4	29.7	37.7	49.9
Abell1795	0.06	0.41	0.12	35.9	38.5	87.5	98.1
Abell553	0.07	0.54	0.17	35.9	38.2	66.3	79.2
Abell644	0.07	0.37	0.09	42.9	46.0	116.5	129.1
Abell399	0.07	0.42	0.10	48.3	51.5	115.2	125.5
Abell2065	0.07	0.74	0.14	82.0	85.4	110.6	122.4
Abell401	0.07	0.54	0.14	51.3	54.3	94.6	107.4
ZwCl1215	0.08	0.44	0.13	33.9	37.1	76.8	88.6
Abell2670	0.08	0.91	0.22	57.7	61.0	63.1	76.0
Abell2029	0.08	0.54	0.12	52.2	55.5	97.3	110.0
Abell2495	0.08	0.41	0.13	29.7	33.2	72.4	84.0
RXSJ2344-04	0.08	0.36	0.15	18.5	21.5	51.4	64.6
ZwCl0628	0.08	0.42	0.10	54.5	58.0	128.6	140.5
Abell2033	0.08	0.56	0.17	33.1	36.5	59.5	73.1
Abell1650	0.08	0.34	0.11	30.0	33.7	88.1	100.0
Abell1651	0.08	0.51	0.14	37.7	41.0	74.3	87.0

Continued on next page...

Table 3.2 continued...

Name	z	GDR	σ_{GDR}	n_g	n_g^{raw}	n_d	n_d^{raw}
Abell2420	0.09	0.68	0.18	47.9	51.2	70.1	84.6
Abell2597	0.09	0.72	0.27	24.0	27.0	33.1	46.0
Abell478	0.09	0.99	0.22	72.1	74.3	73.2	83.6
Abell2440	0.09	0.57	0.15	41.8	44.9	72.7	85.6
Abell2142	0.09	0.57	0.14	54.5	57.1	95.8	109.1
Abell1927	0.09	0.41	0.14	25.9	29.0	62.6	77.0
Abell21	0.09	0.58	0.15	46.1	48.9	79.2	91.6
Abell2426	0.10	0.55	0.13	54.0	58.0	97.4	110.0
Abell2055	0.10	0.44	0.14	28.5	32.0	64.8	78.0
A98	0.10	0.64	0.18	41.0	44.5	64.1	77.4
Abell1285	0.11	0.48	0.13	45.0	48.7	94.1	108.5
Abell7	0.11	0.63	0.18	38.9	42.3	61.3	74.5
Abell2443	0.11	0.44	0.13	37.7	41.3	86.4	98.2
RXCJ0352+19	0.11	0.44	0.20	19.4	23.1	44.5	56.6
Abell2703	0.11	0.38	0.15	26.1	29.9	68.2	83.9
Abell2069	0.12	0.54	0.13	47.8	52.0	88.0	103.0
Abell1361	0.12	0.42	0.18	19.1	22.6	45.9	60.7
Abell2050	0.12	0.71	0.18	51.3	55.0	72.4	85.3
RXCJ0736+39	0.12	0.51	0.22	19.5	24.1	38.2	52.4
Abell1348	0.12	0.46	0.16	25.7	29.5	55.5	71.3
Abell961	0.12	0.44	0.14	30.1	33.6	67.8	83.6
Abell1033	0.13	0.51	0.13	45.3	48.9	89.7	104.8
Abell2627	0.13	0.37	0.16	17.8	22.0	48.1	65.0
Abell655	0.13	0.57	0.13	66.4	70.8	116.6	133.1
Abell646	0.13	0.69	0.26	23.7	27.3	34.3	51.5
Abell1132	0.14	0.44	0.11	45.3	49.3	103.2	119.6
Abell795	0.14	0.67	0.15	66.3	70.2	99.5	115.1
A1882	0.14	0.60	0.18	38.2	42.3	63.5	79.9
Abell1068	0.14	0.43	0.15	26.5	31.0	61.0	78.0
Abell1413	0.14	0.75	0.16	62.7	67.0	84.0	101.0
ZwCl1023	0.14	0.62	0.21	29.2	33.0	47.2	63.0
Abell990	0.14	0.65	0.19	45.1	48.9	69.1	87.4

Continued on next page...

Table 3.2 continued...

Name	z	GDR	σ_{GDR}	n_g	n_g^{raw}	n_d	n_d^{raw}
Abell2409	0.15	0.90	0.20	67.4	71.0	75.2	91.0
A2204	0.15	0.79	0.17	91.8	95.8	116.7	134.8
A545	0.15	0.84	0.15	89.4	93.5	107.0	124.7
A2104	0.16	0.65	0.13	69.5	74.1	106.2	126.2
A2259	0.16	0.57	0.14	44.0	48.0	77.1	96.1
A1234	0.17	0.58	0.16	39.6	43.7	68.5	87.4
A1914	0.17	0.65	0.13	71.9	75.7	109.7	128.1
A586	0.17	0.66	0.15	71.0	75.2	107.5	126.8
A1246	0.19	0.80	0.16	76.4	81.7	95.4	117.1
MS0440	0.19	0.58	0.18	43.6	48.2	75.6	96.5
A115	0.20	0.79	0.19	55.8	60.9	71.1	92.5
A115N	0.20	0.52	0.15	45.8	50.4	88.0	108.7
A2163	0.20	0.71	0.10	128.7	133.6	182.5	204.6
A2261	0.20	0.54	0.11	67.2	71.0	124.8	142.0
A520	0.20	0.68	0.15	57.7	62.1	85.0	105.1
A223a	0.21	0.71	0.17	49.7	54.0	70.5	89.0
A223b	0.21	0.51	0.14	38.7	43.0	75.1	94.0
A1942	0.22	0.62	0.15	51.2	55.5	82.3	100.8
A2111	0.23	0.65	0.14	70.4	75.0	107.7	126.3
A2125	0.25	0.94	0.22	61.4	64.5	65.3	78.3
A1835	0.25	0.68	0.13	75.9	80.2	111.8	126.2
A521	0.25	0.71	0.16	62.1	67.0	87.7	104.0
CL1938	0.26	0.75	0.14	89.0	93.2	118.9	132.0
A1758b	0.28	0.52	0.11	64.4	69.0	123.3	137.0
A697	0.28	0.57	0.12	68.4	72.9	120.7	133.4
A611	0.29	0.74	0.17	57.6	62.4	78.3	91.6
A959	0.29	0.84	0.17	73.4	78.0	87.7	101.0
A2537	0.30	0.83	0.15	97.2	102.0	116.8	129.0
MS1008	0.30	0.92	0.21	66.4	71.5	72.1	84.6
A370	0.38	0.93	0.17	91.6	93.0	98.6	100.0
A851	0.41	1.14	0.26	72.8	77.0	63.8	73.0
RXJ0856	0.41	0.82	0.19	69.2	72.0	84.3	84.0

Continued on next page...

Table 3.2 continued...

Name	z	GDR	σ_{GDR}	n_g	n_g^{raw}	n_d	n_d^{raw}
RXJ2228	0.41	0.87	0.19	73.8	76.0	85.2	85.0
RXJ1003	0.42	0.76	0.21	47.0	48.0	61.9	60.0
MS1621	0.43	0.61	0.14	63.1	65.0	102.8	99.0
CL0910	0.44	0.64	0.18	43.4	47.5	67.8	76.2
MACS1206	0.44	0.69	0.15	78.0	81.0	113.2	103.0
RXJ1347	0.45	0.67	0.15	57.9	62.0	87.0	95.0
RXJ1701	0.45	1.05	0.35	42.9	45.2	40.8	43.2
3C295	0.46	1.01	0.31	41.1	45.0	40.8	48.0
RXJ1524	0.52	0.89	0.28	47.4	50.3	53.5	58.0
MS0451	0.54	1.43	0.33	86.7	93.0	60.5	67.0

Table 3.3: Supplementary data used for investigation into the evolution of the GDR. The columns give the name, the maximum $m_{r'}$ limits used for defining the giant and dwarf samples ($m^g_{r'}$ & $m^d_{r'}$ respectively), the color of the red sequence ($(g'-r')_{rs} \pm 0.01$) - see §3.3.1) and the X-ray temperature (T_x) as measured with ASCA (Horner 2001). Additional temperature measurements are added from BAX and marked with a * in the last column.

Name	$m^g_{r'}$	$m^d_{r'}$	$(g'-r')_{rs}$	T_x	σ_{T_x}	BAX
Abell119	16.1	17.9	0.70	5.93	0.17	
MKW3S	16.2	18.0	0.73	3.41	0.05	
Abell780	16.5	18.3	0.72	3.54	0.06	
Abell754	16.6	18.3	0.72	9.94	0.31	
Abell85	16.6	18.4	0.73	5.73	0.14	
Abell2319	16.6	18.4	0.71	9.62	0.31	
Abell133	16.7	18.5	0.75	3.71	0.07	
Abell1991	16.8	18.6	0.77	5.40	3.00	*
Abell1795	16.9	18.7	0.72	5.49	0.06	
Abell553	17.0	18.8	0.75			
Abell644	17.2	19.0	0.78	7.31	0.14	
Abell399	17.2	19.0	0.71	6.99	0.23	
Abell2065	17.2	19.0	0.77	5.35	0.12	
Abell401	17.3	19.1	0.75	8.07	0.20	
ZwCl1215	17.3	19.1	0.80	6.54	0.21	*
Abell2670	17.3	19.1	0.78	3.98	0.18	
Abell2029	17.4	19.2	0.78	7.30	0.37	
Abell2495	17.4	19.2	0.77			
RXSJ2344-04	17.4	19.2	0.78			
ZwCl0628	17.5	19.3	0.73	6.20	2.50	*
Abell2033	17.5	19.3	0.76	4.16	0.12	
Abell1650	17.6	19.3	0.76	5.89	0.12	
Abell1651	17.6	19.4	0.76	5.87	0.15	
Abell2420	17.6	19.4	0.78	6.00	1.60	*

Continued on next page...

Table 3.3 continued...

Name	$m^g_{r'}$	$m^d_{r'}$	$(g'-r')_{rs}$	T_x	σ_{T_x}	BAX
Abell2597	17.6	19.4	0.81	3.58	0.07	
Abell478	17.7	19.5	0.67	7.07	0.17	
Abell2440	17.7	19.5	0.82	4.31	0.15	
Abell2142	17.8	19.5	0.82	8.24	0.30	
Abell1927	17.9	19.7	0.82			
Abell21	17.9	19.7	0.80			
Abell2426	17.9	19.7	0.78			
Abell2055	18.0	19.8	0.76	5.80		*
A98	18.1	19.8	0.75			
Abell1285	18.1	19.9	0.82	4.10	3.00	*
Abell7	18.1	19.9	0.77			
Abell2443	18.2	19.9	0.81			
RXCJ0352+19	18.2	20.0	0.76			
Abell2703	18.3	20.1	0.84			
Abell2069	18.3	20.1	0.83	6.30	0.20	*
Abell1361	18.3	20.1	0.82			
Abell2050	18.4	20.1	0.87	4.34	0.07	*
RXCJ0736+39	18.4	20.1	0.83			
Abell1348	18.4	20.2	0.84	3.60	0.08	*
Abell961	18.5	20.3	0.85			
Abell1033	18.5	20.3	0.81			
Abell2627	18.5	20.3	0.81			
Abell655	18.5	20.3	0.84			
Abell646	18.6	20.4	0.85			
Abell1132	18.7	20.5	0.85			
Abell795	18.7	20.5	0.87			
A1882	18.7	20.5	0.85			
Abell1068	18.7	20.5	0.85	3.87	0.12	
Abell1413	18.8	20.6	0.86	7.09	0.25	
ZwCl1023	18.8	20.6	0.89			
Abell990	18.8	20.6	0.87	5.75	0.22	
Abell2409	18.9	20.7	0.87	5.50	0.25	*

Continued on next page...

Table 3.3 continued...

Name	$m^g_{r'}$	$m^d_{r'}$	$(g'-r')_{rs}$	T_x	σ_{T_x}	BAX
A2204	18.9	20.7	0.86	7.41	0.26	
A545	19.0	20.8	0.86	5.50	3.00	*
A2104	19.1	20.9	0.85	9.31	0.47	
A2259	19.1	20.9	0.90	5.32	0.27	
A1234	19.1	20.9	0.87			
A1914	19.3	21.0	0.99	9.48	0.45	
A586	19.3	21.0	0.97	6.39	0.60	
A1246	19.5	21.3	0.94	6.04	0.37	
MS0440	19.5	21.3	0.94	5.02	0.50	
A115	19.7	21.4	1.00	6.45	0.31	
A115N	19.7	21.4	0.98	6.45	0.31	
A2163	19.6	21.4	0.88	12.12	0.57	
A2261	19.7	21.5	1.10	6.88	0.41	
A520	19.7	21.4	1.02	7.81	0.64	
A223a	19.8	21.5	1.01	5.12	0.66	
A223b	19.8	21.5	1.03	5.12	0.66	
A1942	19.9	21.6	1.05	5.12	0.56	
A2111	20.0	21.8	1.07	8.02	0.77	
A2125	20.3	22.1	1.36	2.60	0.10	*
A1835	20.2	22.0	1.17	7.65	0.31	
A521	20.2	21.9	1.14	6.74	0.45	
CL1938	20.4	22.1	1.22	7.52	0.37	
A1758b	20.5	22.2	1.23	7.95	0.62	
A697	20.5	22.2	1.28	9.14	0.54	
A611	20.6	22.3	1.24	6.69	0.44	
A959	20.5	22.3	1.19	6.26	0.71	
A2537	20.7	22.5	1.32	6.08	0.49	
MS1008	20.7	22.5	1.29	7.47	1.21	
A370	21.4	23.1	1.54	7.20	0.77	
A851	21.6	23.4	1.47	7.21	1.34	
RXJ0856	21.7	23.4	1.47			
RXJ2228	21.6	23.3	1.51	7.90	0.60	*

Continued on next page...

Table 3.3 continued...

Name	$m^g_{r'}$	$m^d_{r'}$	$(g'-r')_{rs}$	T_x	σ_{T_x}	BAX
RXJ1003	21.7	23.5	1.57			
MS1621	21.8	23.5	1.53	6.54	1.02	
CL0910	21.9	23.6	1.51	6.61	0.60	
MACS1206	21.9	23.6	1.50	10.20	1.00	*
RXJ1347	22.0	23.8	1.57	10.88	0.66	
RXJ1701	22.0	23.7	1.54	4.50	1.00	*
3C295	22.0	23.6	1.48	6.51	0.99	
RXJ1524	22.0	23.4	1.39	5.10	0.36	
MS0451	22.7	24.0	1.46	8.62	1.21	

3.4.3 Sensitivity to Analysis Parameters

One of the issues that complicates the comparison of GDR (and dwarf-to-giant ratio) between studies is the varying selection criteria used to define the dwarf and/or giant populations. The K-correction method, the projected cluster-centric distance within which to include galaxies in the dwarf and giant populations as well as the maximum color-residual with respect to the CMR that defines a red sequence member are examples of parameters that often vary between different studies. In this section, we compute the GDR using a range of selection criteria to see how much of the apparent discrepancy can be explained through these choices.

To examine how our results depend on the adopted K-correction described above, we compare the GDRs obtained using two different K-correction methods. The results are plotted in Figure 3.8. The first K-correction method (K0) is the one outlined above using the CB07 models and assumes solar metallicity and a template age that is determined by matching the observed $(g'-r')$ color. The next method (K2) uses the K-correction code of Chilingarian, Melchior and Zolotukhin (2010) which has been shown to agree with the empirically derived corrections of Blanton & Roweis (2007) up to z=0.5. We also show the results of neglecting the K-correction completely (no K).

The differences in GDR between one K-correction method and another are typically smaller than the GDR error in an individual redshift bin. Moreover, the selection

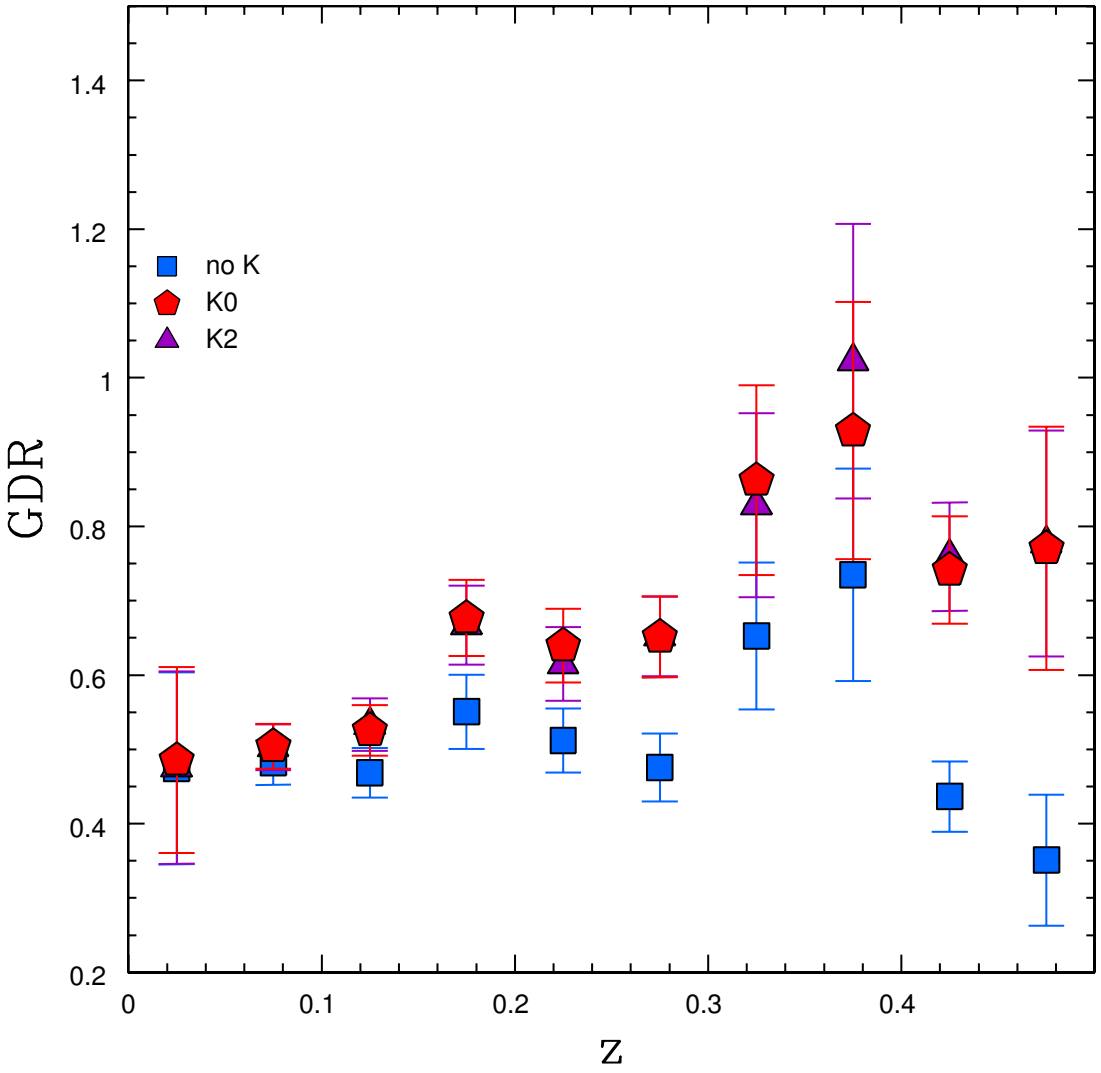

Figure 3.8: The giant-to-dwarf ratio using various methods of K-correction. The different symbols correspond to 2 different K-correction methods (see text for details) as well the effect of neglecting the K-correction.

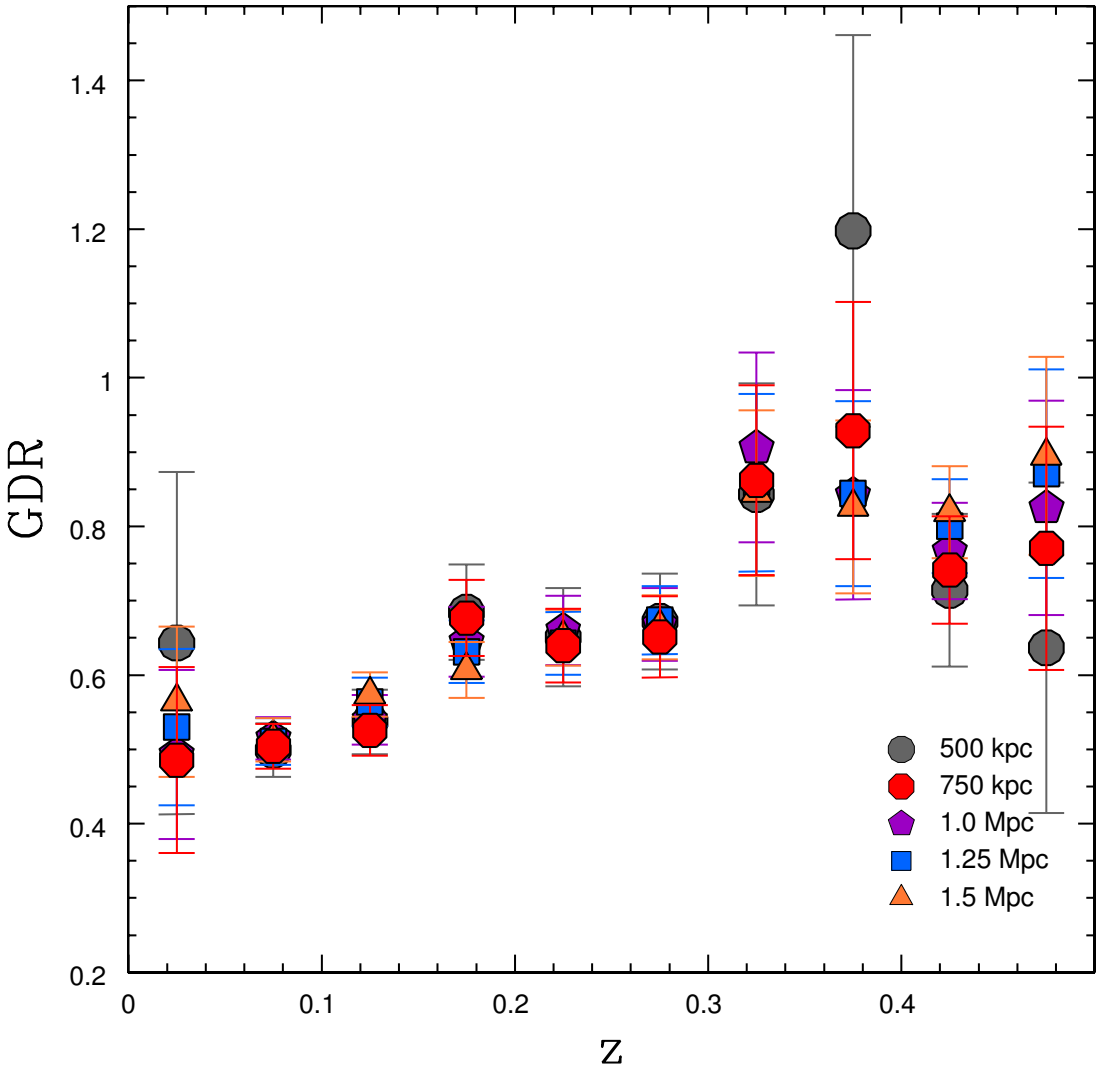

Figure 3.9: The giant-to-dwarf ratio using various apertures sizes for red sequence membership. The different symbols refer to galaxies within r_{lim} in projected distance from the BCG with r_{lim} =500 kpc, 750 kpc, 1000 kpc, 1250 kpc and 1500 kpc.

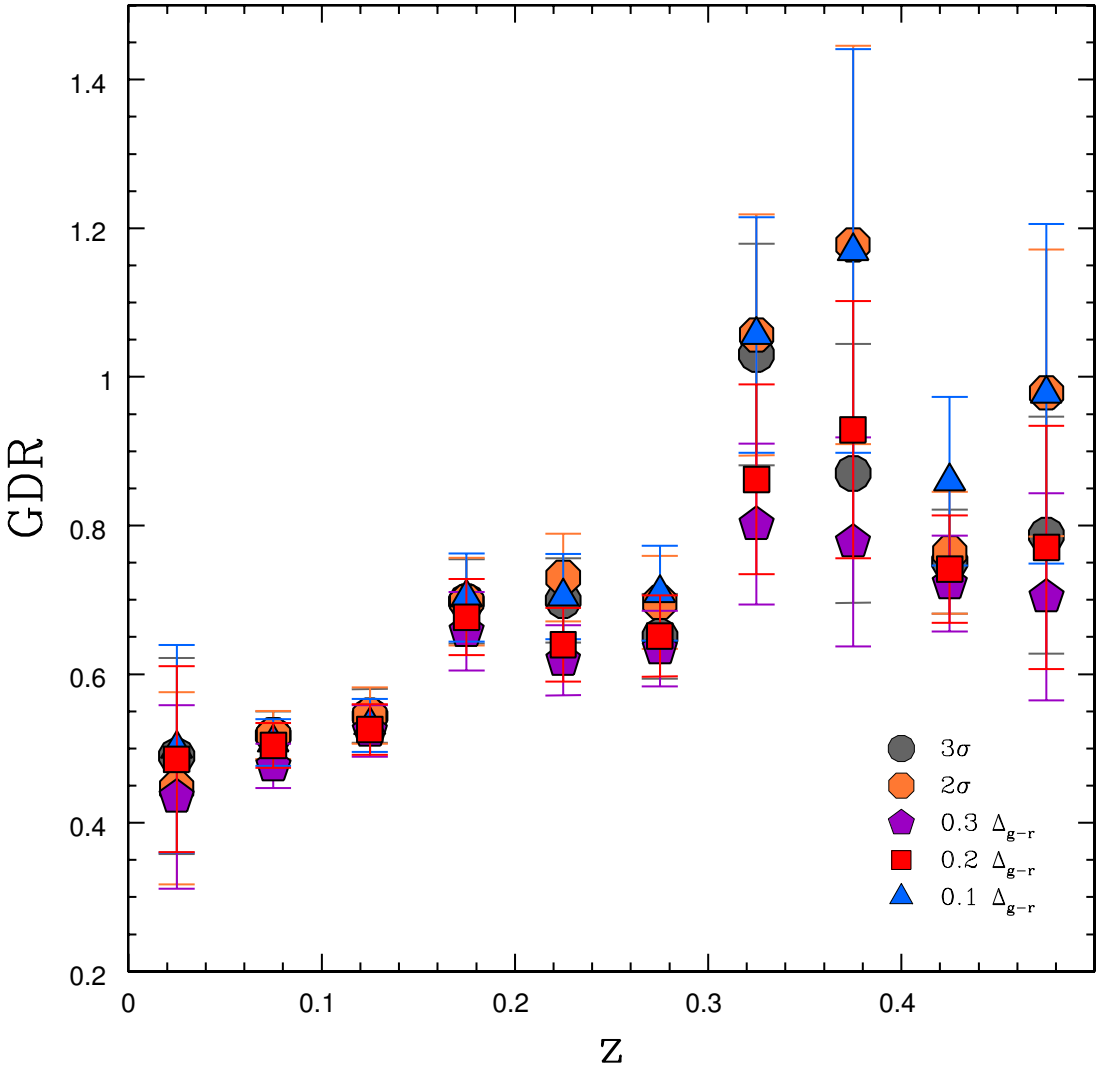

Figure 3.10: The giant-to-dwarf ratio as computed using various color selection criteria. The different symbols show $|\Delta(g'-r')| < 0.1$, $|\Delta(g'-r')| < 0.2$, $|\Delta(g'-r')| < 0.3$, $|\Delta(g'-r')|/\sigma < 2$ and $|\Delta(g'-r')|/\sigma < 3$.

of either K-correction method does not affect the conclusions regarding the presence or absence of a trend with redshift, only how strong this evolution might be. However, neglecting the K-correction would lead to a contradictory view of the redshift evolution in GDR.

Although it is not shown in Figure 3.8, we also test the effect of neglecting the evolution correction (ie. $E = 0$, see §3.3.3). We find that contrary to neglecting the K-correction, this leads to a significant steepening of the GDR vs z relation ($\alpha = 1.61 \pm 0.15$). Therefore, to obtain a flat GDR vs z by varying the E-correction would require E to be parameterized with a significantly stronger redshift dependence than what we have assumed here. Such corrections are unreasonable for the early-type galaxies that make up the red sequence.

Figure 3.9 shows the effect on GDR of varying the aperture size (r_{lim}), centred on the BCG, within which to count red sequence galaxies. The data shown in the figure are for galaxies within a projected radius of 500 kpc, 750 kpc, 1000 kpc, 1250 kpc and 1500 kpc. The variation in the results, most notable in the lowest redshift bin, is all within the error in each individual bin. This shows that the GDR is insensitive to aperture choice on these scales (up to a factor of 3 in BCG-centric distance). Choosing instead a scaled radius (eg. r_{500}) to measure GDR would yield similar results. Using $r_{500} = 2.48(T_x/10 \text{ keV})^{1/2}$ (Evrard et al. 1996) and the T_x data shown in table 3.3, we calculate that the mean value of r_{500} changes by at most a factor of 1.33 when comparing any pair of redshift bins. Since this is well within the factor of 3 range in aperture size over which the GDR measurement is robust, we conclude that the use of scaled radii to measure GDR does not alter the conclusions regarding GDR evolution. We also note that the largest apertures show the smallest GDR errors. This is expected since they are based on Poisson statistics and the GDR is a ratio. As the number of galaxies in the population increases, the error as a percentage on that number decreases. We argue, however, that it is better to use a smaller aperture such as $r_{lim} = 750$kpc because the potential for systematic error introduced by the background subtraction procedure, which is not included in the error estimates shown in Figure 3.9, grows as the aperture size increases.

It is also interesting to examine the differences in the GDR between the cluster centre and cluster outskirts. Such a discussion does not fit well in this section however, which is intended to assess the possible variation in GDR introduced by commonly used selection criteria. For a discussion of the GDR in the inner vs outer parts of clusters we refer the reader to §3.6.

We consider the possibility that BCG position may be a poor indicator of the cluster centre as a function of redshift. Depending on the radial profile of the GDR, this effect could potentially mimic GDR evolution. To test this, we measure the GDR in $0.05 < z < 0.15$ clusters using a centre position that is offset between 0 to 6.5 arcminutes from the BCG. This shift corresponds roughly to 750 kpc at $z = 0.1$. The results are consistent with those obtained using the BCG as the cluster centre, indicating that the GDR evolution is unaffected by centreing errors on these angular scales.

We show in Figure 3.10 how varying the color selection criteria affects the measurement of the GDR. Here we compare several cases of two distinct selection criteria. The first requires galaxies to be within $|\Delta(g'-r')| < 0.2$, which is the assumed criteria throughout the rest of this work, but we also show here the results for $|\Delta(g'-r')| < 0.1$ and $|\Delta(g'-r')| < 0.3$. The second selection method that we investigate is based on the observed scatter in $(g'-r')$ of the red sequence (σ), assuming a gaussian distribution about the best fit color-magnitude relation. Figure 3.10 shows the GDR of galaxies that lie within $|\Delta(g'-r')|/\sigma < 3$ and $|\Delta(g'-r')|/\sigma < 2$. The effect of color selection criteria is larger than that introduced by the r_{lim} selection criteria and comparable to the effect of varying the K-correction method. However, the change in GDR is always smaller than the error in an individual redshift bin, which demonstrates that the choice of a particular color criterion does not affect conclusions about the presence of evolution.

3.4.4 Comparison with Literature

The disagreements in the literature regarding the evolution of the GDR/DGR are primarily driven by the interpretation of various results and not necessarily by disagreements among the data themselves. In a study based on DGR data culled from the available literature, Gilbank and Balogh (2008) show that if one neglects the $z > 1$ clusters of Andreon (2008), where the filters do not bracket the 4000 angstrom break, DGR vs z data is fit reasonably well by a single power law in $(1+z)$. Andreon (2008) puts forth an important caution that one must be careful to account for the presence of an intrinsic scatter in DGR from one cluster to another so as not to be biased by outliers. Andreon (2008) reports an intrinsic scatter $\sigma_{int} = 0.13 \pm 0.06$, arguing that this is enough to reject trends as steep $\alpha \sim 1.3$ found in de Lucia et al. (2007), where σ_{int} was not taken into account. The author also provides a caveat that the observed

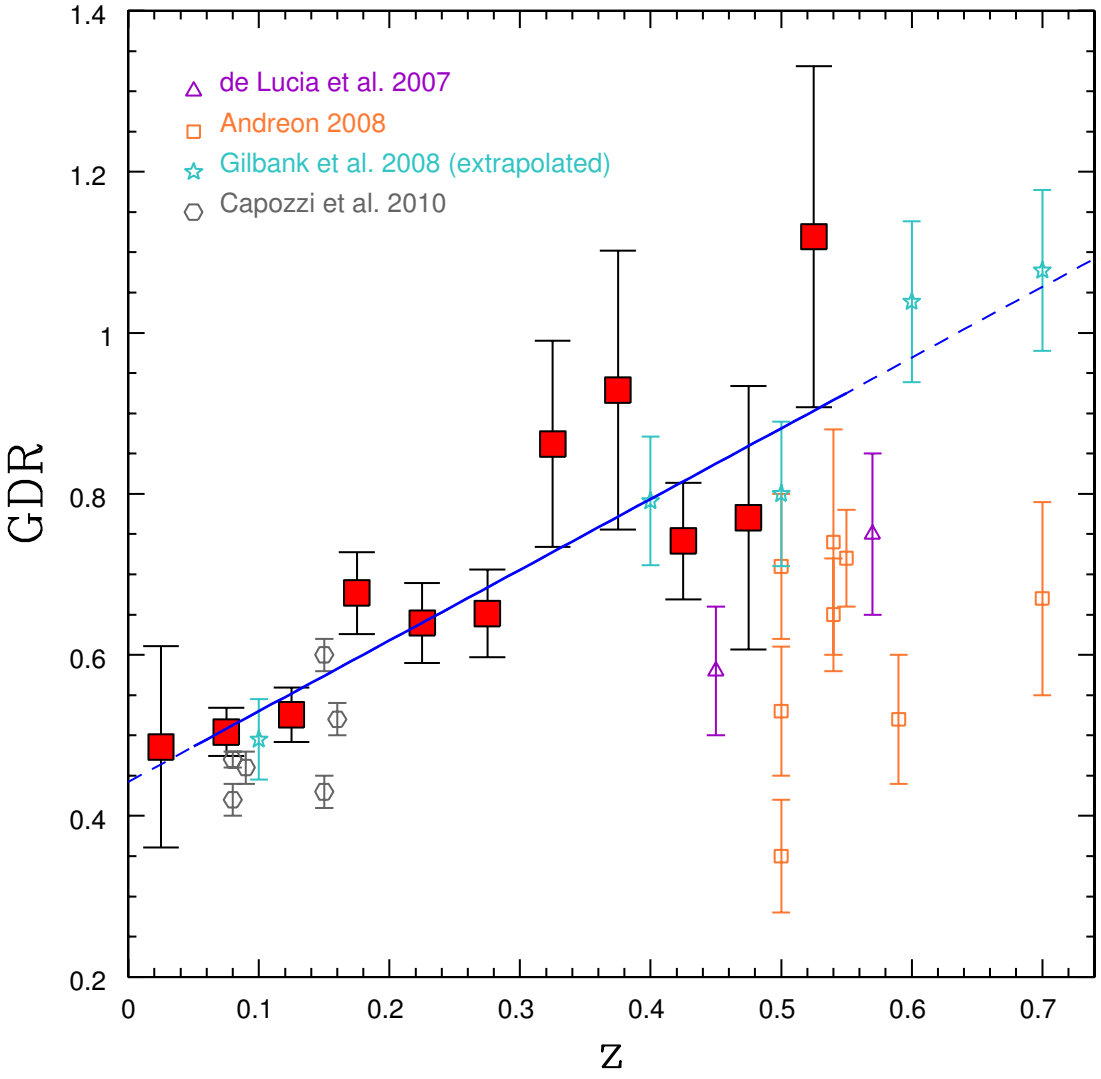

Figure 3.11: The ratio of the number density of giant galaxies to that of dwarf galaxies as a function of redshift. The data has been binned in redshift bins of $\Delta z = 0.05$ (red squares). We also show various data from the literature. Note that the Gilbank et al. (2008) values have been adjusted to be comparable directly with ours (see text for description).

spiral morphologies of some nearby red sequence galaxies (eg. Butcher & Oemler 1984) indicate recent star formation, color transformation and red sequence buildup. However, the associated GDR evolution, if any, is not steep enough to be detected in small samples of ~ 25 clusters. To contribute to this discussion we compare these result with our own for ~ 100 clusters.

As discussed in §3.4.2 we find $\alpha = 0.88 \pm 0.15$, $\beta = 0.44 \pm 0.03$ and σ_{int} consistent with zero. If the large scale structure term is neglected in the GDR uncertainty we obtain a $\sigma_{int} = 0.088 \pm 0.017$ which is consistent with the value inferred by Andreon (2008). Our best fit slope is significant, though not as steep as that found in de Lucia et al. (2007). Figure 3.11 shows how our results compare with those from the literature. The large square symbols indicate the error-weighted mean GDR for our sample in several redshift bins. The solid blue line shows our best fit linear relation described above. Data taken from the literature are overplotted. The Gilbank et al. (2008) results are based on slightly different magnitude limits for defining dwarfs and giants than those used here. To make a fairer comparison we compute the GDR by applying their magnitude cuts to our data, then calculate a correction based on the difference between the best fit α and β from those obtained using our default cuts. We apply this correction to the Gilbank et al. (2008) values and plot the 'extrapolated' values in Figure 3.11. There is very good agreement between our results and the 'extrapolated' values of Gilbank et al. (2008) despite the difference in redshift range and cluster masses probed. Our GDR values are also in agreement with the low redshift GDR results of Capozzi et al. (2010), which are based on SDSS cluster catalogs and the de Lucia et al. (2007) magnitude limits. When compared directly to the de Lucia et al. (2007) results our data do not seem to agree. However, there is an important difference between the two analyses. The magnitudes used in this chapter are taken from SExtractor's MAG_AUTO parameter, which attempts to follow the shape of the galaxy surface brightness profiles. The de Lucia et al. (2007) magnitudes are extracted using apertures of 1.0", significantly smaller than the sizes within which our magnitudes are calculated. Using a 1.0" fixed aperture truncates the galaxies at smaller radii, effectively reducing their fluxes. This imparts a stronger bias against the giants than dwarfs, since the former are intrinsically more extended on the sky leading to a reduction in the value of the GDR and a steepening of the GDR vs z relation. We are not able to fully reproduce an analogous GDR measurement to that of de Lucia et al. (2007) because of the different angular resolution scales of CFHT and HST. As an instructional exercise we remeasure our GDR values using a 3.0" aperture size

for galaxy magnitudes, which is more suitable given the spatial resolution of CFHT. We verify that this leads to a significant reduction in the GDR values compared to our default extraction method. The resulting best fit to the fixed-aperture GDR vs z relation has a slope $\alpha = 1.90$, which represents a steepening of $\Delta\alpha \sim 1$. We also note that because this effect operates more noticeably at lower redshifts as the angular sizes of galaxies grow and the truncation becomes more extreme, it may provide an explanation for the very steep redshift trend seen by de Lucia et al. (2007).

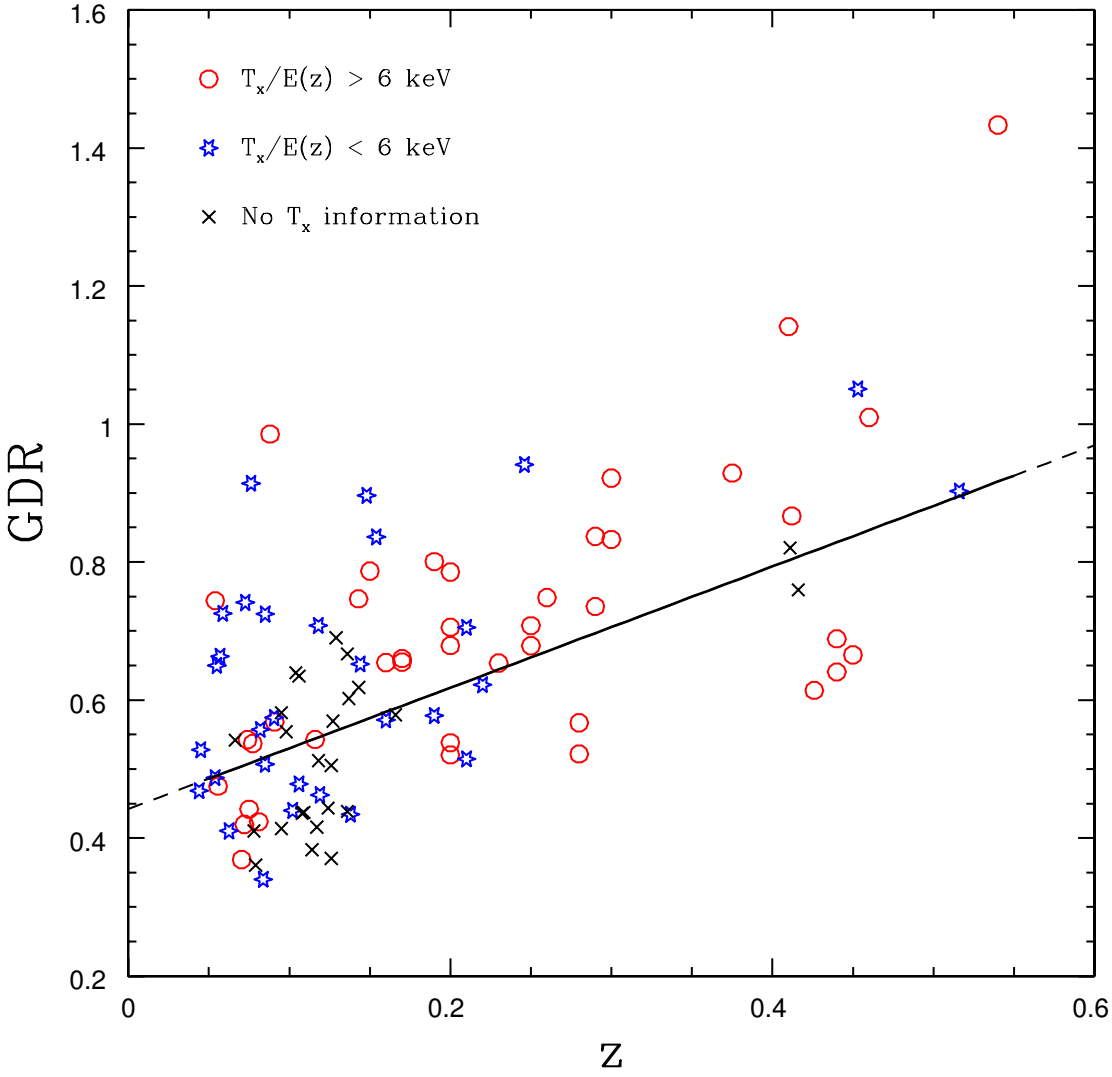

Figure 3.12: GDR versus z with clusters coded by X-ray temperature information. The solid black line shows the best fit linear relation found in §3.4.2. The GDR evolution can be represented by a single function of redshift regardless of $T_x/E(z)$ for the full range of temperature and redshift probed by our sample.

3.5 Dependence on Cluster Mass

As we discuss in the previous section, the GDR data can be modelled by a linear trend with z. After accounting for large-scale structure in the background, we find no intrinsic scatter. This is qualitatively consistent with the results of Lu et al. (2009) who find that the large-scale structure uncertainty comprises a significant portion of the uncertainty in DGR for individual clusters. This result is consistent with a GDR that is a function of redshift only and is independent of any other global cluster properties, at least over the range of redshift and cluster mass investigated here. Several authors in the literature, however, have presented evidence for a dependance of GDR on global properties related to cluster mass. For instance, de Lucia et al. (2007) find a higher GDR in their $\sigma > 600$ km/s sample than that in their $\sigma < 600$ km/s sample, with a difference in GDR of about 0.1 to 0.2. They also analyze data from the SDSS for clusters at $z \sim 0$ and find that this σ dependence is reversed. Gilbank et al. (2008) find an elevated and flatter GDR for poorer clusters. Capozzi et al. (2010) argue that there may be a weak correlation between the GDR and cluster X-ray luminosity. Furthermore, as the GDR is different in the field (Gilbank & Balogh 2008), some mass dependence might be expected. Because our cluster sample is not a representative sample, it may be that some portion of the observed GDR evolution arises as a consequence of potential covariance between redshift and cluster mass (more high mass systems at high z). However, given the good agreement between our GDR results and those based on cluster samples with lower mean mass (eg. Gilbank et al. 2008 and Capozzi et al. 2010) we do not expect this to be the case. Nonetheless, in this section we investigate this possibility in more detail.

Many of the previous results that indicate a dependence on cluster mass are based on using cluster richness as a mass proxy. One problem with using richness is that there is a large scatter in the mass-richness relation of up to $\pm 150\%$ in mass at a given richness (Rozo et al. 2009). Moreover, the richness, which is approximately the number of dwarfs plus giants ($n_d + n_g$) and the GDR (n_g/n_d) are by construction naturally covariant. A better proxy for cluster mass is the X-ray temperature of the hot intra-cluster medium (T_x), which predicts the mass with significantly lower scatter (36% in mass at a fixed T_x inside r_{500}) and is independent of galaxy counting.

A subset of the clusters in our sample have been observed with the Advanced Satellite for Cosmology and Astrophysics (ASCA) and analyzed by Horner (2001). For maximum consistency we take T_x values from the Horner (2001) catalog for as

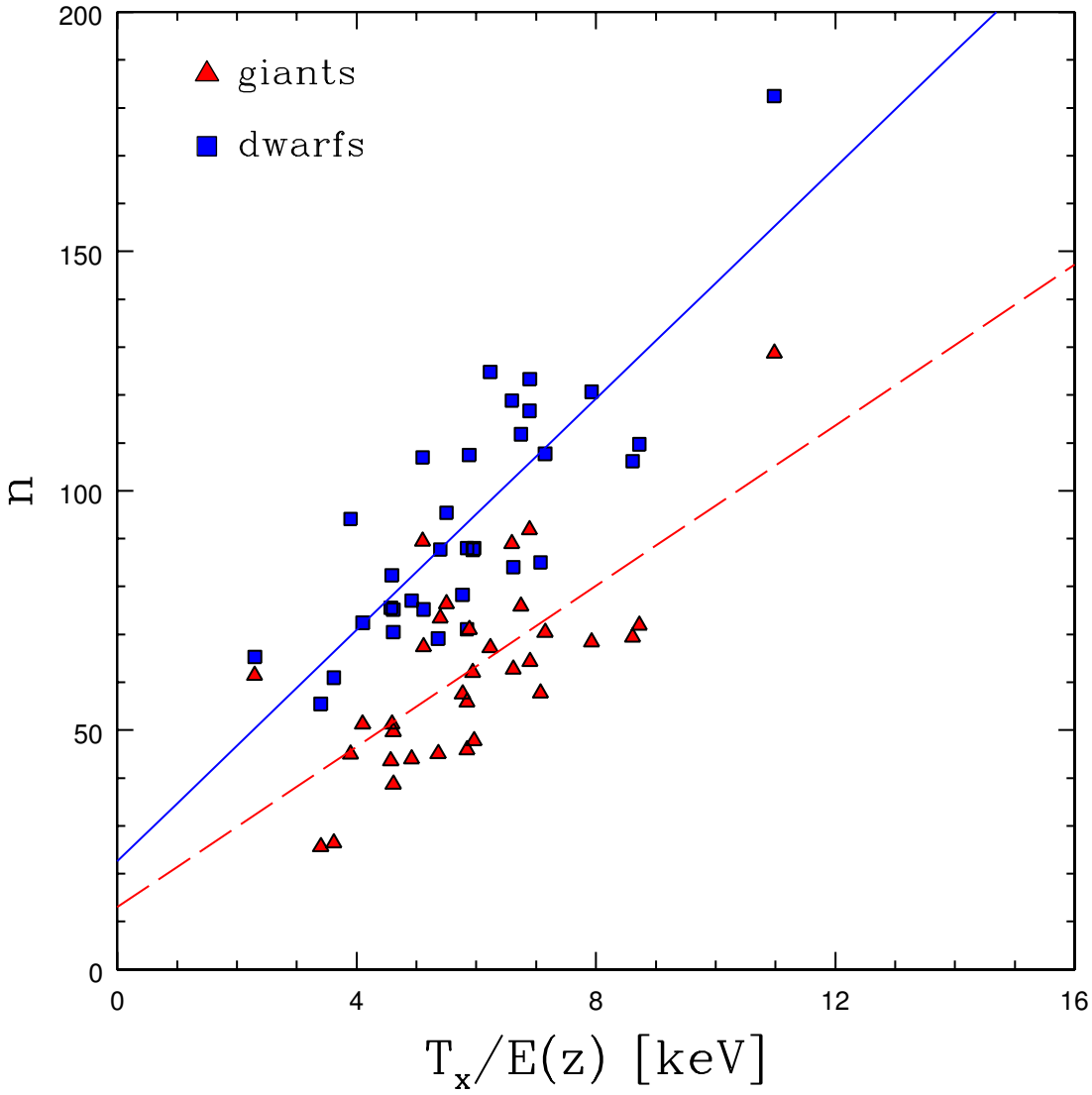

Figure 3.13: The number of giants (red triangles) and dwarfs (blue squares) as a function of cluster $T_x/E(z)$ for clusters in the range $0.1 < z < 0.3$. Solid and dashed lines correspond to the best fit relations for dwarfs and giants respectively.

many of our clusters as possible (59 systems). We supplement this with an additional 15 T_x measurements from the BAX X-ray galaxy cluster database[4] giving us a total of 72. A complete listing of the T_x data is given in Table 3.3. In the analysis that follows, we scale the T_x values by $E(z) = \sqrt{\Omega_m(1+z)^3 + \Lambda}$ to account for evolution in the cosmic background density. We make no attempt to adjust the X-ray data for the presence of cool-cores or cluster-cluster mergers.

To investigate the effect of $T_x/E(z)$ on GDR evolution we show in Figure 3.12 the plot of GDR vs z after separating the data into 3 different $T_x/E(z)$ categories. The data points in Figure 3.12 coded by $T_x/E(z) > 6keV$ (red circles), $T_x/E(z) < 6keV$ (blue snowflakes) and no T_x information (black crosses). Error bars have been omitted for clarity but are listed in Table 3.3. Figure 3.12 shows that indeed there are more high $T_x/E(z)$ systems at the high z end of our sample and conversely more low $T_x/E(z)$ systems at the low z end. Despite this selection effect however, the data in each $T_x/E(z)$ category are consistent with the same best fit GDR vs z relation found in section 3.4.2. Specifically, we find that the best fit parameters are ($\alpha = 0.92 \pm 0.26$, $\beta = 0.49 \pm 0.06$) for the high $T_x/E(z)$ clusters, ($\alpha = 0.90 \pm 0.34$, $\beta = 0.51 \pm 0.05$) for the low $T_x/E(z)$ clusters and ($\alpha = 0.98 \pm 0.28$, $\beta = 0.40 \pm 0.04$) for the clusters with no T_x information. This consistency is compatible with a GDR, and GDR evolution that do not depend on cluster mass over the range of mass and redshift probed by our sample.

A subset of 27 clusters in our sample are part of a more detailed campaign to measure the masses using a combined X-ray + weak lensing method. We compare the GDR directly to the weak-lensing masses (taken from Hoekstra et al. 2012) but find no evidence for a correlation. This is consistent with the result obtained using $T_x/E(z)$ as a mass proxy. From the X-ray portion of the analysis we obtain central entropy values (S_0) for the subset (taken from Mahdavi et al. 2013). The value of S_0 is often used to discriminate between cool-core and non-cool-core clusters, so it is interesting to examine if/how the GDR varies with S_0. We find no correlation between these two parameters, however, indicating that the GDR is similar between cool-core and non-cool-core clusters. Lastly, we consider the GDR as a function of the projected distance between the BCG and the peak of the cluster X-ray emission, an indicator of the dynamical state of the cluster. Using values from Bildfell et al. (2008) we find no evidence for a correlation between GDR and BCG to X-ray peak distance. These results are all consistent with, and expected for a GDR vs z relation

[4]http://bax.ast.obs-mip.fr/

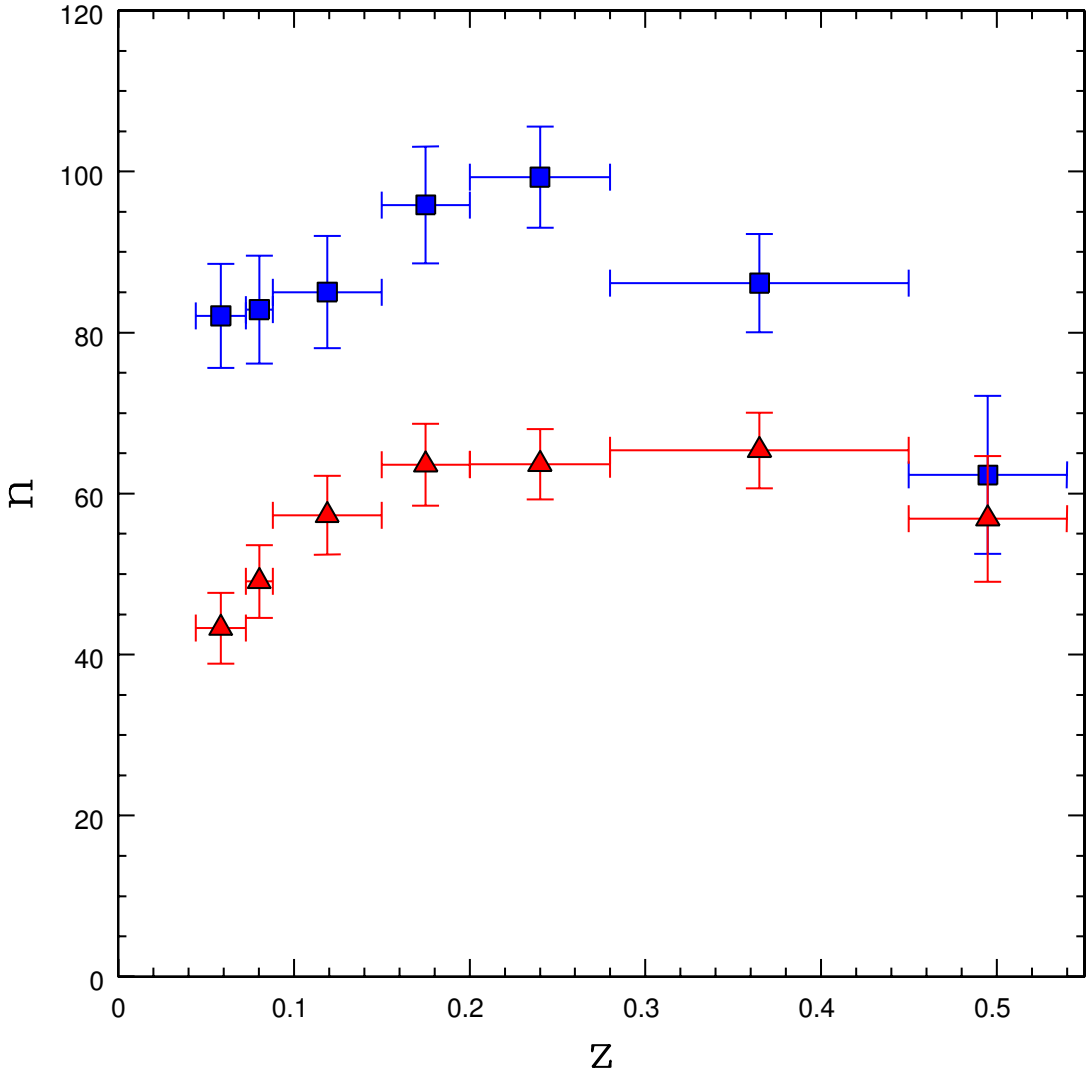

Figure 3.14: The evolution of the number of dwarfs (blue squares) and giants (red triangles) within a projected radius $r < 750$ kpc (default region). The statistics have been corrected for the correlation between mass and richness by scaling to a common cluster temperature $T_x/E(z) = 6$ keV. Vertical error bars show the uncertainty on the error-weighted bin centroid and horizontal error bars indicate the width of the bins.

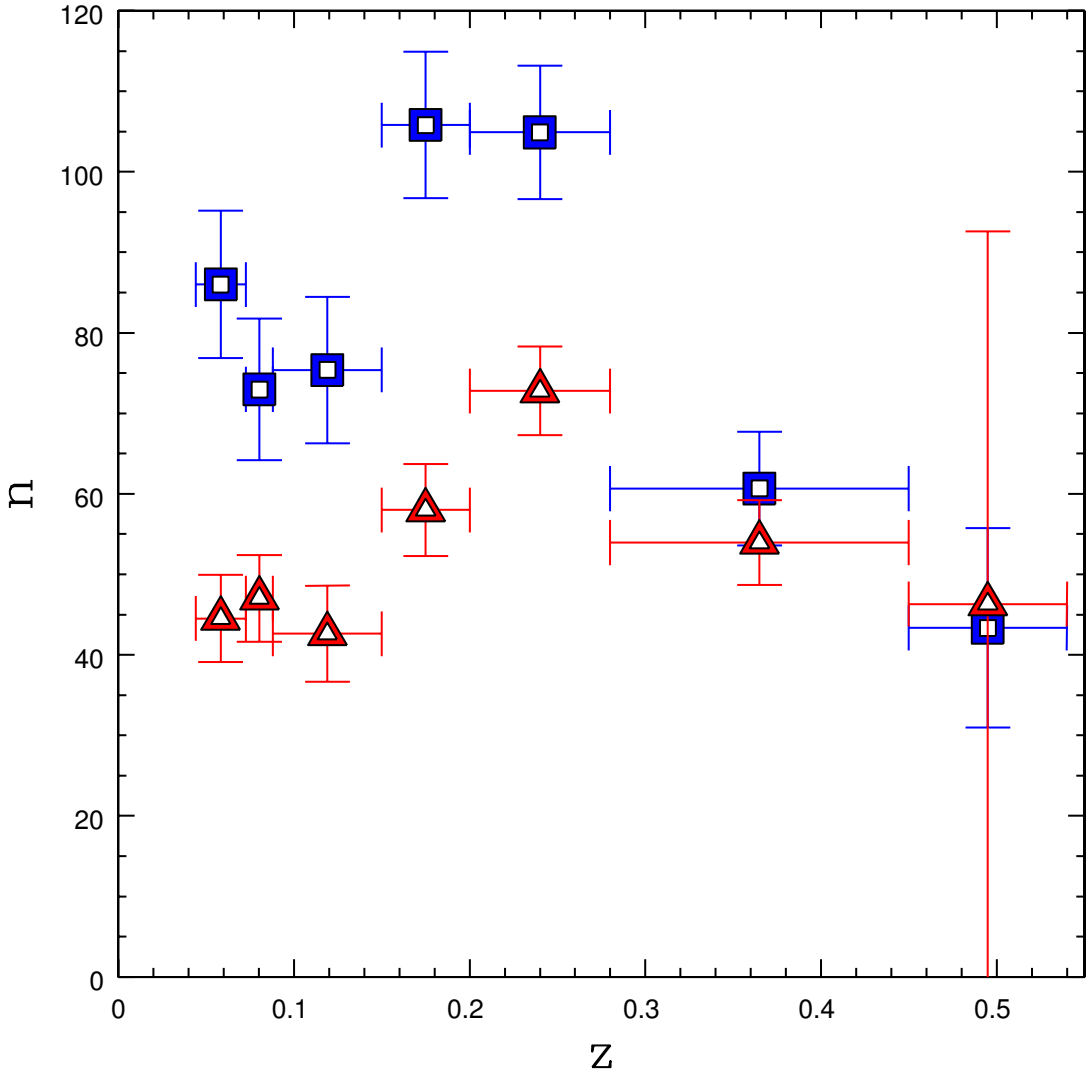

Figure 3.15: The evolution of the number of dwarfs (blue squares) and giants (red triangles) in a region 750 kpc $< r <$ 1500 kpc. The statistics have been corrected for the correlation between mass and richness by scaling to a common cluster temperature $T_x/E(z) = 6$ keV. Vertical error bars show the uncertainty on the error-weighted bin centroid and horizontal error bars indicate the width of the bins.

that shows no intrinsic scatter.

3.6 Driver of Evolution

The physical mechanism(s) responsible for the evolution in the GDR for $0.05 < z < 0.55$ is not evident. The two main processes affecting red sequence galaxies often discussed in the literature are dry mergers, which reduces the number of galaxies on the red sequence and late-time quenching of star formation, which increases the number of galaxies on the red sequence. Both of these mechanisms are taking place in and around clusters but the extent to which they operate and how their behavior may change with redshift remains elusive. Bell et al. (2004) and Faber et al. (2007) argue that both quenching and dry merging are required to explain observations of the red sequence buildup since $z \sim 1$. Observational evidence for dry mergers of early type galaxies at $0 < z < 0.8$ is presented in van Dokkum (2005) and Tran et al. (2005). On the other hand, work by Cimatti et al. (2006) and Scarlata et al. (2007) argue that the buildup of the red sequence since $z \sim 0.7$ and $z \sim 1$, respectively, can be explained by the late-time quenching of star formation alone. With the exception of Tran et al. (2005) however, these studies are based on samples containing galaxies in the field and not exclusively on cluster galaxies where the high-density local environment may be important. To investigate this further, we examine the evolution of the dwarf and giant populations separately.

We showed in §3.5 that the GDR is not strongly dependent on cluster mass (or T_x/E(z)). When considered independently however, n_g and n_d are both expected to scale with cluster mass; similar to the known scaling between richness and T_x (Yee & Ellingson 2003). Such a scaling is implied by the existence of a mass-richness relation. This effect must be accounted for before we examine the evolution of the dwarf and giant populations separately. We show in Figure 3.13 the dependence of galaxy number n_g and n_d on $T_x/E(z)$. The data are fit using a linear relation between number density and $T_x/E(z)$. To minimize the effect of the correlation between $T_x/E(z)$ and z imposed by our sample selection, we only fit clusters in the range $0.1 < z < 0.3$. We find a best fit slope $\alpha_g = 8.4$ keV^{-1} for the giants and $\alpha_d = 12.1$ keV^{-1} for the dwarfs. Based on this temperature dependence we correct all n_g and n_d values to a common $T_x/E(z) = 6$ keV.

We plot the corrected values as a function of redshift in Figure 3.14. The data are combined using a constant number of clusters in each bin (horizontal error bars indicate bin limits). Both the number of dwarfs and the number of giants increase from $z \sim 0.55$ up to $z \sim 0.3$, with the dwarfs showing the more dramatic evolution.

From $z \sim 0.3$ to $z \sim 0.2$ the numbers of dwarfs and giants remain relatively constant. Below $z \sim 0.2$ the number of dwarfs remains constant but the number of giants begins to decrease significantly. The results suggest that the GDR evolution at $z < 0.2$ is dominated by mergers between giant galaxies. When considered with GDR results at higher redshift, the data support a transition in the dominant mechanism governing GDR evolution, which is often attributed to quenching in dwarfs. This interpretation could also explain the findings of Lu et al. (2009), who measure a rapid DGR evolution at $0 < z < 0.2$ and then a flattening of the relation out to $z \sim 0.4$. Though not discussed in their work, Figure 19 of Lu et al. (2009) clearly shows a reduction in the number of giants from $z \sim 0.2$ to $z \sim 0.1$.

Given the evidence supporting merger-driven evolution at low redshift, it is natural to ask whether this result is compatible with theoretical predictions. The orbit of a galaxy about the cluster centre will decay with time due to dynamical friction. The relevant timescale for the orbital decay of an individual galaxy can be expressed as:

$$\begin{aligned} t_{dyn} &\approx 6 \times 10^9 \mathrm{yr} \left(\frac{\sigma_r}{1000 \mathrm{km/s}}\right) \left(\frac{r_c}{0.25 \mathrm{Mpc}}\right)^2 \\ &\quad \times \left(\frac{m}{m^*}\right)^{-1} \left[\frac{(M/L_V)_{gal}}{10 M_\odot / L_\odot}\right]^{-1} \end{aligned} \tag{3.5}$$

with line-of-sight velocity dispersion σ_r, cluster core radius r_c, galaxy mass m and the galaxy's V-band mass-to-light ratio (M/L_V). For a giant galaxy with $m = m^*$ and a $M/L_V = 10 M_\odot/L_\odot$ orbiting near the centre of a cluster where $\sigma_r \sim 600$ km/s and $r_c = 0.25$ Mpc the expected timescale is $t_{dyn} \approx 3.6$ Gyr. Over the redshift range of our data ($0.05 < z < 0.55$) the total change in cosmic time is $\Delta t_{age} = 4.7$ Gyr, which we use as an estimate of the elapsed interaction time. This is considered to be a conservative estimate because these clusters are likely assembled at much earlier epochs. Since $t_{dyn} < \Delta t_{age}$ we should indeed expect to see the signature of the most massive galaxies merging together on these timescales. This prediction is in good qualitative agreement with the decrease in the number of giants galaxies at low redshift in Figure 3.14. Furthermore, quenching is expected to become less important at late times due to the declining specific star formation rate (at fixed galaxy mass) in newly accreted field galaxies (eg. Juneau et al. 2005).

If the GDR evolution seen at low redshift is driven by orbital decay and mergers in the giant population then we might expect to see less of this effect taking place in the

cluster outskirts, where the density of the ambient medium is lower. To test this we plot in Figure 3.15 the number of giants and dwarfs (adjusted to $T_x/E(z) = 6$ keV) in an annulus with the range of projected radii 750 kpc $< r <$ 1500 kpc. The number of giants rises from $z \sim 0.5$ and peaks near $z \sim 0.25$ declining and flattening below $z < 0.15$. The number of dwarfs generally increases from $z \sim 0.5$ to $z \sim 0.05$ but the distribution is somewhat noisier than similar data at smaller projected cluster-centric distance (Figure 3.14). The triggering of star formation as galaxies fall into the cluster, pre-processing of galaxies in groups, and the increased contamination by interloper galaxies may all affect the number counts in the cluster outskirts and complicate their interpretation considerably.

It is difficult to explain all of the features of Figures 3.14 and 3.15 in the context of mergers and quenching alone. The rate of newly infalling cluster galaxies, as it depends on redshift and galaxy mass, is also likely to be a key ingredient. The merger tree models of de Lucia et al. (2011) indicate that up to $\sim 50\%$ of the massive galaxies ($\log M_*/M_\odot > 10$) that fall into clusters do so after $z = 1$. Taking this into consideration, it may be more appropriate to describe the GDR evolution at low redshift as competition between the galaxy infall rate and the effects of dynamical friction, with quenching as a secondary effect.

For a final check we compare in Figure 3.16 the GDR evolution in the cluster outskirts (750 kpc $< r <$ 1500 kpc) with that in the cluster centre ($r <$ 750 kpc). We note however, that the data are slightly incomplete at the lowest redshifts where the field of view of MegaCam extends only to 1490 kpc from the BCG (see §3.2). The results indicate that the GDR evolution, as measured in the cluster interior and outskirts, are in good agreement with each other. This suggests that the physical mechanism(s) responsible for driving the GDR evolution operate both at large and small cluster-centric distance. This may simply reflect the fact that clusters are assembled from groups and that infalling galaxies are likely to have already undergone some processing in high-density environments.

3.6.1 Integrated Stellar Masses

To test the interpretation of a merger-driven GDR evolution at $z < 0.2$, we measure the integrated stellar mass of giants (M_*^g) and dwarfs (M_*^d), separately, as a function of z. We rearrange equation 3.1 to obtain $(K+E)$-corrected $M_{r'}$ values for individual galaxies which are then converted to r'-band luminosities L_r assuming an r'-band

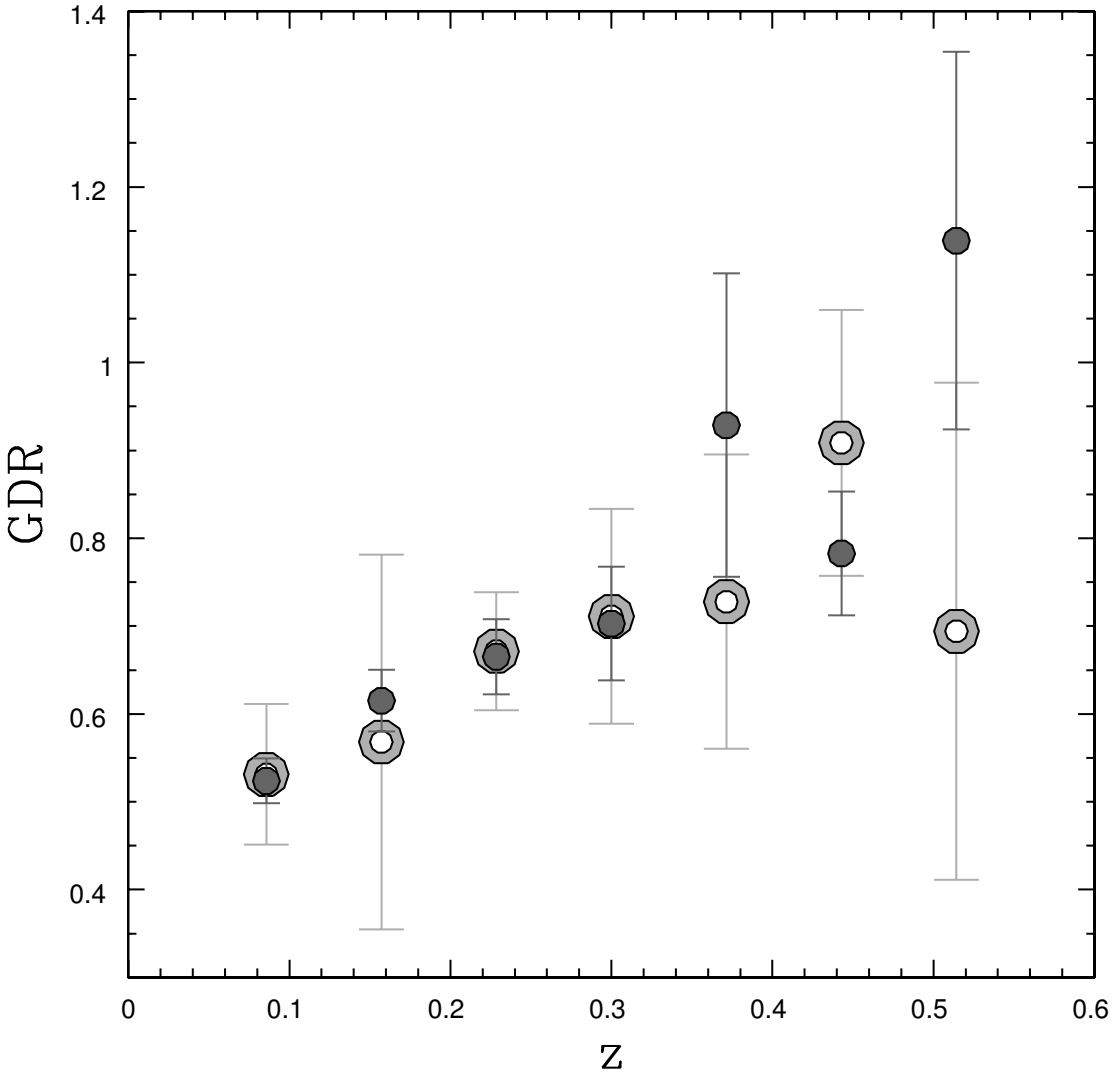

Figure 3.16: The evolution of the GDR in two distinct regions of projected-radius. Filled symbols represent the GDR inside a projected radius limit $r < 750$ kpc (default region), while open symbols represent the GDR in the range 750 kpc $< r <$ 1500 kpc.

absolute magnitude for the sun $M_{r,\odot} = 4.65$ [5]. The luminosities of interloper galaxies are calculated in a similar way using the CFHTLS Deep background populations described in §3.4.1. The integrated dwarf or giant luminosity is obtained for each cluster by summing L_r values for a given population and then subtracting the appropriate background. We also apply the color error correction described in §3.4.1. To convert the luminosity to a stellar mass we assume a universal stellar mass-to-light ratio in the r'-band of $M/L_r = 1.48$, which is obtained from the scaling relation of Zibetti et al. (2009) for elliptical galaxies with $(g-r) = 0.61$. We note however, that the exact normalization is unimportant for our purpose, as we are primarily interested in the relative change in stellar mass.

To make a fairer comparison of the masses, we fit the $\log M_*$ versus $T_x/E(z)$ relation (for $0.1 < z < 0.3$) and correct to a common cluster temperature of $T_x/E(z) = 6$ keV. This procedure is analogous to that in §3.6 regarding the number densities. We show in Figure 3.17 the $T_x/E(z)$-corrected values of M_*^g and M_*^d as a function of redshift. The data reveal that the mean stellar mass in dwarf galaxies ($\langle M_*^d \rangle$) increases from $z \sim 0.55$ to $z \sim 0.25$ and remains roughly constant for $z < 0.25$. In contrast, the mean stellar mass in giants ($\langle M_*^g \rangle$) is roughly constant from $z \sim 0.55$ to $z \sim 0.2$ and then declines at $z < 0.2$.

In §3.6 we propose that the decrease in the number of giants at $z < 0.2$ can be explained by a significant number of giant-giant mergers (merger scenario). If this is the case then one might expect $\langle M_*^g \rangle$ to remain constant over this redshift range. However, there are several reasons why mergers may act to deplete the integrated stellar mass. Tidal features created in mergers are believed to contribute to the production of intra-cluster stars (ICS), which are not gravitationally bound to any particular galaxy and make up $\sim 10\% - 30\%$ of the stellar mass in clusters (Gal-Yam et al. 2003; Gonzalez et al. 2005; Zibetti et al. 2005; Krick & Berstein 2007, Sand et al. 2011). Furthermore, the existence of a tight relationship between effective radius and mean effective surface brightness (Kormendy 1977) implies that as elliptical galaxies grow, they become increasingly diffuse. Consequently, the fraction of a galaxy's stellar mass that is below our detection threshold may be a function of the number of mergers that galaxy has undergone.

We see from Figure 3.14 that there is a $30 \pm 13\%$ reduction in the number density of giants from $z \sim 0.2$ to $z \sim 0.05$. The corresponding reduction in $\langle M_*^g \rangle$ over this period is $38 \pm 14\%$. Assuming the merger scenario is correct, a sizeable fraction of

[5] http://mips.as.arizona.edu/ cnaw/sun.html

the stellar mass involved in a giant-giant mergers, up to 100% in some cases, must be shifted to the ICS or drop below our detection threshold. As a caveat to these statistics, Gonzalez et al. (2007) finds that the ICS fraction scales inversely with the velocity dispersion of the cluster. If ICS production is much more efficient in the lowest mass clusters then this effect may be exacerbating the observed drop in $\langle M_*^g \rangle$ at $z < 0.2$, where our sample is dominated by clusters with low T_x. To test this we repeat our measurement using only those clusters with $T_x/E(z) > 6$ keV. With this selection, the drop in $\langle M_*^g \rangle$ at $z < 0.2$ is less pronounced and $\langle M_*^g \rangle$ is consistent with a constant value over all z. These results are suggestive but their interpretation is limited by the large standard deviation within each bin.

Because of the above mentioned considerations we are unable to confirm/deny the merger scenario with the integrated stellar masses alone. To make progress requires measurement of the ICS fraction for all of the clusters in our sample and better constraints on the redshift-dependance of the ICS fraction, both of which are outside the scope of the current study.

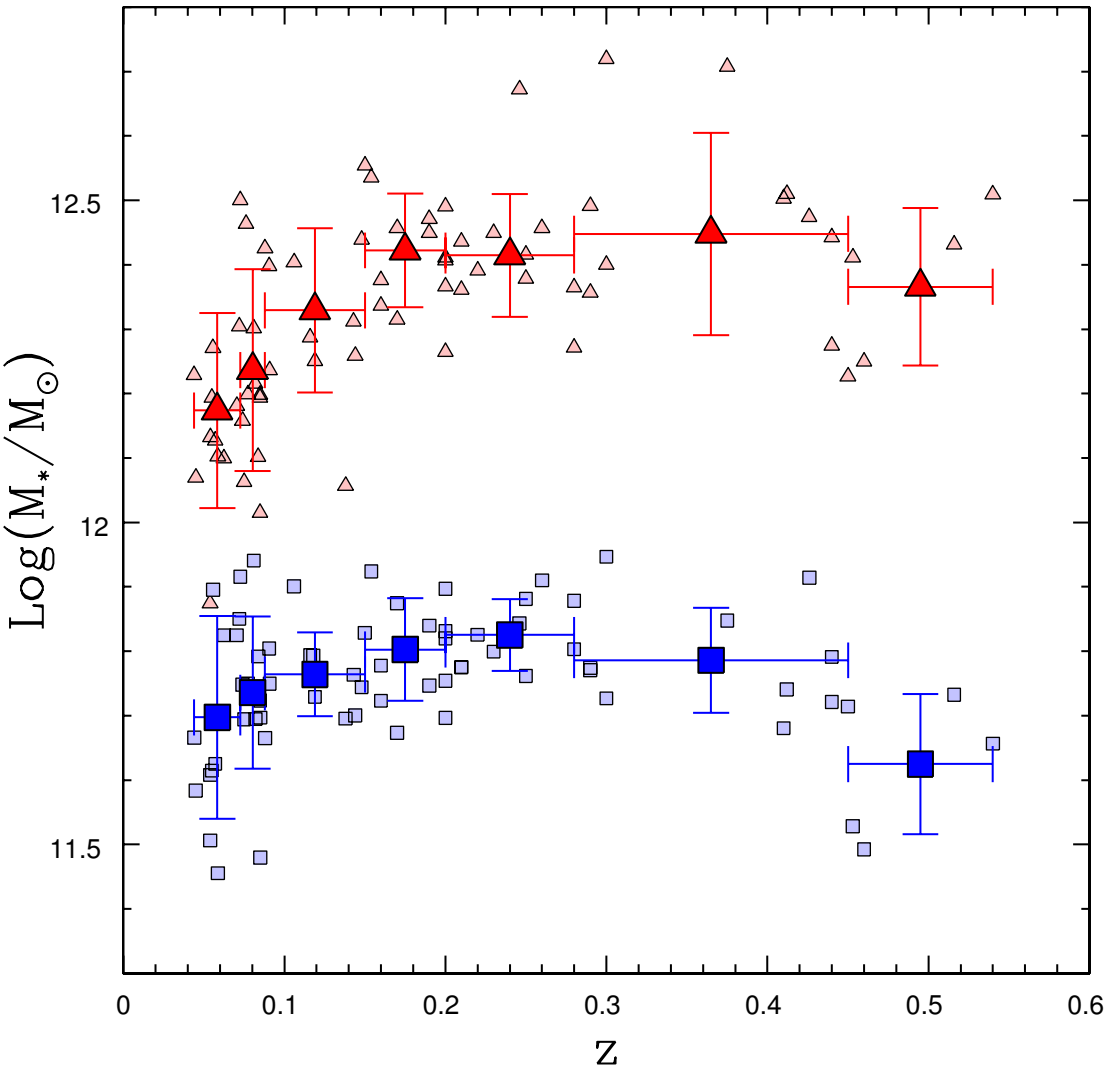

Figure 3.17: Integrated masses of galaxies associated with the dwarf population (blue squares) and giant population (red triangles) as a function of redshift. The data have been scaled to a common cluster Xray temperature $T_x = 6/E(z)$ keV. Individual clusters are shown as smaller, lighter symbols, while binned data is shown as larger, darker symbols. Error bars on binned data indicate the bin width (horizontal) and the standard deviation within the bin (vertical). The mass in dwarf galaxies is roughly constant, while the mass in giants is decreasing below $z < 0.2$.

3.7 Conclusions

We analyzed a large sample of 97 galaxy clusters observed in g' and r' with CFHT-MegaCam. After carefully accounting for several observational biases and statistically removing interloper galaxies using g' and r' galaxy catalogs generated from the CFHTLS Deep fields as a control, we measured the GDR in galaxy clusters over the range $0.05 < z < 0.55$. We find several interesting results, the most important of which we summarize below.

We detect evolution in the GDR over the redshift range $0.05 < z < 0.55$, which can be parametrized by a simple linear relation with z ($GDR = \alpha z + \beta$). The best fit parameters are $\alpha = 0.88 \pm 0.15$ and $\beta = 0.44 \pm 0.03$ with an estimate for the intrinsic scatter in the relation that is consistent with zero. Neglecting the uncertainty introduced by the presence of large-scale structure leads to a perceived intrinsic scatter of $\sigma_{int} = 0.088 \pm 0.017$, which is consistent with previous estimates (Andreon et al. 2008).

Varying the method of selecting dwarf and giant galaxies by altering the BCG-centric distance threshold, color selection criteria or K-correction prescription does not change the GDR significantly. So long as one makes reasonable choices about the selection criteria and K-correction, then varying these parameters cannot hide the signature of an evolving GDR.

The GDR values found here agree well with the those from the literature that are derived directly, solely from measurements of the number of luminous and faint galaxies. However, our GDR results are not in agreement with those that are inferred from parametric fits to the luminosity function (eg. Andreon 2008, Crawford et al. 2009).

The GDR does not correlate with cluster mass estimates via X-ray temperature or weak-lensing. Similarly, we find no evidence for a correlation between GDR and the central entropy of the ICM or the dynamical state of the cluster (BCG to X-ray peak offset). This is further validated by the good agreement between our GDR values and those found in studies based on lower mass clusters (eg. Gilbank et al. 2008, Capozzi et al. 2010). These result agree with our finding that the intrinsic scatter in GDR vs z is consistent with zero. When considered individually however, both the number of dwarfs and the number of giants are strongly correlated with $T_x/E(z)$, which is expected from the known correlation between richness and T_x (Yee & Ellingson 2003).

Separate inspection of the evolving number of dwarfs and giants, after correcting to

a common $T_x/E(z)$, suggests a change in the primary physical mechanism responsible for the evolution in the GDR over the redshift range $0.05 < z < 0.55$. From $z \sim 0.55$ to $z \sim 0.25$ we observe an overall increase in the number of both dwarfs and giants, with a more rapid increase among the dwarfs. Below $z \sim 0.2$ however, the number of dwarfs is roughly constant, while the number of giants decreases significantly. To explain the transition at $z \sim 0.2$, we argue for a significant number of mergers within the giant population, caused by orbital decay due to dynamical friction. This is supported by calculations of the expected orbital decay time for giant galaxies, which yield timescales smaller than the span in look-back time of our sample. In this scenario, the GDR is governed by the competition between mergers, which become dominant at $z < 0.2$, versus the processes that act to increase the relative number of dwarf galaxies on the red sequence, such as the late-time quenching of star formation and the redshift dependence of the accreted-galaxy mass function. We consider the latter to be particularly important given the results of de Lucia et al. (2011) indicating that up to 50% of $\log M_*/M_\odot > 10$ galaxies fall into clusters at $z < 1.0$. A GDR evolution that is driven by a reduction in the number of giants at $z < 0.2$ could also explain why Crawford et al. (2009) find no evolution in the faint-end slope of the luminosity function at low redshift.

To test the merger-driven GDR scenario, we measure the integrated stellar mass in giants and dwarfs as a function of redshift. We find that $\langle M_*^d \rangle$ increases from $z \sim 0.55$ to $z \sim 0.25$ and remains roughly constant for $z < 0.25$, while $\langle M_*^g \rangle$ is roughly constant from $z \sim 0.55$ to $z \sim 0.2$ and then declines at $z < 0.2$. Because of the large scatter present in the values of M_*^g at fixed z and the uncertainty regarding the production of ICS, it is not possible to confirm nor deny the merger scenario with this measurement alone. To make progress requires measurement of the ICS fractions of clusters in our sample and better constraints on the evolution of the ICS.

The results presented in this chapter clearly indicate an evolving GDR in our sample of 97 galaxy clusters at intermediate redshift. We are cautious, however, not to over-interpret the data in light of the fact that the sample is incomplete. Correlation between the GDR and global cluster properties, along with a covariance between said properties and z in our sample, could be misinterpreted as an enhancement of the GDR evolution. The data presented in §3.5, however, along with the good agreement with the literature values over a range of sample selection properties, and an intrinsic scatter that is consistent with zero, all indicate that this effect is negligible. A future study of the GDR using a sample that represents an evolutionary sequence

of clusters (c.f. Hart et al. 2011), along with spectroscopic redshifts for identifying cluster members would be useful to confirm/deny these findings and allow for a clearer interpretation that is unaffected by potential selection biases. Numerical models of cluster formation that focus on the competition between mergers of existing cluster members versus the recent infall of new cluster galaxies, as it depends on galaxy mass and redshift, would be valuable for assessing the proposed mechanisms for driving GDR evolution.

3.8 Acknowledgments

CB would like to acknowledge some very helpful discussions with Gabriella de Lucia, Michael Balogh, Simone Weinmann, Ting Lu, Stephen Gwyn and Diego Capozzi. CB and HH acknowledge support from Marie Curie International Reintegration Grant (number 230924). HH also acknowledges support from a Vidi grant from the Netherlands Organization for Scientific Research (NWO, grant number 639.042.814). AB and CB would like to acknowledge support from NSERC through the Discovery Grant program. They would also like to thank John Criswick for support through his generous gifts to the AB and to the Department of Physics and Astronomy, University of Victoria. This research has made use of the X-Rays Clusters Database (BAX) which is operated by the Laboratoire d'Astrophysique de Tarbes-Toulouse (LATT), under contract with the Centre National d'Etudes Spatiales (CNES). Finally, CB, HH and AB thank the Lorentz centre in Leiden for hospitality and support over the course of the Spring 2010 and Summer 2011 Workshops during which time a significant fraction of the research reported here was carried out.

3.9 References

Andreon S., 2008, MNRAS, 286, 1045
Barkhouse W., Yee H., Lopez-Cruz O., 2007, ApJ, 671, 1471
Beers T., Flynn K., Gebhardt K., 1990, AJ, 100, 32
Bell E. et al., 2004, ApJ, 608, 752
Bertin E, Arnouts S., 1996, A&AS, 317, 393
Bertin E., Mellier Y., Radovich M., Missionnier G., Didelon P., Morin B., 2002, ASPC, 281, 228
Bildfell C., Hoekstra H., Babul A., Mahdavi A., 2008, MNRAS, 389, 1637

Bildfell C., Hoekstra H., Babul A., Sand D., Graham M., Willis J., Urquhart S., Mahdavi A., Pritchet C., Zaritsky D., Franse J., Langelaan P., 2012, MNRAS, 425, 204

Bundy K., Ellis R., Coselice C., 2005, ApJ, 625, 621

Butcher H., Oemler A., 1984, ApJ, 285, 426

Bower R., Lucey J., Ellis R., 1992, MNRAS, 254, 601

Bower R., Benson A., Malbon R., Helly J., Frenk C., Baugh C., Cole S., Lacey C., 2006, MNRAS, 370, 645

Capozzi D., Collins C., Stott J., 2010, MNRAS, 403, 1274

Cardelli J., Clayton G., Mathis J., 1989, ApJ, 345, 245

Cimatti A., Daddi E., Renzini A., 2006, A&A, 453L, 29

Crawford S., Bershady M., Hoessel J., 2009, ApJ, 690, 1158

De Lucia G. et al., 2007, MNRAS, 374, 809

De Lucia G., Blaizot J., 2007, MNRAS, 375, 2

De Lucia G., Weinmann S., Poggianti B., Aragon-Salamanca A., Zaritsky D., 2011, arXiv:1111.6590v1

Evrard A., Metzler C., Navarro J., 1996, ApJ, 469, 494

Faber S. et al., 2007, ApJ, 665, 265

Fukugita M., Ichikawa T., Gunn J., Doi M., Shimasaku K., Schneider D., 1996, AJ, 111, 1748

Gal-Yam A., Maoz D., Guhathakurta P., Filippenko A., 2003, AJ, 125, 1087

Gilbank D., Yee H., Ellingson E., Gladders M., Loh Y., Barrientos L., Barkhouse W., 2008, ApJ, 673, 742

Gilbank D., Balogh M., 2008, MNRAS, 385L,116

Gonzalez A., Zabludoff A., Zaritsky D., 2005, ApJ, 618, 195

Gwyn S., 2008, PASP, 120, 212

Hansen S., Sheldon E., Wechsler R., Koester B., 2009, ApJ, 699, 1333

Hart Q., Stocke J., Evrard A., Ellingson E., Barkhouse W., 2011, ApJ, 740, 59

Hoekstra H., 2007, MNRAS, 379, 317

Hoekstra H., Mahdavi A., Babul A., Bildfell C., 2012, MNRAS, 427, 1298

Horner D., 2001, PhDT, 88

Juneau S. et al., 2005, ApJ, 619L, 135

Kodama T., Arimoto N., 1997, A&A, 320, 41

Kormendy J., 1977, ApJ, 218, 333

Krick J., Bernstein R., 2007, AJ, 134, 466

Lu T., Gilbank D., Balogh M., Bognat A., 2009, MNRAS. 399, 1858
Mahdavi A., Hoekstra H., Babul A., Bildfell C., Jeltema T., Henry P., 2013, ApJ, 767, 116
Markwardt C., 2009, ASPC, 411, 251
Mei S. et al., 2006, ApJ, 644, 759
Pimbblet K., Smail I., Kodama T., Couch W., Edge A., Zabludoff A., O'Hely E., 2002, MNRAS, 331, 333
Rozo E. et al., 2009, ApJ, 699, 768
Scarlata C. et al., 2007, ApJS, 172, 494
Sand D. et al., 2011, 729, 142
Sand D. et al., 2012, ApJ, 746, 163
Sarazin C., 1998, X-ray Emission from Clusters of Galaxies, Cambridge University Press
Schlegel D., Finkbeiner D., Davis M., 1998, ApJ, 500, 525
Stott J., Smail I., Edge A., Ebeling H., Smith G., Kneib J., Pimbblet K., 2007, ApJ, 661, 95
Tran K., van Dokkum P., Franx M., Illingworth G., Kelson D., Schreiber N., 2005, ApJ, 627
van Dokkum P., 2005, AJ, 130, 2647
Visvanathan N., 1978, A&A, 67, L17
Williams M., Bureau M., Cappellari M., 2010, MNRAS, 409, 1330
Yee H., Ellingson E., 2003, ApJ, 585, 215
Zibetti S., White S., Schneider D., Brinkmann J., 2005, MNRAS, 358, 949
Zibetti S., Charlot S., Rix H., MNRAS, 400, 1181

Chapter 4

BCG Velocity Dispersions

4.1 Introduction

Elliptical and lenticular galaxies have been shown to occupy a tight 2D relationship in the 3D parameter space defined by the line-of-sight velocity dispersion (σ) in km s^{-1}, the effective radius (r_e) in kpc and the average intensity inside the effective radius ($\langle I \rangle_e$) in L$_\odot$ pc^{-2}. This 2D relationship is commonly referred to as the fundamental plane (FP). The discovery of the fundamental plane can be attributed to the search for the minimum number of fundamental parameters required to describe galaxies as a class (Djorgovski & Davis 1987, Dressler et al. 1987). This work illustrated that when viewed in this parameter space, or its analog (swapping $\langle I \rangle_e$ for luminosity L), galaxies lie along a relation with a very small scatter of order $\sim 20\%$. This supplanted the Faber-Jackson relation (Faber & Jackson 1976) as the preferred distance estimator for spheroidal systems. The fundamental plane also provides a common context for the Faber-Jackson and Kormendy relations (Kormendy 1977), which can both be shown to be projections of the more general FP.

Completely independent of the empirical evidence, there is also a basic argument rooted in purely theoretical considerations that leads to the expectation of a fundamental plane. The starting point for this derivation is the virial theorem, relating the potential (V) and kinetic energy (T). We then apply this relation to a spheroidal, self-gravitating stellar system under the simplistic assumptions that the kinetic energy can be represented by the velocity dispersion (σ) and the potential energy by the potential at the effective radius (r_e) as follows:

$$T \propto V \tag{4.1}$$

$$\sigma^2 \propto \frac{GM_e}{r_e} \tag{4.2}$$

where M_e is the mass interior to r_e. The assumption that galaxies are homologous, scalable copies of each other, is required in order to neglect effects associated with their internal structure that would otherwise change the constant of proportionality. Expressing the mass in terms of the mass-to-light ratio $(M/L)L$ we obtain:

$$\sigma^2 \propto (M_e/L_e)L_e/r_e \tag{4.3}$$

where L_e is the integrated luminosity interior to r_e and can be expressed as $L_e \propto \langle I \rangle_e r_e^2$. We then obtain:

$$\sigma^2 \propto (M_e/L_e)(\langle I \rangle_e r_e^2)/r_e \tag{4.4}$$

$$\sigma^2 \propto (M_e/L_e)\langle I \rangle_e r_e \tag{4.5}$$

We then solve for r_e and take the logarithm of both sides, giving:

$$\log(r_e) = 2\log(\sigma) - \log(\langle I \rangle_e) - \log(M_e/L_e) + C \tag{4.6}$$

where the effect of the constant of proportionality is captured by parameter C. By equation 4.6 we see that spheroidal galaxies ought to occupy a plane in the 3D parameter space defined by $(\sigma, r_e, \langle I \rangle_e)$. However, observations show that the coefficients of the σ and $\langle I \rangle_e$ terms differ significantly from the expected values of 2 and 1, respectively. The departure from these coefficients is often referred to as the 'tilt' of the fundamental plane and is usually interpreted as either variation in the mass-to-light ratio with galaxy properties or a departure from the assumption of homology. The sensitivity of the fundamental plane to distance, variation in (M_e/L_e) and departure from homology make the fundamental plane a highly useful multi-tool for probing galaxy formation.

Using the FP to obtain distances and peculiar velocities of galaxies, Lynden-Bell et al. (1998) discovered the large-scale streaming of nearby systems to toward the Hydra-Centaurus Supercluster (known as the 'Great Attractor'). Van Dokkum

et al. (1998) use the fundamental plane to rule out cosmological models based on $\Omega_m = 1$ and $\Omega_\Lambda = 0$, providing early support for cosmologies with $\Omega_m = 0.3$ and $\Omega_\Lambda = 0.7$. Using a large data set from the SDSS, von der Linden et al. (2009) show that the fundamental plane of a sample of BCGs is tilted with respect to a sample of color- and magnitude-matched non-BCGs, interpreting this as evidence for an enhancement in the BCG M/L, which they argue is likely due to the boost in dark matter mass provided by the cluster environment. Using the fundamental plane in a similar fashion, Zaritsky et al. (2006) investigate the change in mass-to-light ratio in a wide range of spheroidal systems, finding a dependence of (M/L) on $\log(\sigma)$ that behaves quadratically and causes a change in the tilt of the fundamental plane at the extreme high and low σ values. Folding in this dependence they argue for a unified 'fundamental manifold' of spheroidal systems that seeks to unite galaxies from tiny dwarf ellipticals to the massive extended intra-cluster light profiles in galaxy clusters.

In this chapter we seek to probe the fundamental plane of a sample of 19 BCGs from the CCCP in order to measure the 'tilt' and intrinsic scatter of this important subclass of galaxies. In §4.2 we introduce the data used in this study, with an emphasis towards the first time presentation of our medium-resolution optical spectra. Following this, in §4.3 we describe the basic reduction of the spectra and the combination of the multiple spectra exposures into a single stacked spectrum for each BCG. §4.4 discusses the measurement of velocity dispersions via fits to stellar templates. In §4.5 we describe the measurement and calculations associated with the structural parameters obtained from photometry. The fundamental plane of BCGs is investigated in §4.6 and their dynamical masses are discussed in §4.7. Lastly, we present some concluding statements in 4.8. Throughout this work we assume a Λ-CDM cosmology parameterized by $\Omega_m = 0.3$, $\Omega_\Lambda = 0.7$ and $H_0 = 70$ km s^{-1} Mpc^{-1}.

4.2 Data Description

To study the Fundamental Plane of a sample of galaxies requires measurement of the line-of-sight velocity dispersion σ, determined from spectra, as well as the structural parameters r_e and $\langle I \rangle_e$ as measured from broad-band photometric imaging. In this section we describe the data used to extract these values.

4.2.1 Spectra

The spectra for this study were obtained from the Gemini North and South observatories using the GMOS detector in long-slit mode over the period of 3 semesters from 2007B to 2008B. We use the B600 grating with a central wavelength of 460nm and a slit width of 0.75 arcsec. The slit is aligned with the major axis of the BCG. This instrument configuration is motivated by the work of Barr et al. (2005) and Barr et al. (2006) who use a similar configuration to measure velocity dispersions of early type galaxies in a fundamental plane study of the merging cluster RXJ0142.0 + 2131. We use a 2×2 on-instrument pixel binning which, along with the instrument configuration described above, yields a spectral pixel scale of ~ 0.1 nm/pix and a spatial pixel scale of ~ 0.14 arcsec/pix.

Our observations are centered on 19 BCGs in galaxy clusters drawn from the CCCP survey, selected based on their small projected offset from their host cluster's peak X-ray emission (< 15 kpc). For each cluster we take 4 separate 1800s observations, using small spatial and spectral dithers to mitigate problems introduced by detector defects and chipgaps. There are some exceptions however, as due to scheduling and weather constraints one cluster was observed for less time (2×1800s), while two others were observed for more time (7×1800s and 8×1800s). For further information on our observations a summary description is given in Table 4.1.

4.2.2 Imaging

The imaging data used in this study are taken from the CCCP primary data set. These are a set of images obtained at the Canada-France-Hawaii Telescope (CFHT) using either the CFH12K or MegaCam detector arrays. The clusters were observed at optical wavelengths using a two-channel broad band filter set. The MegaCam clusters were observed with the (g', r') filter combination while the CFH12K clusters were observed with the (B, R) filter combination. Further details on the observing strategy can be found in the introduction to this thesis, as well as references therein.

Table 4.1: Summary description of the observations used in this study.

Name	z	α	δ	$t_{exp,spec}$	Filterset
		hh:mm:ss	dd:mm:ss	s	
Abell2104	0.16	15:40:07.94	-03:18:16.25	4×1800	g', r'
Abell2259	0.16	17:20:09.66	+27:40:08.29	2×1800	g', r'
Abell568	0.17	07:32:20.31	+31:38:01.06	8×1800	g', r'
MS0906+11	0.17	09:09:12.76	+10:58:29.12	4×1800	B, R
Abell1689	0.18	13:11:29.52	-01:20:27.86	4×1800	B, R
Abell383	0.19	02:48:03.38	-03:31:44.93	7×1800	B, R
MS0440+02	0.19	04:43:09.92	+02:10:19.33	4×1800	g', r'
Abell209	0.21	01:31:52.54	-13:36:40.00	4×1800	B, R
Abell963	0.21	10:17:03.63	+39:02:49.67	4×1800	B, R
Abell1763	0.22	13:35:20.12	+41:00:04.30	4×1800	B, R
Abell1942	0.22	14:38:21.88	+03:40:13.34	4×1800	g', r'
Abell2261	0.22	17:22:27.23	+32:07:57.72	4×1800	g', r'
Abell267	0.23	01:52:41.95	+01:00:25.89	4×1800	B, R
Abell2390	0.23	21:53:36.84	+17:41:44.10	4×1800	B, R
Abell1835	0.25	14:01:02.10	+02:52:42.69	4×1800	g', r'
Abell68	0.26	00:37:06.85	+09:09:24.51	4×1800	B, R
MS1455+22	0.26	14:57:15.12	+22:20:34.48	4×1800	B, R
Abell611	0.29	08:00:56.83	+36:03:23.79	4×1800	g', r'
Abell2537	0.30	23:08:22.22	-02:11:31.74	4×1800	g', r'

4.3 Data Reduction

The data reduction for the imaging data are discussed in detail in Hoekstra et al. (2007) and Bildfell et al. (2008). We do not discuss the reduction of the imaging data here and instead, we refer the reader to the above-mentioned publications for further details. Regarding the quality of the imaging data reductions, Bildfell et al. (2008) illustrates that these data are deep enough and of sufficient quality to measure the structural parameters within 68% confidence limits of $< 1\%$ in r_e and to < 0.05 mag in μ_e (for the r' or R band). Such tight constraints on r_e and μ_e are adequate for the purposes of this study. We note that the quoted precision on r_e and μ_e reflect only the formal 'fitting' error on parameter values, and do not take into account any potential systematic sources of uncertainty. The observed scatter of ~ 0.05 mag in the mean k-corrected $(g' - r')$ color of red sequence galaxies presented in Bildfell et al. (2012) indicates that systematic effects on the r' photometry are at most ~ 0.05 mag. They are actually likely to be much smaller than 0.05 mag, since some of the scatter is introduced via the shallower g'-band data and some of the scatter in red sequence color is expected to be intrinsic. The remainder of this section is focused on the data reductions and processing for the spectra observations only.

The primary data reduction steps for the spectra observations are performed using the standard IRAF software package for reducing GMOS data provided by Gemini. We begin by creating a set of bias-subtracted flat field frames to be applied to our science images. The flat field images are not uniformly illuminated, and suffer from an illumination pattern that varies strongly with wavelength (ie. along the x-direction). This illumination pattern is fit with a spline of order 61 in the wavelength direction, which is then divided through the flat field image to obtain a normalized flat field such that only the pixel-to-pixel variations in detector sensitivity remain. We find that using a lower order fit to the illumination pattern leaves large-scale residuals in the flat fields that can lead to a significant systematic error (few percent) in the final science frames. The normalized flat fields are then used to correct the corresponding science frames, arc spectra and standard star observations.

We then use the Cu-Ar arc spectra, together with a well calibrated list of known emission line locations, to generate a set of dispersion functions sampled uniformly at several positions along the slit (ie. in the y-direction). For individual arc spectra, the residuals for known locations of Cu-Ar lines compared to the line locations as predicted by the dispersion solutions show a median RMS of 0.14 $\AA$. The arc spectrum

with the highest precision dispersion solution has an RMS residual of 0.09 $\AA$ while the lowest precision dispersion solution has an RMS residual of 0.18 $\AA$. This translates to a worst-case systematic error of $\sim$ 14 km/s for individual lines, but since our results are based on fitting of order 100 lines for galaxies that have velocity dispersions of $\sim$ 300 km/s, the contribution of this source of systematic error is negligible.

The dispersion solutions are applied to the corresponding science frames and standard star observations to obtain a set of wavelength-calibrated data. The next step in the reduction procedure is sky subtraction. The projected angular scale of the slit on the detector extends for a total of 5.6 armin. Avoiding the edges of the detector and the central 1.1 armin region containing the spectrum of the BCG, we sample the spectra from a 1.9 arcmin region below the BCG and a 1.8 arcmin region above the BCG and sum these together. The extracted spectra are then fit column-by-column (ie. at fixed wavelength) with a linear relation to obtain a background model that varies as a function of wavelength and position along the slit. The background model is then subtracted from the entire image and the process is repeated for all science frames and standard star observations. We note that due to our long exposures, the brightest sky line [OI]5577 is saturated in many of the images and as a result is not properly subtracted. To prevent this from influencing our results, this region of the spectrum is masked out in our velocity dispersion fitting analysis.

The final step in the reduction of the individual science frames is flux calibration. Briefly, the continuum of the observed spectrum of a standard star is fit with a 6^{th}-order cubic spline, which is then compared to a data table of flux-calibrated spectra of that star to generate a sensitivity function. The sensitivity function is then applied to the corresponding science frame observations to transform the spectra in units of counts on the detector to set of spectra in physical units of erg cm^{-2} s^{-1} Å^{-1}. Additionally, we apply a second-order correction for atmospheric extinction at this stage, the specific wavelength dependence of which is supplied by the Gemini observatory via data tables in the Gemini IRAF reduction package.

4.3.1 Combining Spectra

After completing the data reduction steps outlined above, we find that there remain small ($< 10\%$) but significant differences in the fluxes between different observations of the same object. These flux differences are found to be only weakly dependent on wavelength and we speculate that they may originate from slight deviations in the ob-

serving conditions between exposures. Thin cirrus clouds drifting above the telescope, variations in the seeing/PSF and errors in the atmospheric extinction corrections may all play a role. To correct for these differences, we normalize all exposures of a given BCG to that of the brightest exposure, the reference image. Specifically, we extract the spectrum from each exposure, using an aperture ± 10 pixels around the BCG position and then divide by the spectrum extracted from the brightest exposure for that object. These relative spectra are then fit with a linear relation to obtain a scaling function that varies (weakly) with wavelength. The scaling function is then applied to the full 2-D spectrum for the corresponding exposures, which, when repeated for all observations, results in a scaled set of images corrected for any large-scale flux differences.

The scaled images are then aligned to the reference image by shifting in the spatial dimension and interpolating in the spectral dimension. We the stack the spectra using a median-combining algorithm, taking care to mask out the chip gaps and detector defects. Where there are an even number of unmasked pixels contributing to the stack and no clear median value exists, we use the average of the two central values in its place. The stacking process not only yields a deeper image with a higher signal-to-noise ratio, it has the additional benefit of cleaning the spectrum of cosmic ray contamination, which can otherwise lead to significant error in the velocity dispersion measurement. There are still some regions of the stacked image that are based on contributions from only two exposures and in these regions traces of cosmic rays remain, though at a reduced level owing to the averaging.

Using the individual flux-scaled exposures and the combined image we estimate the errors on a pixel-by-pixel basis. The error for the median-combined image at each pixel (σ_f) is calculated by taking the standard deviation of the pixel values. To prevent cosmic rays from biasing the errors too high we use an iterative sigma-clipped estimator, rejecting values that lie outside $\pm 10\sigma_f$ from the median value and repeating the process for 6 iterations. This creates a σ_f array of the same size and dimensions as the combined image, which is later used for the velocity dispersion fitting procedure. We fit the flux error σ_f as a function of wavelength λ on a row-by-row basis, using a linear relation. We use the expected values from the best fit solutions to build a $\sigma_f(\lambda, y)$ for each combined image, where y represents the direction along the slit with the BCG centroid at $y = 0$. The resulting 2-D error array is stored as an error image for later use in the velocity dispersion fitting procedure.

4.4 Velocity Dispersion Measurement

To measure the line of sight (LOS) velocity dispersion σ we use the penalized pixel-fitting code (pPXF) of Cappellari and Emsellem (2004). For each BCG we extract a 1-D spectrum from the 2-D image using a constant physical aperture size that sums all flux within ± 5 kpc from the BCG centroid, along the direction of the slit. The rest-frame wavelength range used in the velocity dispersion fitting is $4050 < \lambda < 4650$ $\mathring{A}$, which is similar to the range used by van Dokkum et al. (1996) in their fundamental plane study. The lower bound is chosen to exclude data shortward of the $4000\mathring{A}$ break, below which the spectrum is dominated by the youngest stars. The upper bound of the fitting range is selected because with our instrumental configuration ($\lambda_{max} \sim 6000\mathring{A}$) it is the maximum rest-frame wavelength observed at the highest redshift of our sample ($1 + z = 1.3$). At lower redshifts this effectively means that we are throwing out data that could otherwise be used to further constrain the model, however, using a fixed fitting range helps to minimize systematic effects that may produce artificial correlations between σ and z.

We assume an instrumental resolution of 3.65 $\mathring{A}$ FWHM as measured from the emission lines in the CuAr arc calibration spectra. The fit is performed using a mask in order to exclude regions of the spectra that overlap with sky lines, which may be affected by imperfect sky subtraction or artifacts resulting from line saturation. We also mask out the regions of the spectrum corresponding to the Balmer series of hydrogen at the redshift of the BCG. This is necessary because several of the spectra show evidence for H_γ and H_δ emission or absorption line infilling, and we seek to measure the velocity dispersion by fitting absorption features only. The stellar templates used in the fitting procedure are drawn from the MILES stellar library[1] (Sanches-Blazquez et al. 2006, Falcon-Barroso et al. 2011). The library spectra begin with a resolution of $2.3\mathring{A}$ and are subsequently convolved to the instrumental resolution of our data prior to running pPXF.

For pPXF to work properly the input spectrum must be velocity-shifted to the rest-frame before fitting the spectral templates. In some cases, where knowledge of the cluster redshift is of poor precision or where the BCG may have a significant peculiar velocity component along the line of sight, a more precise redshift must be measured prior to using pPXF. To this end, we measure the redshifts of the BCGs by locating the peaks of the CaII H+K absorption features at 3968.5 $\mathring{A}$ and 3933.7 $\mathring{A}$,

[1] http://miles.iac.es

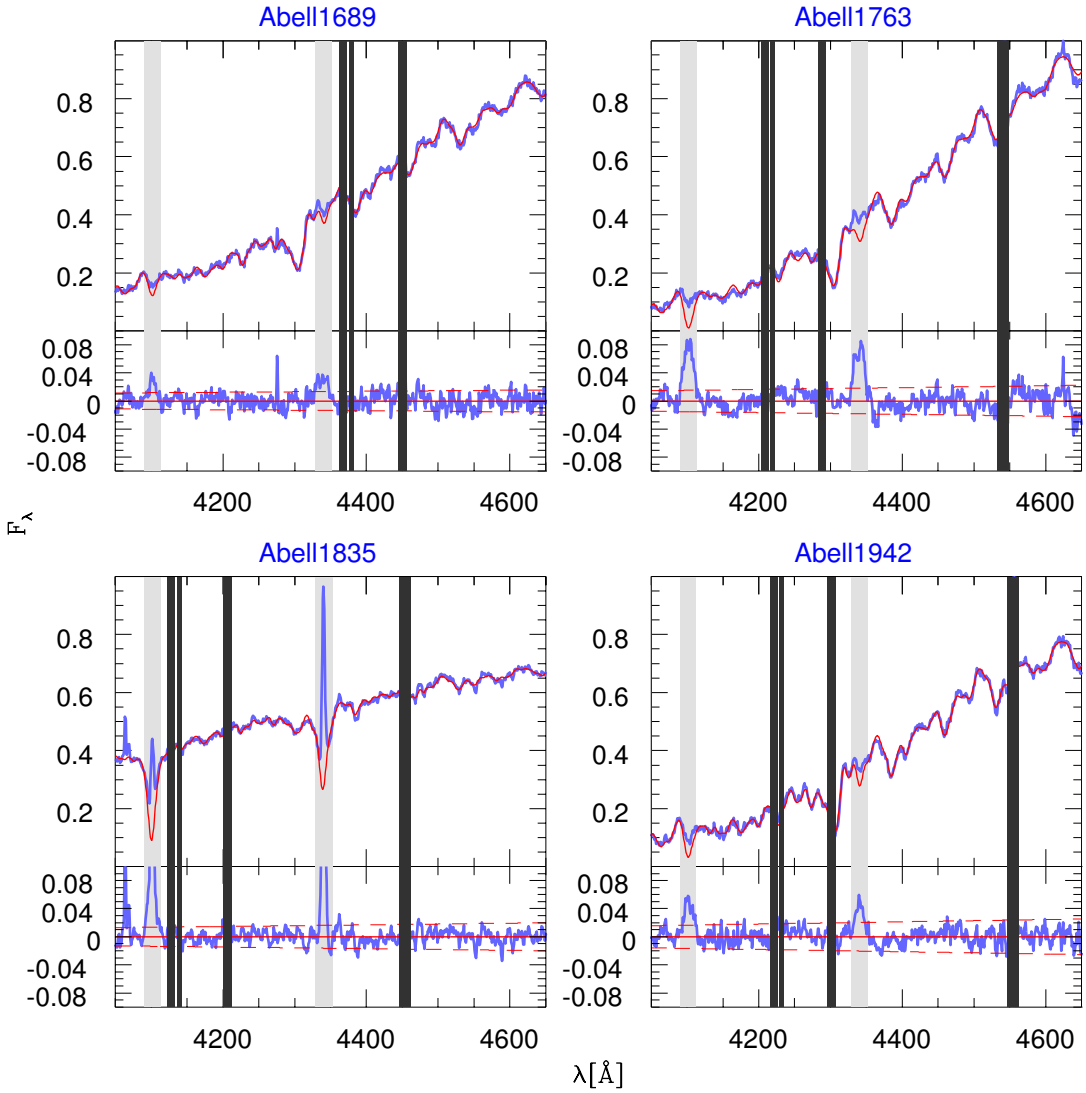

Figure 4.1: The observed spectra of the BCGs are shown as the thick blue line along with the best fit pPXF model overlaid in thin red. The vertical axis shows the flux density F_λ in arbitrary units while the rest-frame wavelength is shown along the horizontal axis. Errors on the data are represented by the dashed lines in the residual plots. The regions of the spectrum that are significantly affected by sky lines are masked out in heavy black bars. The regions of the spectrum potentially affected by emission lines are highlighted with light grey bars. Several of the BCGs in the sample show strong evidence of Balmer line emission in their spectra.

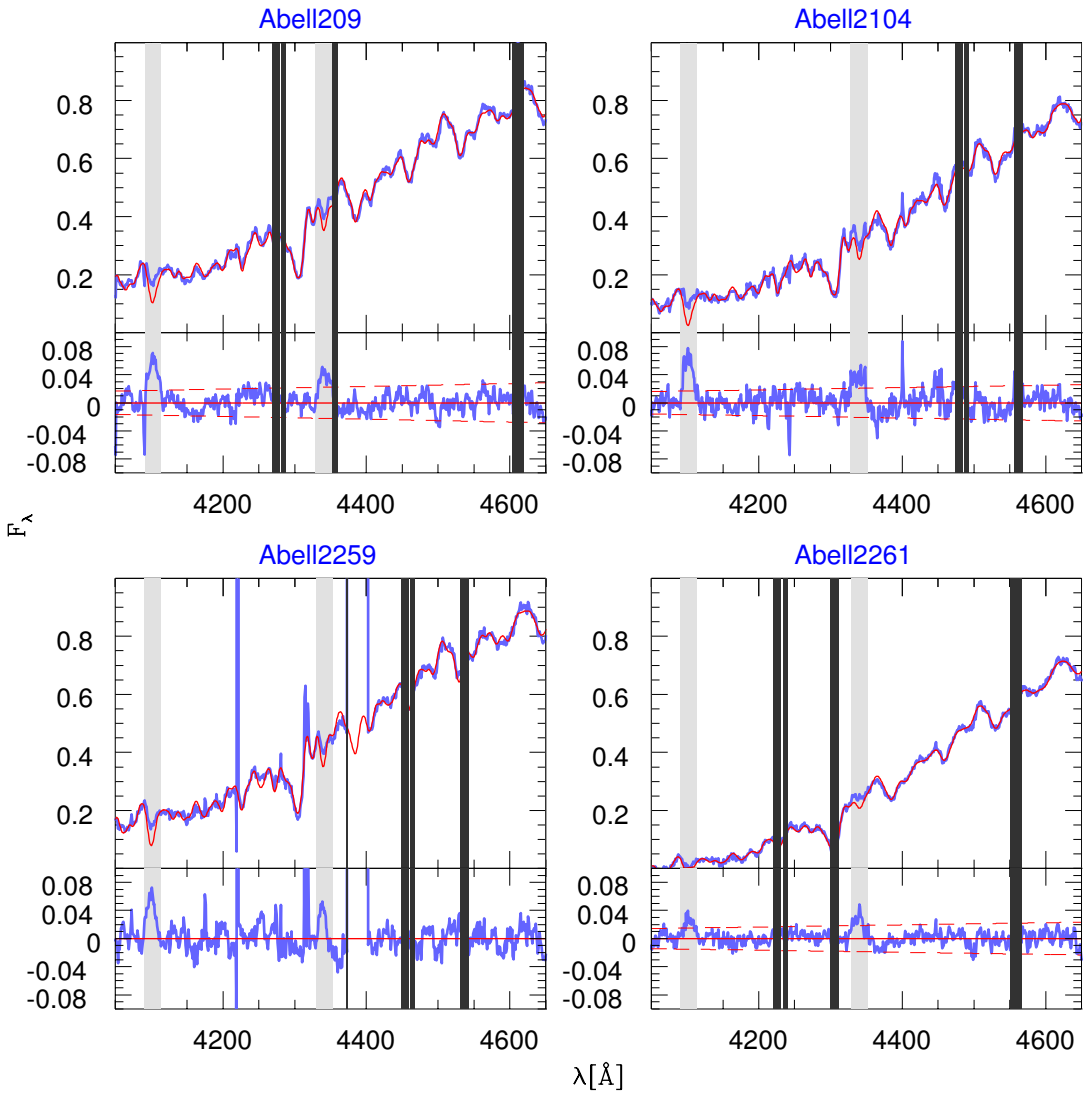

Figure 4.2: Continued from Figure 4.1.

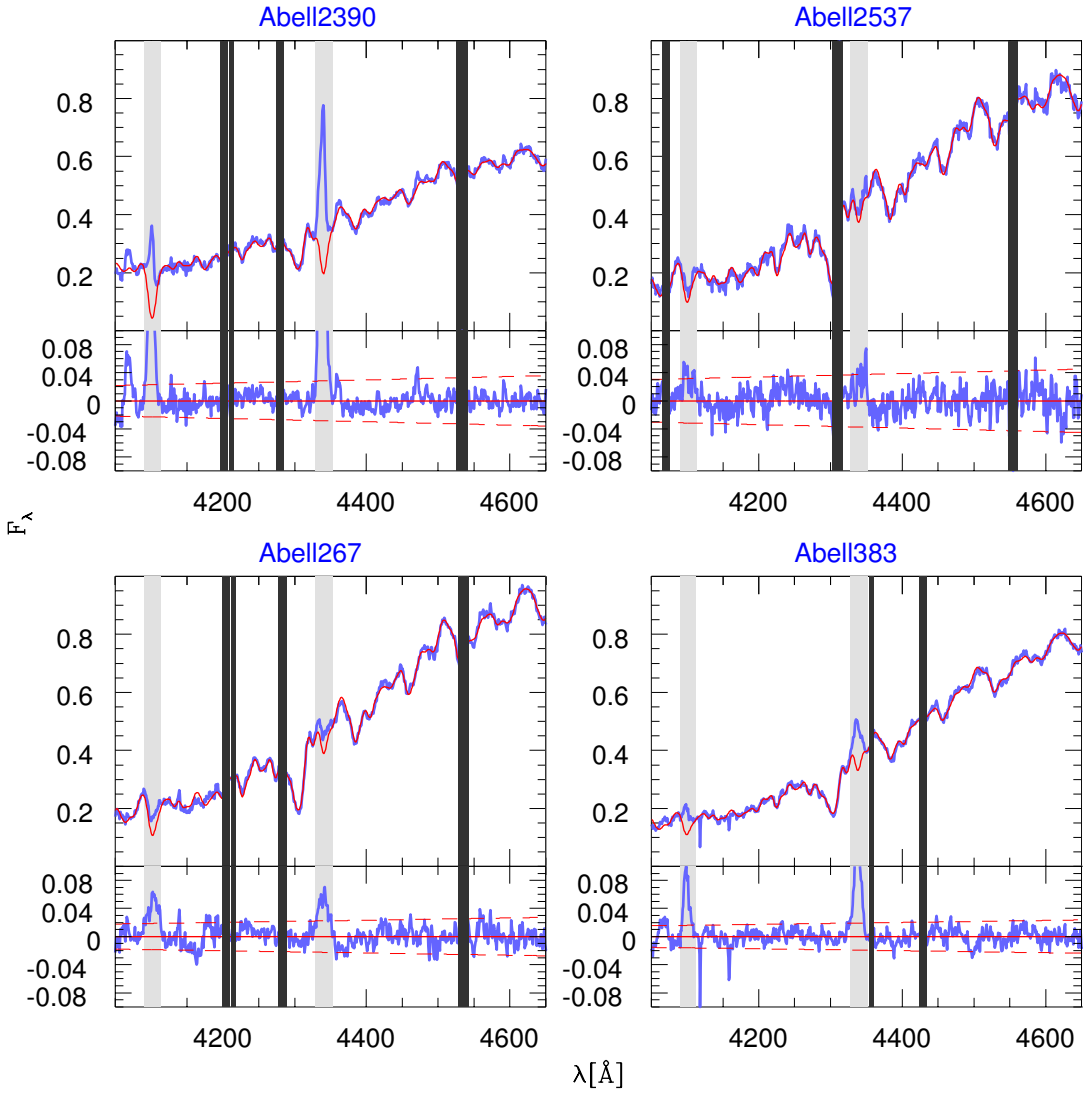

Figure 4.3: Continued from Figure 4.1.

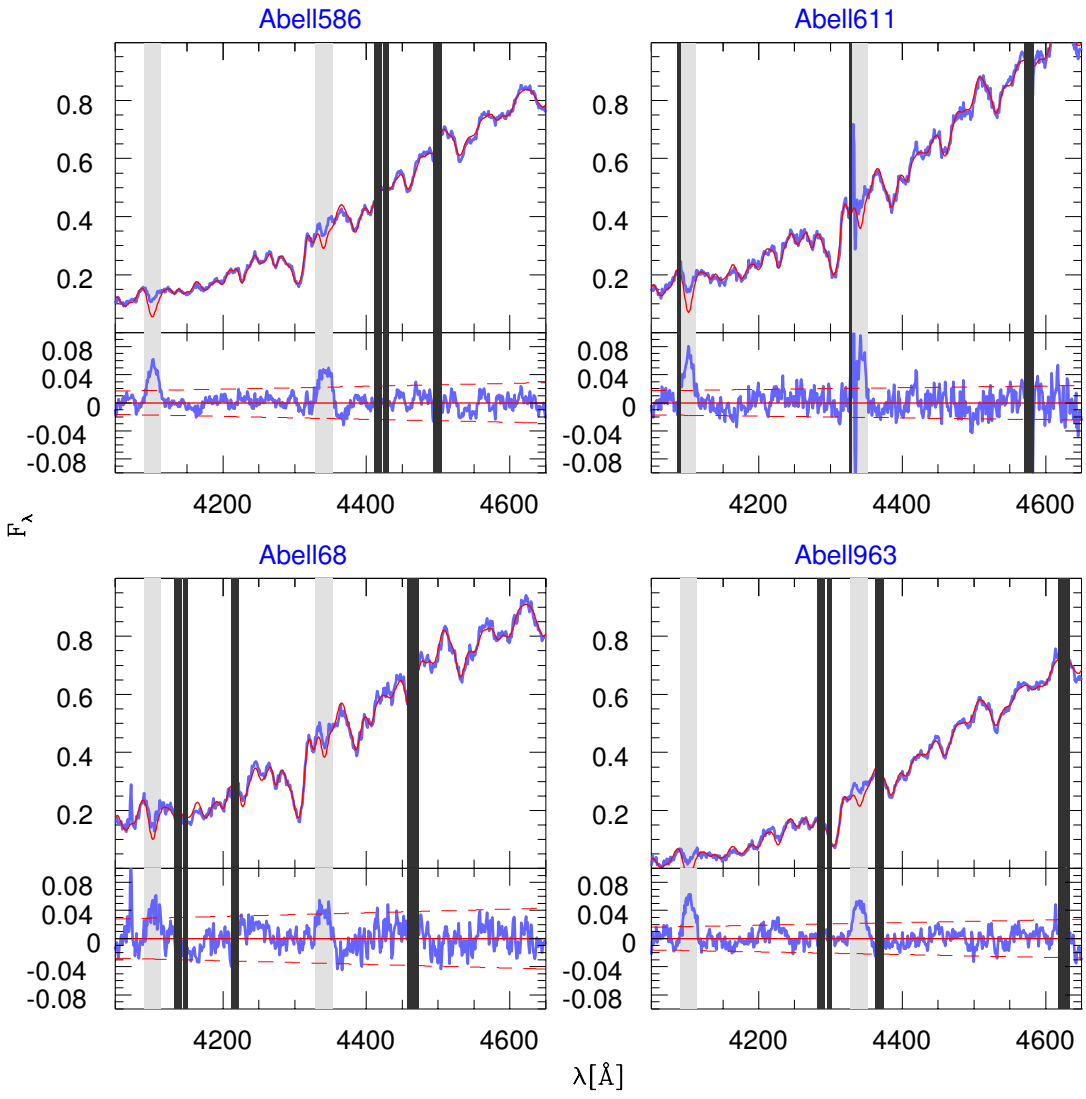

Figure 4.4: Continued from Figure 4.1.

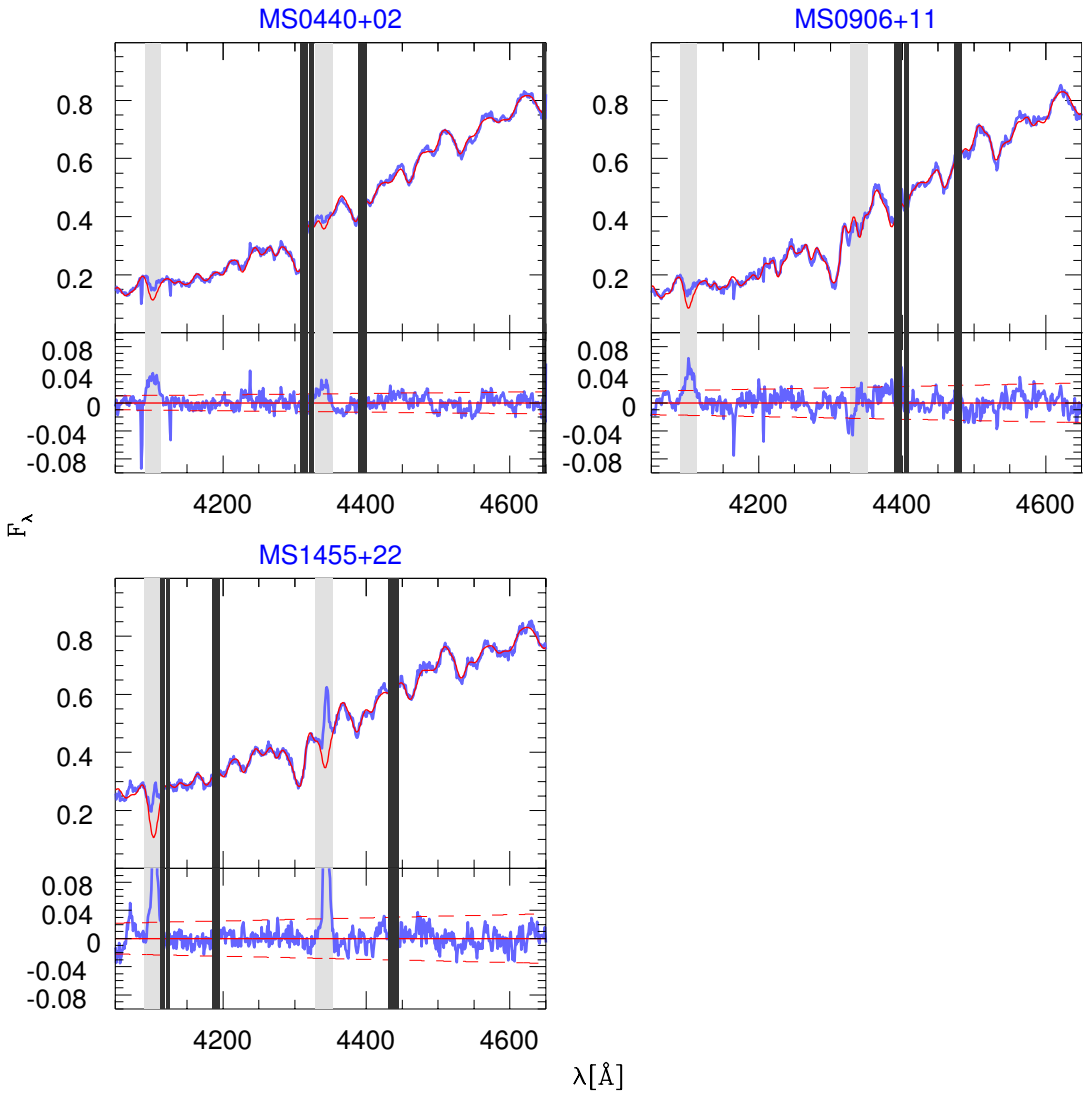

Figure 4.5: Continued from Figure 4.1.

respectively. We use the resulting refined BCG redshifts to transform the spectra to the rest-frame ($z = 0$). Although pPXF does determine the velocity shift of the spectrum as one of the output model parameters, this procedure helps to keep the algorithm from wandering into non-physical regions of parameter space. The refined redshifts are all within $|\Delta z| < 0.01$ from the original redshift estimates, which results in corresponding line-of-sight velocity differences $|\Delta V| < 2000$ km/s with the exception of one system at $\Delta V \sim 2500$ km/s. Given the typical level of precision on redshifts listed in the BAX database ($\delta z \sim 0.01$) we assume that the refined BCG redshifts, measured using the CaII H+K lines, are consistent with the BAX values.

The final ingredient for the velocity dispersion is the error in the flux $\sigma_f(\lambda)$. We calculate $\sigma_f(\lambda)$ using the error image described in §4.3.1. The error function is calculated by summing in quadrature along the direction of the slit:

$$\sigma_f(\lambda) = \sqrt{\sum_{i=1}^{n} \sigma_{f,i}(\lambda)^2} \tag{4.7}$$

where $\sigma_{f,i}$ is the error on the i^{th} pixel and the sum is evaluated over the same n pixels spanning the aperture used to extract the spectrum of the BCG (± 5 kpc). Using this $\sigma(\lambda)$ we run pPXF for 7 iterations, where the final 6 iterations are run with the *CLEAN* parameter set, which helps to remove from the fit any unmasked bad pixels, residual gas emission or cosmic rays. We also allow for an additive 4^{th} degree polynomial to account for variations in the shape of the continuum.

The input spectra and the best fit pPXF solutions are shown in Figures 4.1 through 4.5. The x-axis shows the rest-frame wavelength of the spectra after de-redshifting according to the BCG redshift as measured from the CaII doublet. The y-axis shows the spectral flux density in the rescaled, arbitrary units convenient for pPXF. In these figures the observed spectra are denoted by the thick blue lines, while the best fit pPXF solutions are overlaid as thin red lines. The wavelength regions that are affected by sky lines are shaded out in black, as they have been removed from the fit. Light grey shading indicates regions of the spectrum that are potentially affected by emission lines; specifically H_γ and H_δ.

In general, the best fit model spectra are all in good agreement with the observed spectra. Aside from the regions around the emission lines, which are discussed in more detail below, the residuals show little sign of structure. The χ^2/DOF is below unity for each of the best fit model BCGs, with typical values near $\chi^2/DOF \sim 0.3$.

Trusting our error estimation procedure, at least to within a factor of 2, such low values of the reduced χ^2 indicate some degree of overfitting in the models, which is likely associated with the additional freedom of including an additive polynomial. Although our current error estimates consider Poisson noise on the photon statistics only, the inclusion of additional error components will only exacerbate this problem by increasing the total error, thereby decreasing the value of χ^2/DOF. To compensate for this overfitting, we adjust the errors on the best fit parameters by a factor of $\sqrt{\chi^2/DOF}$ in Table 4.2.

An interesting feature of Figures 4.1 through 4.5 is that many of the BCGs show a considerable level of hydrogen line emission at H_γ and H_δ (grey shaded regions). This is perhaps not unexpected given that these are all massive early-type galaxies, hosting a variety of types of AGN. These emission lines are particularly bright in the BCGs residing in low entropy (cool-core) clusters such as Abell1835, Abell2390, Abell383 and MS1455+22. The spectra of these systems all show narrow line Balmer line profiles that peak well above the best fit continuum flux, consistent with hosting recent star formation. However, Balmer line infilling is also evident in the spectra of each of the remaining galaxies (Abell1689, Abell1763, Abell1942, Abell209, Abell2104, Abell2259, Abell2261, Abell2537, Abell267, Abell586, Abell611, Abell68, Abell963, MS0440+02, MS0906+11), which is particularly visible when examining the residuals. If we take the residuals to be indicative of the shape of the infilling lines we see that they are broad, with velocity widths on the order of hundreds of km/s.

4.4.1 Velocity Dispersions

The values of σ obtained from the best fit pPXF models described in §4.4 and listed in Table 4.2 are plotted as a function of redshift in Figure 4.6. The blue colored symbols represent those BCGs which are classified as blue-core systems in Bildfell et al. (2008). The error bars reflect the errors on velocity dispersion from the pPXF template fitting alone and does not include any contribution from systematic effects. The σ values shown here reflect the line of sight velocity dispersions for a central aperture of diameter 10 kpc. At the highest redshift in our sample ($z = 0.3$) this represents an angular size of 2.25 arcsec, which approximately twice the size of FWHM of the worst-case PSF for our data. As such, we do not expect any PSF-related effects to be significant. Accordingly, we do not apply any aperture corrections to our velocity dispersion measurements and we treat our σ values as 'central' velocity

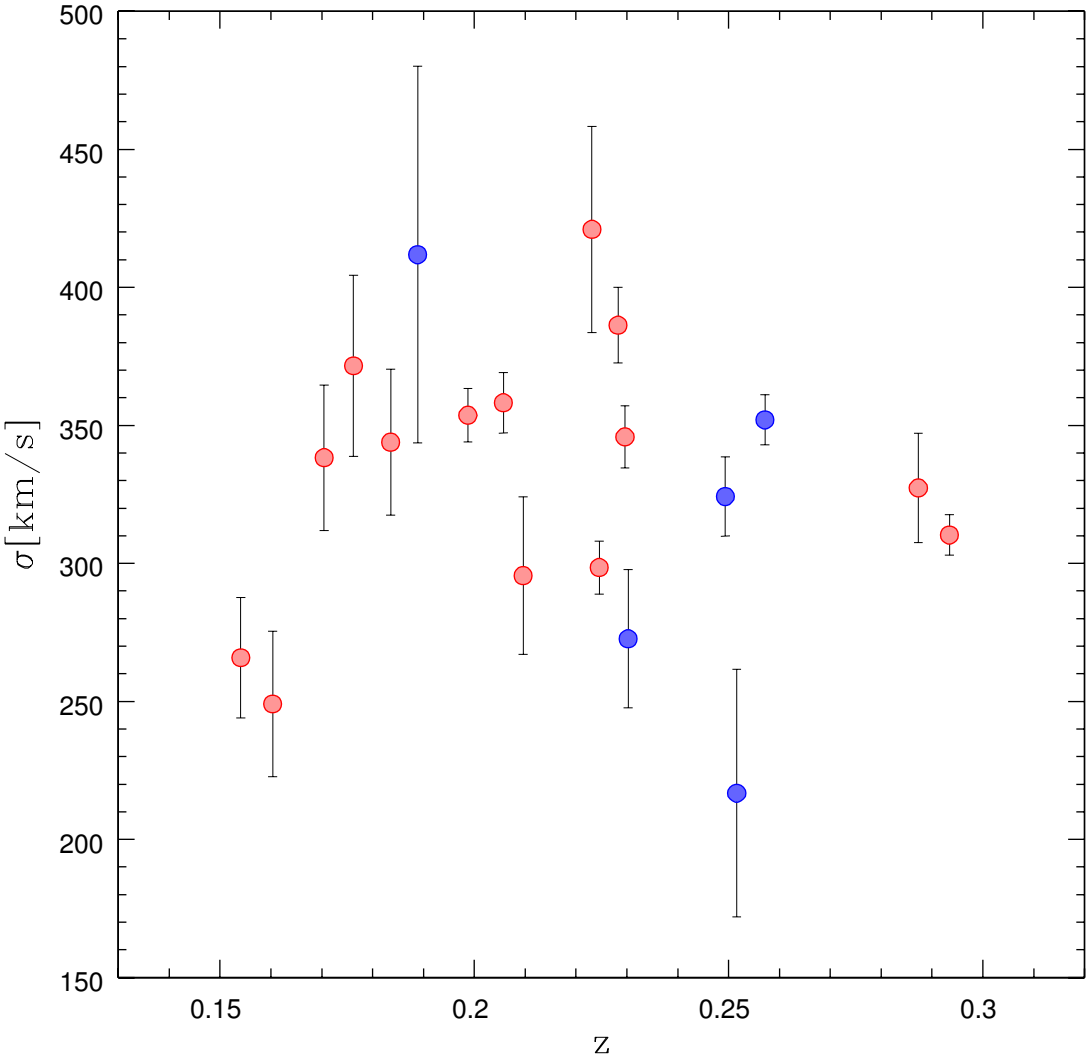

Figure 4.6: Velocity dispersion σ as a function of redshift z. Blue and red symbols denote, respectively, the galaxies identified as blue-core and red-core systems in Bildfell et al. (2008).

dispersions. We note that aperture correction can also be used to transform central velocity dispersions to a measure of the velocity dispersion within a given fraction of r_e (eg. $r_e/4$, $r_e/10$) and that this represents a difference in methodology between those studies and our own that would need to be accounted for prior to making a exact comparison between results.

We compare our results with the BCG velocity dispersion profiles published by Newman et al. (2013). We find good agreement between our results and their measurements of BCG velocity dispersion inside 5 kpc for the 4/5 clusters in common between the two samples. The exception is the BCG in Abell 383 where we find a significantly larger value of $\sigma = 412 \pm 68$ km s^{-1} in contrast with the $\sim 280 \pm 20$ km s^{-1} found in Newman et al. (2013).

There is no correlation between σ and z seen in our sample, which is to be expected and indicates that there are no strong systematic effects related to redshift in our analysis. The σ values range from $\sim$200 km/s to as high as $\sim$400 km/s. Such large velocity dispersions are appropriate for BCGs since they are both the most massive galaxies known and preferentially located near the deepest regions of the cluster potential. The BCG with the lowest velocity dispersion is that in Abell 1835, with a $\sigma = 216 \pm 44$ km/s. This is particularly interesting when considered with the fact that this galaxy has the highest star formation rate of any known BCG, with a $\dot{M}_{SF} > 100\ M_{\odot}$ yr^{-1} (McNamara et al. 2006). This may suggest a link between the velocity dispersion and the star formation rate such that a low σ could facilitate the accretion of large amounts of cold gas that would otherwise not be able to condense as quickly as in a BCG with a larger σ. As cluster gas cools it ought to be deposited in giant molecular clouds that orbit the BCG with velocity $\sim \sigma$. We might expect that at lower values of σ these giant molecular clouds have more opportunity for collisional and dynamical interactions with similar nearby clouds, accelerating relaxation the process by which this gas is deposited onto the core of the BCG.

4.5 Structural Parameters

In addition to the line-of-sight velocity dispersions, constructing the fundamental plane requires knowledge of the structural parameters of BCGs. We obtain the effective radii (r_e) from the results presented in Bildfell et al. (2008), who fit circularly symmetric, PSF-convolved $r^{1/4}$ models to the BCG surface brightness profiles. Using apertures defined by these effective radii (as measured in r' or R band) and the same

images and masks used in the Bildfell et al. (2008) analysis, we compute the $(g' - r')$ or $(B - R)$ color for each BCG, which is used to determine the k-correction (see below). Using the best fit effective surface brightness (μ_e) values from Bildfell et al. (2008) are converted to average surface brightness within the effective radius ($\langle\mu\rangle_e$) using the following relation:

$$\langle\mu\rangle_e = \mu_e - 1.393 \tag{4.8}$$

where the constant term (-1.393) is determined by the shape of the profile, in this case an $r^{1/4}$ profile (Caon et al. 1994, Graham et al. 1997). The resulting values of $\langle\mu\rangle_e$ are then further converted to a mean effective surface brightness $\langle I\rangle_e$ in $L_\odot$ pc^-2 using the relation:

$$\log\left(\langle I\rangle_e\right) = -0.4(\langle\mu\rangle_e + 26.4) \tag{4.9}$$

which is taken from Jorgensen et al. (1999) and is calibrated for data taken in the Gunn r filter, a close analog to the r' to which our $\langle\mu\rangle_e$ values are calibrated (after performing a k-correction). The resulting $\log\left(\langle I\rangle_e\right)$ are used later to examine the BCG fundamental plane. All magnitudes and surface brightnesses are corrected for extinction by the Galactic dust screen.

The data are k-corrected using an identical k-correction procedure as that presented in Bildfell et al. (2012). Specifically, we use the spectral synthesis code of Charlot and Bruzual (2007) to simulate the spectra of a single burst of star-formation with solar metallicity and a Salpeter initial mass function. We also include a 3%-by-mass contribution from ultra-metal-poor stars required to match the $(g' - r')$ color of luminous red galaxies at low-z (Maraston et al. 2009). Using the observed value of the mean $(g' - r')$ or $(B - R)$ color within the effective radius for each BCG, we compare to color of the synthetic spectra to obtain an appropriate template spectrum for that galaxy. The k-correction is then easily calculated by taking the difference between the magnitudes calculated for the redshifted and de-redshifted, matched template spectra.

To compare the observations of objects at different redshifts on equal footing we also correct for the effects of cosmological surface brightness dimming. We correct the fluxes by a factor of $(1 + z)^4$ to compensate for the change in angular diameter distance ($\propto (1+z)^2$), the arrival time delay of the photons ($\propto (1+z)$) and a decrease in photon energies ($\propto (1 + z)$). In the results presented here we do not apply any

correction for passive surface brightness evolution that is expected to occur due to the fading of BCG stellar populations over time.

4.5.1 $(g' - r')$ Color of BCGs

We examine here the $(g' - r')$ aperture colors of BCGs in order to test the quality of our data calibration, namely the k-correction, extinction correction. Figure 4.7 shows redshift dependence of the corrected data after converting the *observed* $(g' - r')$ or $(B - R)$ aperture colors, measured within the r'- or R-band effective radius, to a consistent set of *rest-frame* colors in the $(g'r')$ filter combination. The blue and red symbols indicate BCGs identified as blue-core and red-core systems, respectively, in Bildfell et al. (2008). The statistical errors on the BCG colors are smaller than the sizes of the symbols shown. The grey shaded area shows the mean and standard deviation of the k-corrected color of the red sequence for galaxies in the fixed absolute magnitude bin $-20.82 < M_{r'} < -19.82$ from Bildfell et al. (2012).

Overall, the BCGs in our sample show a reasonable, if somewhat broad, distribution of rest-frame $(g' - r')$ colors. We do not observe any obvious trend with redshift, indicating that the k-correction procedure does not artificially produce one. The typical rest-frame colors of the red-core systems is redder than that of the reference color (grey shaded area), which is to be expected since the BCGs are the brightest member on a red sequence with non-zero slope. There is however a large scatter in BCG colors, which may reflect the diversity in the metallicities and star-formation histories of these complex systems. We measure an rms scatter in $(g' - r')$ color of 0.12, which is only moderately larger than the 0.09 rms scatter in the $(g - r)$ color of BCGs in the Sloan Digital Sky Survey (SDSS) found by Stott et al. (2012). The blue-core systems extend an even further range in $(g' - r')$ color, which is likely a result of the influence of recent star formation. In some cases the additional blue luminosity is enough to change the core color while in others it is not. Because the color shown in Figure 4.7 is measured using apertures set to the effective radius in the r' or R observations, the overall influence of the assumed recent star formation is dependent on the relative extent of the blue-core compared to the effective radius.

The three BCGs displaying the strongest emission lines in their spectra (Abell2390, Abell1835, MS1455+22) all have significantly blue rest-frame colors with $(g' - r') < 0.55$. We also note that these systems all show extreme fluxes in the [OII] 3727 line, which is not shown in Figures 4.1 through 4.5. Using either the $(B\&R)$ or $(g'\&r')$ filter

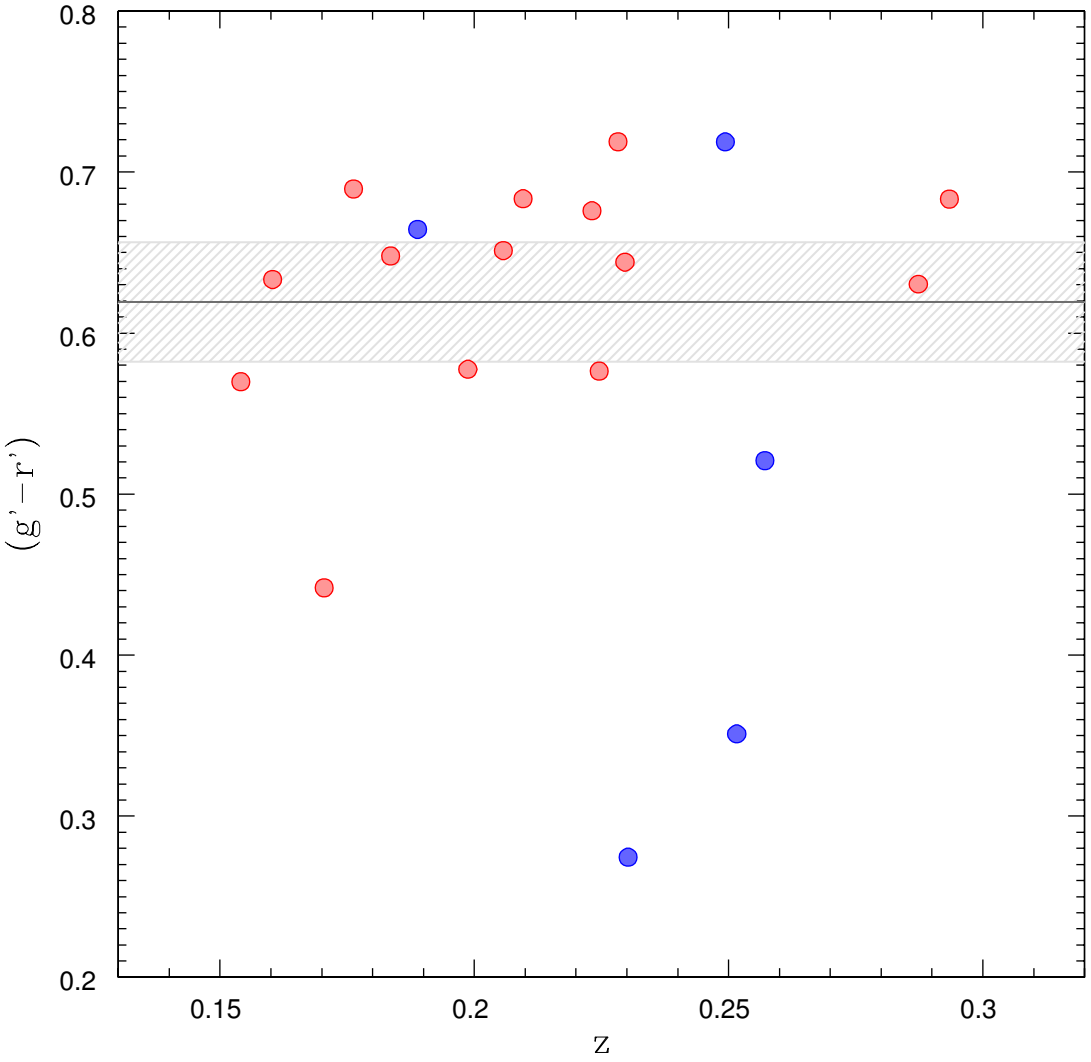

Figure 4.7: Rest frame $(g' - r')$ color as a function of redshift z. K-corrections are based on color-matching to synthetic spectra of a single burst of star formation generated with the code of Charlot and Bruzual (2007). The symbols are color coded according to the BCG core color found in Bildfell et al. (2008).

combinations, there are bright emission lines affecting both the red and blue filters. It is an interesting problem to consider how much of the anomalously blue color in the cores of these BCGs can be attributed to the flux from bright emission lines. To resolve this requires the measurement of both the emission lines and continuum fluxes, along with their contribution to the magnitudes through convolution with the detailed filter-response curves. Furthermore, the contributions from emission lines and continuum are likely to have different radial dependancies, which would also need to be taken into account to match the varying apertures (r_e) used to create Figure 4.7. Such an investigation is beyond the scope of the work discussed here but will be examined in a future paper.

There is one BCG in Figure 4.7 at $z \sim 0.17$ with an anomalously blue color of $(g' - r') \sim 0.45$, given that it is identified as a red-core system. We identify this object as the BCG in Abell 586. The effective radius of this galaxy is $\sim$ 60kpc, and its color within this aperture is dominated by the outer envelope. The extended color profile shows a steep gradient towards the blue beyond 10 kpc (see Figure 2.14). Examination of the red-sequence of Abell 586 shown in Figure A.4 does not show any evidence for large zero point shifts in the photometry.

Table 4.2: Fundamental Plane Data. We list here all of the data used to conduct our analysis of the BCG Fundamental Plane as well as the BCG dynamical masses.

Name	r_e kpc	$\log \langle I \rangle_e$ $L\odot \mathrm{pc}^{-2}$	σ km s^{-1}	χ^2/DOF	$\log M_{dyn}$ $M_\odot$	$T_x(0.3R_{500})$ keV
A1689	$46.6^{+0.4}_{-0.3}$	$1.727^{+0.004}_{-0.005}$	344± 26	0.625	12.54± 0.07	10.7
A1763	$25.5^{+0.2}_{-0.2}$	$2.078^{+0.006}_{-0.006}$	386± 14	0.494	12.38± 0.03	6.4
A1835	$66.4^{+0.6}_{-0.5}$	$1.386^{+0.006}_{-0.006}$	217± 45	0.351	12.30± 0.18	8.1
A1942	$43.7^{+0.2}_{-0.2}$	$1.689^{+0.003}_{-0.003}$	298± 10	0.290	12.39± 0.03	4.7
A209	$89.8^{+0.6}_{-0.5}$	$1.324^{+0.004}_{-0.004}$	296± 29	0.341	12.70± 0.08	7.7
A2104	$56.5^{+0.4}_{-0.4}$	$1.401^{+0.005}_{-0.005}$	266± 22	0.455	12.40± 0.07	6.1
A2259	$44.9^{+0.5}_{-0.4}$	$1.679^{+0.007}_{-0.008}$	249± 26	0.018	12.25± 0.09	5.7
A2261	$36.1^{+0.1}_{-0.1}$	$2.022^{+0.003}_{-0.003}$	421± 37	0.233	12.61± 0.08	8.7
A2390	$18.4^{+0.3}_{-0.2}$	$1.983^{+0.010}_{-0.012}$	273± 25	0.191	11.94± 0.08	9.2
A2537	$46.4^{+0.4}_{-0.5}$	$1.709^{+0.007}_{-0.006}$	310± 7	0.217	12.45± 0.02	15.5
A267	$76.7^{+0.7}_{-0.7}$	$1.514^{+0.007}_{-0.007}$	346± 11	0.362	12.76± 0.03	8.1
A383	$27.0^{+0.2}_{-0.1}$	$2.072^{+0.004}_{-0.004}$	412± 68	0.291	12.46± 0.15	5.8
A586	$58.0^{+0.5}_{-0.5}$	$1.462^{+0.005}_{-0.005}$	338± 26	0.184	12.62± 0.07	5.9
A611	$34.4^{+0.3}_{-0.3}$	$1.896^{+0.006}_{-0.007}$	327± 20	0.541	12.37± 0.05	5.8
A68	$85.8^{+0.8}_{-0.8}$	$1.172^{+0.006}_{-0.006}$	324± 14	0.246	12.76± 0.04	7.1
A963	$60.0^{+0.3}_{-0.4}$	$1.598^{+0.004}_{-0.004}$	358± 11	0.262	12.69± 0.03	7.1
MS0440p02	$102.0^{+0.3}_{-0.3}$	$1.341^{+0.002}_{-0.002}$	354± 10	0.466	12.91± 0.02	4.8
MS0906p11	$55.3^{+0.4}_{-0.3}$	$1.557^{+0.004}_{-0.005}$	372± 33	0.298	12.68± 0.08	4.3
MS1455p22	$24.8^{+0.5}_{-0.5}$	$2.157^{+0.015}_{-0.013}$	352± 9	0.190	12.29± 0.02	6.0

4.6 Fundamental Plane

The Fundamental Plane (FP) describes a tight relation between the dynamical and structural properties (σ, r_e, $\langle I_e \rangle$) of early-type galaxies, the discovery of which is usually attributed to Dressler et al. (1987) and Djorgovski & Davis (1987). The FP relation exhibits a smaller intrinsic scatter than similar well known galaxy scaling relations like the Kormendy relation and Faber-Jackson relation, which have both been shown to be equivalent to various projections of the FP. One of the reasons that the FP, and other galaxy scaling relations, have garnered so much attention is because they are widely believed to be the consequence of the rules that govern the formation and evolution of massive (elliptical) stellar systems. Furthermore the low intrinsic scatter of the FP makes it an excellent tool for studying mass-to-light ratios and measuring distances.

In this section we combine the measured values of σ, r_e and $\langle I \rangle_e$ in order to construct and investigate the properties of the FP of the BCGs in our sample. All of the data used for this analysis is listed in table 4.2. To construct the FP of BCGs we fit a model to our data of the form:

$$\log(r_e) = \alpha \log(\sigma) + \beta \log(\langle I \rangle_e) + \gamma \tag{4.10}$$

where the model coefficients (α, β, γ) define a plane in $(r_e, \log(\sigma), \log(\langle I \rangle_e))$-space. We follow the 'orthogonal fit' procedure of Jorgensen et al. (1996). This procedure is based on varying α and β in order to minimize the sum of the absolute residuals (Δ) perpendicular to the plane, which can be written as follows:

$$\sum_{i=1}^{N_{BCG}} |\Delta_i| = \sum_{i=1}^{N_{BCG}} \left| \frac{\log(r_e)_i - \alpha \log(\sigma)_i - \beta \log(\langle I \rangle_e)_i}{\sqrt{1 + \alpha^2 + \beta^2}} \right| \tag{4.11}$$

where N_{BCG} describes the total number of galaxies in our sample. The third parameter γ is then determined after fitting for α and β by solving equation 4.10 for each BCG, obtaining a set of γ_i's. We then take the median value of γ_i as the best fit value of γ. We find the best fit parameters for equation 4.10 are $\alpha = 1.24 \pm 0.08$, $\beta = -0.80 \pm 0.11$ and $\gamma = (0.3 \pm 2.0) \times 10^{-4}$. The errors quoted on the best fit parameters are determined from a bootstrapping procedure using 256 realizations. The relevant values are consistent with the best fit FP parameters of Jorgensen et al. (1996) who find $\alpha = 1.24 \pm 0.07$ and $\beta = -0.82 \pm 0.02$ for their full sample. When considering only the subsample of galaxies with $\log \sigma > 2.0$, however, Jorgensen et

al. (1996) find that the best fit FP parameters are $\alpha = 1.35 \pm 0.05$, $\beta = -0.82 \pm 0.03$; indicating a marginally inconsistent α when comparing with our results. Our best fit value of γ is consistent with zero, which is to be expected because we calculate r_e in kpc using the z-dependent angular-diameter distance and the surface brightness data have already been corrected for the effects of cosmological dimming.

We show in 4.8 the FP of the BCGs in our sample as viewed along the edge-on projection indicated by the best fit parameters α and β described above. We measure the scatter in the y-direction to be 0.076, which is comparable but slightly smaller than that found in Jorgensen et al. (1996) using their entire sample. When restricted to the galaxies with velocity dispersions above 100 km s^{-1}, a more appropriate comparison with our sample, they measure a scatter of 0.074, which is nearly identical to our own. Taking the mean error on the combination of $\alpha \log(\sigma) + \beta \log(\langle I \rangle_e)$ we find that the typical (random) uncertainty in the y-direction is 0.037. Using this value we 'subtract in quadrature' from the full observed scatter to obtain an estimate of the intrinsic scatter (δ_{int}) in the FP $\delta_{int} = (0.076^2 - 0.037^2)^{1/2} = 0.066$. We also calculate an error on the intrinsic scatter using a bootstrap method to obtain $\delta_{int} = 0.066 \pm 0.010$. We stress that this value of (δ_{int}) is derived while neglecting any potential contributions from sources of systematic uncertainty and should accordingly be taken as a conservative upper limit. If the contribution from systematics is comparable or larger than the random measurement error then the intrinsic scatter would be decreased. However, the $\delta_{int} = 0.066$ measured here for the BCG FP is only marginally larger than the $\delta_{int} = 0.057$ found by Jorgensen et al. (1996) for galaxies with $\sigma > 100$ km s^{-1} and is less than their value of $\delta_{int} = 0.070$ found for their entire sample. The comparable intrinsic scatter estimates suggest that the contribution from systematics in our measurements are insignificant when compared with the level of random error. Alternatively, the systematics may be significant but then the real intrinsic scatter would need to be even less than the $\delta_{int} = 0.066$ quoted above, which would indicate that BCGs are a more well behaved subgroup of galaxies than more regular cluster ellipticals and lenticulars. Lastly, as mentioned in §4.5, our data have not been corrected for passive evolution of BCG stellar populations over time. The effect of passive evolution correction on the scatter measured in the FP is expected to be small here, since the redshift range of our targets is narrow. Nonetheless, if applied, we expect that correction for passive evolution would act to decrease the measured intrinsic scatter even further.

The BCGs in Figure 4.8 are color-coded according to the core-color classification

of Bildfell et al. (2008). The blue symbols represent the blue-core systems, thought to host sites of recent star formation, while the red symbols represent the more ordinary BCGs that are similar in color to non-BCG ellipticals. Given that we estimate a significant amount of intrinsic scatter (see above) it is interesting that the BCGs do not segregate according to core color along the observed width of the fundamental plane. Equivalently, we find no relationship between the BCG FP residuals and the color of their cores. To explore the possible effects of cluster environment we compare the FP residuals to the results from the cluster X-ray analysis of Chandra and XMM-Newton data, presented in Chapter 2. We find no obvious correlations of BCG FP residual with either the central entropy (S_0) nor central cooling time ($t_{c,0}$) of the host cluster. The lack of FP residual correlations with BCG core-color, S_0 and $t_{c,0}$ of the host cluster (all of which are probes of the cooling state of the ICM) indicates that the source of intrinsic scatter in the FP is sufficiently distinct from the mechanism which gives rise to cool-cores in clusters.

In Figure 4.9 we plot our data using the (σ, r_e, $\langle I_e \rangle$) combinations that correspond to the edge-on FP view according to the analysis of Jorgensen et al. (1996). The Jorgensen et al. (1996) one-to-one relation is shown as a solid line overplotted with the data. The dashed line indicates the results of a weighted least-squares fit to our data for the coordinate combinations $x = \log(r_e)$ and $y = 1.24\log(\sigma) - 0.83\log(\langle I \rangle_e)$, which is found to be $y = 1.015x - 0.029$. While this model does not have a simple physical interpretation, it is useful for evaluating the level of agreement between our FP and that of Jorgensen et al. (1996). This best fit model for BCGs (dashed line in Figure 4.9) appears to agree well with the Jorgensen et al. (1996) FP, however, the results are not identical. Focusing on the y-intercept alone, this implies a difference in the combination $1.24\log(\sigma) - 0.83\log(\langle I \rangle_e)$ of -0.029. As mentioned earlier, we have not included any corrections for the passive evolution (dimming) of the stellar populations that is expected between the observed epoch and $z = 0$. Attributing all of the observed difference in y-intercept to this effect implies that for a passive evolution correction parameterized by $\Delta\mu = \eta\log(1+z)$ the coefficient η required to obtain a null y-intercept is $\eta \sim 1.1$, which is reasonable for old, passively evolving elliptical galaxies. Based on this calculation, we conclude that the small difference observed in the Jorgensen et al. (1996) FP projection can be entirely accounted for by the effects of passive evolution.

Figure 4.10 shows the combination of (σ, r_e, $\langle I_e \rangle$) that yields the face-on projection of the fundamental plane according to Jorgensen et al. (1996). Our data are shown as

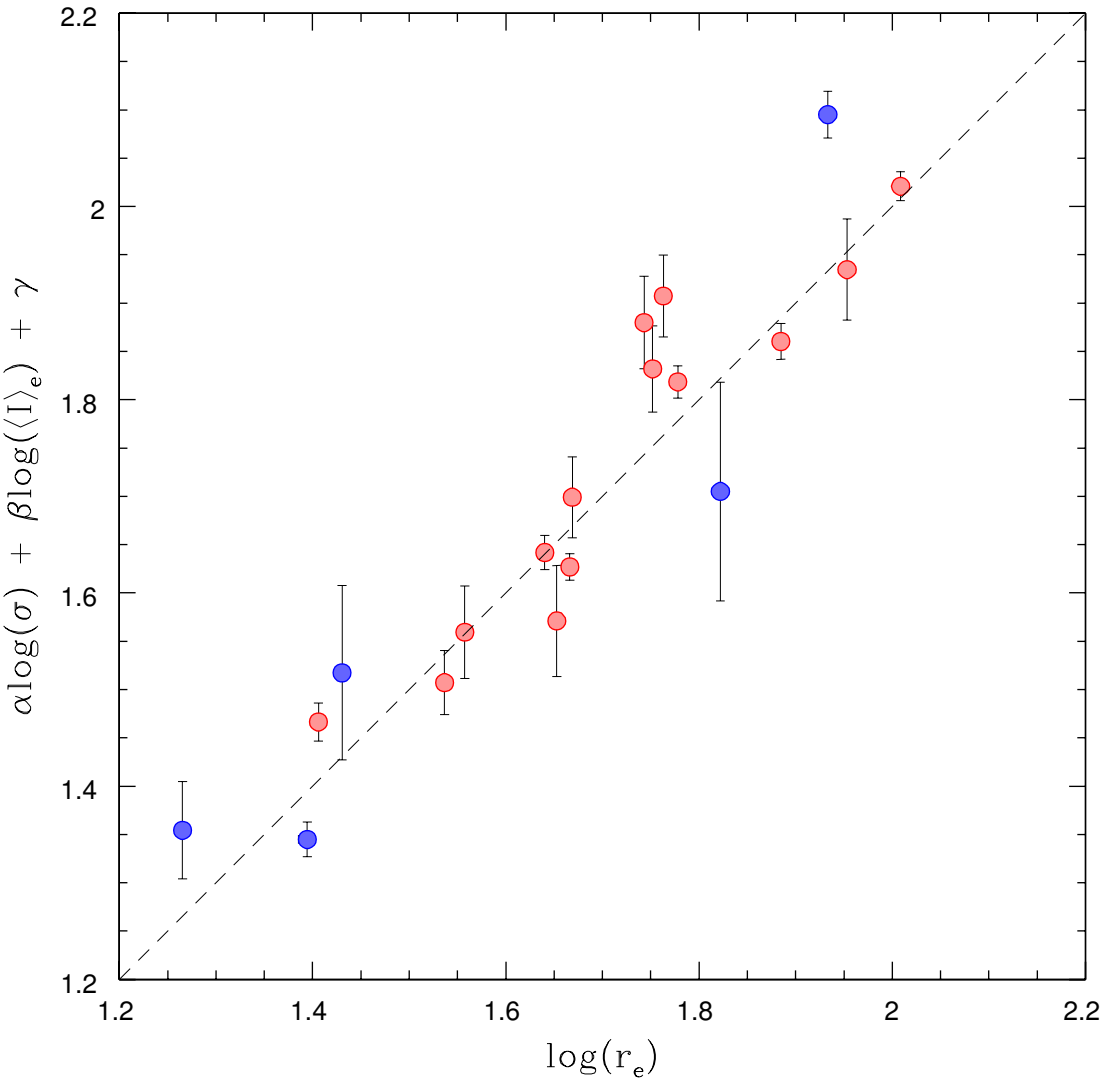

Figure 4.8: Edge-on projection of the fundamental plane for the BCGs in our sample using a model described by $\log(r_e) = \alpha\log(\sigma) + \beta\log(\langle I\rangle_e) + \gamma$. The solid line shows the relationship predicted by the best fit parameters (α, β, γ) found to be $(1.24, -0.80, 3 \times 10^{-5})$, respectively. Blue and red symbols denote the BCG core-color classification (Bildfell et al. 2008). The scatter in the y-direction is measured to be 0.076. When measurement error is accounted for we estimate an intrinsic scatter in the y-direction is 0.066, which is similar to that found by Jorgensen et al. (1996).

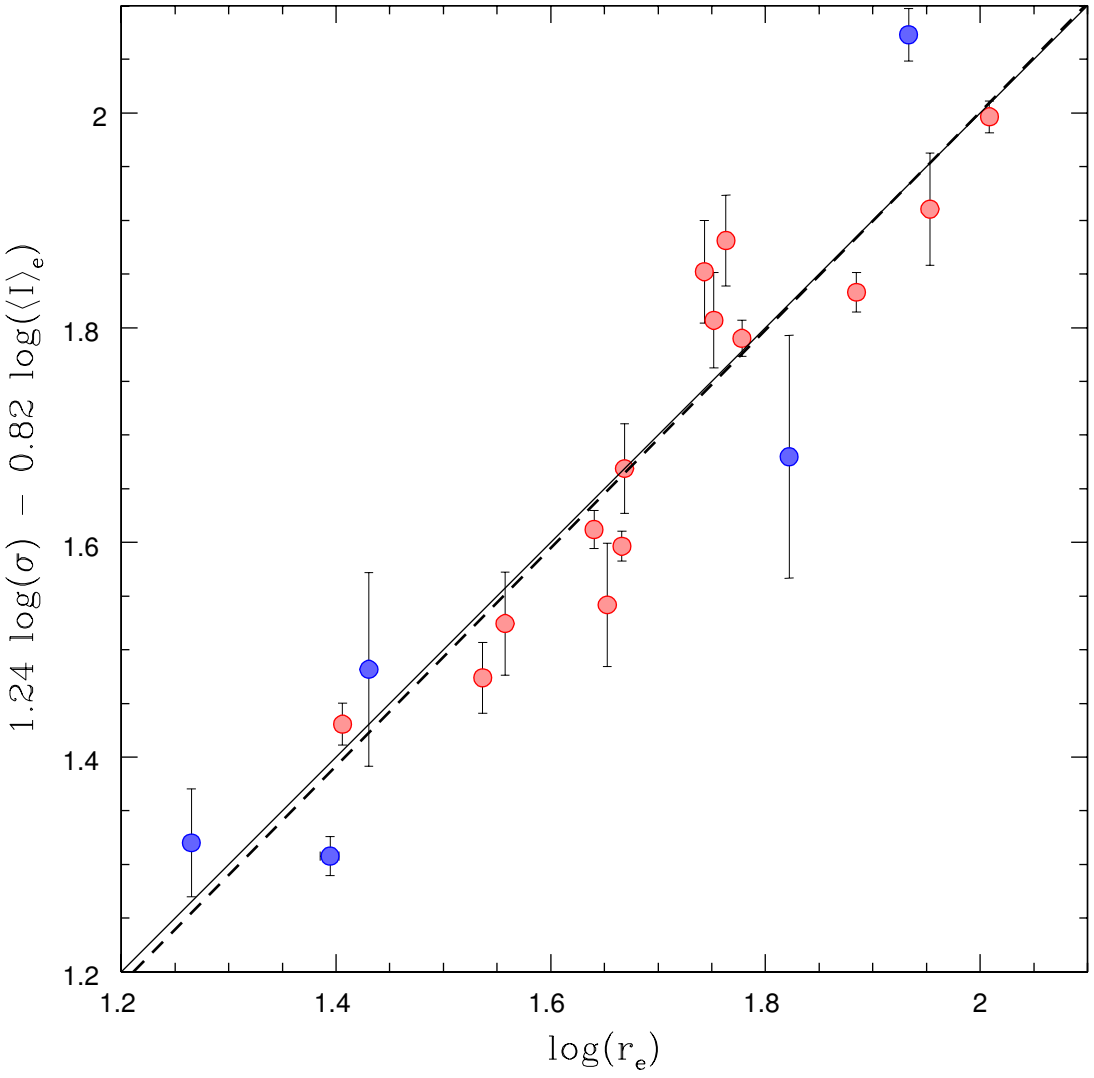

Figure 4.9: Combination of (σ, r_e, $\langle I_e \rangle$) corresponding to the edge-on view of the FP as measured by Jorgensen et al. (1996). Blue (red) symbols correspond to the blue-core (red-core) classification of Bildfell et al. (2008). The solid line indicates the best fit FP relation found by Jorgensen et al. (1996). The dashed line show the results of a linear fit $y = a_0 + a_1 x$ for our BCG sample.

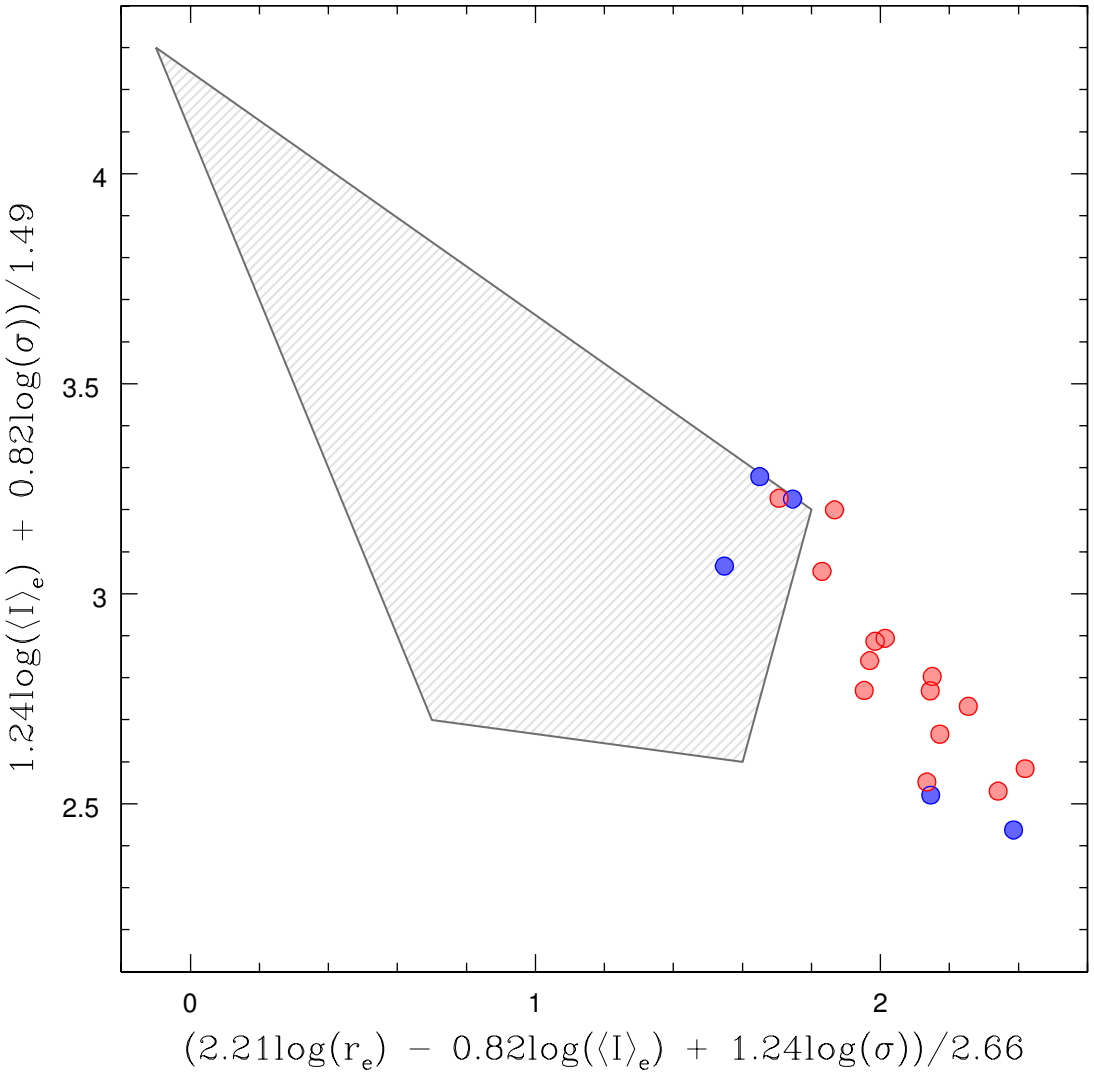

Figure 4.10: Combination of (σ, r_e, $\langle I_e \rangle$) corresponding to the face-on view of the FP as measured by Jorgensen et al. (1996). Blue (red) symbols correspond to the blue-core (red-core) classification of Bildfell et al. (2008). The grey hatched area shows the approximate region of parameter space probed by Jorgensen et al. (1996), showing little to no overlap with our own sample.

the red (red-core) and blue (blue-core) symbols, while the grey shaded region shows the approximate data range investigated by Jorgensen et al. (1996). It is clear that the two studies are probing very different regions of galaxian parameter space, which is expected since BCG represent the most massive galaxies exclusively. Furthermore, our data occupy a much narrower range compared to theirs, which may explain the relatively large uncertainty on our best fit β parameter. Nonetheless, it is interesting that we achieve such good agreement on α and β given the large differences sample properties.

Given the good agreement between our results and those of Jorgensen et al. (1996) we conclude that there is no significant evidence for a change in the 'tilt' of the FP between BCGs and more regular cluster ellipticals. Although there is some tension in the α parameter when comparing our results to those obtained for the subsample of Jorgensen et al. (1996) galaxies with $\log \sigma > 2.0$, this inconsistency is only marginal. The observed agreement between FP for these two similar but distinct families of galaxies is qualitatively consistent with the results of Oegerle & Hoessel (1991) who find that a single FP (parameterized by $re, \langle\mu\rangle_e, \sigma$) is a good match to both BCGs and regular ellipticals. Our results may be at odds with those of von der Linden et al. (2009), who find that 'tilt' of the FP varies between BCG and a control sample of non-BCGs. However, they argue that this difference is driven primarily by the galaxies with small radii and/or high surface brightness, the likes of which are not present in our sample. Due to this difference in sample properties, it is difficult to definitively claim disagreement between our study and theirs.

4.7 Dynamical Mass

Measuring accurate galaxy masses is a challenging task. Most often in studies of the evolution of galaxies one must rely on masses inferred from luminosities measured in a particular wave band, which are then converted into masses via a more locally calibrated mass-to-light ratio. This sample provides an excellent opportunity to study the masses of BCGs using the kinematics of their stellar populations to obtain a dynamical mass; a more direct measure. We estimate the dynamical mass inside the effective radius as:

$$M(r_e) = f\frac{\sigma^2 r_e}{G} \tag{4.12}$$

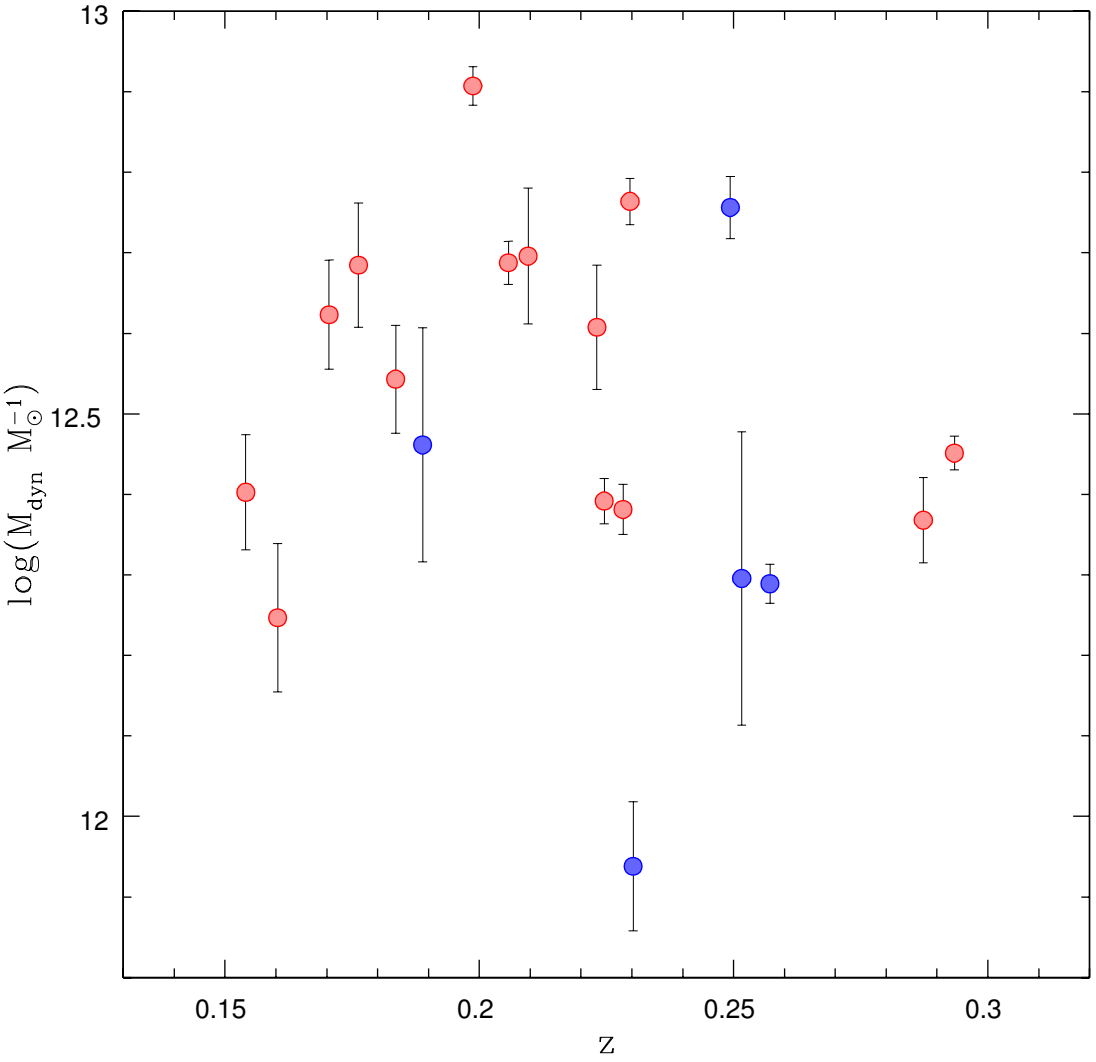

Figure 4.11: The BCG dynamical mass M_{dyn} interior to r_e versus redshift z. Data points are color coded according to the presence (blue) or absence (red) of blue cores in the BCG optical surface brightness profile (Bildfell et al. 2008).

where the coefficient f captures the effects of varying the geometry of the mass distribution as well as the effects of orbital anisotropy. We follow the procedure of von der Linden et al. (2007) for measuring BCG dynamical masses and select a value of $f = (1.65)^2$ (Padmanabhan et al. 2004).

Figure 4.11 shows the resulting dynamical masses of the BCGs in our sample as a function of z. The mean dynamical mass of our BCG sample is $3.58{\times}10^{12}$ $M_{\odot}$ with a standard deviation of $1.79{\times}10^{12}$ $M_{\odot}$. When considered along with the typical stellar mass of BCGs of a few 10^{11} $M_{\odot}$ (Stott et al. 2012) this implies a stellar mass fraction in these systems of order ~ 0.1. The true stellar-to-dynamical mass ratio is likely even smaller than this since the stellar mass is a 2D mass while the dynamical mass is a 3D mass. It is estimated that for early-type galaxies in the SDSS, the 3D stellar mass within the half-light radius is $\sim 50\%$ of the total 2D stellar mass (Padmanabhan et al. 2004). From Figure 4.11 it is apparent that there is no correlation between M_{dyn} and z for our sample of BCGs. Furthermore, there is no systematic difference in dynamical mass between blue-core and red-core systems. This is in qualitative agreement with the fact that any recent star formation in BCGs at this redshift represents at most only a few percent of the stellar mass of these systems (Pipino et al. 2009).

We also show, in Figure 4.12, the dynamical masses of BCGs as a function of their effective radii. We note that these quantities are not independent, as can be seen from equation 4.12. Excluding the BCGs with the most extreme high and low effective radii however, it is interesting that at fixed r_e there is a large range in M_{dyn}. This illustrates that the observed range in dynamical mass is not simply a consequence of a large range in effective radii and that, neglecting biases introduced by eccentricity and orbital anisotropy, there are genuine differences in the masses of BCGs of similar size.

We fit a linear relation $\log(M_{dyn}) = a_0 + a_1 \log(r_e)$ using a least-squares fitting procedure in order to explore how accurately one can predict the dynamical mass of a BCG given its effective radius for an $r^{1/4}$ surface-brightness profile. The best-fit relation has a slope of $a_1 = 0.87$, a normalization of $a_0 = 11.04$ and is shown as the dashed line in Figure 4.12. The scatter about the best fit is measured to be 0.14 in the $\log(M_{dyn})$-direction and appears to be dominated not by measurement error but by intrinsic scatter. This should be viewed as more of a lower limit on the scatter in the true relation between the effective radius and dynamical mass since the latter was estimated using the former (Equation 4.12), which will act to artificially reduce the observed scatter.

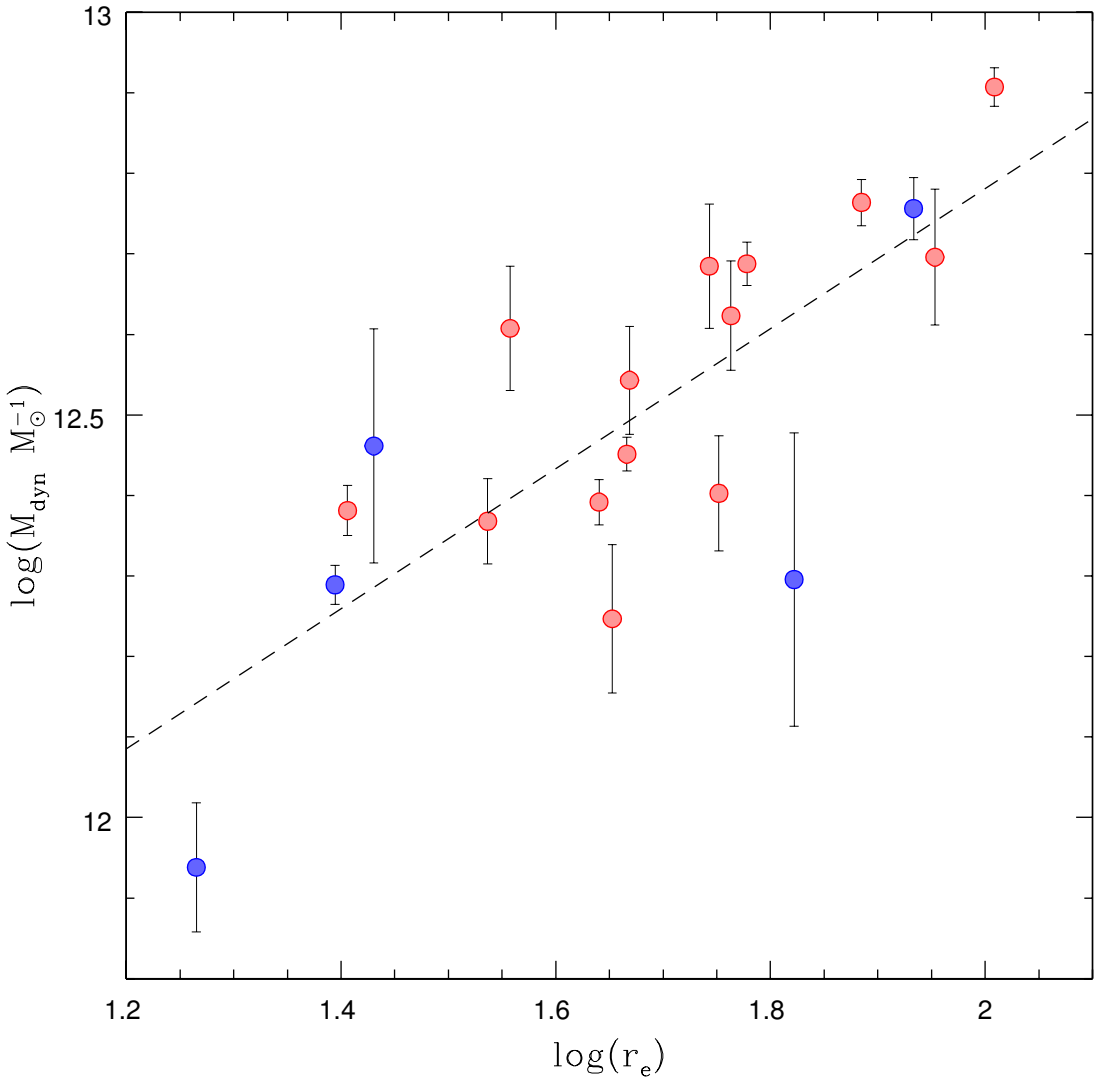

Figure 4.12: The BCG dynamical mass M_{dyn} interior to r_e versus effective radius r_e. Data points are color coded according to the presence (blue) or absence (red) of blue cores in the BCG optical surface brightness profile (Bildfell et al. 2008). The dashed line shows the best fit relation $\log(M_{dyn}) = a_0 + a_1 \log(r_e)$ where $a_0 = 11.04$ and $a_1 = 0.87$.

4.7.1 The Maximum Mass for BCGs

There is a longstanding notion that BCGs represent a maximum galaxy mass and that once a galaxy reaches a certain mass ceiling it must cease to grow. One test of the validity of this picture is to examine whether or not the mass of BCGs correlates with the mass of the main cluster halo. Several studies in the literature have sought to test this condition (eg. Postman et al. (1995), Lin et al. (2004)), albeit indirectly, using BCG luminosity (B and K -band) and the richness and (low-resolution) X-ray temperature for proxies of the cluster masses.

To investigate this more directly, we plot in Figure 4.13 the dynamical mass of the BCG versus the X-ray temperature as measured at $0.3R_{500}$ from the analysis of high-resolution X-ray data (Chandra, XMM-Newton) presented in Chapter 2. The X-ray temperature is a good proxy for the cluster mass as shown in Mahdavi et al. (2013), which shows that the scatter in the X-ray to weak lensing mass correlation inside R_{500} is only 17%. We interpolate the X-ray temperature at $0.3R_{500}$ as this distance is well outside the core where the temperature is unaffected by AGN contamination or central temperature decrements associated with radiative cooling. Using temperatures at larger radii such as $0.5R_{500}$ or R_{500} leads to increased measurement errors due to a drop in X-ray surface brightness towards the outer regions of the cluster. The data in Figure 4.13 show that there is no obvious correlation between M_{dyn} of the BCGs and their host cluster T_x, and by proxy, cluster mass. For completeness we also compare in Figure 4.14 the dynamical mass estimate for our BCGs versus the number of giants (n_g) within an aperture of 750 kpc from the BCG position, where available, as measured from Bildfell et al. (2012). The number of giants provides another mass proxy for the cluster mass through the mass-richness relation (see Yee & Ellingson 2003, Rozo et al. 2009). The work of Bildfell et al. (2012) concentrated only on sufficiently rich clusters that were observed using MegaCam and as a result n_g is only available for 9 systems that overlap with our current sample. From Figure 4.14 we find a lack of correlation between the BCG dynamical mass and the number of giants. This is in qualitative agreement with the lack of correlation between M_{dyn} and $T_x(0.3R_{500})$ and should be expected since the X-ray temperature is a superior proxy for cluster mass compared to richness.

These results support the case for an upper limit on the masses of BCGs, at least at the cluster mass scales probed by our survey. The data imply that for clusters in this mass range the mass of BCGs is $(2.9 \pm 1.8) \times 10^{12} M_{\odot}$. To the best of our

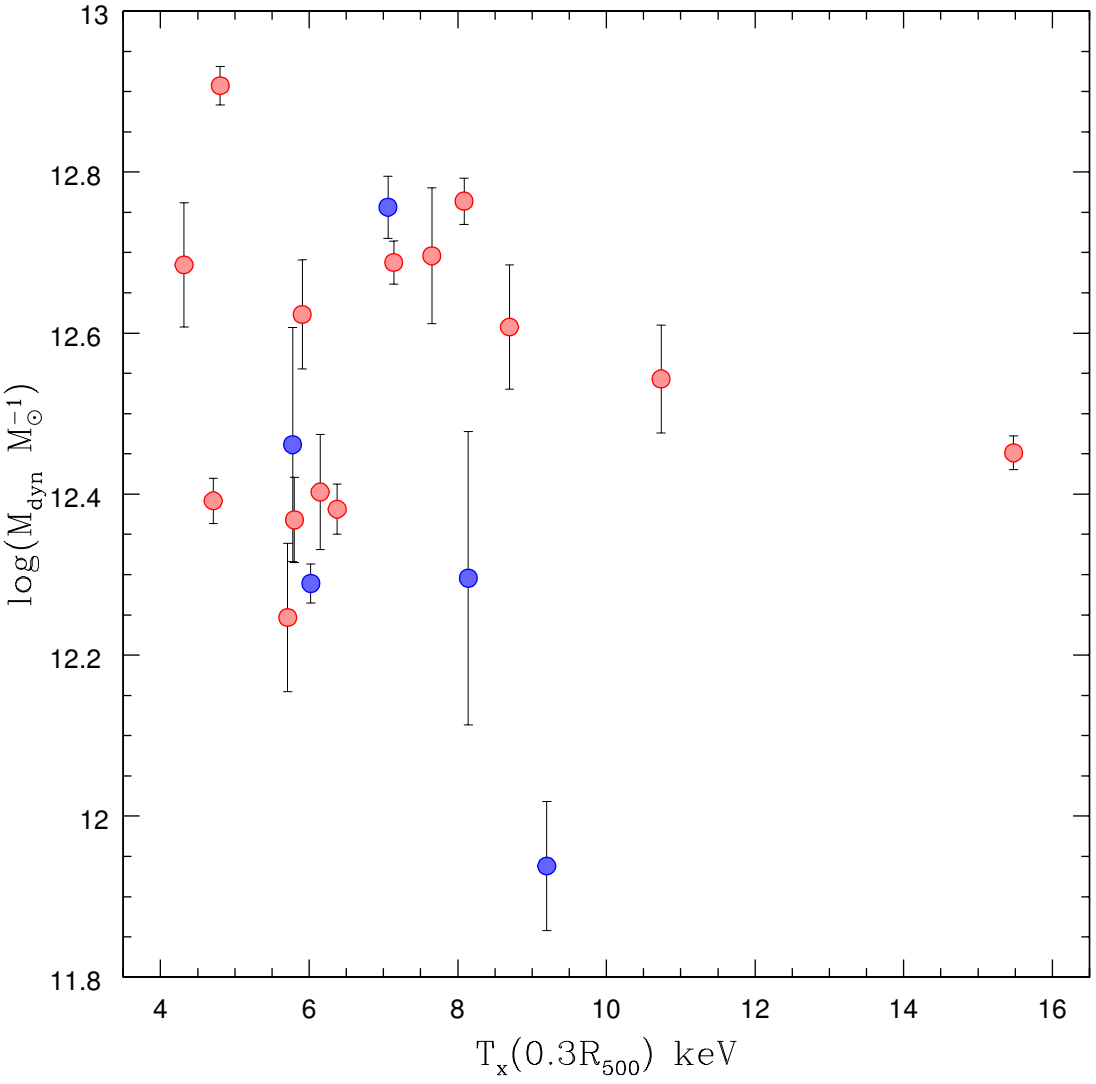

Figure 4.13: The BCG dynamical mass M_{dyn} interior to r_e versus the X-ray temperature (T_x) measured at $0.3R_{500}$. Data points are color coded according to the presence (blue) or absence (red) of blue cores in the BCG optical surface brightness profile (Bildfell et al. 2008).

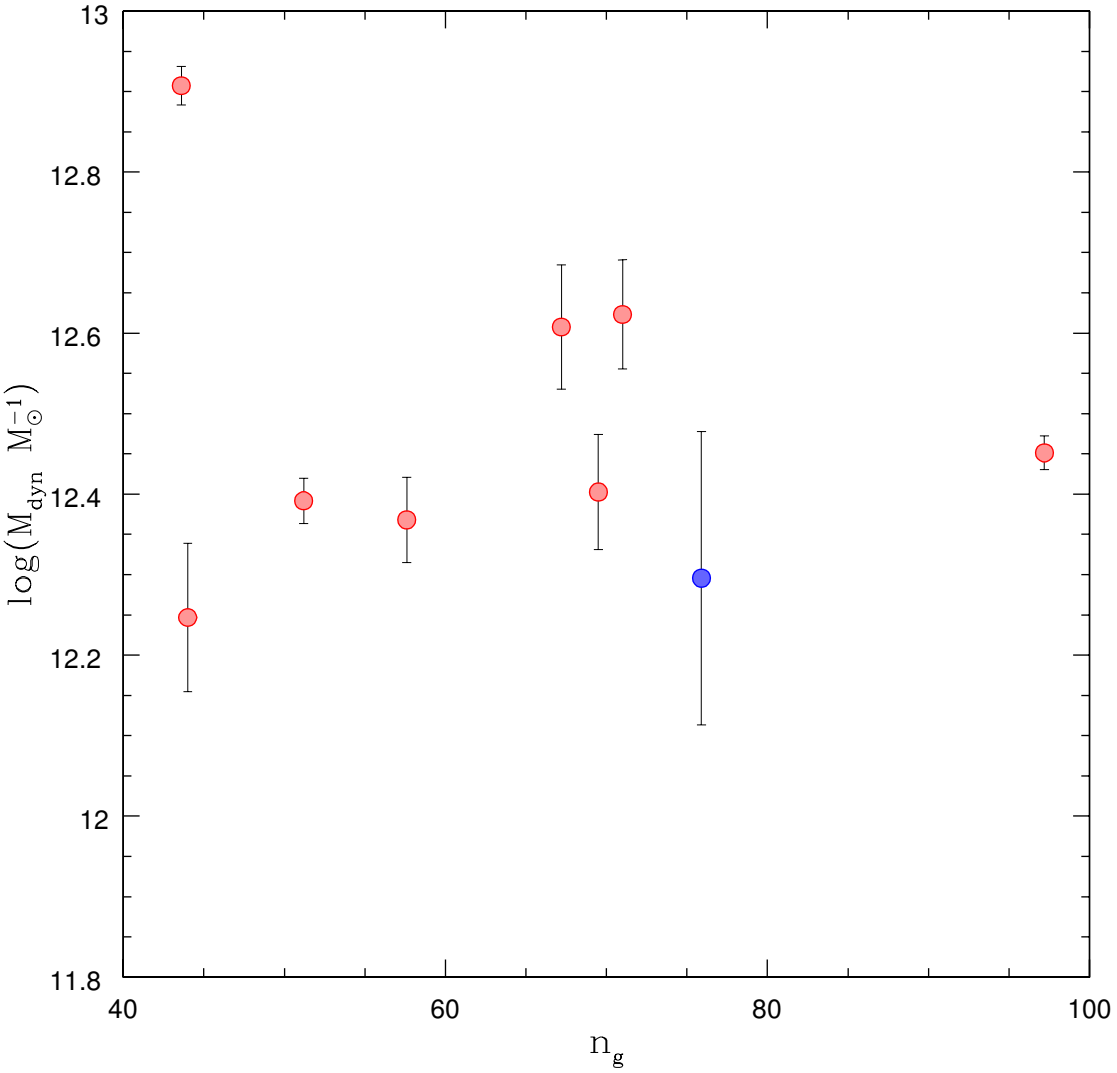

Figure 4.14: The BCG dynamical mass M_{dyn} interior to r_e versus the number of giants measured in Bildfell et al. (2012). Data points are color coded according to the presence (blue) or absence (red) of blue cores in the BCG optical surface brightness profile (Bildfell et al. 2008).

knowledge this represents the most direct BCG mass to cluster mass comparison performed to date. A consequence of this scenario is that late-time major mergers with the BCG, if taking place at significant rates, must be an extremely efficient channel for the production of intra-cluster stars (ICS).

If we assume a constant BCG B-band mass-to-light ratio (M/L_B) as a function of cluster mass, the lack of dependence of M_{dyn} on T_x and n_g is in qualitative agreement with the findings of Postman et al. (1995), who find that there is no correlation between B-band luminosity and cluster richness. It is more difficult, however, to reconcile the findings of Lin et al. (2004), who observe a weak correlation between the K-band luminosity and cluster mass (via X-ray temperature). Taken together, these results seem to suggest that M/L_B is independent of cluster mass but the K-band mass-to-light ratio (M/L_K) is not. Alternatively, since the L_K - M_{T_x} relation of Lin et al. (2004) is only a weak correlation ($L_K \propto M_{T_x}^{0.26}$) with a fairly large scatter of 34%, it may be that with our smaller sample of BCGs (19 compared to their ~ 40 clusters in the same mass range) is insensitive to such a weak dependence on cluster mass. A direct comparison of BCG masses and luminosities is further complicated by the different techniques used in these studies. For instance we measure the mass interior to the effective radius, whereas Lin et al. (2004) use isophotal estimates of the luminosity. Similarly, Lidman et al. (2012) find a correlation between cluster mass (using a variety of proxies) and BCG stellar mass (albeit with a large intrinsic scatter). This apparent disagreement with our results may again be a consequence of the low number of systems in our sample with which to probe a BCG mass-cluster mass relation of significant scatter. Alternatively, it may simply reflect the difference in the range of cluster masses probed between our study and theirs, which contains a significant number of clusters with lower masses (few $10^{14} M_{\odot}$).

It is also worth considering the selection effects associated with the requirement that all of the BCGs investigated here are all within 15 kpc in projection from the peak in their host cluster X-ray emission, thus likely to be in the deepest regions of the cluster potential. Small cluster-centric distance may aid in BCG mass accretion as infalling satellite galaxies experience enhanced dynamical friction in this region via interaction with a denser cluster environment. Furthermore, this extremely dense ambient environment may impose a mass-ceiling for BCG growth via competition between the BCG and cluster potential. Specifically, as mass is added to the BCG via mergers, the BCG is dynamically heated, increasing the ratio of its size-to-tidal radius. This causes the outer regions to become more loosely bound, enhancing the

rate of tidal stripping by the cluster potential, which contributes directly to the ICS.

4.8 Conclusions

In this chapter we measure the line-of-sight velocity dispersions (σ) from medium-resolution optical spectra for 19 BCGs selected from the CCCP survey. We combine the resulting σ measurements with the effective radii (r_e) and average effective intensities ($\langle I \rangle_e$) to explore the properties of the fundamental plane for BCGs. In addition to this, we use the σ and r_e values, along with some simplifying assumptions, to estimate the dynamical mass (M_{dyn}) interior to the effective radius. We summarize our most important findings below.

We present deep co-added spectra for the 19 BCGs in our sample. The spectra are extracted using an extraction aperture with a constant physical diameter of 10 kpc along the slit, representing the 'central' spectra. Though we present only a limited portion of the full observed wavelength range here, these spectra show a range of continuum shapes, absorption and emission line strengths. All of the spectra analyzed show some form of Balmer line activity, either via bright emission lines or absorption line infilling. The BCGs with the strongest color profile inversions in their cores from Bildfell et al. (2008) are also the ones that host the strongest emission lines. A full analysis of emission line strengths, absorption line indices and stellar populations, along with constraints on their radial dependence, will be presented in future work.

The spectra described above are fit with a set of stellar templates using the pPXF code of Cappellari & Emsellem (2004) to extract the central velocity dispersion σ for each BCG. We find that the BCG show a wide range in central velocity dispersion from $217 < \sigma < 421$ km s^{-1}. Somewhat surprisingly, the BCGs with the most significant optically blue core in our sample (Abell1835) also has the lowest measure of σ.

Combining our σ results with the structural parameter r_e and μ_e (measured for an $r^{1/4}$ in the r'-band) from Bildfell et al. (2008), we investigate the properties of the fundamental plane for BCGs as parameterized by $(\sigma, r_e, \langle I \rangle_e)$. Our BCGs occupy a tight FP that is fit with a model parameterized by $\log(r_e) = \alpha \log(\sigma) + \beta \log(\langle I \rangle_e) + \gamma$, where the best fit values obtained are: ($\alpha = 1.24 \pm 0.08$, $\beta = -0.80 \pm 0.1$, $\gamma = (0.3 \pm 2.0) \times 10^{-4}$). We measure a small but significant intrinsic scatter $\delta_{int} = 0.066 \pm 0.011$ in r_e which agrees well with previous results for regular cluster ellipticals. The presence of intrinsic scatter indicates that additional parameters may be important

in determining the position of a BCG in $(\sigma, r_e, \langle I \rangle_e)$-space. We find, however, that there is no obvious correlation between the BCG FP residuals with either the BCG core-color, nor with the host cluster X-ray properties S_0 and $t_{c,0}$.

Based on the agreement between our BCG FP parameters and those of Jorgensen et al. (1996) for more regular cluster galaxies, we conclude that there is no strong evidence for a change in the 'tilt' (ie. curvature) of the FP over the range in $(\sigma, r_e, \langle I \rangle_e)$ space probed by these data sets.

Using the measured values of r_e and σ, we estimate the dynamical masses (M_{dyn}) of BCGs inside r_e. Comparing M_{dyn} with $T_x(0.3R_{500})$ and n_g, both proxies for cluster mass, we find that the BCG dynamical mass does not correlate with the mass of the host cluster. This suggests that there is a maximum mass for BCGs, which we estimate to be $M_{dyn} = (2.9 \pm 1.8) \times 10^{12} M_{\odot}$. Furthermore, this demonstrates that BCGs can be used as 'standard dumbbells', at least over the large cluster masses probed by our sample.

Future work in this area will include an investigation of BCG dynamical masses in comparison with their g'- and r'-band luminosities. The mass-to-light ratios of BCGs are not yet well constrained and this data set has the potential to improve upon the current state of the literature.

We would like to thank Inger Jorgensen and John Blakeslee for their support and useful discussion. This work is based on observations obtained at the Gemini Observatory, which is operated by the Association of Universities for Research in Astronomy, Inc., under a cooperative agreement with the NSF on behalf of the Gemini partnership: the National Science Foundation (United States), the National Research Council (Canada), CONICYT (Chile), the Australian Research Council (Australia), Ministério da Ciência, Tecnologia e Inovação (Brazil) and Ministerio de Ciencia, Tecnología e Innovación Productiva (Argentina)

4.9 References

Barr, J., Davies, R., Jorgensen, I., Bergmann, M., Crampton, D., 2005, AJ, 130, 445
Barr, J., Jorgensen, I., Chiboucas, K., Davies, R., Bergmann, M., 2006, ApJ, 649L, 1
Bildfell, C., Hoekstra, H., Babul, A, Mahdavi, A., 2008, MNRAS, 389, 1637
Bildfell, C., Hoekstra, H., Babul, A., Sand, D., Graham, M., Willis, J., Urquhart, S., Mahdavi, A., Pritchet, C., Zaritsky, D., Franse, J., Langelaan, P., 2012, MNRAS, 425, 204

Lin, Y., Mohr, J., 2004, ApJ, 617, 879
Caon, N., Capaccioli, M., D'Onofrio, M., Longo, G., 1994, A&A, 286, 39
Cappellari, M., Emsellem, E., 2004, PASP, 116, 138
Djorgovski, S., Davis, M., 1987, ApJ, 313, 59
Dressler, A., Lynden-Bell, D., Burstein, D., Davies, R., Faber, S., Terlevich, R., Wegner, G., 1987, ApJ, 313, 42
Faber, S., Jackson, R., 1976, ApJ, 204, 668
Falcon-Barroso, J., Sanchez-Blazquez, P., Vazdekis, A., Ricciardelli, E., Cardiel, N., Cenarro, A., Gorgas, J., Peletier, R., 2011, A&A, 532, 95
Graham, A., Colless, M., 1997, MNRAS, 287, 221
Hoekstra, H., 2007, MNRAS, 379, 317
Jorgensen, I., Franx, M., Hjorth, J., van Dokkum, P., 1999, MNRAS, 308, 833
Jorgensen, I., Franx, M., Kjaergaard, P., 1996, MNRAS, 280, 167
Lidman, C., Suherli, J., Muzzin, A., Wilson, G., Demarco, R., Brough, S., Rettura, A., Cox, J., DeGroot, A., Yee, H., Gilbank, D., Hoekstra, H., Balogh, M., Ellingson, E., Hicks, A., Nantais, J., Noble, A., Lacy, M., Surace, J., Webb, T., 2012, MNRAS, 427, 550
Kormendy, J., 1977, ApJ, 218, 333
Lynden-Bell, D., Faber, S., Burstein, D., Davies, R., Dressler, A., Terlevich, R., Wegner, G., 1998, ApJ, 326, 19
Mahdavi, A., Hoekstra, H., Babul, A., Bildfell, C., Jeltema, T., Henry, J., 2013, ApJ, 767, 116
Maraston, C., Stromback, G., Thomas, D., Wake, D., Nichol, R., 2009, MNRAS, 394, 107
McNamara, B., Rafferty, D., Birzan, L., Steiner, J., Wise, M., Nulsen, P., Carilli, C., Ryan, R., Sharma, M., 2006, ApJ, 648, 164
Newman, A., Treu, T., Ellis, R., Sand, D., Nipoti, C., Richard, J., Jullo, E., 2013, ApJ, 765, 24
Padmanabhan, N., Seljak, U., Strauss, M., Blanton, M., Kauffmann, G., Schlegel, D., Tremonti, C., Bahcall, N., Bernardi, M., Brinkmann, J., Fukugita, M., Ivezic, Z., 2004, New Astron., 9, 329
Pipino, A., Kaviraj, S., Bildfell, C., Babul, A., Hoekstra, H., Silk, J., 2009, MNRAS, 395, 462
Postman, M., Lauer, T., 1995, ApJ, 440, 28
Rozo, E., Rykoff, E., Evrard, A., Becker, M., McKay, T., Wechsler, R., Koester, B.,

Hao, J., Hansen, S., Sheldon, E., Johnston, D., Annis, J., Frieman, J., 2009, 699, 768
Sanchez-Blazquez, P., Peletier, R., Jimenez-Vicente, J., Cardiel, N., Cenarro, A., Falcon-Barroso, J., Gorgas, J., Selam, S., Vazdekis, A., 2006, MNRAS, 371, 703
Stott, J., Hickox, R., Edge, A., Collins, C., Hilton, M., Harrison, C., Romer, K., Rooney, P., Kay, S., Miller, C., Sahlen, M., Lloyd-Davies, E., Mehrtens, N., Hoyle, B., Liddle, A., Viana, P., McCarthy, I., Schaye, J., Booth, C., 2012, MNRAS, 422, 2213
van Dokkum, P., Franx, M., 1996, MNRAS, 281, 985
van Dokkum, P., Franx, M., Kelson, D., Illingworth, G., 1998, ApJ, 504, L17
von der Linden, A., Best, P., Kauffmann, G., White, S., 2007, MNRAS, 379, 867
Yee H., Ellingson E., 2003, ApJ, 585, 215
Zaritsky, D., Gonzalez, A., Zabludoff, A., 2006, ApJ, 638, 735

Chapter 5

Conclusions

Galaxy clusters represent the ultimate sinks of mass assembly in the Universe. In order to fully understand the evolution of cosmic structure, to explain the mass distribution in the Universe and to predict its future, we must have a clear understanding of the details of cluster formation and evolution. While the majority of the mass in clusters is in the form of an invisible dark matter component, the primary source of empirical constraints, which are necessary to test theoretical predictions, must come from observations of the luminous, baryonic component. Gravitational lensing is perhaps an exception to this, as it probes the cluster potential directly. In this thesis we have concentrated on three important aspects of the stellar content in galaxy clusters. We have focused primarily on the properties of the brightest cluster galaxies (BCGs), however, we also examine some of the statistical properties of a sample of more ordinary, bright cluster galaxies on the red sequence.

A summary of the specific topics explored in this thesis follows here. In chapter 2 we examine the optical color profiles of BCGs for a large sample of 108 galaxies in the combined MENeaCS+CCCP surveys. We focus primarily on the color of the BCG core, which we use as an indicator of recent star formation and/or AGN activity. We confront these data with various X-ray properties of the host clusters in order to aid in understanding the source of cold gas required to fuel the aforementioned activity. In chapter 3 we study the evolution of the ratio of giants-to-dwarfs on the red sequence in a sample of 97 galaxy clusters drawn from the CCCP+MENeaCS surveys, which is supplemented with additional data from the CFHT archive. We use a predefined set of magnitude limits (from De Lucia et al. 2007) with which to identify and measure the number of giants and dwarfs. We combine these statistics with a mass proxy for a subsample of clusters to aid our understanding of the driving

mechanism that governs the evolution in the giant-to-dwarf ratio. In chapter 4 we present optical spectra for a subset of 19 BCGs from the CCCP, taken with GMOS on Gemini North and Gemini South. We fit these spectra with a velocity-broadened set of stellar templates in order to obtain a measure of the line-of-sight component of their central stellar velocity dispersions. These results are then combined with previous measurements of the BCG structural parameters (r_e, μ_e) from Bildfell et al. (2008) in order to estimate BCG dynamical masses and examine the properties of the BCG fundamental plane.

This thesis represents a collection of results obtained over a multi-year research effort. As such there are numerous interesting scientific conclusions within. In the sections that follow, we describe only the most important of these conclusions, but for a more complete description of our conclusions we refer the reader to the 'Conclusions' sections of each individual chapter.

5.1 BCG Color Profiles

We present $(g' - r')$ and $(B - R)$ color profiles for 108 BCGs in clusters in the redshift range $0.05 < z < 0.55$. We find that the majority of the BCGs in our sample have shallow, negative color gradients similar to those observed in more regular elliptical galaxies, consistent with metallicity profiles that decrease from the central region outward. However, we also find that 22% of the BCGs in our sample have spatially resolved inversions in their color profiles such that they get bluer with decreasing radius (blue cores).

Comparing the value of the BCG inner color gradients $\gamma_{(g'-r')}$ with the entropies S_0 and central cooling times $t_{c,0}$ of the ICM in their host clusters, we find that there are thresholds in both S_0 and $t_{c,0}$ above which blue core BCGs are rare, but below which they are almost ubiquitous. Specifically, where X-ray comparison is possible, nearly all blue-core BCGs (13/15) are found to be in clusters with $S_0 < 40$ keV cm^2 and $t_{c,0} < 1$ Gyr. Furthermore, we find that all blue-core BCGs are centrally located in the cluster, with $D_{XO} < 15$ kpc. These results confirm that the blue-core BCG phenomenon is directly linked to the radiative cooling of the ICM. The large angular sizes of the blue regions (greater than the PSF scale) favor the explanation that the recent star formation is responsible for the anomalously blue color and not AGN.

While no strong trend exists between the $\gamma_{(g'-r')}$ of the BCG and metallicity Z of the ICM, we do find that the mean metallicity of blue-core BCGs ($\langle Z/Z_\odot \rangle =$

0.517 ± 0.016) is higher than that of the red-core BCGs ($\langle Z/Z_{\odot} \rangle = 0.487 \pm 0.014$) albeit with marginal significance. This result, when considered with those discussed above, is qualitatively consistent with previous work (Leccardi et al. 2010) finding metallicity enhancement in cool-core clusters (low S_0) compared to non cool-cores (high S_0).

Lastly, we use data from the FIRST survey to examine the relationship between $P_{1.4\mathrm{GHz}}$, S_0 and the BCG core color. All of the 9 visually-identified blue-core BCGs are associated with 1.4 GHz radio sources, however, the majority of BCGs (21/35) in the FIRST survey footprint are not detected. We confirm the presence of an entropy threshold (Cavagnolo et al. 2008) at $S_0 < 40$ keV cm^2, below which all BCGs are radio-bright ($P_{1.4\mathrm{GHz}} > 4.0 \times 10^{25}$ W Hz^{-1}). Below this threshold in S_0 the range in radio power is significantly more broad.

We have demonstrated that for the MENeaCS + CCCP sample the core color of BCGs is correlated with the X-ray properties of the ICM in their host clusters. The leading explanations for the anomalously blue core color are the recent onset of star formation or AGN (or both). The X-ray to optical correlations investigated herein are consistent with this recent activity being linked to the radiative cooling properties of the ICM such that the activity is present in the most strongly cooling systems but absent from the systems which are not strongly cooling. Of the two mechanisms for blue-core production, AGN versus star formation, we have argued that the data favor the star formation scenario. However, if the AGN are able to ionize and heat emission line nebulae at large distances from the central engine in the BCG nucleus then it could be possible to produce similarly extended blue cores. To distinguish between these two scenarios requires a large survey with spatially resolved spectra (eg. using an integral-field unit, long-slit or multi-object spectrograph) that is capable of detecting blue continuum emission from a young stellar population. While some such studies of emission nebulae in BCGs have been done (eg. Edwards et al. 2009, McDonald et al. 2010), they are based on only a few BCGs and lack the sensitivity to the continuum, relying on heating and ionization models to distinguish between these scenarios. The results of these heating and ionization models are not conclusive, though we note that differences exist between their samples and methodology. Edwards et al. (2009) find a mix of ionization mechanisms (star formation, AGN) while McDonald et al. (2012) argue for a single low-ionization source like star formation. More sensitive observations, with larger samples would likely resolve this apparent discrepancy.

5.2 The Giant-to-Dwarf Ratio

We analyzed a large sample of 97 galaxy clusters observed in g' and r' with CFHT-MegaCam. After carefully accounting for several observational biases and statistically removing interloper galaxies using g' and r' galaxy catalogs generated from the CFHTLS Deep fields as a control, we measured the GDR in galaxy clusters over the range $0.05 < z < 0.55$. We find several interesting results, the most important of which we summarize below.

We detect evolution in the GDR over the redshift range $0.05 < z < 0.55$, which can be parametrized by a simple linear relation with z ($GDR = \alpha z + \beta$). The best fit parameters are $\alpha = 0.88 \pm 0.15$ and $\beta = 0.44 \pm 0.03$ with an estimate for the intrinsic scatter in the relation that is consistent with zero.

Varying the method of selecting dwarf and giant galaxies by altering the BCG-centric distance threshold, colour selection criteria or K-correction prescription does not change the GDR significantly. So long as one makes reasonable choices about the selection criteria and K-correction, then varying these parameters cannot hide the signature of an evolving GDR.

The GDR values found here agree well with the those from the literature that are derived directly, solely from measurements of the number of luminous and faint galaxies. However, our GDR results are not in agreement with those that are inferred from parametric fits to the luminosity function (eg. Andreon 2008, Crawford et al. 2009).

The GDR does not correlate with cluster mass estimates via X-ray temperature or weak-lensing. Similarly, we find no evidence for a correlation between GDR and the central entropy of the ICM or the dynamical state of the cluster (BCG to X-ray peak offset). These result agree with our finding that the intrinsic scatter in GDR vs z is consistent with zero. When considered individually however, both the number of dwarfs and the number of giants are strongly correlated with $T_x/E(z)$, which is expected from the known correlation between richness and T_x (Yee & Ellingson 2003).

Separate inspection of the evolving number of dwarfs and giants, after correcting to a common $T_x/E(z)$, suggests a change in the primary physical mechanism responsible for the evolution in the GDR over the redshift range $0.05 < z < 0.55$. From $z \sim 0.55$ to $z \sim 0.25$ we observe an overall increase in the number of both dwarfs and giants, with a more rapid increase among the dwarfs. Below $z \sim 0.2$ however, the number of dwarfs is roughly constant, while the number of giants decreases significantly.

To explain the transition at $z \sim 0.2$, we argue for a significant number of mergers within the giant population, caused by orbital decay due to dynamical friction. This is supported by calculations of the expected orbital decay time for giant galaxies, which yield timescales smaller than the span in look-back time of our sample. In this scenario, the GDR is governed by the competition between mergers, which become dominant at $z < 0.2$, versus the processes that act to increase the relative number of dwarf galaxies on the red sequence, such as the late-time quenching of star formation and the redshift dependence of the accreted-galaxy mass function. We consider the latter to be particularly important given the results of de Lucia et al. (2011) indicating that up to 50% of $\log M_*/M_\odot > 10$ galaxies fall into clusters at $z < 1.0$. A GDR evolution that is driven by a reduction in the number of giants at $z < 0.2$ could also explain why Crawford et al. (2009) find no evolution in the faint-end slope of the luminosity function at low redshift.

To test the merger-driven GDR scenario, we measure the integrated stellar mass in giants and dwarfs as a function of redshift. We find that $\langle M_*^d \rangle$ increases from $z \sim 0.55$ to $z \sim 0.25$ and remains roughly constant for $z < 0.25$, while $\langle M_*^g \rangle$ is roughly constant from $z \sim 0.55$ to $z \sim 0.2$ and then declines at $z < 0.2$. Because of the large scatter present in the values of M_*^g at fixed z and the uncertainty regarding the production of ICS, it is not possible to confirm nor deny the merger scenario with this measurement alone. To make progress requires measurement of the ICS fractions of clusters in our sample and better constraints on the evolution of the ICS.

The results presented in here clearly indicate an evolving GDR in our sample of 97 galaxy clusters at intermediate redshift. We are cautious, however, not to over-interpret the data in light of the fact that the sample is incomplete. Correlation between the GDR and global cluster properties, along with a covariance between said properties and z in our sample, could be misinterpreted as an enhancement of the GDR evolution. The data presented in §3.5, however, along with the good agreement with the literature values over a range of sample selection properties, and an intrinsic scatter that is consistent with zero, all indicate that this effect is negligible. A future study of the GDR using a sample that represents an evolutionary sequence of clusters (c.f. Hart et al. 2011), along with spectroscopic redshifts for identifying cluster members would be useful to confirm/deny these findings and allow for a clearer interpretation that is unaffected by potential selection biases. Numerical models of cluster formation that focus on the competition between mergers of existing cluster members versus the recent infall of new cluster galaxies, as it depends on galaxy mass

and redshift, would be valuable for assessing the proposed mechanisms for driving GDR evolution.

5.3 BCG Velocity Dispersions

In this chapter we measure the line-of-sight velocity dispersions (σ) from medium-resolution optical spectra for 19 BCGs selected from the CCCP survey. We combine the resulting σ measurements with the effective radii (r_e) and average effective intensities ($\langle I \rangle_e$) to explore the properties of the fundamental plane for BCGs. In addition to this, we use the σ and r_e values, along with some simplifying assumptions, to estimate the dynamical mass (M_{dyn}) interior to the effective radius. We summarize our most important findings below.

We present deep co-added spectra for the 19 BCGs in our sample. The spectra are extracted using an extraction aperture with a constant physical diameter of 10 kpc along the slit, representing the 'central' spectra. Though we present only a limited portion of the full observed wavelength range here, these spectra show a range of continuum shapes, absorption and emission line strengths. All of the spectra analyzed show some form of Balmer line activity, either via bright emission lines or absorption line infilling. The BCGs with the strongest color profile inversions in their cores from Bildfell et al. (2008) are also the ones that host the strongest emission lines.

The spectra described above are fit with a set of stellar templates using the pPXF code of Cappellari & Emsellem (2004) to extract the central velocity dispersion σ for each BCG. We find that the BCG show a wide range in central velocity dispersion from $217 < \sigma < 421$.

Combining our σ results with the structural parameter r_e and μ_e (measured for an $r^{1/4}$ in the r'-band) from Bildfell et al. (2008), we investigate the properties of the fundamental plane for BCGs as parameterized by $(\sigma, r_e, \langle I \rangle_e)$. Our BCGs occupy a tight FP that is fit with a model parameterized by $\log(r_e) = \alpha \log(\sigma) + \beta \log(\langle I \rangle_e) + \gamma$, where the best fit values obtained are: ($\alpha = 1.24 \pm 0.08$, $\beta = -0.80 \pm 0.1$, $\gamma = (0.3 \pm 2.0) \times 10^{-4}$). We measure a small but significant intrinsic scatter $\delta_{int} = 0.066 \pm 0.010$ in r_e which agrees well with previous results for regular cluster ellipticals. The presence of intrinsic scatter indicates that additional parameters may be important in determining the position of a BCG in $(\sigma, r_e, \langle I \rangle_e)$-space. We find, however, that there is no obvious correlation between the BCG FP residuals with either the BCG core-color, nor with the host cluster X-ray properties S_0 and $t_{c,0}$.

Based on the agreement between our BCG FP parameters and those of Jorgensen et al. (1996) for more regular cluster galaxies, we conclude that there is no strong evidence for a change in the 'tilt' (ie. curvature) of the FP over the range in $(\sigma, r_e, \langle I \rangle_e)$ space probed by these data sets.

Using the measured values of r_e and σ, we estimate the dynamical masses (M_{dyn}) of BCGs inside r_e. Comparing M_{dyn} with $T_x(0.3R_{500})$ and n_g, both proxies for cluster mass, we find that the BCG dynamical mass does not correlate with the mass of the host cluster. This indicates that there is a maximum mass for BCGs, which we estimate to be $M_{dyn} = (2.9 \pm 1.8) \times 10^{12} M_{\odot}$. Furthermore, this demonstrates that BCGs can be used as 'standard dumbbells', at least over the large cluster masses probed by our sample.

5.4 Final Comments

These conclusions, taken together, support a picture of significant late-time evolution in the stellar content of galaxy clusters. Clusters are clearly evolving, dynamic systems that have yet to reach a steady state. We have shown evidence of this dynamic behaviour in the statistics of cluster galaxy populations, the continued recent activity in the cores of BCGs, and by inference, an ever growing population of intra-clusters stars. Future work geared towards constraining the ICS fraction and measuring its evolution will be highly important for validation of this interpretation.

The work presented here represents a significant personal achievement. I would to say thank you to anyone that takes the time to read and consider my findings. A special thank you goes out my supervising committee for not only reading, but also editing this thesis. It has been a great pleasure and privilege to be able to make this small yet significant contribution to the collective human knowledge in the field of extra-galactic astronomy.

Appendix A

Red Sequence Fitting

As mentioned in §3.3.1 we use the biweight estimator of Beers et al. (1990) to fit the color-magnitude relation (CMR) for the galaxy distribution inside a projected radius of 500 kpc from the BCG. Lacking spectroscopic redshifts for the cluster galaxies, we begin the fitting procedure by estimating a region in the CMD that is likely to be minimally contaminated by interloper galaxies. To the points lying inside this region we then apply a red sequence fitting procedure similar to that used by Pimbblet et al. (2002). We first determine the probability that a galaxy belongs to the field population using equation A.1:

$$P_f(m_{r'}, g'-r') = \frac{\Sigma_f(m_{r'}, g'-r')}{\Sigma_f(m_{r'}, g'-r') + \Sigma_c(m_{r'}, g'-r')} \tag{A.1}$$

where Σ_f is the surface density of field galaxies, Σ_c is the surface density of cluster galaxies and both are functions of $m_{r'}$ and $(g'-r')$. The surface densities are estimated by generating a 2-d histogram of galaxies in color-magnitude space using a bin height and width of $\Delta(g'-r') = 0.078$ and $\Delta m_{r'} = 0.56$. The denominator in equation A.1 is calculated using galaxies within a projected radius of 500 kpc from the BCG where there is a mix of the cluster and field populations, while the numerator is calculated using galaxies that are outside a projected radius of 1.5 Mpc where the sample should be more dominated by the field population. We chose the 1.5 Mpc limit in order to be as far away from the BCG as possible while maintaining a large enough field-sampling region at the low redshift end of the survey $z \sim 0.05$. At this redshift roughly 45% of the image is available for estimating the field population. With each galaxy assigned a probability of being a field member (P_{field}) and a probability of being a cluster member ($1 - P_{field}$) we then fit the red sequence to the points inside

the selection box. We randomly reject points inside the initial selection box based on their probability of being members of the field and then perform an unweighted, linear least-squares fit on the remaining data. This procedure is repeated 100 times. We take the median values of these 100 solutions as the best fitting slope and intercept parameters with their errors determined by the standard deviation.

The results of the red sequence fitting for all clusters are plotted in figure A.1 through A.6. In each panel we show, for a given cluster, the best fit red sequence, a model red sequence for comparison and the dwarf/giant magnitude limits at the corresponding redshift. The model red sequence is constructed assuming that the correlation between galaxy color and magnitude is driven solely by an increasing metallicity with stellar mass. We use the Charlot & Bruzual (2007) synthetic stellar population code (hereafter CB07) with a Salpeter initial mass function and a single burst of star formation at $z = 3$ to compute synthetic galaxy colors over a range of metallicities. Each model CMR also contains a small contribution (3% by mass) of ultra metal-poor stars, which Maraston et al. (2009) find is necessary to reproduce the $(g' - r')$ color of early type galaxies at similar redshifts. Without this component the models are up to 0.1 magnitudes too blue. The model is then calibrated to reproduce the magnitude vs metallicity relation Kodama & Arimoto (1997). It can be seen from Figures A.1 through A.6 that the model CMR is in qualitative agreement with the observations, including their evolution. The model CMR slope however is typically shallower than the best fit CMR and this difference in slope can vary appreciably from cluster to cluster. This is likely a consequence of the over-simplicity of calibration to a fixed magnitude metallicity relation and the use of a single stellar population. We take the model as illustrative only and for the purposes of classifying giants and dwarfs we use the CMR as defined by the fit.

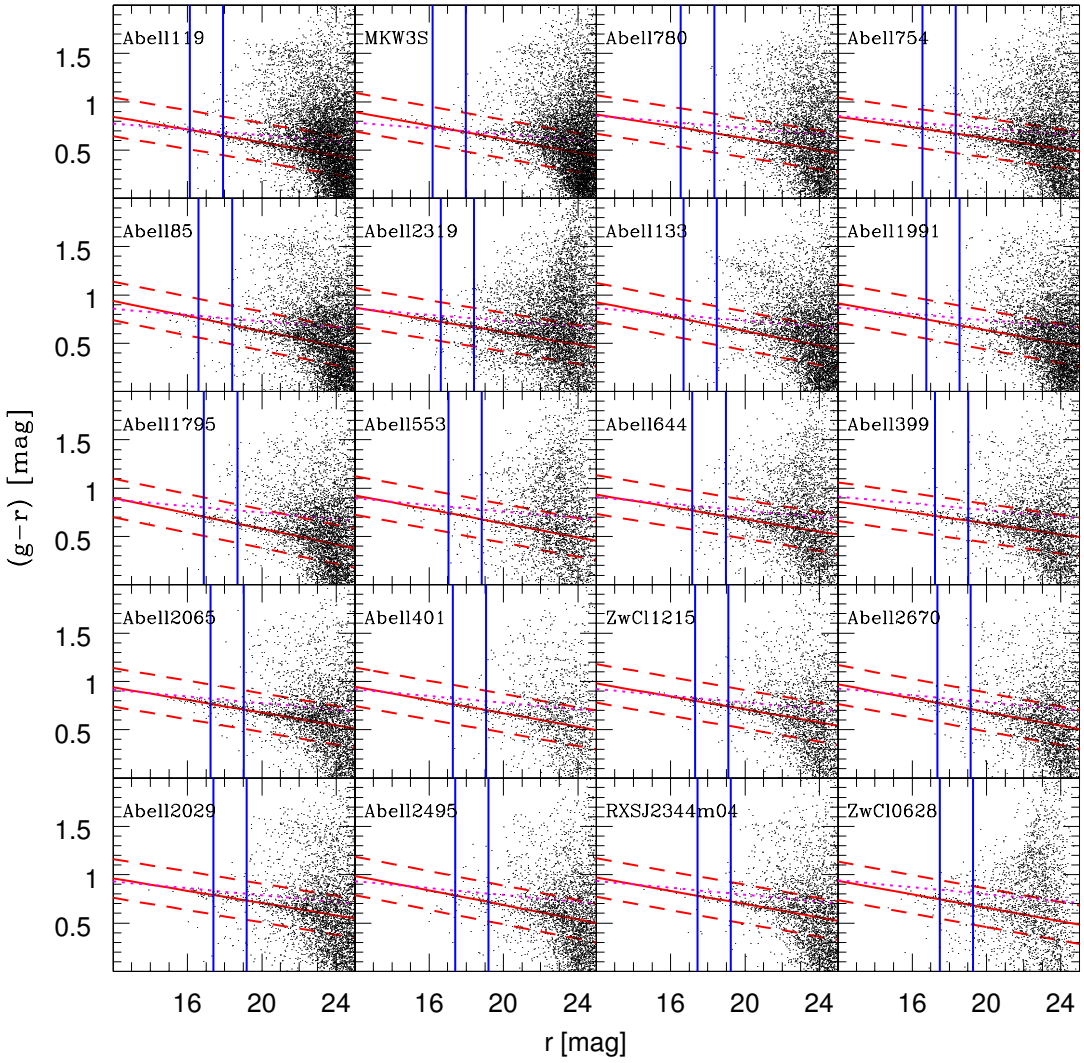

Figure A.1: Illustration of our red sequence fitting procedure. Clusters are arranged in increasing redshift from the top left. The solid red line shows the CMR according to a linear fit to the data while the dotted magenta line shows the CMR defined by a stellar population that was created in a burst at $z = 3$ and aged passively (see text). The dashed red lines show the color offset $\Delta(g' - r') = \pm 0.2$ used for selecting red sequence members. The vertical blue lines show the limits to classify dwarfs and everything brighter than this is classified as a giant.

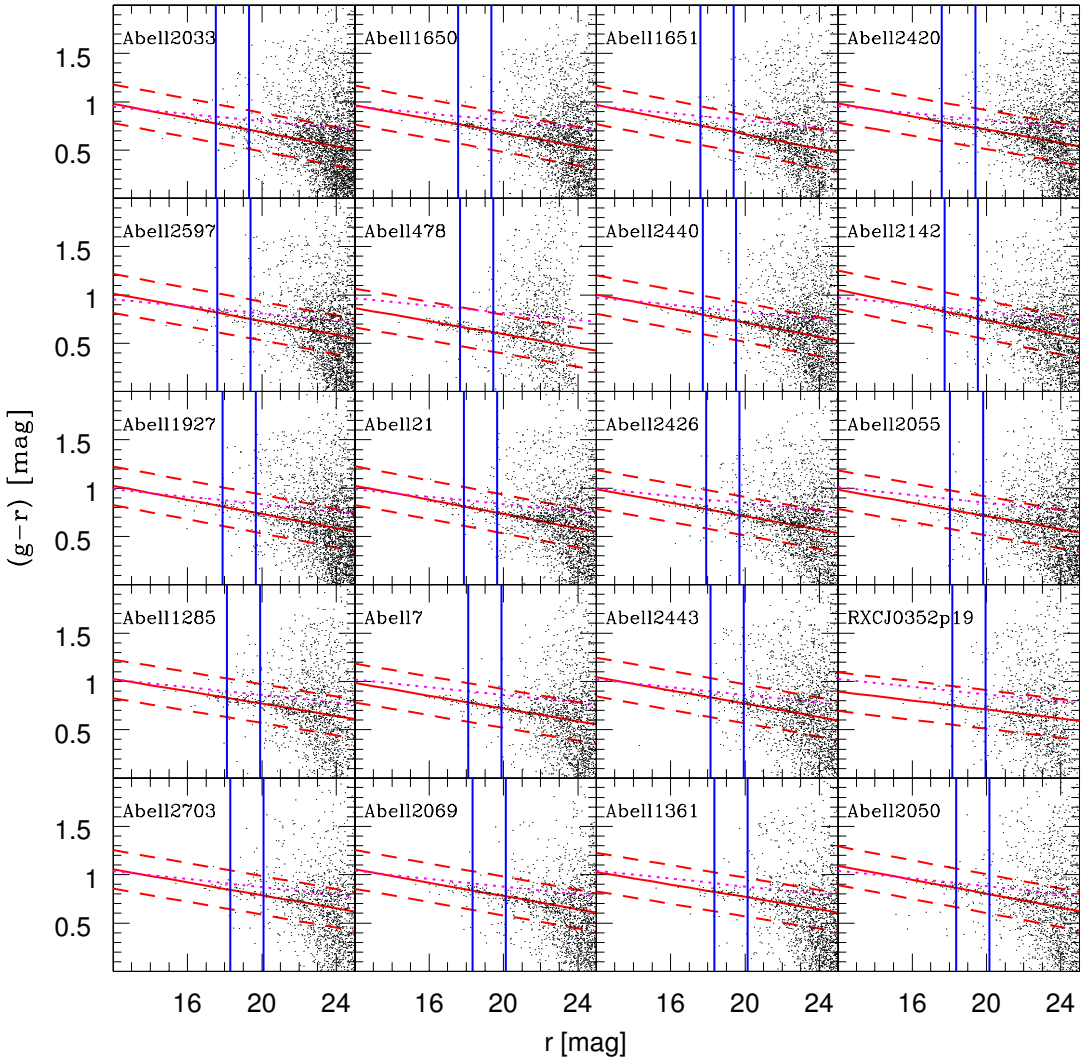

Figure A.2: Illustration of our red sequence fitting procedure (continued). Clusters are arranged in increasing redshift from the top left. The solid red line shows the CMR according to a linear fit to the data while the dotted magenta line shows the CMR defined by a stellar population that was created in a burst at $z = 3$ and aged passively (see text). The dashed red lines show the color offset $\Delta(g' - r') = \pm 0.2$ used for selecting red sequence members. The vertical blue lines show the limits to classify dwarfs and everything brighter than this is classified as a giant.

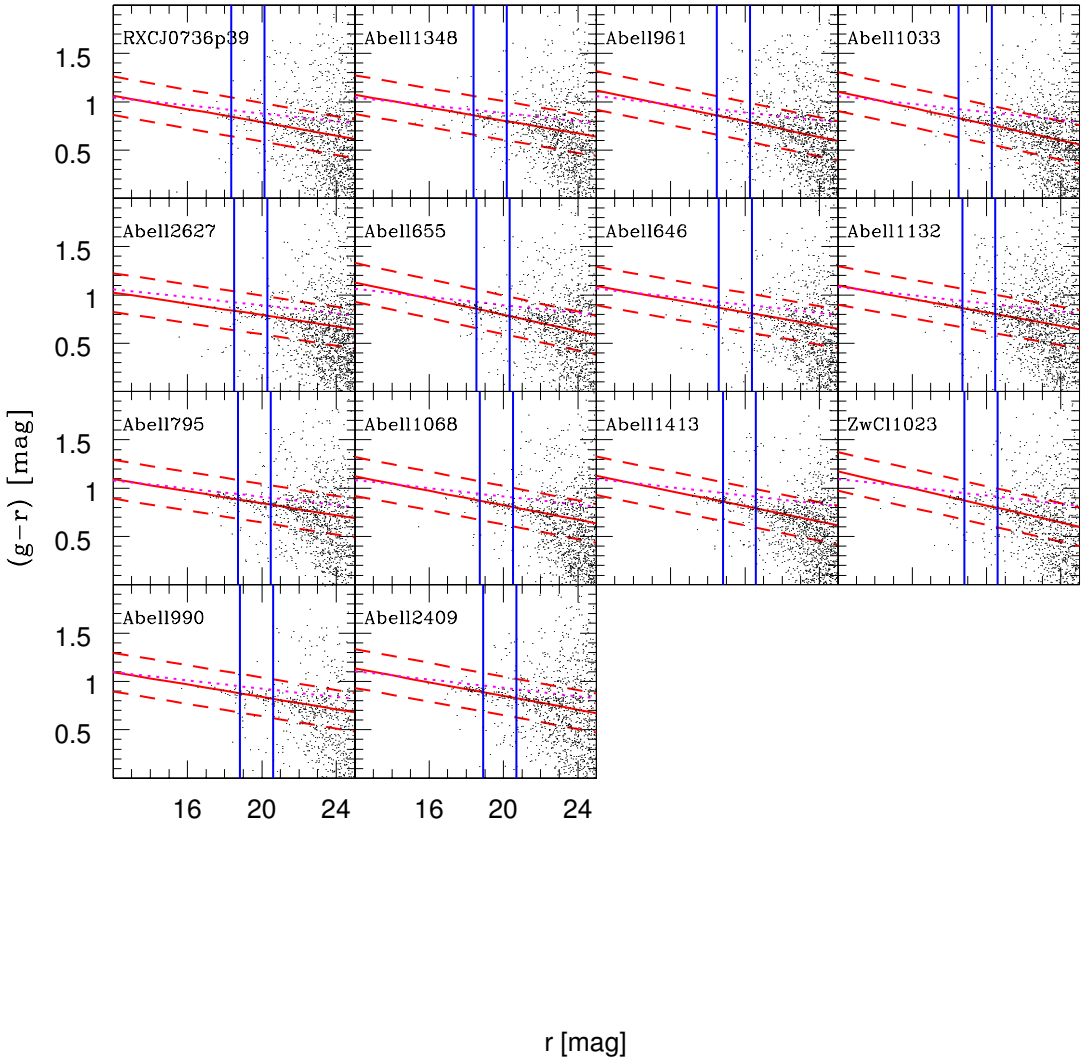

Figure A.3: Illustration of our red sequence fitting procedure (continued). Clusters are arranged in increasing redshift from the top left. The solid red line shows the CMR according to a linear fit to the data while the dotted magenta line shows the CMR defined by a stellar population that was created in a burst at $z = 3$ and aged passively (see text). The dashed red lines show the color offset $\Delta(g' - r') = \pm 0.2$ used for selecting red sequence members. The vertical blue lines show the limits to classify dwarfs and everything brighter than this is classified as a giant.

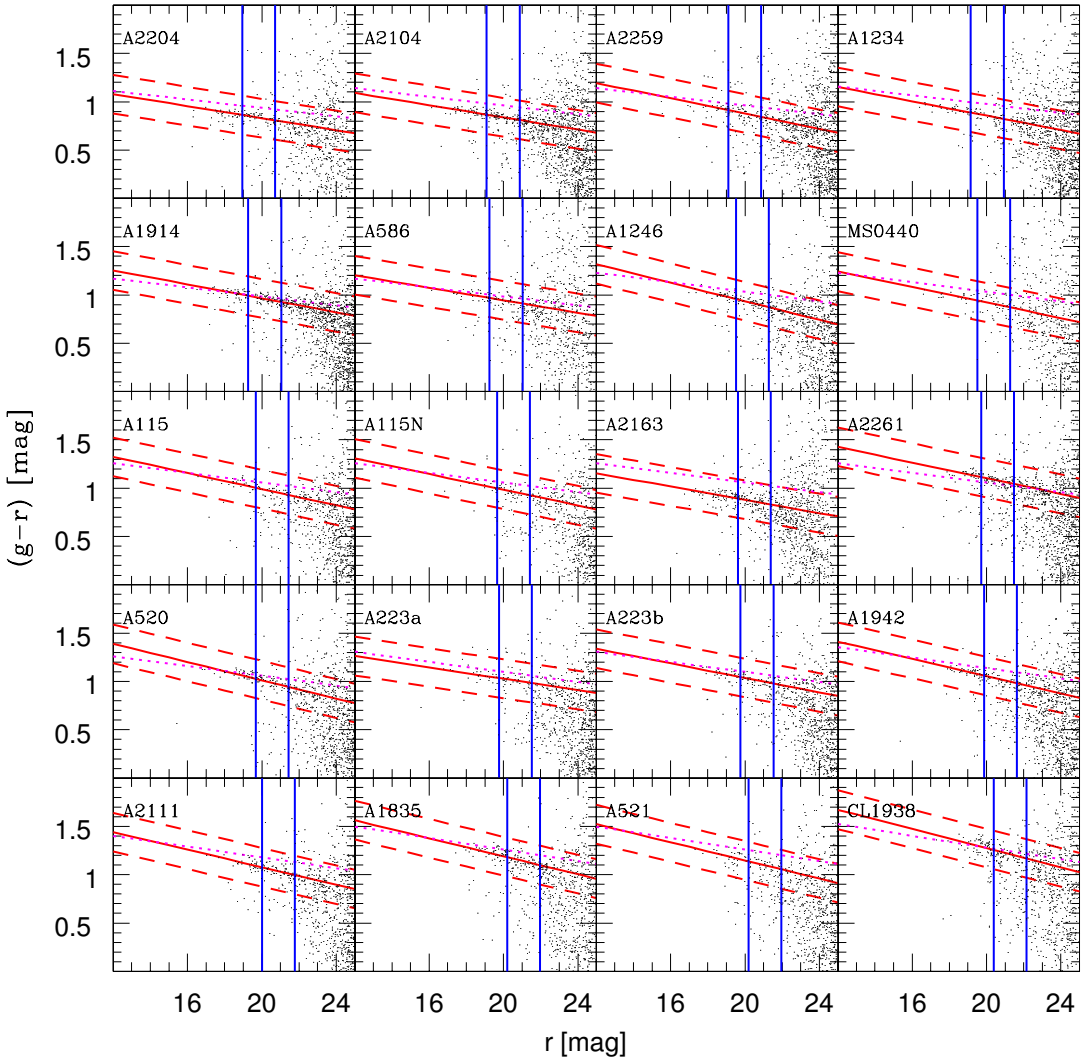

Figure A.4: Illustration of our red sequence fitting procedure (continued). Clusters are arranged in increasing redshift from the top left. The solid red line shows the CMR according to a linear fit to the data while the dotted magenta line shows the CMR defined by a stellar population that was created in a burst at $z = 3$ and aged passively (see text). The dashed red lines show the color offset $\Delta(g' - r') = \pm 0.2$ used for selecting red sequence members. The vertical blue lines show the limits to classify dwarfs and everything brighter than this is classified as a giant.

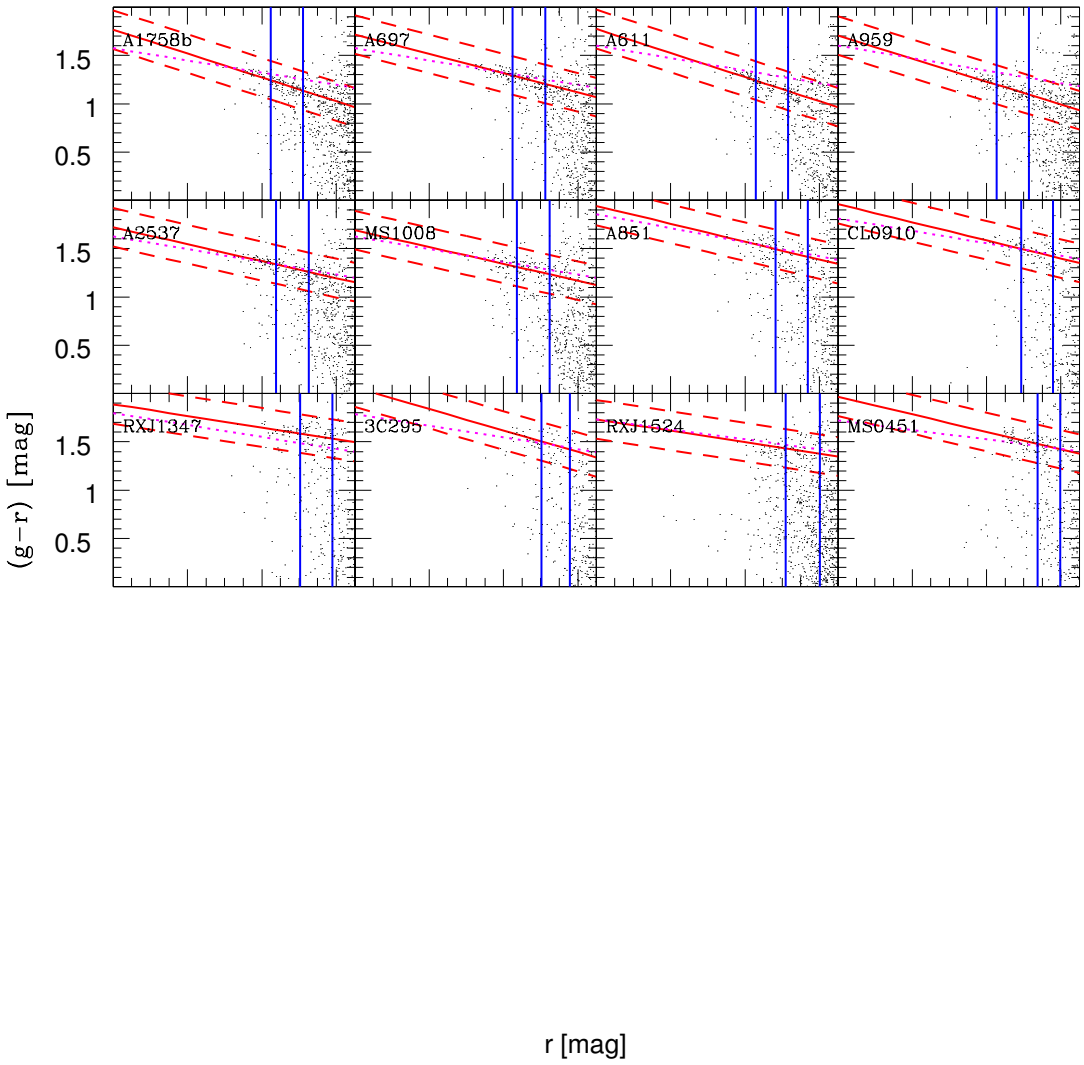

Figure A.5: Illustration of our red sequence fitting procedure (continued). Clusters are arranged in increasing redshift from the top left. The solid red line shows the CMR according to a linear fit to the data while the dotted magenta line shows the CMR defined by a stellar population that was created in a burst at $z = 3$ and aged passively (see text). The dashed red lines show the color offset $\Delta(g' - r') = \pm 0.2$ used for selecting red sequence members. The vertical blue lines show the limits to classify dwarfs and everything brighter than this is classified as a giant.

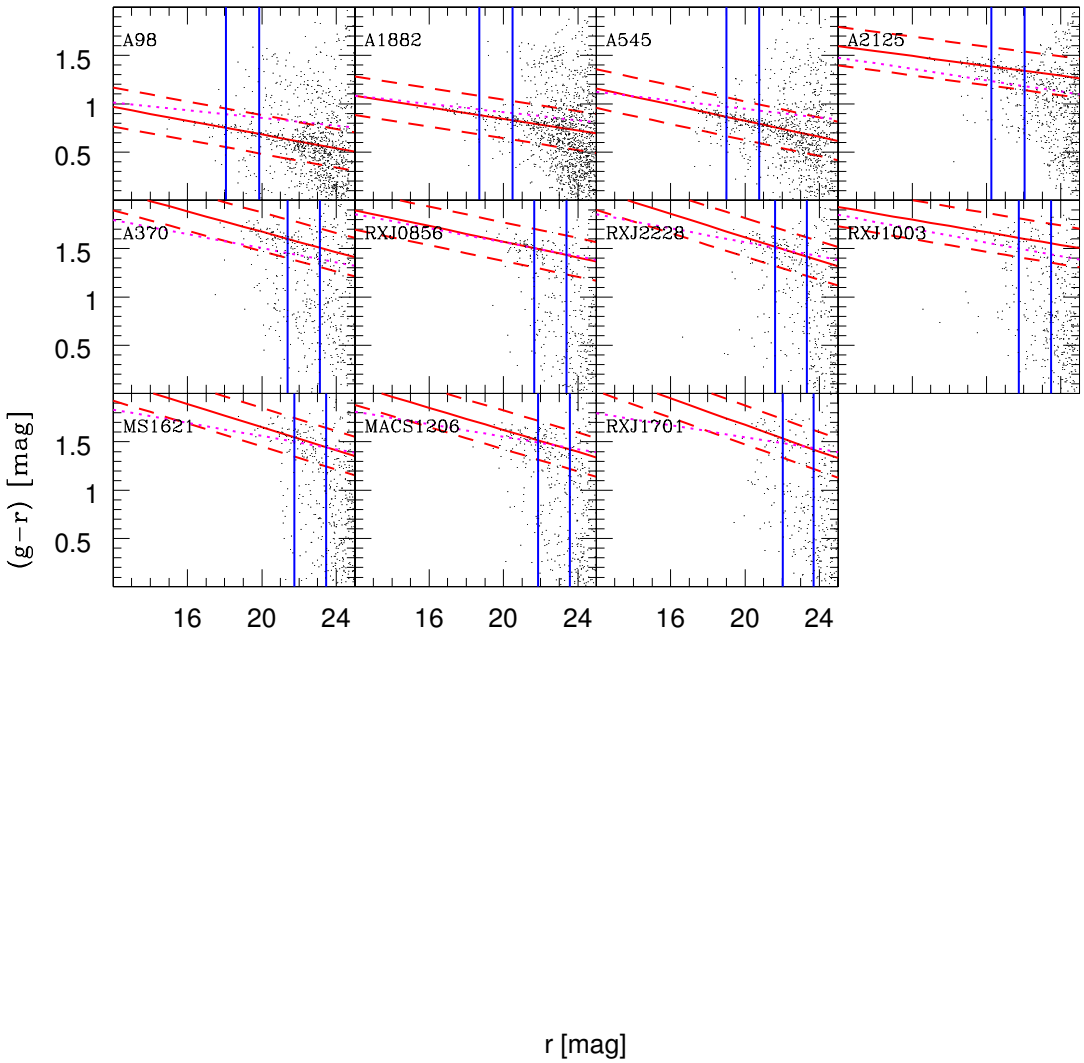

Figure A.6: Illustration of our red sequence fitting procedure (continued). Clusters are arranged in increasing redshift from the top left. The solid red line shows the CMR according to a linear fit to the data while the dotted magenta line shows the CMR defined by a stellar population that was created in a burst at $z = 3$ and aged passively (see text). The dashed red lines show the color offset $\Delta(g' - r') = \pm 0.2$ used for selecting red sequence members. The vertical blue lines show the limits to classify dwarfs and everything brighter than this is classified as a giant.

Appendix B

Commonly Used Terms and Acronyms

The following table shows a list of terms and acronyms, along with their definitions, that are used often throughout this thesis.

Table B.1: This table list commonly used terms and acronyms (first column) along with a brief definition/description for each (second column).

Term	Definition
2MASS	two micron all-sky survey
A&A	Astronomy & Astrophysics
AGN	active galactic nucleus
AJ	Astronomical Journal
ApJ	Astrophysical Journal
arXiv	astro-ph preprint server
ASCA	advanced satellite for cosmology and astrophysics
ASPC	Astronomical Society of the Pacific
BAX	online database for X-ray observations of clusters
BCG	brightest cluster galaxy
CB07	synthetic stellar spectra code
CC cluster	cool core cluster
CCCP	Canadian cluster comparison project
	Continued on next page...

Table B.1 continued...

Term	Definition
CDM	cold dark matter
CFH12K	optical camera on CFHT
CFHT	Canada-France-Hawaii telescope
CFHTLS	Canada-France-Hawaii telescope legacy survey
Chandra	space-based X-ray telescope
CMB	cosmic microwave background
CMD	color-magnitude diagram
CMR	color-magnitude relation
CL09	CL 09104+4109 (galaxy cluster)
DGR	dwarf-to-giant ratio
DM	dark matter
DOF	degrees of freedom
DTD	delay time distribution
E	elliptical (galaxy morphology)
FIRST	faint images of the radio sky at twenty centimetres
FP	fundamental plane
FWHM	full width at half maximum
GALEX	space-based UV telescope
GALFIT	galaxy morphology modelling code
GDCD	giant-to-dwarf color difference
GDR	giant-to-dwarf ratio
GMRT	giant metrewave radio telescope
HST	Hubble space telescope
HLIRG	hyper-luminous infra-red galaxy
ICM	intra-cluster medium
IGM	intra-group medium
ICL	intra-cluster light
ICS	intra-cluster stars
IC SN	intra-cluster supernova
IDL	interactive data language (programming environment)
IFU	integral field unit (spectrograph type)
IMF	initial mas function

Continued on next page...

Table B.1 continued...

Term	Definition
IR	infra-red
Irr	irregular (galaxy morphology)
JACO	joint analysis of cluster observations
K-correction	magnitude correction for spectral shift
LCDM	Λ cold dark matter
λCDM	Λ cold dark matter
LINER	low-ionization nuclear emission line region
LOS	line of sight
MegaCam	optical camera on CFHT
MENeaCS	multi-epoch nearby cluster survey
Millennium Simulation	cosmological dark matter simulation
MMT	multiple mirror telescope (optical telescope)
MNRAS	Monthly Notices of the Royal Astronomical Society
MPFITEXY	data fitting routines with errors in both x and y
NCC cluster	non-cool core cluster
PhDT	PhD thesis
pPXF	galaxy spectrum modelling code
PSF	point spread function
RMS	root mean square
S	spiral (galaxy morphology)
S0	lenticular (galaxy morphology)
SDSS	sloan digital sky survey (ground-based optical)
SExtractor	source extractor (image analysis code)
SF	star formation
SN	supernova
SNe	supernovae (plural)
SNIa	type Ia Supernova
SNII	type II Supernova
SSP	single stellar population (model)
SZ effect	Sunyaev-Zel'dovich effect
UV	ultra-violet
VLA	very large array (radio telescope)

Continued on next page...

Table B.1 continued...

Term	Definition
WFPC2	camera on HST
WL	weak gravitational lensing
WMAP	Wilkinson microwave anisotropy probe
XMM-Newton	space-based X-ray telescope